

---

# Investigating the 3D chromatin architecture with fluorescence microscopy

Dissertation der Fakultät für Biologie  
der Ludwig-Maximilians-Universität München



Katharina Brandstetter

München, 15. Dezember 2020



---

Diese Dissertation wurde angefertigt  
unter der Leitung von Herrn Prof. Dr. Heinrich Leonhardt  
im Bereich Humanbiologie und BioImaging  
an der Ludwig-Maximilians-Universität München.

Erstgutachter: Prof. Dr. Heinrich Leonhardt

Zweitgutachter: Prof. Dr. Peter Becker

Tag der Abgabe: 15.12.2020

Tag der mündlichen Prüfung: 16.02.2021

#### EIDESTÄTTLICHE VERSICHERUNG UND ERKLÄRUNG

Ich versichere hiermit an Eides statt, dass ich meine Dissertation selbstständig und ohne unerlaubte Hilfsmittel angefertigt habe.

Die vorliegende Dissertation wurde weder ganz noch teilweise bei einer anderen Prüfungskommission vorgelegt.

Ich habe noch zu keinem früheren Zeitpunkt versucht, eine Dissertation einzureichen oder an einer Doktorprüfung teilzunehmen.

München, den 15.12.2020

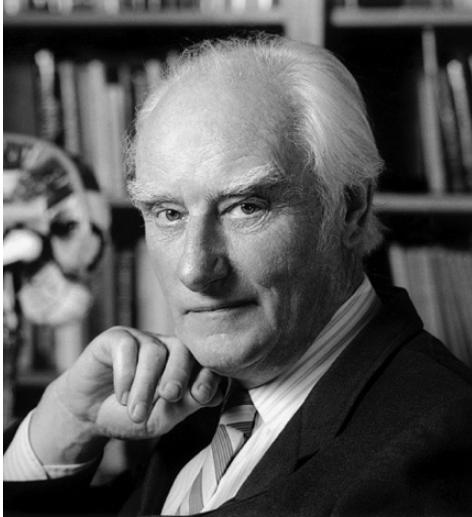
---

Katharina Brandstetter



---

## 1978: Francis H. C. Crick's view on the future of chromosome research



Francis Crick (1916 – 2004)  
(NobelPrize.org, 2020)

“The most general unanswered question appears to be: how much does the 3D structure of the eukaryotic genome matter for expression, compared to the 1D structure? ... The methods of studying 3D structures with precision are far more difficult than the methods available for sequencing DNA. Thus, if it turns out ... that the 3D structure is not merely a packaging device needed mainly for mitosis but is also of primary importance for gene expression, then ... we will need a more devious and ingenious plan of attack. Only time can show which alternative is preferred by nature and how difficult the problem will turn out to be.” (Crick, 1978)

---

## List of publications

Parts of this thesis have been published elsewhere or are in preparation for publication:

Cremer, M.\* , **Brandstetter, K.\*** , Maiser, A., Rao, S.S.P., Schmid, V.J., Guirao-Ortiz, M., Mitra, N., Mamberti, S., Klein, K.N., Gilbert, D.M., *et al.* (2020a). Cohesin depleted cells rebuild functional nuclear compartments after endomitosis. *Nature Communications* *11*, 6146.

Schwach, J., Kolobynina, K., **Brandstetter, K.**, Gerlach, M., Ochtrop, P., Helma, J., Hackenberger, C.P.R., Harz, H., Cardoso, M.C., Leonhardt, H., *et al.* (2020). Site-Specific Antibody Fragment Conjugates for Reversible Staining in Fluorescence Microscopy. *Chembiochem*.

**Brandstetter, K.\***, Zülske, T.\* , Ragoczy, T., Hörl, D., Stamatoyannopoulos, J.A., Leonhardt, H., Wedemann, G., and Harz, H. (in preparation). Comparison of DNase I hypersensitive and insensitive chromatin in human cells by super-resolution microscopy and computer simulations.

\* equal contribution

---

# TABLE OF CONTENTS

<b>1</b>	<b>SUMMARY</b>	<b>9</b>
<b>2</b>	<b>ZUSAMMENFASSUNG</b>	<b>10</b>
<b>3</b>	<b>INTRODUCTION</b>	<b>12</b>
<b>3.1</b>	<b>HISTORICAL VIEW ON CHROMATIN ARCHITECTURE</b>	<b>12</b>
<b>3.2</b>	<b>METHODS TO STUDY CHROMATIN ORGANIZATION AND THEIR FINDINGS</b>	<b>15</b>
3.2.1	CONFORMATION CAPTURE TECHNIQUES	16
3.2.2	FLUORESCENCE IN SITU HYBRIDIZATION (FISH)	18
3.2.3	SUPER-RESOLUTION LIGHT MICROSCOPY	21
3.2.4	ELECTRON MICROSCOPY	23
3.2.5	LIVE CELL IMAGING	24
3.2.6	DNASE-SEQ	26
3.2.7	MNASE-SEQ	27
3.2.8	CHIP-SEQ	28
3.2.9	COMPUTATIONAL MODELS	30
<b>3.3</b>	<b>REMAINING DISCREPANCIES</b>	<b>32</b>
<b>4</b>	<b>RESULTS</b>	<b>34</b>
<b>4.1</b>	<b>COHESIN DEPLETED CELLS REBUILD FUNCTIONAL NUCLEAR COMPARTMENTS AFTER ENDOMITOSIS</b>	<b>34</b>
<b>4.2</b>	<b>SITE-SPECIFIC ANTIBODY FRAGMENT CONJUGATES FOR REVERSIBLE STAINING IN FLUORESCENCE MICROSCOPY</b>	<b>68</b>
<b>4.3</b>	<b>COMPARISON OF DNASE I HYPERSENSITIVE AND INSENSITIVE CHROMATIN IN HUMAN CELLS BY SUPER-RESOLUTION MICROSCOPY AND COMPUTER SIMULATIONS</b>	<b>92</b>
<b>5</b>	<b>DISCUSSION</b>	<b>125</b>
<b>5.1</b>	<b>EFFECTS OF COHESIN LOSS ON THE FUNCTIONAL CHROMATIN LANDSCAPE</b>	<b>125</b>
<b>5.2</b>	<b>FLUORESCENCE IN SITU HYBRIDIZATION LABELING STRATEGIES</b>	<b>128</b>
<b>5.3</b>	<b>CHARACTERIZATION OF ACTIVE AND INACTIVE INTERPHASE CHROMATIN</b>	<b>131</b>
<b>5.4</b>	<b>CONCLUSION</b>	<b>134</b>

---

<b>6</b>	<b>REFERENCES</b>	<b>135</b>
----------	-------------------	------------

<b>7</b>	<b>APPENDIX</b>	<b>157</b>
----------	-----------------	------------

<b>7.1</b>	<b>ABBREVIATIONS</b>	<b>157</b>
------------	----------------------	------------

<b>7.2</b>	<b>DECLARATION OF CONTRIBUTION</b>	<b>159</b>
------------	------------------------------------	------------

<b>7.3</b>	<b>CURRICULUM VITAE</b>	<b>FEHLER! TEXTMARKE NICHT DEFINIERT.</b>
------------	-------------------------	---

## I SUMMARY

Chromatin is an assembly of DNA and nuclear proteins, which on the one hand has the function to properly store the 2 meters of DNA of a diploid human nucleus in a small volume and on the other hand regulates the accessibility of specific DNA segments for proteins. Many cellular processes like gene expression and DNA repair are affected by the three-dimensional architecture of chromatin.

Cohesin is an important and well-studied protein that affects three-dimensional chromatin organization. One of the functions of this motor protein is the active generation of specific domain structures (topologically associating domains (TADs)) by the process of loop extrusion. Studies of cohesin depleted cells showed that TAD structures were lost on a population average. Due to this finding, the question arose, to what extent the functional nuclear architecture, that can be detected by confocal and structured illumination microscopy, is impaired when cells were cohesin depleted. The work presented in this thesis could show that the structuring of the nucleus in areas with different chromatin densities including the localization of important nuclear proteins as well as replication patterns was retained. Interestingly, cohesin depleted cells proceeded through an endomitosis leading to the formation of multilobulated nuclei. Obviously, important structural features of chromatin can form even in the absence of cohesin.

In the here presented work, fluorescence microscopic methods were used throughout, and an innovative technique was developed, that allows flexible labeling of proteins with different fluorophores in fixed cells. With this technique DNA as well as peptide nucleic acid (PNA) oligonucleotides can be site-specifically coupled to antibodies via the Tub-tag technology and visualized by complementary fluorescently labeled oligonucleotides. The advantages and disadvantages of PNAs as docking strands are discussed in this thesis as well as the use of PNAs in fluorescence in situ hybridization (FISH).

In the next study, which is part of this work, a combination of FISH and super-resolution microscopy was used. There it could be shown that DNA segments of 5 kb can form both compact and elongated configurations in regulatory active as well as inactive chromatin. Coarse-grained modeling of these microscopic data, in agreement with published data from other groups, has suggested that elongated configurations occur more frequently in DNA segments in which the occupancy of nucleosomes is reduced. The microscopically measured distance distributions could only be simulated with models that assume different densities of nucleosomes in the population. Another result of this study was that inactive chromatin - as expected - shows a high level of compaction, which can hardly be explained with common coarse-grained models. It is possible that environmental effects that are difficult to simulate play a role here.

Chromatin is a highly dynamic structure, and its architecture is constantly changing, be it through active processes such as the effect of cohesin investigated here or through thermodynamic interactions of nucleosomes as they are simulated in coarse-grained models. It will take a long time until we adequately understand these dynamic processes and their interplay.

## 2 ZUSAMMENFASSUNG

Chromatin ist Aggregat aus DNA und Kernproteinen, das einerseits die Aufgabe hat die 2 Meter DNA eines diploiden menschlichen Zellkerns in einem kleinen Volumen sicher zu verpacken und andererseits die Zugänglichkeit einzelner DNA-Abschnitte für Proteine regelt. Viele zelluläre Funktionen sind von der 3D-Architektur des Chromatins abhängig. Diese beeinflusst unter anderem die Regulation der Genexpression und notwendige DNA-Reparaturprozesse.

Cohesin ist eines der wichtigsten und am besten untersuchten Proteine, welches wesentlichen Einfluss auf die Chromatinstruktur nimmt. Eine der Funktionen dieses Motorproteins ist die aktive Erzeugung bestimmter Domänenstrukturen (sog. „topologically associating domains“ (TADs)) durch sog. „loop extrusion“. Studien, bei denen der Cohesin-Gehalt in Zellen stark vermindert wurde, zeigten, dass in der Folge auch die TAD-Strukturen im Populationsmittel verschwinden. Das warf die Frage auf, inwieweit die funktionale Kernarchitektur, wie sie mit konfokaler Mikroskopie und Mikroskopie mit strukturierter Beleuchtung erfasst werden kann, beeinträchtigt ist, wenn die Zellen an Cohesin verarmt sind. Eine Studie der vorliegenden Arbeit zeigt, dass die Strukturierung des Kerns in Bereiche unterschiedlicher Chromatindichte samt der zugehörigen Lokalisation wichtiger Kernproteine sowie der Replikationsstrukturen erhalten bleiben. Auffällig ist, dass die Zellen nur eine Endomitose durchlaufen, so dass multilobulierte Kerne entstehen. Offensichtlich können sich wichtige strukturelle Eigenschaften des Kerns auch in Abwesenheit von Cohesin bilden.

In der vorliegenden Arbeit wurden an vielen Stellen fluoreszenzmikroskopische Methoden eingesetzt und eine innovative Methode wurde entwickelt, mit der Proteine in fixierten Zellen flexibel mit verschiedenen Fluorophoren markiert werden können. Mit dieser Technik können sowohl DNA als auch Peptidnukleinsäure (sog. peptide nucleic acid (PNA)) mittels der sogenannten Tub-Tag-Technologie ortsspezifisch an Antikörper gekoppelt werden. Diese gekoppelten Oligonukleotide können dann durch komplementäre fluoreszenzmarkierte Oligonukleotide ausgelesen werden. Vor- und Nachteile der PNAs als sog. „Docking“-Stränge werden ebenso diskutiert wie der Einsatz von PNAs in der Fluoreszenz In Situ Hybridisierung.

Eine weitere Studie, in der eine Kombination aus sehr hoch auflösender Mikroskopie und Fluoreszenz In Situ Hybridisierung verwendet wurde, konnte zeigen, dass 5 kb lange DNA-Abschnitte neben kompakten auch sehr gestreckte Konformationen sowohl in regulatorisch aktivem wie auch inaktivem Chromatin ausbilden können. Coarse-Grained Modelle dieser Daten hat in Übereinstimmung mit kürzlich publizierten Daten anderer Gruppen nahegelegt, dass die gestreckten Konformationen häufiger in DNA-Abschnitten vorkommen, bei denen die Belegungsdichte von Nukleosomen reduziert ist. Die mikroskopisch gemessenen Abstandsverteilungen konnten nur mit Modellen simuliert werden, die unterschiedliche Belegungsdichten von Nukleosomen in der Population annehmen. Ein weiteres Ergebnis dieser Studie ist, dass inaktives Chromatin -wie erwartet- eine große Kompaktierung aufweist, die mit

gängigen Coarse-Grained Modellen aber kaum zu erklären ist. Möglicherweise spielen hier schwer zu simulierende Umgebungseffekte eine Rolle.

Chromatin ist eine hochdynamische Struktur, deren Architektur sich ständig ändert, sei es durch aktive Prozesse wie der Wirkung des hier untersuchten Cohesins oder auch durch thermodynamische Wechselwirkungen von Nukleosomen wie sie in Coarse-Grained Modellen simuliert werden. Es wird noch viel Zeit vergehen, bis diese Prozesse und ihr Zusammenspiel hinreichend verstanden sind.

### 3 INTRODUCTION

#### 3.1 Historical view on chromatin architecture

There are and have always been a lot of researchers who contributed to the field of chromatin research. Unfortunately, I can only name a few here but the passionate work and crucial findings of each one of them paved the way to what is known today and have to be appreciated. A timeline of the most important findings regarding chromatin and its organization from 1879 to 1985 are depicted in Figure 1 (for review, see Cremer and Cremer (2010); Deichmann (2015); Olins and Olins (2003)).

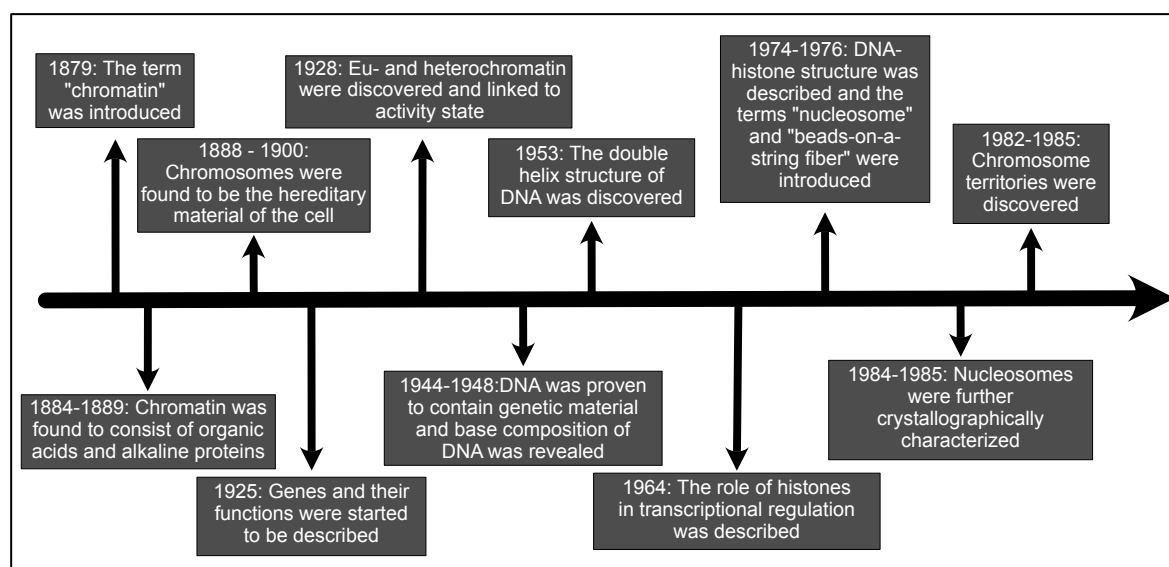


**Figure 1:** Timeline of the most important findings in the field of chromatin from 1879 until 1985.

In the late 19<sup>th</sup> century biochemistry and microscopy were on the rise (Bracegirdle, 1989; Bradbury, 1989) and helped to facilitate an increasing number of studies on the hereditary material of eukaryotic cells. In 1869, Friedrich Miescher isolated the contents of nuclei of lymphocytes which he called "nuclein" and therefore defined the genetic material as a distinct molecule (Miescher-Rüsch, 1871). The German cytologist Walther Flemming introduced the term "chromatin" in 1879 while he studied mitosis in a light microscope and described the easily stainable structure in the nucleus with this term (Flemming, 1882; Hughes, 1959; Paweletz, 2001). He suggested that chromatin and nuclein might be the same structure. In 1884, Alfred Kossel and, in 1889, Richard Altmann discovered that nuclein or chromatin consisted of organic acids, which he called nucleic acids, and alkaline proteins, which were later called histones (Altmann, 1889; Kossel, 1911). In the same year, Wilhelm Waldeyer coined the term "chromosome" for the chromatin segments which were visible during mitosis as rod-like structure (Waldeyer, 1888). Many of the biologists, including Edmund Wilson and Theodor Boveri, during that time, thought that chromosomes are the hereditary material of a cell which is divided during mitosis and passed on to the daughter cells (Boveri, 1888; Wilson, 1896). Especially August Weismann's work connected chromatin and

heredity (Weismann, 1883; Weismann et al., 1891). During the late 19<sup>th</sup> and the early 20<sup>th</sup> century, the concept became more and more accepted and the importance of chromosomes as hereditary material and basis was recognized. The beginning of the 20<sup>th</sup> century was also the time when Gregor Mendel's studies on single genes were in the focus of the field. He and other geneticists studied the effects of the chromosomal location and the environment on genes. In 1925, Alfred Sturtevant and Hermann Muller, who joined Thomas H. Morgan's research group, found that the position of a gene on the chromosome has an effect on its function (Muller, 1927; Sturtevant, 1925). Muller also described inactive regions of chromatin which were later connected to heterochromatin which was found by Emil Heitz (Heitz, 1928a; Muller, 1946). By improvement of cytological staining methods, Heitz discovered that staining density varied between parts of mitotic chromosomes and defined these regions as euchromatin and heterochromatin. He suggested that heterochromatin represents genetically passive regions (Berger, 2019).

In 1944, Oswald Avery, together with Colin MacLeod and Maclyn McCarty, demonstrated with an experiment using bacterial transformation that deoxyribonucleic acid (DNA) is the material that contains genetic information and transforms bacteria (Avery et al., 1944). A few years later, Avery's fellow Rollin Hotchkiss used paper chromatography to study the base composition of DNA and found that different species have different base ratios. During these experiments, Hotchkiss not only found the four DNA bases adenine, thymine, guanine, and cytosine but also a slightly different form of cytosine which he called epicytosine and was later found to be the methylated form of cytosine (Hotchkiss, 1948; Witkin, 2005). Another researcher who greatly contributed to DNA research was Erwin Chargaff. He discovered that the number of guanines is equal to the number of cytosines and the number of thymines is equal to the number of adenines in the DNA which hinted at the base pairing in DNA. Secondly and independently of Hotchkiss, he proposed that the ratios of the four bases differ from species to species (Chargaff et al., 1950). His two proposed rules paved the way for Francis Crick, James Watson, and Maurice Wilkins for their discovery of the double-helix structure of DNA for which they were awarded the Nobel prize in 1962 (Watson and Crick, 1953; Wilkins et al., 1953). Based on fundamental studies using X-ray crystallography by Rosalind Franklin, Raymond Gosling, and Maurice Wilkins (Franklin and Gosling, 1953), they developed a model that the DNA molecule has a helical structure with antiparallel orientation in 1953.

In the 1960s, many researchers studied the structure and function of chromatin. Vincent Allfrey and Alfred Mirsky confirmed in 1964 that histones inhibit transcription and found that histone modifications like methylation and acetylation are associated with gene expression (Allfrey et al., 1964). Also, E.W. Johns found evidence for interactions between histones and DNA and the effect on gene control (Johns, 1969). In 1974, R. Kornberg and J. Thomas discovered and chemically characterized the complex formed out of four histone proteins and approximately 200 base pairs of DNA (Kornberg, 1974; Kornberg and Thomas, 1974). The structure received its name "nucleosome" in 1975 (Oudet et al., 1975). The electron microscopic identification of nucleosomes

and DNA by Donald Olins and Ada Olins (Olins and Olins, 1974) and in parallel C.L.F. Woodcock (Woodcock, 1973; Woodcock et al., 1976) brought new advances in the field of chromatin research in the 1970s. The discovery of nucleosomes and the postulation of models that DNA is wrapped around the histones forming a beads-on-a-string fiber and therefore being accessible for other DNA binding proteins was revolutionary and the nucleosome became the fundamental unit for chromatin and chromatin function (for review, see Olins and Olins (2003)). The view on higher-order packaging of DNA and DNA-based processes changed during that time. The crystal structure of the nucleosome was of major interest and two groups worked on solving the structure. In 1984 and 1985, T. Richmond (Richmond et al., 1984) and G. Bunick (Uberbacher and Bunick, 1985) published the first papers on the crystal structure of the nucleosome. Both groups kept working on crystallography of nucleosomes and later on both groups solved the structure at a higher resolution (Harp et al., 2000; Luger et al., 1997; Richmond and Davey, 2003). The core of the nucleosome, where 146 bp of DNA are wrapped around, consists of an octamer of four pairs of different histone proteins (H2A, H2B, H3, and H4). All of the four core proteins contain a protein tail which is used for posttranslational modifications affecting gene expression. The length of linker DNA between core particles varies between species and between different chromatin regions. The complex of nucleosomes and DNA is highly conserved in eukaryotes (for review, see Olins and Olins (2003)).

Already in 1885, Carl Rabl suggested that chromosomes follow a territorial organization in interphase nuclei of animal cells (Rabl, 1885). The term chromosome territories (CT) was later introduced by Theodor Boveri, who proposed that chromosomes which are individually visible during mitosis maintain their individuality in interphase (Boveri, 1909). In the 1950s, electron microscopy studies suggested that chromatin fibers intermingle, and individual chromosomes cannot be seen in interphase nuclei. In the 1970s and 1980s, only a few researchers believed in the concept of CTs. Among these researchers were William Dewey, David Brown, and Stephen Stack who found clumps of condensed chromatin in different cell types after a modified Giemsa staining which led them to the conclusion that interphase chromosomes stay within their distinct domain (Stack et al., 1977). Further experiments using laser-UV-microirradiation brought another evidence for CTs (Cremer et al., 1982a; Cremer et al., 1982b; Zorn et al., 1979; Zorn et al., 1976). A small part of the nuclei of living Chinese hamster cells was UV-damaged with a laser-microbeam in G1 phase and pulse-labeled with  $^3\text{H}$ -thymidine to test the following two hypotheses: (1) if the chromatin fibers of different chromosomes are distributed throughout the whole nucleus, the microirradiation with subsequent pulse-labeling of damaged DNA would lead to a scattered pattern on many different chromosomes; (2) if the chromosomes occupy distinct territories in the interphase nucleus, the damaged DNA after microirradiation would be found on only a few different chromosomes. The detection of the damaged DNA by autoradiography in cells fixed directly after the pulse or in metaphase spreads fixed after the next mitosis showed that the small part of DNA that was UV-damaged constitutes only a small fraction of the chromatin fibers and

therefore confirmed hypothesis (2) and the CT concept. The development of fluorescence in situ hybridization (FISH) techniques in the mid 1980s facilitated the direct visualization of CTs (Manuelidis, 1985; Schardin et al., 1985). By generation of chromosome-specific probes painting of individual chromosomes was possible. Based on FISH experiments, CTs were shown to be non-randomly distributed in the nucleus. Gene-rich chromosomes were found in the nuclear interior in many different cell types, whereas gene-poor chromosomes were located at the periphery of nuclei (Cremer et al., 2003; Cremer et al., 2001; Croft et al., 1999). Therefore, the distribution of chromatin was shown to be non-random, radial, and gene density-dependent (Boyle et al., 2001). Typically, the nuclear interior constitutes a transcriptionally active compartment, whereas heterochromatin and silent genes can be found at the nuclear periphery (for review, see Cremer and Cremer (2010)).

The advances in the field of chromatin architecture showed that chromatin in interphase nuclei is organized on multiple levels. On the one end, the first step of higher-order chromatin structure is the beads-on-a-string fiber, whereas on the other end chromosomes form their own territories. By the end of the 20<sup>th</sup> century, the concepts of DNA being wrapped around nucleosomes and chromosomes being organized in specific territories in interphase were widely accepted. By that time, it was thought that chromatin follows a hierarchical organization where the beads-on-a-string fiber folds and coils into higher-order compaction steps like the 30-nm fiber until it ends as mitotic chromosomes. This hierarchical model could be found in textbooks for a long time (for review, see Hansen et al. (2018)). By now, it is known that the 30-nm fiber does not occur in cells in vivo and that there have to be other organizational structures which compact the two meters of DNA in the nucleus but keep its function.

### **3.2 Methods to study chromatin organization and their findings**

During the last 40 years, many powerful methodologies in the fields of light and electron microscopy, labeling and dyes, ligation-based chromatin capture, and many more have been developed which promote studies on chromatin organization and drive the advances in the field (Figure 2) (for review, see Lakadamyali and Cosma (2020)). All of these studies helped to understand the complexity of the cell nucleus and still many more phenomena remain to be solved. However, understanding chromatin organization is essential to elucidate how the information in eukaryotic genomes is organized and accessed to function correctly.

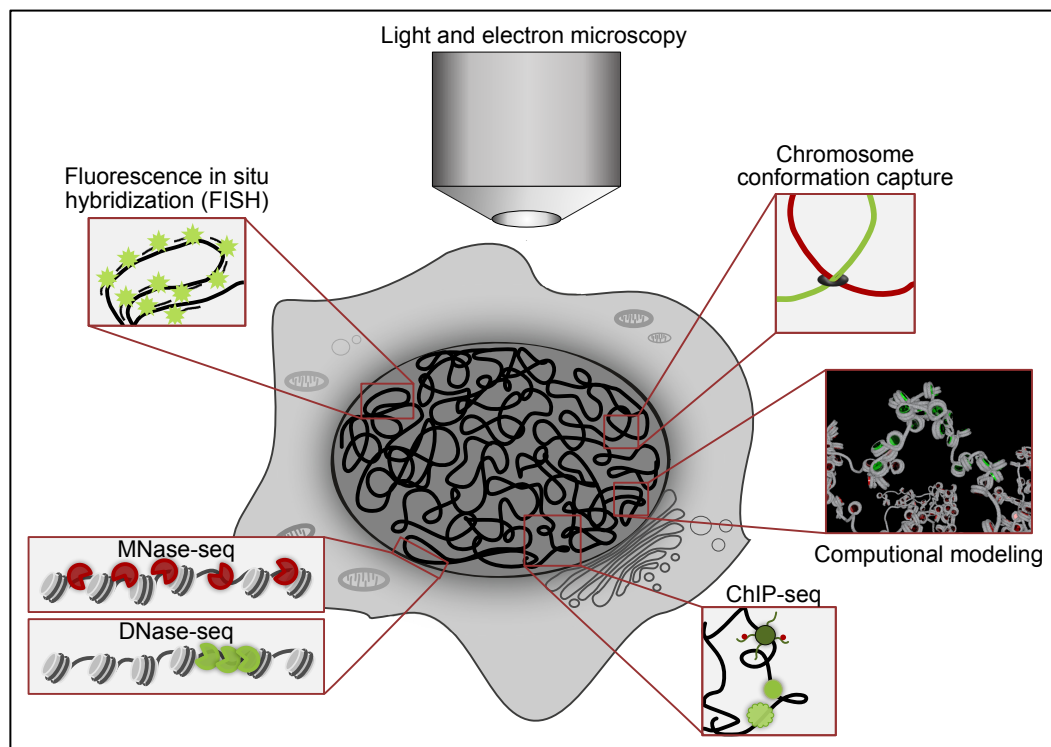


**Figure 2: Many different techniques are available to study chromatin architecture.** The nucleus of a cell contains an assembly of DNA and proteins, called chromatin. The spatial organization of chromatin can be studied using different methods. With light and electron microscopy, chromatin can be imaged. By fluorescence in situ hybridization DNA can be sequence-specifically visualized for example for fluorescence light microscopy. Chromosome conformation capture techniques (3C, 4C, 5C, Hi-C) can be used to detect contact frequencies between genomic loci. By digestion of chromatin with MNase and subsequent sequencing nucleosome positions can be determined. Active regulatory elements, which are characterized by nucleosome-free DNA stretches, can be detected by digestion with DNase 1 and sequencing. ChIP-seq can identify binding sites of chromatin-associated proteins. Furthermore, computational models like coarse-grained simulation can support interpretation and understanding of complex datasets generated by all the different experimental methods and help filling the gaps of experimental methods.

### 3.2.1 Conformation capture techniques

Regulation of gene expression in complex eukaryotic genomes is often regulated by spatial proximity of distant genomic elements like promoters and enhancers. In order to investigate these long-range spatial interactions and the underlying mechanisms, the technique of chromosome conformation capture (3C) was introduced in 2002 by Dekker et al. (Dekker et al., 2002). By using 3C, the lab of Wouter de Laat showed that the locus control region (LCR) of the  $\beta$ -globin locus physically associates with the active globin gene even if the LCR is 10 to 60 kb upstream of the genes (Tolhuis et al., 2002). The 3C technology enabled the identification of many more long-range interactions, for example in the  $\alpha$ -globin locus (Vernimmen et al., 2007; Zhou et al., 2006) and the interleukin gene cluster (Spilianakis and Flavell, 2004). Later on, various adaptations of 3C were developed like chromosome conformation capture-on-chip and circular chromosome conformation capture (4C) (Simonis et al., 2006; Zhao et al., 2006). With the 4C methods interactions of a single locus with regions throughout the whole genome can be identified and cis-regulatory landscapes of genes have been investigated (Franke et al., 2016; Symmons et al., 2016).

The further extension which is called chromosome conformation capture carbon copy (5C) can be used to map physical interactions in a larger region of interest (Dostie et al., 2006). 5C has been used to identify compartmentalization of chromosomes into topologically associating domains (TADs) of the X-chromosome (Nora et al., 2012). The development of Hi-C which combines the proximity-based ligation and high-throughput sequencing has led to major advances in the field of three-dimensional chromatin organization (Figure 3), in particular the identification of higher-order chromatin interactions genome-wide (Lieberman-Aiden et al., 2009). The lab of Bing Ren has used Hi-C to describe topological domains in the whole genome for the first time and characterize their properties (Dixon et al., 2012). They identify topological domains which are megabase-sized local chromatin interaction domains in human and mouse genomes in embryonic stem cells and terminally differentiated cell types. Dixon and colleagues found that these domains are both stable across embryonic and differentiated cell types and highly conserved between mouse and human. Furthermore, boundaries of heterochromatin mark H<sub>3</sub>K<sub>9</sub>me<sub>3</sub> are correlated with the boundaries of these topological domains. In addition, they identified factors which are enriched at domain boundaries like the CCCTC-binding factor (CTCF), housekeeping genes, tRNAs, and retrotransposons. Later on, different studies showed that the emergence of TADs is driven by loop extrusion by cohesin, which is a ring-like multi-subunit protein complex (Davidson et al., 2019; Fudenberg et al., 2017; Rao et al., 2017). The frequency of the interactions identified by conformation capture-based methods is more complicated to be measured and the models developed from these methods often do not reflect the highly dynamic nature of spatial interactions in the genome.

Another feature of genome architecture which could be identified using Hi-C is the compartmentalization of the genome in the nucleus. By applying a principal component analysis to Hi-C data ligation events were separated into two compartments. These two compartments correlated to the activity state of chromatin. The A compartment contains transcriptionally active, open chromatin, which has a high DNase I hypersensitivity, whereas the B compartment consists of repressed, closed chromatin marked by repressive histone modifications (Lieberman-Aiden et al., 2009). A mechanism that drives compartmentalization could be similar to microphase segregation and mediated by higher affinity between heterochromatic regions (reviewed in Mirny et al. (2019)).

Hi-C has also been used to study how chromatin organization is re-established after mitosis which disrupts the organization into TADs and compartments (Abramo et al., 2019; Zhang et al., 2019). At the telophase stage, a transient intermediate is formed after condensin-mediated mitotic loops are lost. During cytokinesis, TAD positions start to emerge when the cohesin-mediated CTCF-CTCF loops start to form. A and B compartments also form early after mitosis and expand and intensify during G<sub>1</sub> phase.

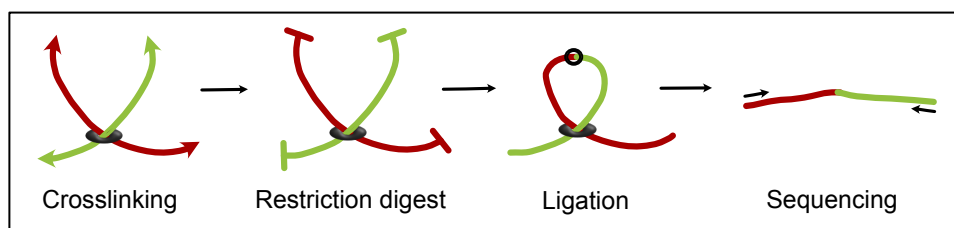


**Figure 3: Principle of chromosome conformation capture techniques.** DNA contacts are crosslinked by fixation. Subsequently DNA is digested, and the neighboring open DNA ends are ligated. By sequencing these ligated DNA fragments contacts between loci can be identified (modified from McCord et al. (2020)).

### 3.2.2 Fluorescence In Situ Hybridization (FISH)

Since its development fluorescence in situ hybridization (FISH) has been a powerful tool to label specific genomic regions and its sensitivity and versatility were improved and refined since then. In situ hybridization techniques are based on the ability of the DNA double-strand to reform after denaturation (Figure 4). The first in situ hybridization experiment in 1969 used radioactive labels to detect a specific DNA sequence in the nucleus of frog eggs with autoradiography (Gall and Pardue, 1969). A few years later, fluorescent labels were introduced (Rudkin and Stollar, 1977) and today mostly fluorescent labels for fluorescence microscopy are used.

The protocols for in situ hybridization involve many different steps. Cells, metaphase spreads of chromosomes or tissues have to be fixed, washed with different salt solutions and treated with chaotropic reagents like formamide as a preparation for the actual hybridization step. The DNA double-strand is denatured by heat or chemicals and the DNA probe can subsequently hybridize to its complementary sequence. Probes can be directly labeled or an additional step to label the hybridized probe might be necessary. After the hybridization more washing steps are required to avoid background signal from unspecifically bound probes.

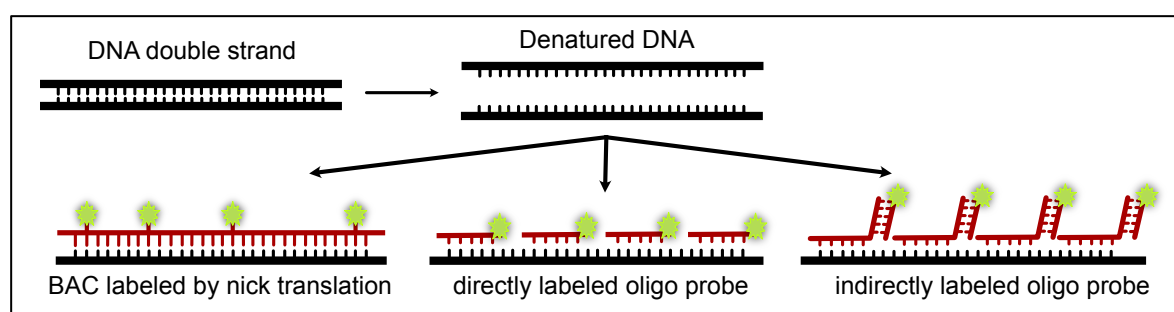


**Figure 4: Principle of fluorescence in situ hybridization (FISH).** The DNA double strand is denatured by heat and different types of probes can be hybridized to the single-stranded DNA. Bacterial artificial chromosomes (BACs) contain segments of the respective genome e.g., the human genome. They are usually labeled by nick translation where fluorescently labeled nucleotides are incorporated. Oligo-based probes can be directly labeled (middle) or can have overhangs that are labeled by a second fluorescently labeled probe.

Many cytogeneticists use FISH for clinical diagnostics of various chromosomal abnormalities like deletions, duplications, and translocations. The hybridization probes mostly used for diagnostics

are bacterial artificial chromosome (BAC) clones (Figure 4) from the Human Genome Project (Cheung et al., 2001). This collection of BAC clones contains over 7000 DNA clones of specific bands on human chromosomes and for every megabase segment of the genome at least one clone is available. Not only cytogeneticists but also genome biologists use DNA FISH to study three-dimensional genome organization. Several studies using FISH have led to key findings in the field. For example, chromosomes occupying their specific chromosome territories (Beliveau et al., 2012; Bienko et al., 2013; Rosin et al., 2018) (for review, see Cremer and Cremer (2010)), topologically associating domains (TADs) (Bintu et al., 2018; Cattoni et al., 2017; Szabo et al., 2018; Wang et al., 2016) and chromatin conformation in different epigenetic states (Boettiger et al., 2016) have been visualized. Additionally, the spatial positioning of genomic loci within the nucleus has been studied revealing that repressed genes are often closer to the nuclear lamina than active genes (Boyle et al., 2001; Ferrai et al., 2010). Recent high-throughput imaging using FISH has revealed a large cell-to-cell and allele-to-allele variability of spatial genome organization like gene positioning and TAD organization (Finn et al., 2019). These FISH results correlate with Hi-C findings meaning that regions which have a higher contact frequency in Hi-C tend to be on average spatially closer in FISH experiments. However, they also show that on a single cell level these regions can have a spatial distance similar to regions with very low contact frequency.

The use of BAC clones as FISH probes is a powerful method but has limitations. One of the limitations is the large size that the probes span (~100 kb) and which impairs the detection of small loci. The advances in DNA sequencing and synthesis have facilitated the development of probes made of chemically synthesized oligonucleotides (oligos). Oligo probes helped to overcome the limitation of large target sizes and enabled the visualization of small genomic loci that only span a few kilobases. Not only the ability to target small regions is a major advantage of synthetic oligo probes but also the possibility to precisely engineer and optimize the sequences to avoid repetitive sequences and off-target binding, have specific thermodynamic properties, GC content, and degree of secondary structure and integrate different labeling techniques (Figure 4). The possibility to generate complex oligo libraries and from them DNA FISH probes by PCR-based methods like Oligopaints (Beliveau et al., 2017; Beliveau et al., 2012) allowed the labeling of single-copy regions and transcripts (Boyle et al., 2011; Yamada et al., 2011). In order to support the design of such high complexity oligo probe sets several computational tools have been developed like OligoMiner (Beliveau et al., 2018), iFISH4U (Gelali et al., 2019) and PaintSHOP (Hershberg et al., 2020). By appending synthetic barcode sequences to the probe oligos the Oligopaints approach allows multiplexing experiments. The number of targets is increased in sequential rounds of imaging beyond the chromatic limits by labeling the barcodes with fluorescently labeled secondary probes via hybridization. The advances in robotics and microfluidics facilitate further improvements for multiple labeling rounds. Multiplexing is for example used in DNA FISH studies (Bintu et al., 2018; Cardozo Gizzi et al., 2019; Mateo et al., 2019; Wang et al., 2016) and in

studies investigating spatial transcriptomics of mRNA molecules (Chen et al., 2015; Levesque and Raj, 2013; Shah et al., 2018).

The potential of DNA probes for multiplexed imaging has also been used for other types of detection. DNA-PAINT is a labeling technique for multiplexed super-resolution microscopy which is based on transient binding of short fluorescently labeled oligos. First, DNA-PAINT was implemented to image DNA nanostructures. The nanostructures contain unlabeled docking strands which are complementary to fluorescently labeled imager strands. By repetitive transient binding of these complementary strands fluorescence switches between on- and off-state and can, therefore, be used for detection with single molecule localization microscopy (SMLM). Since the binding between docking and imager strand is transient multiplexing and multicolor imaging is straightforward (Exchange PAINT). By coupling spectrally distinct dyes to unique DNA sequences (barcodes) the specificity for multiplexing experiments is ensured. Several studies showed multicolor imaging of DNA nanostructures using DNA-PAINT (Derr et al., 2012; Johnson-Buck et al., 2013; Jungmann et al., 2012; Jungmann et al., 2010; Lin et al., 2012). Coupling of antibodies or nanobodies to DNA docking strands and subsequently labeling with complementary imager strands allows multiplexed immunodetection of proteins in fixed cells with a single fluorophore and laser line (Jungmann et al., 2014; Schueder et al., 2017; Werbin et al., 2017).

In addition to DNA oligonucleotides, artificial oligonucleotides from peptide nucleic acids (PNA) can be used as labeling probes, imager strands or coupled to antibodies or nanobodies. PNAs were introduced by Nielsen et al. in 1991 (Nielsen et al., 1991). These synthetic DNA analogs have a peptidic backbone instead of a phosphoribosyl backbone like DNA (Figure 5) and PNA molecules can easily be labeled with biotin or fluorophores. The peptidic backbone of PNAs is uncharged, thus, repulsion by the negatively charged DNA backbone is less which allows varying hybridization conditions and more efficient invasion into double-stranded DNA. PNA-DNA duplexes are more stable than DNA-DNA double strands and thus melting temperature increases. Another feature of the unnatural backbone of PNAs is that it is resistant to nuclease or protease degradation. PNAs were also shown to be more sensitive to base mismatches than DNA leading to a higher specificity. Furthermore, they are able to bind under low ionic strength conditions. In situ hybridization, their properties lead to a lower background which makes them versatile FISH probes. PNA-FISH has been used for quantitative analysis of human telomeric repeat sequences (Lansdorp et al., 1996). Another study used PNA-FISH for chromosomal analysis of human spermatozoa which have rather inaccessible chromatin. PNAs were shown to specifically bind their target even in compacted sperm chromatin and the hybridization time for PNAs was drastically reduced in comparison to DNA-FISH (Pellestor et al., 2003). The high binding stability can also be a disadvantage when a readout probe has to be washed out for sequential labeling. The high cost in comparison to DNA oligonucleotides leads to a less routine use of PNAs. However, their unique properties make PNAs a versatile tool for broad use in biological applications (for review, see Pellestor and Paulasova (2004); Saarbach et al. (2019)).

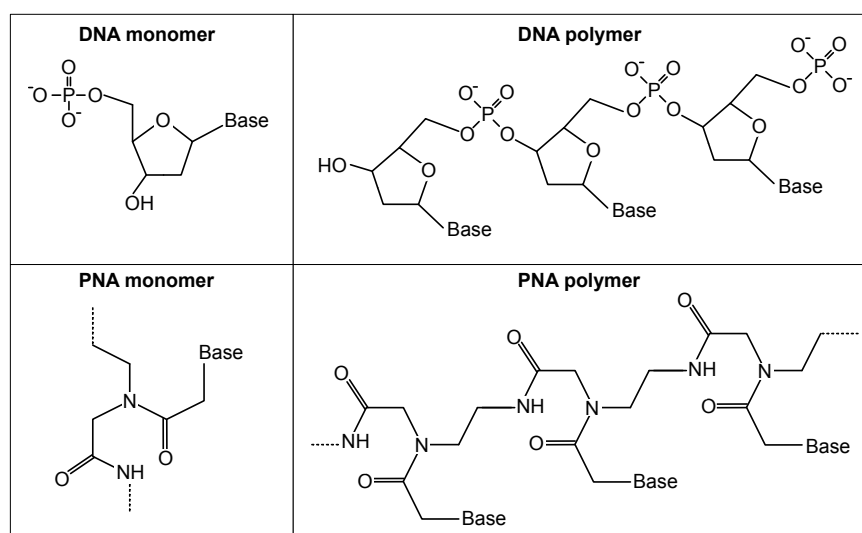


**Figure 5: Molecular structure of deoxyribonucleic acid (DNA) and peptide nucleic acid (PNA).** The DNA monomer or also called deoxyribonucleotide consists of the sugar deoxyribose, a phosphoryl group and a nitrogenous base. By phosphodiester bonds between the OH-group of one nucleotide and the phosphate group of another nucleotide the DNA polymer with a sugar-phosphate backbone is formed. The backbone is negatively charged because of the phosphate residues. The DNA analog peptide nucleic acid (PNA) contains the peptide N-(2-aminoethyl)-glycine instead of the sugar. To this peptide the nitrogenous bases can be bound. By peptide bonds these subunits are linked and a PNA polymer with an uncharged peptide backbone is formed.

### 3.2.3 Super-resolution light microscopy

The development of super-resolution microscopy technologies leads to an improvement of the spatial resolution in  $xy$  from  $\sim 250$  nm to 10 – 50 nm (Sahl et al., 2017). The resolution limit of light microscopy has been a fundamental limit for studies of genome organization. Super-resolution technologies like structured-illumination microscopy (SIM) (Gustafsson, 2005), single-molecule localization microscopy (SMLM, including STORM and PALM) (Betzig, 1995; Moerner and Kador, 1989), and stimulated emission depletion (STED) (Figure 6) (Hell and Wichmann, 1994) microscopy have been used to visualize nuclear structures smaller than the diffraction limit. Together with advanced labeling techniques and fluorescent dyes, these imaging methods foster our understanding of the nuclear organization.

Especially SMLM has been used to study chromatin structure. Ricci et al. visualized nucleosome organization in the nucleus by using STORM and revealed that nucleosomes form heterogeneous groups, so-called nucleosome clutches (Ricci et al., 2015). These clutches cluster and form so-called clutch domains. Similar to recent EM studies, they did not find evidence for 30-nm fibers and a hierarchical organization of the genome. Between clutches, which correspond to a few kilobases of DNA, nucleosome-poor regions were found. Size and density of nucleosome clutches are cell type specific. Pluripotent embryonic stem cells show a smaller clutch size and density than somatic cells. Clutch size is also dependent on histone modifications. Repressive histone marks like H3K27me3 lead to larger nanodomains, while active marks (H3K9ac, H3K4me3) correspond to less compact domains (Otterstrom et al., 2019; Ricci et al., 2015). In addition, another super-resolution

study which used inhibition of histone deacetylase (HDAC) to induce hyperacetylation showed that hyperacetylated cells have smaller and looser nanodomains (Xu et al., 2018). Boettiger et al. used STROM imaging combined with Oligopaint (OligoSTORM) to compare the occupied volume between regions with different epigenetic marks and therefore different activity states (active, inactive, Polycomb repressed) in *Drosophila* cells (Boettiger et al., 2016). Active regions were less compacted and occupied a larger volume than inactive and repressed regions. Interestingly, they found that distinct patterns of folding and compaction were also present in large inactive regions of the genome (depleted of specific histone H<sub>3</sub> marks). OligoSTORM has also been used to walk along chromosomes and trace the folding of DNA strands in 3D (Bintu et al., 2018; Mateo et al., 2019; Nir et al., 2018; Wang et al., 2016). With a resolution of 30 kb, Bintu et al. (Bintu et al., 2018) generated distance heat maps for these 30 kb segments and revealed that these heat maps showed highly heterogeneous boundaries of TADs in single-cells but when averaged over hundreds of cells the same TAD structure like Hi-C maps with strong boundaries at CTCF and cohesin sites could be found. Depletion of cohesin resulted in more variable boundary positions in single cells but did not eliminate globular TAD structures. The method called optical reconstruction of chromatin architecture (ORCA) has enabled to decrease the step size of sequentially labeled chromosome segments to 2-10 kb (Mateo et al., 2019). This study used DNA and RNA FISH in cryosections of *drosophila* embryos and found that the correlation between spatial proximity of promoter and enhancer and active transcription was weak and that many active promoters were not physically close to their enhancer.

In comparison to SMLM there are fewer studies using STED to image chromatin. STED imaging requires large laser powers to achieve a resolution increase (Figure 6). Therefore, dyes that can be used for STED microscopy need to fulfill many properties. The advantages of STED microscopy are that its photodetectors directly count photons per pixel and no image reconstruction is needed which enables quantitative assessment of images. Many STED systems use red and far-red excitation lasers and a depletion laser at 775 nm. Thus, dyes have to be depletable at 775 nm, very bright and photostable. As a DNA dye that is suitable for imaging with far-red excitation, SiR-Hoechst was developed. It is bisbenzimidazole-silicone-rhodamine conjugated to the bisbenzimidazole center of Hoechst 33342, which makes it suitable for live-cell microscopy (Lukinavičius et al., 2015). By using this so-called SiR-DNA, Lukinavičius et al. showed that live HeLa cells have chromatin structures of a size below 100 nm. A study using antibody labeling of histone H<sub>3</sub> in combination with STED microscopy showed that chromatin in cardiomyocytes is organized in domains with a size of 40-70 nm which are rearranged to more open domains upon acute stimuli (Mitchell-Jordan et al., 2012). Similar to SiR-DNA, the dye JF646-Hoechst is a combination of the far-red dye JF646 and Hoechst33342. Its reversible binding properties allow constant exchange of photobleached fluorophores with intact fluorophores and thus long-term live-cell STED acquisitions (Spahn et al., 2019). Another study used the intercalating DNA dye YOYO-1 to visualize single DNA molecules by STED (Persson et al., 2011). STED in combination with 3D-SIM and genome-wide

sequencing has also been used to identify elementary units of phospho-H2AX-labeled chromatin during DNA double-strand break repair in human cells (Natale et al., 2017). Live cell imaging with STED microscopy of endogenously tagged proteins is still challenging because of high laser powers leading to high phototoxicity, unsuitable fluorescent proteins and slow acquisition but the development of SNAP- and Halo-tag made it also possible to label proteins in vivo with chemical dyes (Keppler et al., 2003; Los et al., 2008). In a recent live-cell STED study (Gu et al., 2020), the endogenous integration of the Halo-tag was used in combination with another genetically encoded fluoromodule called dL5, which non-covalently binds the fluorogen malachite green ester to quantitatively study CTCF organization in live mouse embryonic stem cells. Gu et al. found that CTCF forms clusters of 2-8 molecules and that 25 % of clusters are coupled to cohesin. In addition, they showed that transcriptional inhibition and degradation of cohesin unloader WAPL resulted in increased CTCF clustering.

Taken together, all of the above-mentioned super-resolution microscopy techniques have their advantages and disadvantages and they have helped studying spatial organization of chromatin on a fine scale.

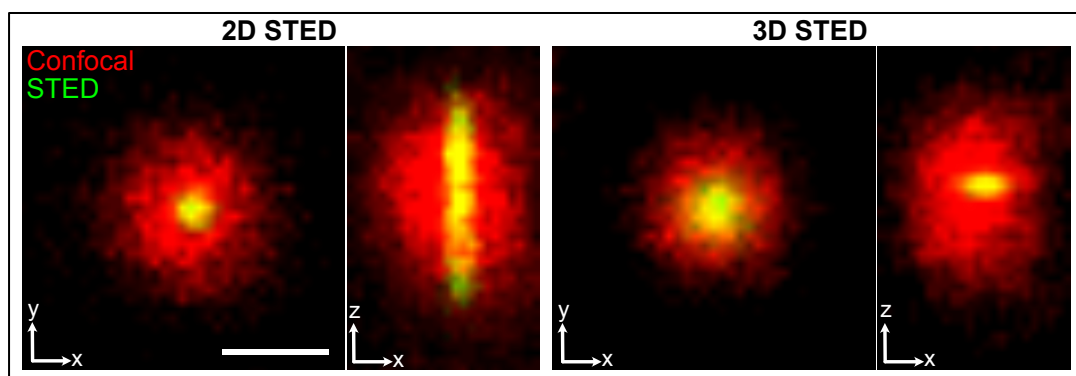


**Figure 6: Stimulated emission depletion (STED) super-resolution microscopy.** In STED the emission light of the confocal signal (red) is depleted by the STED laser (not depicted) and only the signal that lies in the minimum of the depletion laser remains (green). The depletion laser in STED can have two different modi: 2D and 3D. In 2D STED the resolution is improved in x and y but not in z (left panel). In 3D STED the resolution improves in x, y and z but the xy resolution improvement is not as high as for 2D STED. Scale bar: 250 nm

### 3.2.4 Electron microscopy

Electron microscopy has been used to study genome organization early on and has led to major advances. For example, the discovery of nucleosome-DNA complexes which form a beads-on-a-string fiber has played an important role in the field (Olins and Olins, 1974; Woodcock et al., 1976). However, the use of electron microscopy for visualization of chromatin in intact cells has been challenging because of the high density of nucleic acids and proteins in the nucleus leading to low contrast. Therefore, in vitro reconstituted chromatin fibers have been used for a lot of early electron microscopy studies. Nucleosomes were assembled with DNA, which contained strong nucleosome positioning sequences. Addition of linker histones and specific ionic strength conditions further compacted the DNA bound by nucleosomes (Song et al., 2014). For other early

EM studies, cells were hypotonically lysed and nuclei were treated with  $MgCl_2$  (Scheffer et al., 2011). These EM studies suggested a model that chromatin folds into a 30-nm fiber and forms regular higher-order structures. However, studies using cryo-electron microscopy, X-ray scattering and electron spectroscopy imaging (Ahmed et al., 2010; Bouchet-Marquis et al., 2006; Chen et al., 2016; Eltsov et al., 2008; Fussner et al., 2012; Gan et al., 2013; Hansen et al., 2018; Joti et al., 2012; McDowall et al., 1986; Nishino et al., 2012) do not support the existence of 30-nm fibers or hierarchical folding of chromatin in situ but revealed that chromatin has a homogenous grainy texture at the size scale of 11 nm. The most recent study providing evidence against the hierarchical folding model used electron tomography in combination with an electron microscopy compatible DNA dye which increased the contrast by photo-oxidation (Ou et al., 2017). Ou and colleagues showed that chromatin is a disordered 5- to 24-nm curvilinear chain which is compacted at different 3D volume concentrations in interphase (12 – 52 %) and mitotic cells (> 40 %).

### 3.2.5 Live cell imaging

FISH-based approaches have led to major advances in the field of chromatin organization. However, these approaches can only be used in fixed cells. To study genome dynamics visualization methods to label specific genomic regions in live cells are required (Figure 7). There are different techniques that have been used to image specific genomic loci in living cells.

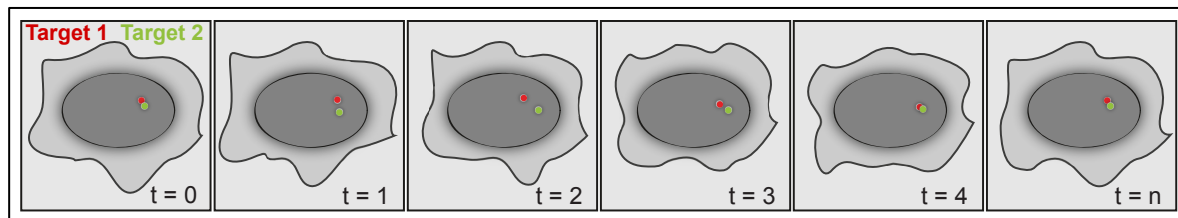


**Figure 7: Imaging of labeled chromatin stretches in a living cell.** Targets 1 (red) and 2 (green) e.g., enhancer and promoter, can be visualized by different labeling strategies. The movement and behavior of these two targets can be followed over time ( $t = 0$  until  $t = n$ ).

The incorporation of repeat elements like the Lac- and Tet-operator or the ANCH sequence into the genome and subsequent labeling with fluorescently tagged repeat binding proteins has been a valuable tool to accumulate sufficient fluorescent molecules at a genomic site for detection (Chubb et al., 2002; Germier et al., 2017; Hajjoul et al., 2013; Heun et al., 2001; Levi et al., 2005; Lucas et al., 2014; Marshall et al., 1997). Dultz et al. used insertion of LacO and TetO repeats and visualization of these repeats with LacI-GFP and TetR-mCherry, respectively, to study chromatin compaction of transcribed and silent states of the GAL7-10-1 locus in yeast cells (Dultz et al., 2018). Using this approach, they showed that upon activation of the GAL locus measured distances within the locus increased significantly. The decompaction is dependent on the functioning SWI/SNF complex or the histone chaperone complex FACT. Alexander et al. (Alexander et al., 2019) used the TetO/TetR and CuO/CymR systems, super-resolution chromatin tracking, and live-

cell imaging to study Sox2 and its control region. They found that the promoter of Sox2 can be transcriptionally activated without physical proximity between the promoter and the enhancer.

Other approaches rely on the use of sequence-specific DNA binding proteins like dCas9 (catalytically dead Cas9) or transcription activator-like effectors (TALEs). Both proteins have been used to label regions containing highly repetitive sequences like centromeres and telomeres (Anton et al., 2014; Chen et al., 2013; Miyanari et al., 2013; Thanisch et al., 2014). Especially the CRISPR-Cas9 system has been optimized for genome visualization for example regarding guide RNA delivery and fluorescent labeling enabling detection of low- and non-repetitive loci (Chen et al., 2018a; Ma et al., 2015; Ma et al., 2018; Neguembor et al., 2018; Qin et al., 2017).

Using the CRISPR-Cas9 system Gu et al. (Gu et al., 2018) labeled promoters and enhancers which are associated with changes of transcriptional activity during embryonal development, and tracked their movement over time during these differentiation-associated transcriptional activity changes in live mouse embryonic stem cells. They found that the mobility of the regulatory elements increased when the transcriptional activity of the locus was higher. When the activity of RNA polymerase II (RNA pol II) was perturbed the activity-linked mobility decreased. Their findings suggest that transcriptionally active regions have a higher probability to be captured in a variety of conformations. The increased locus mobility upon transcription by RNA pol II might lead to an increased frequency with which regulatory elements (enhancers and promoters) come close to each other. These findings, however, stand in contrast to the more recent findings of Alexander et al. (see above) showing the need to further optimize live-cell chromatin imaging to study dynamics of e.g., enhancer-promoter loop formation in many more loci and understand the functional principles of such events.

Similar to the CRISPR-Cas9 system TALE proteins have been optimized for visualization of genomic loci. They have been conjugated to split fluorescent proteins to improve the signal-to-background ratio (Hu et al., 2017). When labeled with quantum dots TALEs have been used to label and map single-copy HIV-1 provirus loci in live host cells (Ma et al., 2017). However, in comparison to the CRISPR-Cas9 system, where specificity to a genomic region is only mediated by the guide RNA, the use of TALE proteins to label single loci is more challenging. For CRISPR/Cas9, the Cas9 protein can be endogenously expressed and only the different guide RNAs have to be transfected. In contrast, TALE proteins contain repeat variable domains which are responsible for recognition of specific bases (Deng et al., 2012; Mak et al., 2012). Cloning of these highly repetitive domains and transfection of many TALE proteins as plasmids at once are challenging. One way to overcome the problem of transfecting many plasmids is transfection of in-vitro transcribed mRNA of the different TALE proteins.

All of the approaches to label and image chromatin organization and dynamics in live cells are challenging. Insertion of repeats like LacO or anchor sequences like ParB into the genome at the locus of interest can disrupt locus dynamics and function due to silencing of these foreign DNA sequences. The use of CRISPR-based techniques can also perturb locus organization due to

disruption of the DNA double-strand by the guide RNA or binding of large amounts of protein to the DNA. TALE proteins also disrupt the native locus environment by binding to the DNA in large amounts and perturbing nucleosome positioning. Taken together, live-cell imaging approaches to visualize genomic elements were extensively studied and improved, however, there is no standard method, yet, which enables robust single locus detection.

### 3.2.6 *DNase-seq*

Active regulatory elements are characterized by nucleosome-free stretches and can be mapped by their high accessibility to nucleases like Deoxyribonuclease I (DNase I) (DNase-seq) (Figure 8) (Gross and Garrard, 1988), hyperactive Tn5 transposase (ATAC-seq) (Buenrostro et al., 2013) or the cross-linking properties of nucleosome-bound and -free DNA (FAIRE-seq) (Giresi et al., 2007). Mapping of sites which are hypersensitive to DNase I has been a tool for more than 40 years (Stalder et al., 1980; Wu, 1980) and DNase I hypersensitive sites (DHSs) have been used as reliable marker for regulatory DNA in complex genomes (Chung et al., 1993; Gross and Garrard, 1988; Li et al., 2002; McGhee et al., 1981; Mills et al., 1983). Profiling of DHSs has supported the characterization of all classes of regulatory elements like promoters, enhancers, silencers, insulators, and locus control regions. Advances in high-throughput sequencing have enabled genome-wide mapping of DHSs in many different cell and tissue types (Boyle et al., 2008; Crawford et al., 2004; John et al., 2011; Sabo et al., 2006). Within the ENCODE project, DHSs have been profiled for 125 human cell types both in normal and malignant states (Thurman et al., 2012). In total, 2.9 million DHSs have been identified and 3% of the mammalian genome is DNase I hypersensitive. Of the identified 2.9 million DHSs a small minority of 3692 was found in all tested cell types. In a more recent large-scale approach to precisely map human DHSs, 438 cell or tissue types and states in 733 biosamples were used to profile a total of 77 million DHSs which led to an index of 3.6 million human DHSs (Meuleman et al., 2020). The average width of the mapped DHSs is 204 bp with an average DHS core of 55 bp. The study also provides a framework to annotate biological contexts to novel and previously mapped elements. DNase I footprinting also enables the identification of DNA sites bound by regulatory DNA-binding factors like transcription factors. By integrating ChIP-seq data direct and indirect occupancy can be identified. Vierstra et al. provide a precise global map of transcription factor footprints in 243 human cell and tissue types (Vierstra et al., 2020).

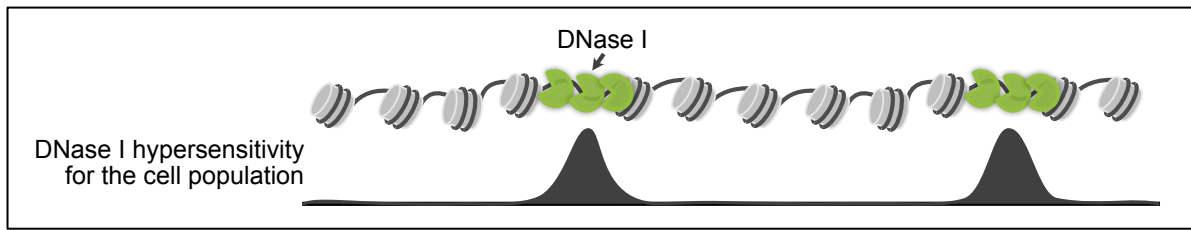


**Figure 8: Principle of DNase-seq.** Deoxyribonuclease 1 (DNase I, green) cleaves DNA (dark gray) of nucleosome-free, active regulatory elements. By high-throughput sequencing, a DNase I hypersensitivity track can be generated for a cell population. This track helps to identify active regulatory elements like enhancers and promoters in the genome.

### 3.2.7 MNase-seq

The repetitive nature of nucleosomes on DNA was not only discovered by electron microscopy but also by digestion with micrococcal nuclease (MNase) which led to the classic beads-on-a-string chromatin model (Figure 9) (Kornberg, 1974; Olins and Olins, 2003; Woodcock et al., 1976). MNase cleaves linker DNA between nucleosomes and partial digestion of chromatin leads to a ladder pattern on an electrophoresis gel representing fragments with different amounts of nucleosomes. Another result from early MNase experiments was the finding that nucleosome repeat length (NRL) varies between species, cell types, developmental stages and chromatin regions with different activity (Compton et al., 1976; Eissenberg et al., 1985; Godde and Widom, 1992). In vitro assays with self-assembled chromatin showed that DNA and nucleosomes alone have a much shorter linker length due to charge neutralization of the DNA. In vivo other cations like magnesium, H1 linker proteins, basic amino acids, like lysine, in histone tails and other DNA-associated proteins contribute to neutralize the charge of the DNA (Garcia-Ramirez et al., 1992; Noll and Kornberg, 1977). Additionally, nucleosome remodeling factors, like the ISWI remodelers, catalyze nucleosome sliding by ATPase activity (Becker and Hörz, 2002). Other types of remodelers, like SWI/SNF, are able to evict nucleosomes at regulatory sites, like promoters and enhancers, where they make the DNA accessible for transcription factors (Becker and Workman, 2013). Global genome-wide studies of nucleosome positioning became possible when high-throughput sequencing technologies were developed (MNase-seq) and applied to many different organisms and cell types (Albert et al., 2007; Chodavarapu et al., 2010; Kent et al., 2011; Mavrich et al., 2008; Teif et al., 2012; Valouev et al., 2011). In animals, there are only a few regions where nucleosomes are well-positioned like the first nucleosomes adjacent to the transcription start site of expressed genes (Lai and Pugh, 2017). Most of the other genomic regions have a poor positioning with irregular spacing (Valouev et al., 2011). By using single-cell MNase-seq in human cells, Lai et al. showed that nucleosomes are most regular in silent chromatin and heterochromatin and least regular in active regions (Lai et al., 2018). The correlation between transcriptional silencing and nucleosome regularity is probably not only a cause but also a consequence of silencing since polymerases perturb nucleosome organization during transcription. Novel methods like Micro-C, which combines conformation capture and MNase digestion, enable a further improvement in

resolution of nucleosome organization. Hsieh et al. found enhanced contacts between nucleosomes that are separated by one nucleosome in yeast suggesting a zigzag structure of chromatin fibers (Hsieh et al., 2015). Another study which combined Micro-C with simulations revealed two distinct tetranucleosomal folding motifs which are typically found in different part of a gene in yeast (Ohno et al., 2019). Such insights are mostly missing for more complex genomes. Many details of nucleosome organization like positioning, regularity and folding patterns in vivo are still missing and the field profits from developments in sequencing and imaging methods (for review, see Baldi et al. (2020)).

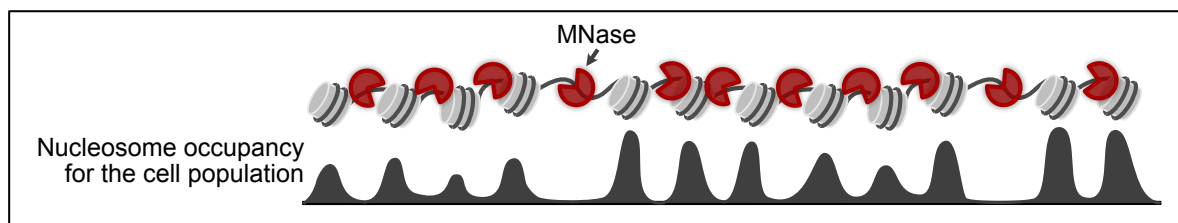


**Figure 9: Principle of MNase-seq.** Micrococcal nuclease (red) cleaves linker DNA (dark gray) between nucleosomes (light gray) and in combination with high-throughput sequencing leads to a nucleosome occupancy track for a whole cell population (lower track) which can be used to determine nucleosome positions.

### 3.2.8 ChIP-seq

In 1984, John Lis and his graduate student David Gilmour developed chromatin immunoprecipitation (ChIP) to investigate the interactions between proteins and DNA in the cell (Gilmour and Lis, 1984; Gilmour and Lis, 1985). Since its development, ChIP-based methods were further improved and serve as powerful tools in the research of chromatin and its interactions with proteins. The combination of ChIP with massively parallel DNA sequencing (ChIP-seq) enabled global mapping of protein binding sites (Figure 10) (for review, see Park (2009)).

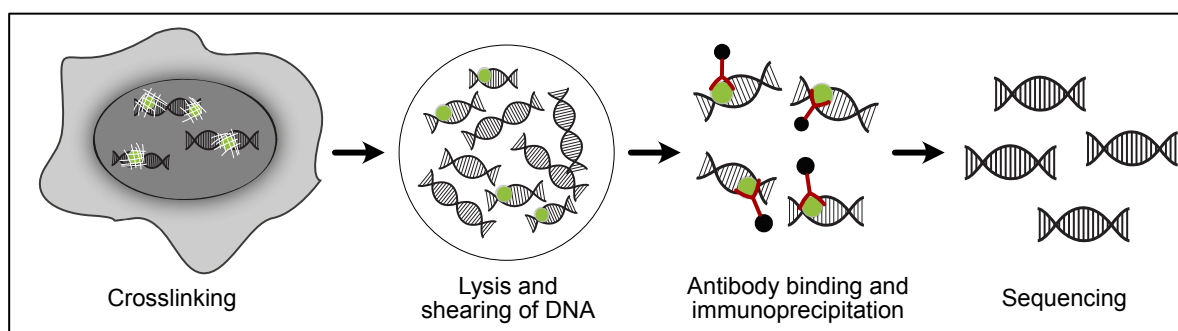


**Figure 10: Principle of ChIP-seq.** To study the interaction between proteins and DNA, chromatin immunoprecipitation with high-throughput sequencing (ChIP-seq) has been developed. Cells are fixed and the protein of interest (green) is crosslinked to the DNA region where it is bound (black). Chromatin is extracted by lysis and fragmented by sonication. The protein of interest crosslinked to DNA is immunoprecipitated by antibodies (red). After removing the antibodies and proteins the DNA stretches are sequenced.

ChIP-seq data of CTCF in combination with Hi-C data revealed that the transcription factor CTCF plays a key role in establishing active boundaries between chromatin domains (Rao et al., 2014; Zhang et al., 2020). CTCF has been shown to mediate DNA loops together with cohesin (Phillips and Corces, 2009). By binding to itself CTCF forms homodimers (Yusufzai et al., 2004), which function as loop anchors in convergent orientation (Rao et al., 2014). Depletion of CTCF leads to loss of many domain boundaries (Nora et al., 2017; Wutz et al., 2017). Next to CTCF one of the key players in chromatin organization is cohesin, which consists of the subunits RAD21, Smc1, Smc3, SAI1 and SAI2 in vertebrates that form a ring-like structure (Nasmyth and Haering, 2009). Cohesin is responsible for cohesion between replicated sister chromatids and influences chromosome segregation during mitosis (Peters et al., 2008). By ChIP-seq combined with Hi-C, the cohesin complex was shown to be often found at CTCF mediated loop borders (Rao et al., 2014). Later on, increasing evidence indicated that TADs and loop domains (sub-compartments of TADs) are formed by a mechanism called loop extrusion (Fudenberg et al., 2016; Mayerova et al., 2020). During loop extrusion, the cohesin ring is loaded onto DNA by the factor NIPBL-MAU2 and starts to form a progressively larger loop. Loop extrusion is stopped at convergent CTCF sites and is dependent on cohesin's ATPase activity (Alipour and Marko, 2012; Davidson et al., 2019).

ChIP-seq studies of posttranslational histone modifications have helped to identify specific genomic distributions of histone marks, e.g. H3K27ac at enhancers (Creyghton et al., 2010), H3K4me3 at active transcription start sites and promoters (Benayoun et al., 2014), H3K9me3 in HP1-mediated heterochromatin (Allshire and Madhani, 2018) and H3K27me3 in Polycomb-repressed chromatin (Hansen et al., 2008). These modifications of histone tails not only regulate internucleosomal interactions but also recruit chromatin-associated regulatory proteins like nucleosome remodelers (Bannister and Kouzarides, 2011). The code generated by histone modifications is very complex and many details remain to be elucidated (Huang et al., 2014).

Another example where ChIP-seq was successfully used are studies of lamin A/C and B which allowed to identify lamina-associated domains (LADs) (Gesson et al., 2016; Lund et al., 2015; Peric-Hupkes et al., 2010; Sadaie et al., 2013; Shah et al., 2013). The lamina is a tethering point for chromatin which can modulate spatial genome organization by interaction and contributes to the radial topology of chromatin where heterochromatin is located at the nuclear periphery. LADs correspond to gene-poor regions and are replicated in late S-phase (for review, see Briand and Collas (2020)). LADs are mainly found in B compartments (Zheng et al., 2018).

Since ChIP-seq is dependent on high-quality antibodies, there are also chromatin-associated proteins which are challenging to study by ChIP-seq. One of them is linker histone H1. DNA entering and exiting nucleosomes and linker DNA between nucleosomes is bound and protected by linker histone H1 (Brockers and Schneider, 2019). Studies on the localization of bulk H1 found that H1 is depleted from transcription start sites, enhancers and CTCF binding sites (Woodcock et al., 2006). Another study showed that in mouse embryonic stem cells H1 variants H1d and H1c are colocalized with H3K9me3 and are negatively correlated with H3K4me3 (Cao et al., 2013). Both are

depleted from gene-rich and GC-rich regions and active promoters and are enriched at major satellites and AT-rich regions. However, there are 12 different variants of HI, and their heterogeneity and complexity make studies on localization, dynamics and function challenging. Overall, ChIP-seq, especially in combination with other methods, provides a powerful tool to study interactions between proteins and DNA. These DNA interacting proteins play key roles in chromatin organization and function. The ENCODE project provides very rich ChIP-seq datasets for the most important chromatin-associated proteins, histone modifications and histone variants (Consortium, 2012).

### 3.2.9 *Computational models*

Computational models and simulations play an important role in understanding spatial chromatin structure. Due to the advances in next-generation sequencing and imaging methods more and more very rich and complex datasets are generated. However, these datasets can be difficult to interpret, and chromatin organization and function occur dynamically on many length scales which are in between the resolution limits of the currently available experimental methods. Thus, different computational models can support interpretation and understanding of these complex datasets and help filling the gaps of experimental methods.

#### *Models of chromatin fibers on different scales*

There are different classes of models which range from all-atom models of individual nucleosomes, to mesoscale coarse-grained models of DNA fibers with tens to hundreds of nucleosomes, to polymer or continuum models of megabase-sized regions to whole chromosomes (for review, see Brackey et al. (2020); Moller and de Pablo (2020)). Bottom-up approaches focus mainly on modeling of nucleosomes and their role in chromatin regulation and dynamics on a scale up to 100 kb. Since the crystal structure of nucleosomes was resolved (Luger et al., 1997; Richmond and Davey, 2003) the first models of nucleosomes were developed and nucleosome dynamics were studied (Bishop, 2005; Eslami-Mossallam et al., 2016). Further development of these models enabled to study the impact of nucleosome-binding proteins (Öztürk et al., 2018), histone variants (Bowerman and Wereszczynski, 2016; Melters et al., 2019) and posttranslational histone modifications (Li and Kono, 2016; Zhang et al., 2017). Coarse-grained models have also been used to simulate multi-nucleosome chains where linker DNA length and internucleosomal interaction have to be considered (Figure 11) (Routh et al., 2008; Song et al., 2014). Internucleosomal interactions have been difficult to be quantified but it is thought that especially histone tails influence these interactions. Positively charged residues of the H4 tail, in particular H4K16, were shown to bind to the neighboring nucleosome. H4K16ac disrupts and reduces this electrostatic attraction and leads to a relaxation of the chromatin structure (Moller et al., 2019; Zhang et al., 2017). The mesoscale of coarse-grained models enables simulation of longer DNA chains with nucleosomes where a bead in the model represents a few base pairs of DNA or the nucleosome

(Figure 11) (Arya and Schlick, 2009; Arya et al., 2006). Such models can also include epigenetic phenomena like linker histone H1 binding (Luque et al., 2014; Perišić et al., 2019). In order to incorporate in vivo nucleosome positioning data into such models tools like the NucPosSimulator have been developed to transfer experimental MNase-seq data (Zhang and Pugh, 2011) into nucleosome positions at a specific locus in a specific cell type (Schopflin et al., 2013).

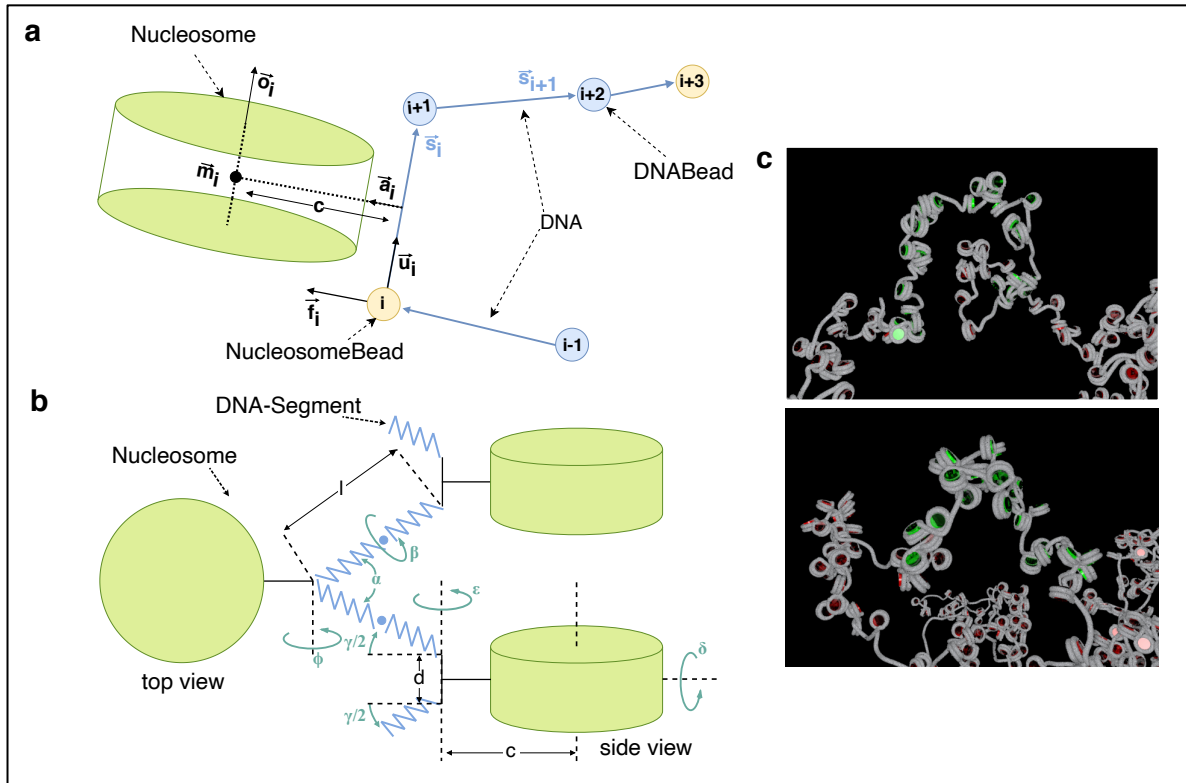


**Figure 11: Coarse-grained modeling (modified from Brandstetter et al., in preparation).** (a-b) Model of a nucleosome chain indicating parameters relevant for coarse-grained modeling (for a detailed figure legend, see Supplementary figures 6 and 7 in Brandstetter et al.) (c) Example images of coarse-grained modeled chromatin fibers with nucleosomes in red and green and DNA in gray.

Top-down approaches use for example contact frequency data to understand chromatin on the scale of larger domains to whole chromosomes. Since the resolution of Hi-C data is relatively coarse, polymer models have been used for interpretation of these contact frequency data (Rosa and Everaers, 2008). To predict the heterogeneity of chromatin contact probability polymer models have to incorporate other factors than ideal polymer models (Huang et al., 2020). Especially the process of chromatin looping has to be integrated into the models (Barbieri et al., 2012; Brackley et al., 2017; Fiorillo et al., 2019; Fudenberg et al., 2016; Nuebler et al., 2018). Studies using these models facilitate understanding of properties of chromatin observed in vivo. For example, Rosa et al. studied time scales of chromosome dynamics and revealed that intermingling of two chromosomes would require hundreds of years which explains why individual chromosomes keep their territory in the interphase nucleus (Rosa and Everaers, 2008). A more recent study has also included DNA binding proteins and their binding sites in the polymer model.

With this model using only one active factor and one repressive factor, it was possible to predict Hi-C maps and 85% of domain boundaries (Brackley et al., 2016). Another study (Falk et al., 2019) which combines Hi-C, microscopy and simulations on inverted nuclei of rods in nocturnal mammals found that the attraction between heterochromatic regions (B compartments) drives compartmentalization of active and inactive chromatin in conventional and inverted nuclei. The attraction between heterochromatin and the lamina leads to the shell of heterochromatin at the nuclear periphery in conventional nuclei.

Taken together, both bottom-up and top-down modeling of chromatin are useful to understand chromatin organization and function. Application of models to experimental data as well as testing of potential new mechanisms with simulations serves as powerful tool. However, computational models of chromatin also face problems and cannot solve all open questions in the field of chromatin organization.

### *Models of different chromatin states*

Computational models are also used to characterize and classify chromatin states. Histone modifications in different combinations are thought to encode specific biological functions, it is, however, difficult to understand the biological role of these combinations. By analyzing available ChIP-seq data of 38 different histone methylation and acetylation marks, histone variant H2AZ, RNA pol II and CTCF, the multivariate Hidden-Markov-based model ChromHMM characterizes 51 chromatin classes in five large functional groups genome-wide in human CD4<sup>+</sup> T-cells (Ernst and Kellis, 2010). The ChromHMM segmentation was applied to nine different cell types with the input of nine chromatin marks to define 15 chromatin states (Ernst et al., 2011). Another method which classifies chromatin is Segway, a dynamic Bayesian network method. Segway uses ChIP-seq data of histone modifications and transcription factors, DNase-seq and FAIRE-seq data from the ENCODE project (Hoffman et al., 2012; Hoffman et al., 2013). Within the ENCODE project, the ChromHMM was extended by DNase-seq and FAIRE-seq data and applied to 6 different cell types and a combined segmentation from Segway and ChromHMM was applied to data from 6 cell types. This consensus merge uses seven comprehensive states and provides a helpful resource to characterize specific genomic elements and their biological function (Consortium, 2012).

### **3.3 Remaining discrepancies**

Combining all the findings and conclusions of the methods described above is as complex as the eukaryotic genome itself. There is a fine interplay between chromatin structure with all its molecular details and chromatin functions which are fundamental for cellular processes like transcription and replication (Bickmore, 2013). Cause and consequence are often unclear, and some discrepancies remain. An important reason for such discrepancies is whether conclusions are drawn from data from individual cells or population averages because chromatin-dependent processes are highly dynamic and lead to large differences from cell to cell.

An example is the apparent contradiction between Hi-C- and imaging-based studies of the effects of cohesin loss. Cohesin has been shown to not only mediate sister chromatid cohesion but also form TADs by loop extrusion (Davidson et al., 2019; Kim et al., 2019). Hi-C studies found that TADs were lost in cohesin depleted cells and cells depleted from the cohesin loading factor NIPBL (Rao et al., 2017; Schwarzer et al., 2017). Since for Hi-C a whole cell population is used, TAD and loop organization is only shown for the population average. In contrast, an imaging-based study (Bintu et al., 2018), which generated distance heat maps similar to Hi-C maps, showed that on a single-cell level TAD-like domains could still be found. Only the positions of boundaries between domains were more variable across the genomic region and not located preferentially at CTCF sites. However, this study also only showed organization for limited genomic regions and the effect of cohesin depletion on global higher-order chromatin structure and other important cellular mechanisms like replication and cell division remains elusive. We study these effects in our publication “Cohesin depleted cells rebuild functional nuclear compartments after endomitosis” (Cremer et al., 2020a). For this study, I designed and performed live-cell imaging and confocal microscopy experiments and carried out quantitative image analysis (for details, see appendix). Another reason for discrepancies is the different point of view between biochemical and microscopic approaches. For example, models of chromatin that are based on Hi-C data are very different from microscopy-based models. In Hi-C only DNA contacts are observed, which leads to a model of the nucleus which is completely filled with loops of chromatin. Microscopic images from super-resolution imaging show that nuclei are not completely filled with chromatin but that there are chromatin-free areas which are as important as chromatin itself. These interchromatin areas play a role in storage and transport of proteins, mRNAs and other important factors like splicing speckles (Cremer et al., 2020b). This example shows that the efforts to combine findings from different methods to generate a consensus view on chromatin organization will become more and more important. In two of our studies, we combine microscopic techniques with other methods to integrate a broader view on our findings. The study mentioned above uses a combination of live-cell imaging, super-resolution microscopy, Hi-C and Repli-seq (Cremer et al., 2020a). In another study, we characterize structural changes in short (5 kb) chromatin segments in active and inactive interphase chromatin by combining super-resolution microscopy with computational modeling (Brandstetter et al., in preparation). For this study, I generated samples and designed as well as performed super-resolution microscopy. In addition, I analyzed and interpreted the acquired data (for details, see appendix). In addition to these multi-method studies of chromatin architecture, an alternative labeling strategy for probes used in microscopy is shown here (Schwach et al., 2020). Here, I contributed by performing spinning disk confocal microscopy (for details, see appendix). The continuous improvement of such labeling techniques also drives progress in this area.

## **4 RESULTS**

### **4.1 Cohesin depleted cells rebuild functional nuclear compartments after endomitosis**

# Cohesin depleted cells rebuild functional nuclear compartments after endomitosis

Marion Cremer <sup>1,11</sup>✉, Katharina Brandstetter <sup>2,11</sup>, Andreas Maiser <sup>2</sup>, Suhas S. P. Rao<sup>3,4</sup>, Volker J. Schmid <sup>5</sup>, Miguel Guirao-Ortiz <sup>2</sup>, Namita Mitra<sup>3</sup>, Stefania Mamberti <sup>6</sup>, Kyle N. Klein<sup>7</sup>, David M. Gilbert <sup>7</sup>, Heinrich Leonhardt <sup>2</sup>, M. Cristina Cardoso <sup>6</sup>, Erez Lieberman Aiden<sup>3,8,9,10</sup>, Hartmann Harz <sup>2</sup>✉ & Thomas Cremer <sup>1</sup>✉

Cohesin plays an essential role in chromatin loop extrusion, but its impact on a compartmentalized nuclear architecture, linked to nuclear functions, is less well understood. Using live-cell and super-resolved 3D microscopy, here we find that cohesin depletion in a human colon cancer derived cell line results in endomitosis and a single multilobulated nucleus with chromosome territories pervaded by interchromatin channels. Chromosome territories contain chromatin domain clusters with a zonal organization of repressed chromatin domains in the interior and transcriptionally competent domains located at the periphery. These clusters form microscopically defined, active and inactive compartments, which likely correspond to A/B compartments, which are detected with ensemble Hi-C. Splicing speckles are observed nearby within the lining channel system. We further observe that the multilobulated nuclei, despite continuous absence of cohesin, pass through S-phase with typical spatio-temporal patterns of replication domains. Evidence for structural changes of these domains compared to controls suggests that cohesin is required for their full integrity.

<sup>1</sup>Anthropology and Human Genomics, Department Biology II, Ludwig-Maximilians-Universität München, München, Germany. <sup>2</sup>Human Biology & Bioluminescence, Center for Molecular Biosystems, Department Biology II, Ludwig-Maximilians-Universität München, München, Germany. <sup>3</sup>Center for Genome Architecture, Department of Molecular and Human Genetics, Baylor College of Medicine, Houston, TX, USA. <sup>4</sup>Department of Structural Biology, Stanford University School of Medicine, California, USA. <sup>5</sup>Bayesian Imaging and Spatial Statistics Group, Department of Statistics, Ludwig-Maximilians-Universität München, München, Germany. <sup>6</sup>Cell Biology and Epigenetics, Department of Biology, Technische Universität Darmstadt, Darmstadt, Germany. <sup>7</sup>Department of Biological Science, Florida State University, Tallahassee, FL, USA. <sup>8</sup>Center for Theoretical Biological Physics, Rice University, Houston, TX, USA. <sup>9</sup>Broad Institute of the Massachusetts Institute of Technology and Harvard University, Cambridge, MA, USA. <sup>10</sup>Departments of Computer Science and Computational and Applied Mathematics, Rice University, Houston, TX, USA. <sup>11</sup>These authors contributed equally: Marion Cremer, Katharina Brandstetter. ✉email: [Marion.Cremer@lrz.uni-muenchen.de](mailto:Marion.Cremer@lrz.uni-muenchen.de); [harz@biologie.uni-muenchen.de](mailto:harz@biologie.uni-muenchen.de); [Thomas.Cremer@lrz.uni-muenchen.de](mailto:Thomas.Cremer@lrz.uni-muenchen.de)

**C**ohesin, a ring-like protein complex with its major subunits RAD21, SMC1, and SMC3 exerts its key functions by tethering distant genomic loci into chromatin loops. It is involved in sister chromatid entrapment to ensure proper chromosome segregation during mitosis, in double-strand break repair and gene regulation, and importantly was found essential for chromatin loop extrusion by shaping loops in the sub-Mb range anchored at CTCF/cohesin binding sites<sup>1–6</sup>, for reviews see<sup>7–13</sup>. These results have argued for an essential role of cohesin in the formation of a functional nuclear architecture.

Studies of the impact of cohesin depletion on nuclear structure and function have become greatly facilitated by an auxin-inducible degron (AID) system, which triggers rapid and selective proteolysis of RAD21 after addition of auxin to the culture medium resulting in the loss of cohesin from chromatin<sup>14</sup>. Using this system in the colon cancer-derived HCT116-RAD21-mAC cell line, we previously demonstrated the rapid disappearance of chromatin loop domains with a concomitant loss of topologically associated domains (TADs) in Hi-C contact matrices averaged over large cell populations, with only minor effects of cohesin depletion on gene expression<sup>15</sup>. Other studies, using different cell types and approaches for cohesin elimination yielded similar results, reviewed in ref. 16.

In this work, we investigate the fate of cohesin depleted cells up to 30 h with both live-cell and super-resolved quantitative microscopy and ensemble Hi-C. These approaches complement each other in ways that cannot be achieved by either method alone. We show that cohesin depleted interphase cells are able to pass through an endomitosis yielding a single postmitotic cell with a multilobulated cell nucleus (MLN). Higher-order chromatin architecture and compartmentalization, typical for cells studied in the presence of cohesin, is maintained after cohesin depletion and even fully restored in MLN as indicated by chromosome territories (CTs), co-aligned active and inactive nuclear compartments (ANC/INC) based on microscopic studies, reviewed in<sup>17,18</sup>, as well as the reconstitution of A and B compartments detected by ensemble Hi-C experiments, whereas TADs remain missing. In line with these principal features of a functional nuclear architecture, we find that MLN are able to initiate and traverse through S-phase with typical stage-specific patterns of replication domains (RDs). Quantitative 3D image analyses indicate a larger number of RDs together with an increased heterogeneity of RD volumes. Evidence for structural changes of RDs compared to controls, however, suggests that cohesin is required for their full integrity<sup>19</sup>. A joint presentation of results from quantitative 3D microscopy and Hi-C studies is complicated by a different terminology to describe the structural and functional higher-order chromatin entities discovered by either approach. For a glossary of terms, as we use them below, we refer readers to Supplementary Table 1.

## Results

**Validation of auxin-induced proteolysis of the cohesin subunit RAD21.** All experiments of this study were performed with the human colon cancer-derived cell line HCT116-RAD21-mAC, where an AID is fused to both endogenous RAD21 alleles together with a sequence coding for a fluorescent reporter<sup>14</sup>. About 98% of nuclei in untreated control cell cultures expressed RAD21-mClover. Selective degradation of RAD21 under auxin treatment (6 h in 500  $\mu$ M auxin) was shown by negative immunostaining with a RAD21 antibody, while epitopes of cohesin subunits SMC1 and SMC3 remained intact under auxin (Supplementary Fig. 1a). RAD21-mClover degradation was quantitatively assessed by intensity measurements recorded from high-throughput imaging of single cells after 6 h auxin treatment (Supplementary Fig. 1b).

A visible decline of RAD21-mClover fluorescence was first noted in time-lapse images 30 min after incubation of cells in 500  $\mu$ M auxin and appeared completed within 4:00 h (Supplementary Fig. 2a). Furthermore, quantitative measurements of RAD21-mClover decline over time were performed on a single-cell level (for details see Supplementary Fig. 2b, c). Notably, ~4% of cells escaped auxin-induced RAD21 degradation. In order to exclude non-responsive cells from further analyses of the impact of cohesin depletion, RAD21-mClover fluorescence was routinely recorded in all experiments with auxin-treated cell populations except for 3D-FISH experiments where DNA heat denaturation degrades the reporter fluorescence<sup>20</sup>.

### Cohesin depleted cells pass through a prolonged endomitosis yielding a daughter cell with one multilobulated nucleus (MLN).

Using time-lapse imaging over 21 h at  $\Delta t = 15$  min, we compared entrance into mitosis, mitotic progression and exit in parallel in untreated controls and in cohesin depleted cells, where auxin was added just before starting live-cell observations. In control cells ~80% of all recorded mitoses ( $n = 45$ ) passed mitosis within <1 h and formed two inconspicuous daughter nuclei. A second mitosis observed for individual nuclei ~20 h after the first division demonstrates their capacity to divide again under the given observation conditions (Fig. 1a). Notably, about 20% of mitoses recorded in untreated control cells revealed prolonged mitoses (>2 h) followed by transition into an abnormal cell nucleus (for detailed information on individual nuclei see Supplementary D 1), a feature which is not unusual in tumor cell lines (reviewed in ref. 21). In cohesin depleted cells ( $n = 36$ ) mitotic entrance was inconspicuous (Fig. 1b), mitotic progress, however, was consistently delayed up to 14 h (median 4.5 h, for detailed information on individual nuclei see Supplementary D 1). This prolonged mitotic stage raised the mitotic index in cohesin depleted cell cultures after 6 h in auxin to almost 30% versus ~4% in control cultures (Supplementary Fig. 3). The delayed mitotic passage was associated with the formation of abnormal, e.g., multipolar mitotic figures persisting over several hours (Fig. 1b). Figure 1c depicts a mitotic cell apparently approaching the stage of two separated daughter nuclei. Despite their seemingly complete separation, these daughter nuclei were presumably still connected by filaments (see below and Supplementary Fig. 4) and did not complete karyokinesis. All cohesin depleted cells that were followed through an entire mitosis ( $n = 23$ , Supplementary D 1) resulted in the formation of a single MLN within one daughter cell, indicative for an endomitotic event<sup>22</sup>. As a consequence, in cell cultures fixed 30 h after cohesin depletion, MLN accumulated up to ~60% versus ~2% in control cultures (Supplementary Fig. 3).

### (Super-resolution) microscopy demonstrates the persistence of global features of higher-order chromatin organization after cohesin depletion and their restoration after endomitosis in MLN.

The capability of cohesin depleted cells to pass through an endomitosis prompted a careful comparison of the architecture of MLN compared with nuclei from control cultures and cohesin depleted cells on their way towards endomitosis (referred to as pre-mitotic cohesin depleted nuclei below). Maintenance of a territorial organization of interphase chromosomes in pre-mitotic, cohesin depleted cells and the reconstitution of chromosome territories (CTs) after endomitosis was demonstrated by the painting of CTs 4, 12, and 19 (Fig. 2). In line with the near-diploid karyotype of HCT116 cells<sup>23</sup>, two homologous territories of each painted chromosome were detected in interphase nuclei of both control (Fig. 2a) and pre-mitotic cohesin depleted cells fixed after 6 h in auxin (Fig. 2b). Mitoses occurring in cohesin

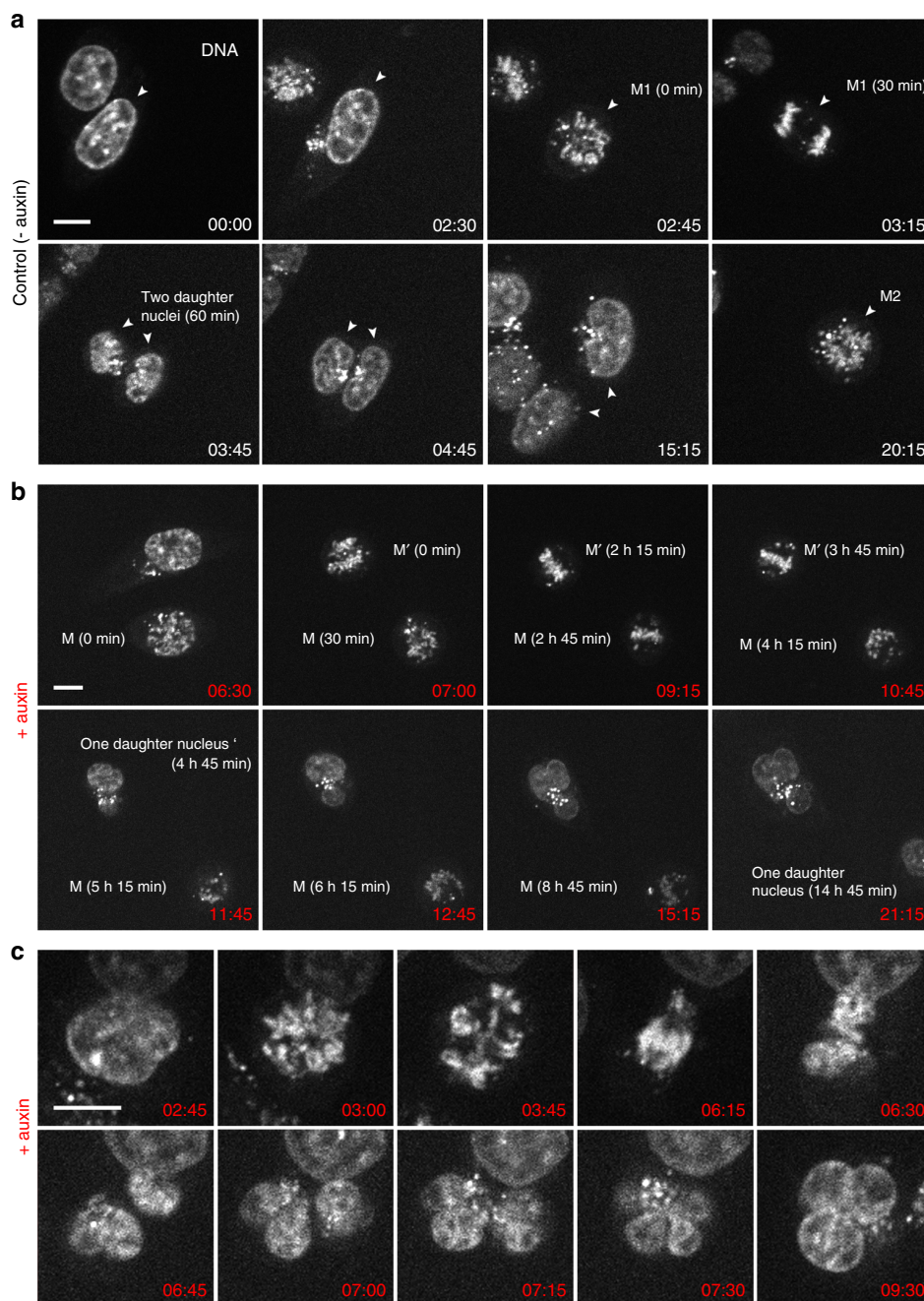


**Fig. 1 Live-cell microscopy demonstrating prolonged abnormal mitosis with subsequent formation of one endomitotic multilobulated nucleus (MLN) in cohesin depleted cells.** **a** Selected points from time-lapse imaging ( $\Sigma t = 21$  h,  $\Delta t = 15$  min) of untreated control cells ( $-$  auxin) with the accomplishment of mitosis (M1) with in 1h (time 02:45–03:45) and subsequent formation of two daughter nuclei. DNA stained with SiR-DNA. A second mitosis (M2) of one daughter nucleus is shown at time 20:15. **b** Selected time lapse images of nuclei after cohesin degradation ( $+$  auxin) conducted in parallel to control cells demonstrate a prolonged mitotic stage. Mitosis (M) emerges at time 6:30 after auxin treatment, transition into one abnormal multilobulated daughter nucleus (MLN) is seen 14:45 h later (time 21:15). Mitosis (M') emerges 7 h after auxin treatment (time 07:00), transition into an MLN is seen 4:45 h later (time 11:45). **c** Time-lapse imaging from the same series at a higher zoom shows an aberrant mitosis with an adumbrated formation of two daughter nuclei (time 06:45), that finally appear as one MLN at time 7:15. Scale bar: 10  $\mu$ m. M, M1, M2, M' denote different mitoses. Images shown in **a–c** show representative nuclei from one of three independent experiments.

depleted cell cultures observed at this time revealed chromatid segregation, though frequently with misalignment (Fig. 2c). Most MLN fixed in cultures after 30 h of auxin treatment revealed four painted territories for each delineated chromosome (Fig. 2d). Some MLN showed more than four painted regions with variable

sizes, which were occasionally connected by thin chromatin bridges (Fig. 2d right panel, Supplementary Fig. 4). These observations may indicate that chromatids were torn apart by mechanic forces during lobe formation. Such disruptions might be enhanced, if we assume a higher level of relaxation and

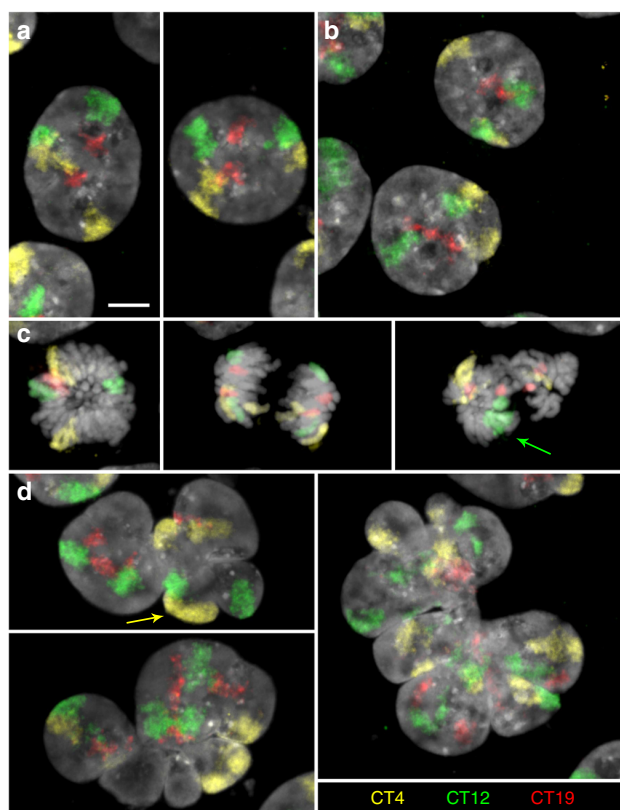


**Fig. 2 Maintenance of chromosome territories (CTs) in cohesin depleted nuclei and their reconstitution after endomitosis. a–d** Z-projections of entire DAPI-stained nuclei (gray) with painted territories of chromosomes 4 (CT4, yellow), 12 (CT12, green) and 19 (CT19, red) acquired by confocal fluorescence microscopy. **a** control nuclei and **b** pre-mitotic cohesin depleted nuclei after 6 h in auxin show two inconspicuous copies for each CT. **c** Mitoses from 6 h auxin-treated cultures with two coherent chromosomes in a (presumably early) metaphase plate (left), after chromatid segregation (mid) and missegregation of chromosome 12 (arrow) in an abnormal mitotic figure (right). **d** left: two endomitotic multinucleated nuclei (MLN) with four copies for each CT. Arrow marks two CTs 4 that are overlaid in the z-projection. Right: Large MLN with a torn-up appearance of CTs with seemingly >4 painted regions for each CT (compare also Supplementary Fig. 4). Scale bar: 5  $\mu$ m. Images shown in **a–d** show representative nuclei from two independent experiments.

increased mechanical instability of chromosomes in cohesin depleted nuclei.

Next, we tested the ability of cohesin depleted cells to preserve in addition to CTs other structural features of a compartmentalized nuclear architecture with active and inactive nuclear compartments described in the ANC-INC model<sup>17,18</sup>. For this, we compared DAPI-stained nuclei of cohesin depleted cells fixed after 6 h in auxin, mostly comprising nuclei of the pre-mitotic interphase, and post-endomitotic MLN fixed after 30 h auxin treatment with control nuclei of cells cultured without auxin. Functionally relevant markers, delineated by immuno-detection, included SC35, an integral protein of splicing speckles involved in co-transcriptional splicing and transcriptional elongation<sup>24</sup>, Ser5P-RNA Pol II, representing a transcription initiating form<sup>25</sup> (further referred to as RNA Pol II), and histone H3K27me3 conveying a repressed chromatin state<sup>26</sup>. 3D structured illumination microscopy (3D-SIM) was used to obtain stacks of nuclear serial sections from representative samples for further evaluation with our previously developed toolbox for 3D image analysis<sup>27</sup>.

This toolbox allowed highly resolved measurements of DNA intensity differences as proxies for chromatin compaction combined with the assignment of functional markers to regions of different compaction.

Figure 3a–c shows typical mid-plane SIM sections of a control nucleus (a), a pre-mitotic cohesin depleted nucleus (b), and a post-endomitotic MLN (c). Color-coded voxels were attributed to seven intensity classes with equal intensity variance and represent the range of DAPI fluorescence intensities in 3D SIM nuclear serial sections. These color heat maps visualize local differences in DNA compaction<sup>27</sup>. According to the ANC-INC model (see also Supplementary Table 1 for details of terminology), class 1 represents the interchromatin compartment (IC) with only sparse occurrence of DNA (blue). Chromatin domains (CDs) attributed to classes 2–7 form chromatin domain clusters (CDCs) with a nanoscale zonation of euchromatic and heterochromatic regions<sup>18,28</sup>. Classes 2 and 3 (purple and red) comprise less compacted chromatin, including purple-coded chromatin directly bordering the IC, termed perichromatin region (PR). Classes 4–6 (orange, light brown, yellow) comprise facultative heterochromatin with higher compaction, class 7 (white) reflects the most densely compacted, constitutive heterochromatin. Enlargements of boxed areas in the three mid-plane nuclear sections of Fig. 3a–c exemplify CDCs with a zonal organization of less compact chromatin domains at the periphery adjacent to the IC and higher compacted chromatin located in the CDC interior. Each CT is built from a number of CDCs, which in turn form higher-order chromatin networks expanding throughout the nuclear space, where 3D FISH with appropriate probes is required to identify individual CTs (compare Fig. 2) and CDCs (see Discussion).

Relative fractions of voxels assigned to each of the seven DAPI intensity classes yielded similar patterns for control nuclei, pre-mitotic cohesin depleted nuclei, and post-endomitotic MLN (Fig. 3d). Figure 3e presents estimates of nuclear volumes derived from 3D SIM serial sections. Whereas volumes of pre-mitotic cohesin depleted nuclei are similar to controls, the distinctly increased nuclear volume in MLN (30 h auxin) corresponds with a further increase of a 2n DNA content immediately after endomitosis to a 4n DNA content (Supplementary Fig. 5) after passing through another round of DNA replication (see below). IC-channels expanding between lamina associated chromatin further illustrate the strikingly similar nuclear topography of higher-order chromatin organization present in control nuclei, pre-mitotic cohesin depleted nuclei, and post-endomitotic MLN (Supplementary Fig. 6). 3D image stacks reveal the integration of IC-channels and lacunas into an interconnected 3D network with direct connections to nuclear pores<sup>18,29</sup>.

Figure 4a–f shows nuclear sections with DAPI-stained DNA (gray) together with immunostained SC35 (red) and H3K27me3 (green) (Fig. 4a–c) or immunostained RNA Pol II (green) (Fig. 4d–f). In 3D SIM stacks of control and cohesin depleted nuclei we determined the relative fractions of voxels representing SC35, H3K27me3, and RNA Pol II, respectively, in relation to the seven DAPI intensity classes<sup>27</sup>. By comparison of the relative fractions of marker voxels with DAPI related voxels, we tested for each class, whether a given marker showed a relative enrichment (over-representation) or relative depletion (under-representation) compared with the null-hypothesis of a random distribution (Fig. 4g, h). These data present the combined results from two independent experiments (replicates 1 and 2) that were performed with an interval of several months to test their long-term reproducibility. Statistical tests are listed in the source data file. Figure 4g indicates a pronounced enrichment of SC35 in class 1 (IC), a relative depletion in classes 2 and 3 (PR), and a virtual absence in higher classes. In contrast, H3K27me3, a marker of facultative heterochromatin, was under-represented in classes 1 and

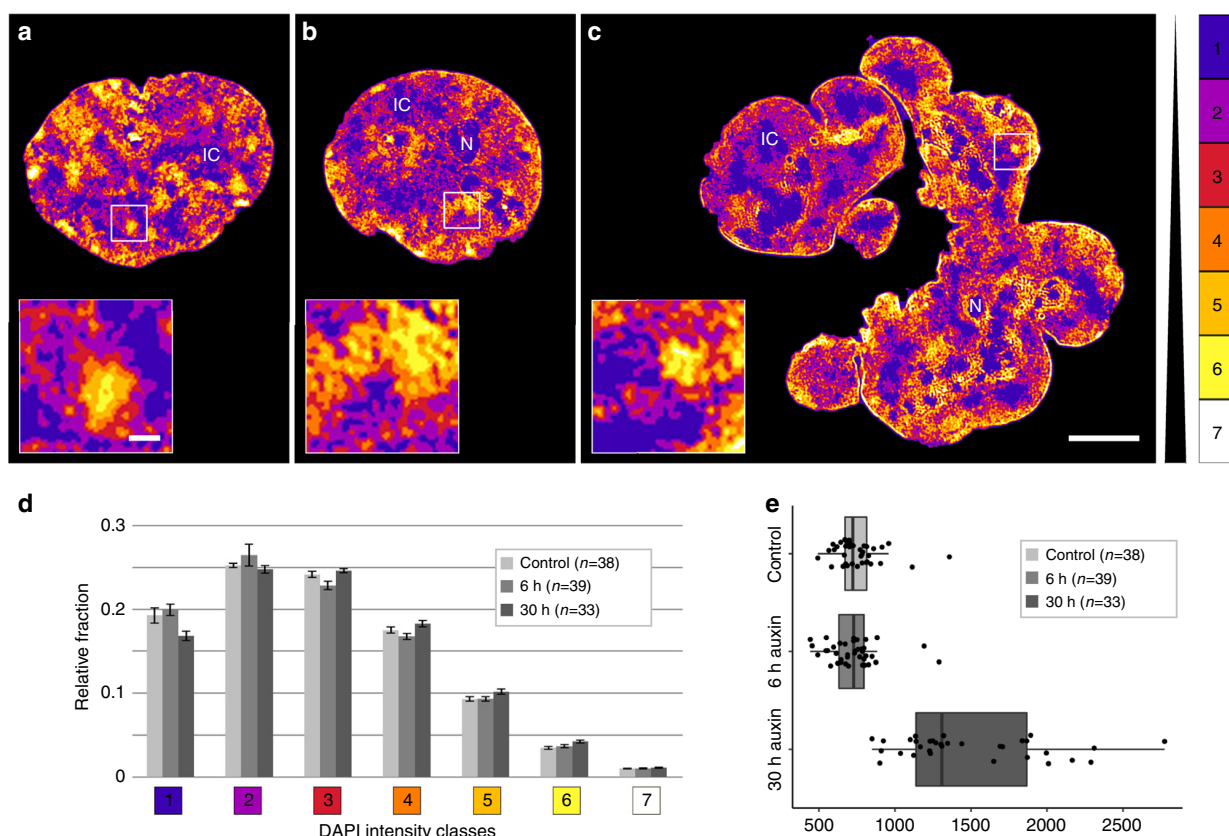


**Fig. 3** Compartmentalized architecture with an interchromatin (IC) channel network pervading chromatin domain clusters (CDC) with zonal compaction differences both in controls and cohesin depleted, pre- and post-endomitotic nuclei. **a–c** DAPI-stained mid-sections of representative nuclei acquired by 3D-SIM from **a** control nucleus; **b** cohesin depleted nucleus (6 h auxin); **c** cohesin depleted multilobulated nucleus (MLN) (30 h auxin) are displayed by seven DAPI intensity classes in false colors, used as proxies for chromatin compaction. The color code on the right indicates the assignment of DAPI signals into seven classes with equal intensity variance. This approach allows threshold-independent signal intensity classification based on the intensity of an individual voxel. Class 1 (blue) pixels close to background intensity, largely reflecting the interchromatin compartment (IC) with only sparse DNA, class 7 (white) pixels with the highest intensities. All nuclei in **a–c** reveal a network of chromatin domain clusters (CDCs) comprising a compacted core and a surrounding low-density zone co-aligned with class 1 regions that meander between CDCs as part of the IC (see insets). Likewise, all nuclei display a rim of compacted (hetero)chromatin at the nuclear periphery. N = nucleolus; IC = interchromatin channels/lacunae. Images in **a–c** show representative nuclei from two independent experiments. Scale bars: 5 µm, insets: 0.5 µm. **d** Relative 3D signal distributions of DAPI intensity classes in control nuclei and cohesin depleted nuclei show an overall similar profile. (control:  $n = 38$ , 6 h:  $n = 39$ , 30 h:  $n = 33$  cells from two independent experiments). 6 and 30 h, respectively denote incubation time in auxin. Data are represented as mean  $\pm$  SEM. **e** Average nuclear volumes ( $\mu\text{m}^3$ ) from the same series of nuclei. The  $\sim 2$ -fold increase of nuclear volumes in (post-endomitotic) MLN after 30 h auxin likely reflects their further increase of a 2n DNA content immediately after endomitosis to a 4n DNA content after another round of DNA replication (Supplementary Fig. 5), for statistical tests see Source Data file. Data in **e** are represented as boxplot where the middle line indicates the median, the lower and upper hinges correspond to the 25 and 75% quartiles, the upper whisker extends to the largest value no further than  $1.5 \times \text{IQR}$  (inter-quartile range) from the hinge and the lower whisker extends to the smallest value from the hinge at most  $1.5 \times \text{IQR}$ . In addition, all data points are plotted individually. Source data are provided as a Source Data file.

2, but clearly enriched in classes 4 and 5. For RNA Pol II (Fig. 4h) we noted the most pronounced relative enrichment in class 2 and relative depletion in classes 4–7. The separate presentation of both replicates (Supplementary Fig. 7a, b) consistently support an enrichment of SC35 in class 1, and of H3K27me3 in class 4 and 5. The particular enrichment of H3K27me3 in classes 3 and 4 and depletion in class 7 is in line with its assignment as a marker for facultative heterochromatin<sup>30</sup>. Enrichment-depletion patterns of RNA Pol II in the two replicates agree with respect to a general enrichment of RNA Pol II in the ANC (class 1–3), and a depletion within the INC, but differ markedly in quantitative details. Whereas replicate 1 shows a pronounced relative enrichment of this enzyme in class 1 and 2 in line with a relative depletion in classes 3 to 7, replicate 2 shows modest RNA Pol II enrichments in classes 2 and 3, together with relative depletions in classes 5–7, but unexpectedly also in class 1 (IC).

It is important to emphasize that relative enrichments and depletions of epigenetic markers and functional proteins were defined in the 7 DAPI intensity classes. Differences between replicates 1 and 2 that represent snap-shots from the respective experiments may be attributed to unperceived variations of cell culture conditions. Supplementary Fig. 7c–e demonstrates for example a range of compaction differences between SC35 marked speckles in both control and cohesin depleted nuclei. These examples illustrate the cell-to-cell variability of the nuclear landscape, which cannot be captured by a typical one-for-all image. We did not further pursue the question, whether this structural variability reflects functional differences between individual cells in the non-synchronized cell populations studied here.

Notwithstanding these differences, both replicates support our major conclusion: Principal features of a compartmentalized

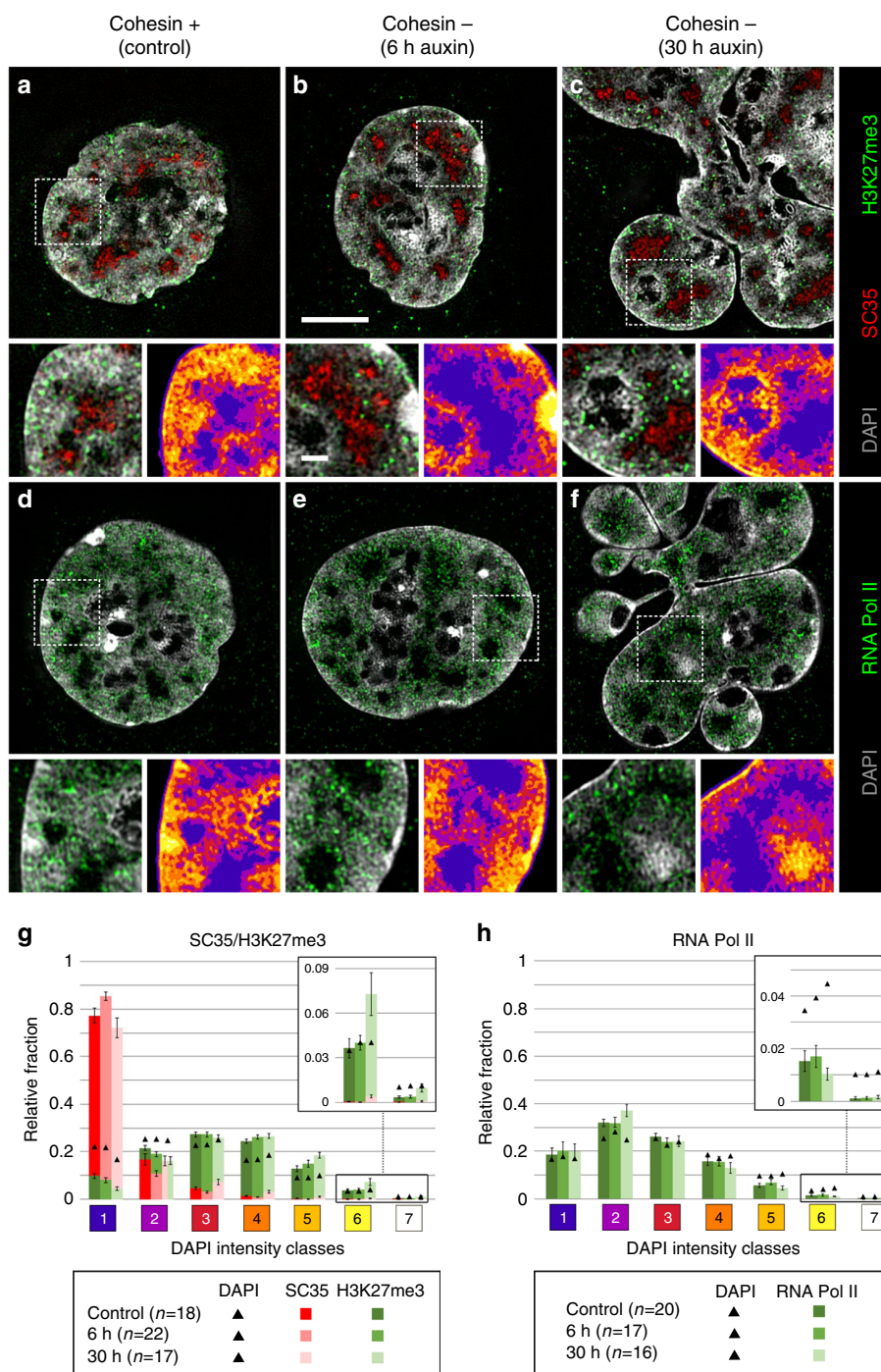


**Fig. 4 Congruent 3D topology of SC35, H3K27me3, and RNA Pol II in nuclei of control and cohesin depleted cells.** **a–f** DAPI-stained nuclear mid-sections (gray) displayed from 3D SIM image stacks of control nuclei (**a, d**), of pre-mitotic cohesin depleted nuclei after 6 h auxin treatment (**b, e**), and post-endomitotic MLN after 30 h auxin treatment (**c, f**) reveal the topography of immunostained SC35 (red) and H3K27me3 (green) (**a–c**), and active RNA Pol II (red) (**d–f**). Scale bar: 5  $\mu$ m. An enlargement of a representative boxed area is shown beneath each mid-section together with the color-coded DAPI intensity heat map (compare Fig. 3). Scale bar: 1  $\mu$ m. SC35 marked splicing speckles are located in the interchromatin compartment (IC, blue), H3K27me3 marks are distributed within neighboring chromatin domain clusters; RNA Pol II is mainly enriched in chromatin lining the IC (purple), but also extends into the IC, whereas it is largely excluded from densely compacted chromatin regions (brown and yellow). **g, h** 3D image analyses of 3D SIM stacks show the relative fraction of **g** SC35 (red) and H3K27me3 (green) signals (control:  $n = 18$ , 6 h:  $n = 22$ , 30 h:  $n = 17$  cells from two independent experiments), and **h** of active RNA Pol II (green) (control:  $n = 20$ , 6 h:  $n = 17$ , 30 h:  $n = 16$  cells from two independent experiments) in comparison to DAPI intensity classes 1–7 marked as black triangles. 6 and 30 h, respectively, denote incubation time in auxin. Data are represented as mean  $\pm$  SEM. Source data are provided as a Source Data file.

organization with CTs and CDCs, pervaded by the IC in control nuclei were maintained in pre-mitotic, cohesin depleted nuclei and were rebuilt in post-endomitotic MLN, where individual macromolecules may penetrate into highly compacted CDs while macromolecular aggregates, such as a transcription machinery (RNA Pol II) or splicing machinery (SC35) may be excluded<sup>17,31</sup>.

#### **In situ Hi-C data indicate the maintenance/rebuilding of A and B compartments in cohesin depleted pre-mitotic nuclei and post-endomitotic MLN despite the loss of loop domains.**

In situ Hi-C of cell cultures, treated with auxin for 6 and 28 h, respectively, prior to fixation, confirmed the disappearance of loop domains (Fig. 5a) in contrast to control cultures, whereas A and B compartments were maintained (Fig. 5b; for terminology see Supplementary Table 1b). Since most cells had passed an endomitosis with the formation of MLN after 28–30 h auxin treatment (Supplementary Fig. 3), we conclude that these findings are representative for both cohesin depleted pre-mitotic nuclei and post-endomitotic MLN. A heightened compartmentalization was noted in particular with regard to B-type chromatin, as previously described for pre-mitotic cohesin depleted cells<sup>15</sup>. Strengthened interactions between this B-type compartment could be readily observed even in our low depth data from 28 h auxin-treated cells (Fig. 5c, lower right panel, interactions between loci annotated in yellow). While the functional identity or significance of this particular B-type subcompartment remains unknown, we were able to identify by k-means clustering of histone modification data for HCT116-RAD21-mAC cells<sup>15</sup> a histone modification cluster (consisting of depletion of both activating marks like H3K36me3 and H3K27ac and repressive marks such as H3K27me3 and H3K9me3, but a mild enrichment of H3K79me2) that corresponded to the positions of this particular B-type subcompartment (Fig. 5d, e; cluster 4). Genome-wide analysis of the average Hi-C contact frequencies between the histone modification clusters demonstrated a strong enrichment for within-cluster contacts for this B-type subcompartment at both 6 and 28 h after cohesin degradation, and additionally, at 28 h, mild cohesin-degradation induced enrichment of interactions between this B-type subcompartment and clusters enriched for repressive histone modifications as well as depletion of interactions with clusters enriched for activating histone modifications. The comparison of ensemble Hi-C data with microscopic data described above supports the argument that A/B compartments and ANC/INC compartments reflect the same structures (see Discussion).

#### **Persistence of typical S-phase stage replication patterns after cohesin depletion.**

The following part of our study shows that the structural compartmentalization of pre-mitotic, cohesin depleted cells and post-endomitotic MLN corresponds with their functional capability to maintain RDs and to proceed through S-phase. The temporal order of replication is highly coupled with genome architecture, resulting in typical patterns for early, mid, and late replication timing<sup>32</sup>. RDs were chosen in our study as microscopically visible reference structures, which correspond to microscopically defined chromatin domains (CDs) and persist as stable chromatin entities throughout interphase and during subsequent cell cycles<sup>33–35</sup> (Supplementary Table 1a). Replicating DNA was visualized by pulse replication labeling (RL) (see Methods). Control cultures were fixed 6 h after RL (Fig. 6a), cultures prepared for cohesin depletion were further grown after RL for 1 h under normal medium conditions and then exposed to auxin for 6 h (Fig. 6b, c) or 30 h (Fig. 6d) before fixation. Both controls (a) and auxin-treated cells (b, d) revealed nuclei with typical RD patterns for different S-phase stages. This experiment demonstrates that different RD patterns persist during the

subsequent pre-mitotic interphase of cohesin depleted cells (Fig. 6b) and can be fully reconstituted in post-endomitotic MLN (Fig. 6d). Notably, structural entities reflecting RDs pulse-labeled during S-phase can also be identified along mitotic chromosomes (Fig. 6c). MLN are able to initiate a new S-phase with the formation of typical replication patterns, shown in Fig. 6e, where RL was performed in cultures after 30 h of auxin treatment (Fig. 6e).

**Replication timing is preserved upon cohesin depletion.** Using Repli-Seq<sup>36,37</sup> and Hi-C analysis, replication timing was measured by the ratio of early to late replicating DNA and was found preserved upon cohesin depletion (Fig. 7a, b), consistent with a prior report<sup>38</sup>. In addition, the tight relationship between genome A/B compartmentalization and replication timing was similarly maintained in the absence of cohesin, exemplified for chr. 8 (Fig. 7a). Data were based on at least two replicates of each timepoint and confirmed the reproducibility of results.

#### **Structural changes of RDs in cohesin depleted nuclei.**

Finally, we tested whether cohesin depletion results in structural changes of individual RDs, detectable on the resolution level of 3D-SIM (Fig. 8). For this purpose, RD counts and RD volumes were evaluated in nuclei of three cultures: The control culture was fixed 6 h after RL together with the 6 h auxin culture, which was incubated with auxin immediately after RL. The 30 h auxin culture was fixed after 30 h in auxin, when most cells had passed an endomitosis yielding a multilobulated cell nucleus. Nuclei with RD patterns typical for early S-phase at the time of pulse labeling were identified in the three fixed cultures and 3D serial image stacks of such nuclei were recorded with SIM and used for measurements in entire nuclei. It is important to note that an RD pattern generated by pulse labeling in a given nucleus is maintained after S-phase and after mitosis, independent of the time of fixation during the post-endomitotic interphase of MLN. Therefore, controls and auxin-depleted cells fixed 6 h after RL proceeded to G2, but still showed the early S-phase RD pattern. In the culture fixed 30 h in auxin, we identified MLN also showing early replication patterns. Figure 8a shows examples of such nuclei from the control culture (left), the 6 h cohesin depleted culture (middle) and from 30 h cohesin depleted MLN cells (right). Figure 8b presents average numbers of segmented RDs for individual nuclei and Fig. 8c shows the results of volume estimates for individual RDs from the respective nuclei. Compared with controls, we noted an increase of both RD numbers and volumes together with an increase of heterogeneity (broader range of number and size distribution) in cohesin depleted pre-mitotic nuclei and post-endomitotic MLN. Based on the concordant increase of counts and volumes of segmented RDs in cohesin depleted nuclei in comparison with control nuclei, we tentatively conclude that cohesin is indispensable to prevent disintegration and decompaction of RDs (see Discussion).

#### **Effect of cohesin depletion on DNA halo induced chromatin loops.**

An effect of cohesin depletion on chromatin loop structure was supported by a DNA halo approach, a technique to investigate changes in chromatin organization at the level of DNA loops<sup>39</sup>. Histone extraction in interphase nuclei by high-salt incubation triggers the extrusion of chromatin loops from a densely stained central chromatin core thus providing a measure of their size. DAPI-stained nuclei of cohesin depleted cells (6 h auxin treatment) exhibited halos that were significantly larger and more variable in shape in comparison to the defined and compacted halos of control cells (Supplementary Fig. 8) in line with the recently described observation that the cohesin-NIPBL complex compacts DNA by extruding DNA loops<sup>19</sup>.

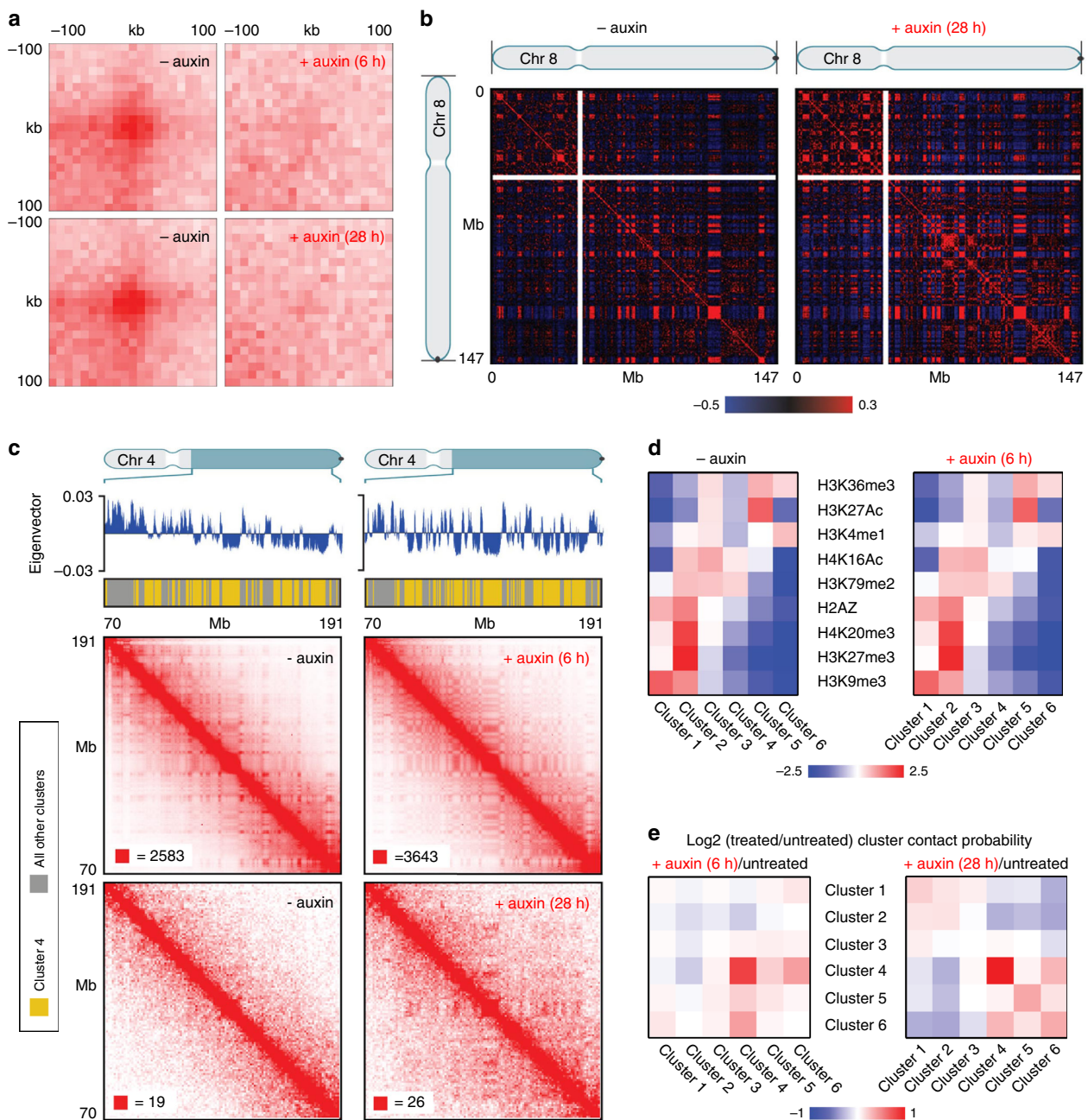


**Fig. 5** Hi-C data indicate elimination of chromatin loops, but the maintenance of A and B compartments in cohesin depleted pre- and postmitotic cells. **a** Aggregate peak analysis (APA) plots using loops identified in HCT116-RAD21-mAC cells before and after 6 h of auxin treatment (top) or before and after 28 h of auxin treatment (bottom). For each of the treated timepoints, the matched untreated control (harvested at the same time) is plotted next to it. The plot displays the total number of contacts that lie within the entire putative peak set at the center of the matrix. Loop strength is indicated by the extent of focal enrichment at the center of the plot. **b** Pearson's correlation maps at 500 kb resolution for chromosome 8 before (left) and after (right) 28 h of auxin treatment. The plaid pattern in the Pearson's map, indicating compartmentalization, is preserved in cohesin depleted nuclei even after 28 h of auxin treatment. **c** Contact matrices for chromosome 4 between 70 and 191 Mb at 500 kb resolution before (left) and after (right) cohesin depletion. The 6 h cohesin depletion time is shown on top, and 28 h depletion time on the bottom. K-means clustering of histone modifications at 25 kb resolution into six clusters annotates loci corresponding to specific subcompartments. Interactions for loci in cluster 4 (arbitrary numbering, annotated in yellow on top tracks) are strengthened after both 6 and 28 h of cohesin depletion. All loci belonging to clusters other than cluster 4 are annotated in gray in the top track. The max color threshold (red) of the heatmap is illustrated in the lower-left corner of each heatmap, the minimum color threshold (white) is 0 reads. **d** Log<sub>2</sub> fold ratios of between-cluster Hi-C contact probabilities post- and pre-cohesin degradation are shown for the six clusters identified via K-means clustering of histone modifications. Cluster 4 shows strong contact probability enrichment after cohesin degradation at both the 6 h and 28 h timepoints. **e** For each of the six histone modification clusters, the average log<sub>2</sub>-fold enrichment for each histone modification over all loci in that cluster is shown both post- and pre-cohesin degradation. Patterns of histone modifications across the clusters as unchanged by cohesin degradation.

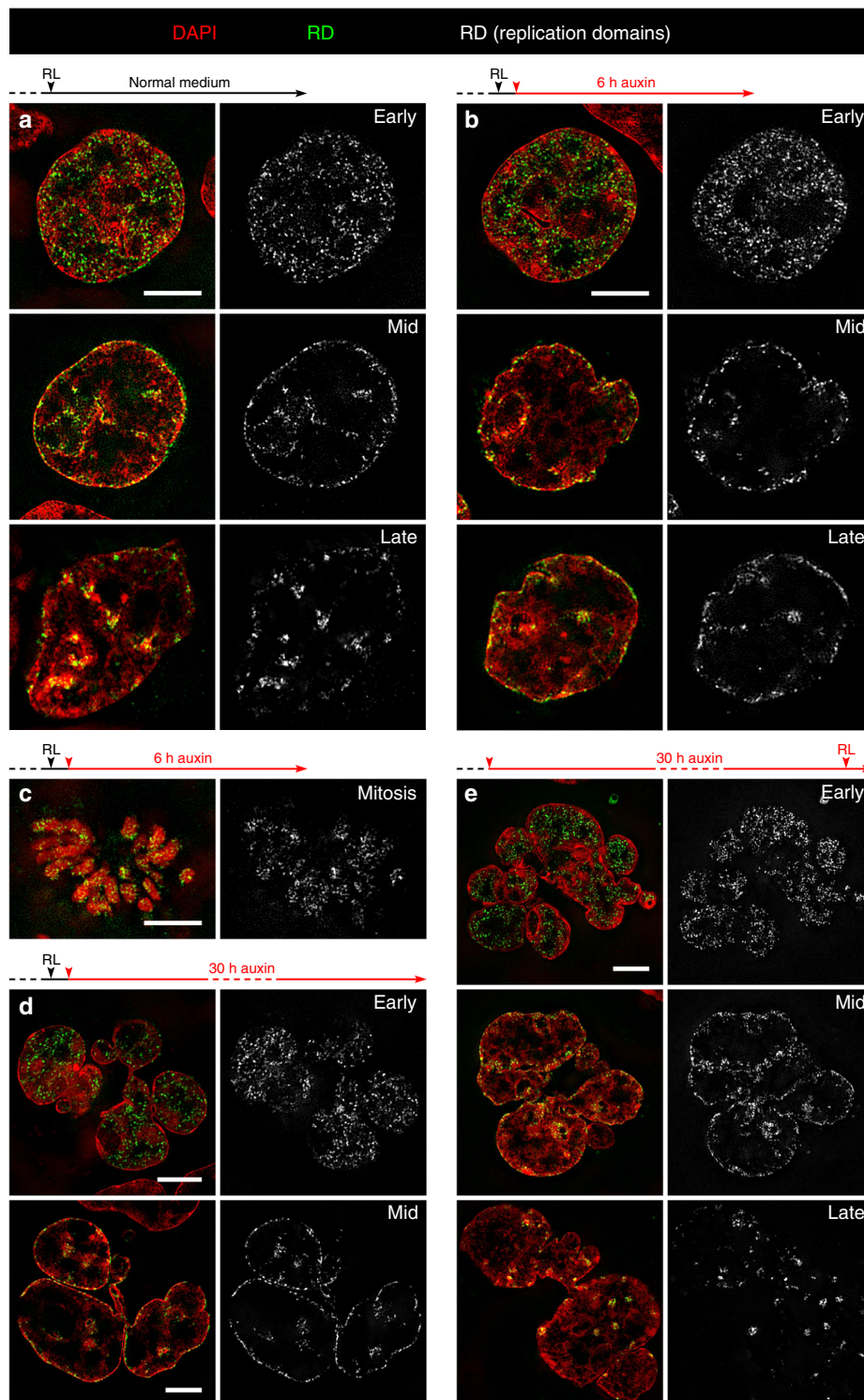


**Fig. 6 Maintenance, postmitotic rebuilding and de novo formation of typical replication patterns after cohesin depletion. a–e** Overlay images (left) show representative SIM sections of DAPI-stained nuclei (red) with replication domains (RDs)(green) identified by replication labeling (RL) in different stages of S-phase. RDs in the same nuclear sections are also displayed in gray (right). **a** Control nuclei fixed 6 h after RL with typical patterns for early, mid and late replication, respectively. **b** Maintenance of the same typical replication patterns in nuclei of cohesin depleted, pre-mitotic cells fixed 6 h after RL. **c** Cohesin depleted mitotic cell with replication labeled chromatin domains obtained under conditions as described in **b**. **d** RD patterns in individual lobuli demonstrate the ability of post-endomitotic MLN to restore RD patterns, generated by RL during the previous cell cycle. Cells were treated with auxin for 30 h after RL. **e** RL carried out with MLN obtained after ~30 h auxin treatment demonstrates de novo DNA synthesis with the formation of new typical replication patterns. Scale bar: 5  $\mu$ m. Images shown in **a–e** show representative nuclei from three independent experiments.

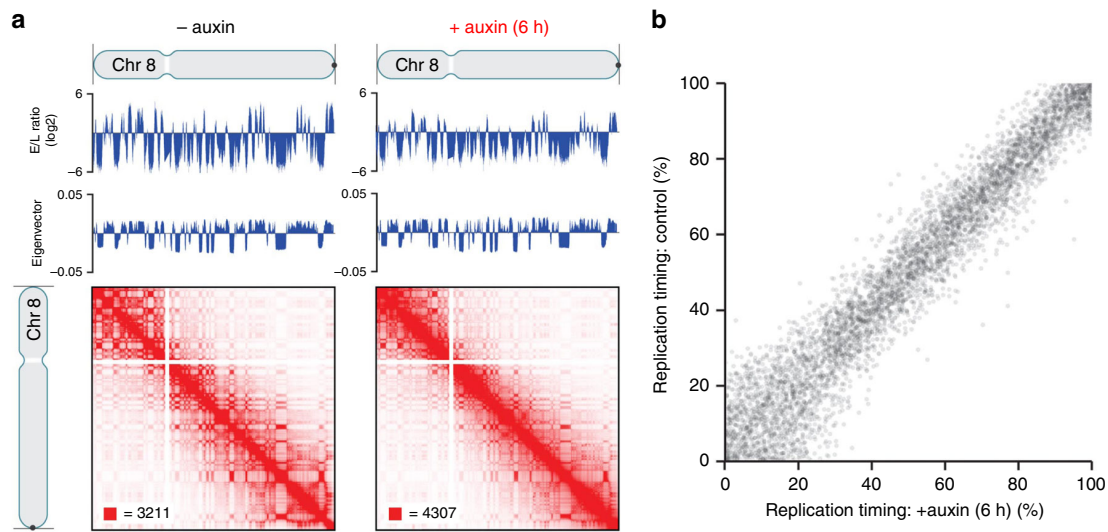


**Fig. 7 Hi-C and Repli-Seq data demonstrate the same replication timing for cohesin depleted and non-depleted control cells. a** Contact matrices of chromosome 8 at 500 kb resolution along with the corresponding Repli-Seq early-to-late (E/L) ratio tracks at 50 kb resolution and the first eigenvectors of the Hi-C matrices corresponding to A/B compartmentalization. Replication timing along the genome is conserved, as shown by the correspondence of the untreated and auxin-treated Repli-Seq tracks. In addition, the correspondence between replication timing and genome compartmentalization (as indicated by the plaid pattern in the Hi-C map and the first eigenvector of the Hi-C matrices) is preserved after auxin treatment. **b** Scatter plot of replication timing (percentile of E/L ratio) in RAD21-mAC cells before (y-axis) and after (x-axis) auxin treatment.

## Discussion

Our study demonstrates that multilobulated nuclei (MLN), that arise from cohesin depleted cells after passing through an endomitosis, retain the ability to rebuild a compartmentalized nuclear architecture. Whereas ensemble Hi-C confirmed the continued absence of chromatin loops and TADs in MLN as in pre-mitotic cohesin depleted nuclei, A and B compartments were fully restored in MLN in line with active and inactive nuclear compartments (ANC and INC<sup>17,18</sup>) revealed by 3D SIM. In light of the fundamental roles ascribed to cohesin, the capacity of MLN to initiate another round of DNA replication with stage-specific patterns of RDs was not expected.

Progression of cells into a disturbed and prolonged mitosis after cohesin depletion by Rad21 siRNA transfection was described in previous live-cell studies covering ~4 h<sup>40</sup>. By extending the live-cell observation period up to 21 h, we discovered a so far unreported endomitosis with chromatid segregation, but apparent failure to complete karyokinesis and cytokinesis. This failure may be attributed to the impact of cohesin for proper spindle pole formation and kinetochore-microtubule attachment (reviewed in refs. 7,8). Notably, in vertebrates loading of cohesin onto DNA already occurs in telophase<sup>7,41</sup>, which may be essential for subsequent cytokinesis and daughter cell formation. Factors promoting endomitosis and the formation of MLN are, however, complex and certainly diverse<sup>42</sup>. Multipolar endomitosis with the formation of polyploid MLN occurs physiologically in megakaryocytes<sup>43</sup> and in (cohesin competent) tumor cell lines<sup>44</sup>, in part entailing extensive chromosomal rearrangements<sup>45</sup>. The observation of MLN as the mitotic outcome in ~2% of HCT116-RAD21-mAC control cells exemplifies the spontaneous occurrence of MLN in a near-diploid tumor cell line.

Hi-C and related methods offer the great advantage of a genome-wide approach to explore a nuclear compartmentalization at the DNA sequence level. This approach demonstrated a compartmentalized architecture of the landscape in cohesin depleted cell nuclei<sup>4,16</sup>, but failed to detect the profound global morphological changes in post-endomitotic cohesin depleted

MLN compared to cohesin depleted nuclei before passing through endomitosis. High-resolution microscopy is also the method of choice to examine the 3D structure of chromatin domain clusters (CDCs) with a zonal organization of repressed (condensed) and transcriptionally competent (decondensed) chromatin domains and the actual 3D configuration of the interchromatin compartment (IC)<sup>46</sup> with its supposed function as storage and transport system<sup>17</sup> that co-evolved with higher-order chromatin organization<sup>47</sup>. Our results exemplify the necessity to combine bottom-up with top-down approaches in ongoing 4D nucleome research, aimed at a comprehensive understanding of the structure-function relationships in complex biological systems.

We propose that microscopically defined ANC/INC compartments and A/B compartments, detected by ensemble Hi-C, represent the same functional compartments. Chromatin that contributes to the ANC and compartment A, respectively, is gene rich, transcriptionally active, and typically located preferentially in the interior of mammalian cell nuclei, whereas both the INC and compartment B comprise gene poor, transcriptionally repressed chromatin of higher compaction, which is more prominent at the nuclear periphery (for review see refs. 18,48). We further propose to equate microscopically defined chromatin domains (CDs)/RDs comprising several hundred kb (see below) that constitute functional building blocks of the ANC and INC with similarly sized compartment domains (see Supplementary Table 1c) as functional building blocks of A and B compartments rather than with TADs<sup>49–51</sup>. A correspondence of microscopically discernible RDs with TADs mapped by ensemble Hi-C has been favored in some studies<sup>50,51</sup>.

TADs represent genomic regions between several 100 kb up to >1 Mb in length, where DNA sequences physically interact with each other more frequently compared to sequences outside a given TAD<sup>48,52–54</sup>. TADs, however, do not represent an individual chromatin structure, but a statistical feature of a cell population. Boundaries detected in Hi-C experiments are noted as transition points between TAD-triangles. They constrain, but do not restrict completely the operating range of regulatory

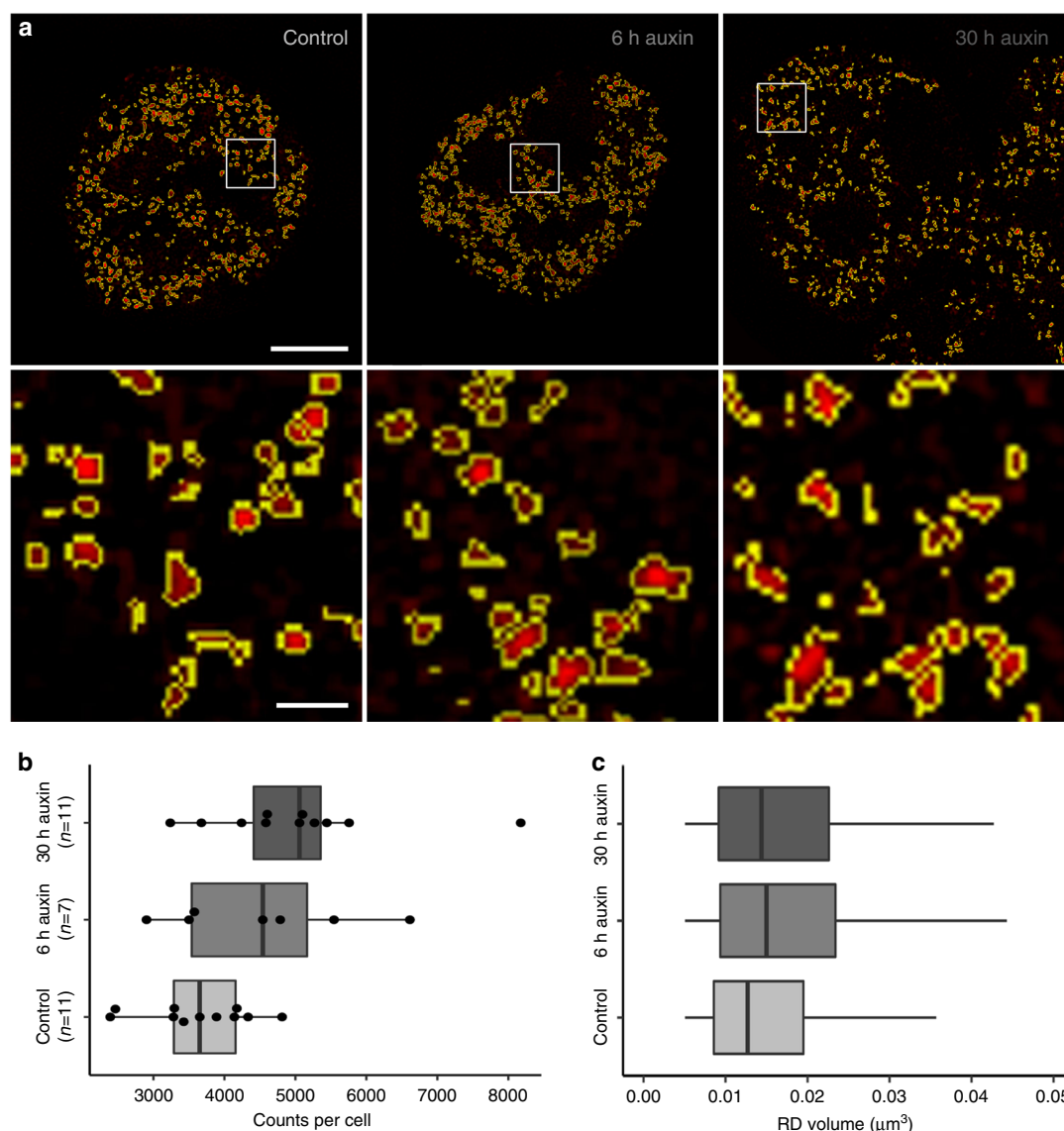


**Fig. 8 Segmentation of individual replication domains (RDs), pulse-labeled in early S-phase, indicate structural changes after cohesin depletion.** **a** SIM nuclear mid-sections of nuclei with typical early S-phase patterns of replication domains (RDs) from a control culture (left), a 6 h auxin-treated culture (middle), both fixed 6 h after RL, and a multilobulated nucleus (right) obtained after 30 h auxin treatment (compare Fig. 6a–d). Enlargements of boxed areas show individual, segmented RDs displayed in red with segmented borders lined in yellow. Scale bar: 4  $\mu\text{m}$ , 0.5  $\mu\text{m}$  in inset magnifications. **b** Counts of segmented RDs plotted for control nuclei, cohesin depleted nuclei after 6 h auxin and MLN after 30 h auxin are presented as dots (control:  $n = 11$ , 6 h:  $n = 7$ , 30 h:  $n = 11$  nuclei from two independent experiments). **c** Boxplots with corresponding volume distributions of segmented individual RDs (control:  $n = 39.334$ , 6 h:  $n = 31.467$ , 30 h:  $n = 55.153$ ). The non-parametric two-sided Mann-Whitney test revealed significant differences of RD counts between control nuclei and MLN ( $p = 0.012$ ) and for RD volumes ( $p < 0.0001$  for control  $\leftrightarrow$  6 h auxin, control  $\leftrightarrow$  30 h auxin, and 6 h auxin  $\leftrightarrow$  30 h auxin). Volumes of RDs with dimensions below the resolution limit of 3D-SIM ( $\sim 120$  nm lateral/ $300$  nm axial) show the same size and were excluded from consideration. Accordingly, the lower limits of volumes between control nuclei and cohesin depleted nuclei are identical in contrast to the differences of the upper volume limits. Data in **b**, **c** are represented as boxplots where the middle line indicates the median, the lower and upper hinges correspond to the 25 and 75% quartiles, the upper whisker extends to the largest value no further than  $1.5 \times \text{IQR}$  (inter-quartile range) from the hinge and the lower whisker extends to the smallest value from the hinge at most  $1.5 \times \text{IQR}$ . In **b**, all data points are plotted individually. Source data are provided as a Source Data file.

sequences<sup>55</sup>. Recently, super-resolution microscopy demonstrated the presence of TAD-like domains at the single-cell level<sup>56</sup>. In cohesin depleted cells, a more stochastic placement of borders between TAD-like domains was detected<sup>57</sup>. A role of IC-channels as additional structural boundaries between CDs and CDCs located on both sides, has been considered but not proven<sup>17</sup>.

Early microscopic studies of the replicating genome during S-phase provided a first opportunity to explore its genome-wide

partitioning into discrete structural entities with a DNA content of  $\sim 1$  Mb, called RDs or replication foci<sup>58,59</sup>. We adopted the term  $\sim 1$  Mb chromatin domains in line with evidence that RDs persist as similarly sized stable chromatin units throughout interphase and during subsequent cell cycles<sup>33,34</sup>. Later studies assigned an average DNA content of 400–800 kb to RDs/CDs<sup>37</sup>, which can be optically resolved down to clusters of a few single replicons (150–200 kb)<sup>35,60</sup>. Gene rich, early replicating domains

form the A compartment, gene poor, later replicating domains the B compartment<sup>37</sup>.

Our study confirms previous reports, which showed the maintenance of pulse-labeled RDs and the formation of S-phase specific replication patterns in cohesin depleted, pre-mitotic interphase cells<sup>28,38</sup>. In addition, our study demonstrates the ability to re-constitute RDs in a typical pattern arrangement in post-endomitotic MLN. Moreover, MLN were able to initiate a new round of DNA replication with the formation of typical stage-specific replication patterns under continued absence of cohesin.

These observations, however, do not imply that cohesin would be dispensable for RD structure. A comparison of numbers (counts) and volumes of individual RDs generated in early S-phase in nuclei of control cells and cells treated with auxin for 6 and 30 h revealed a significant increase both of RD numbers and RD volumes and also in a remarkably increased heterogeneity of these parameters after cohesin depletion. The near double amount of RD numbers in MLN (30 h auxin) compared to controls was expected since MLN are generated as a result of an endomitosis with full separation of sister chromatids harboring RDs where labeled nucleotides were incorporated into both newly synthesized DNA strands in the previous cell cycle. In cohesin depleted cells treated with auxin after RL for 6 h the increase of discernible RDs may result from an enhanced untethering of labeled sister chromatids compared to controls. At the time of fixation, both controls and cohesin depleted cells had likely reached the late S or G<sub>2</sub>-phase and labeled RDs had formed two separate sister chromatids within a given CT. Sister chromatids are kept together by cohesin at some sites, but are untethered at other sites and can dissociate from each other up to few hundred nm<sup>61</sup>. In cohesin depleted nuclei these untethered sites are likely increased. An increase of RD counts based on RD splitting should correspond with a decrease of RD volumes. Unexpectedly, we observed a remarkable volume increase in individual segmented RDs. This observation supports a role of cohesin in the compaction of chromatin structures exerted by chromatin loop extrusion<sup>19</sup> which could affect contact frequencies and thus explain at least in part the loss of TAD patterns in ensemble Hi-C experiments. Due to the resolution limit of 3D-SIM (~120 nm lateral/300 nm axial) these results must be viewed with caution: a fraction of RDs with sizes below this limit would show a putative size reflecting the diffraction limit, resulting in an overestimate of their volumes. To overcome these method-inherent limitations, imaging approaches with higher resolution, such as STORM/SMLM or STED are required to further clarify the influence of cohesin on RD structure<sup>61,62</sup>. The increased heterogeneity of RD volumes in cohesin depleted nuclei compared with controls, likely reflects the cell-to-cell shift of boundaries described for TAD-like domains in cohesin depleted cells<sup>57</sup>. In summary, the current study supports our previous conclusion<sup>15</sup> that cohesin plays an indispensable role for the structure of RDs/CDs, but is dispensable for the formation of a compartmentalized nuclear organization with preserved A and B compartments. These earlier results are substantially enhanced through the microscopic observations described in the present study, which demonstrates that cohesin depleted cells passing through an endomitosis are able to rebuild a cell nucleus with the basic features of the ANC and INC, respectively. It is of note to emphasize here that Hi-C alone did neither allow to detect the drastic changes of the global architecture between cohesin depleted cells studied before and after endomitosis nor the added topographical features of IC-channels and lacunas. The current study may help to stimulate integrated research strategies with the goal to better understand the structure-function implications of the nuclear landscape.

New methods of super-resolved optical reconstruction of chromatin organization with oligopaints technology<sup>56</sup> or the combination of serial block-face scanning electron microscopy with in situ hybridization (3D-EMISH)<sup>63</sup> have opened up new ways to explore the geometrical variability of TAD-like structures in comparison with TADs identified by ensemble Hi-C and to close current gaps of knowledge on nuclear compartmentalization. Despite compelling evidence for chromatin loops, their actual 3D and 4D (space-time) organization is not known. Microscopic evidence for the formation of higher-order chromatin arrangements based on nucleosome clutches or nanodomains<sup>28,56,57,64–66</sup> suggests that loops may be organized as much more compact structures with the potential implication that the diffusion of individual macromolecules into their interior may be constrained and the penetration of macromolecular aggregates is fully excluded<sup>31</sup>. As a consequence, transcription and other nuclear functions may preferentially occur at the surface of chromatin clusters, dynamically remodeled to fulfill this condition. How dynamic changes of functionally defined higher-order chromatin structures in space and time are related to changing functional requirements of cells at different levels of a hierarchical chromatin organization, defines major challenges for future studies. Such studies should also advance our still incomplete knowledge of cohesin functions.

## Methods

**Cells and culture conditions.** HCT116-RAD21-mAID-mClover cells (referred to as HCT116-RAD21-mAC cells in the manuscript) were generated and kindly provided by the Kanemaki lab (Mishima Shizuoka, Japan). For a detailed description see ref. <sup>14</sup>. Cells were cultured in McCoy's 5A medium supplemented with 10% FBS, 2 mM L-glutamine, 100 U/ml penicillin, and 100 µg/ml streptomycin at 37 °C in 5% CO<sub>2</sub>. For data shown in Supplementary Fig. 1b and 8 HCT116-RAD21-mAC cells and HCT-116 wild-type cells were grown in DMEM medium supplemented with 10% FCS, 2 mM L-glutamine, 50 µg/ml gentamicin. Cells were tested for mycoplasma contamination by confocal microscopy.

**Auxin-induced RAD21 proteolysis.** Degradation of AID-tagged RAD21 was induced by the addition of auxin (indole-3-acetic acid; IAA, Sigma Aldrich) to the medium at a final concentration of 500 µM (auxin stock solution 2 M in DMSO). In long-term cultures fresh auxin-medium was added after ~18 h.

**Immunodetection.** Immunodetection was performed on cells grown to 60–80% confluency on high precision borosilicate glass coverslips (170 µm ± 5 µm thickness) with the following antibodies: cohesin subunits RAD21 (Abcam), SMC1 and SMC3 (both Bethyl laboratories) were detected with Cy3-conjugated goat anti rabbit antibodies (Dianova). Primary antibodies against SC35 (Sigma), RNA Pol II (Abcam), and H3K27me3 (Active Motif) were detected with either donkey anti-mouse Alexa 488 (Life technologies) or donkey-anti rabbit Alexa 594 (Life technologies). To meet the requirements for super-resolution microscopy with respect to an optimal signal-to-noise ratio and preservation of 3D chromatin structure, a protocol described in<sup>67</sup> was followed: Cells were washed with 1×PBS (pH = 7.4 w/o Ca/Mg) and fixed in 4% paraformaldehyde / PBS for 10 min. During the last 3 min the fixative was stepwise replaced by PBS/0.02% Tween followed by 2 × 5 min washing with PBS/0.02% Tween. The samples were quenched with 20 mM glycine/PBS for 10 min, washed with PBS/Tween, permeabilized with 0.5% Triton X-100/PBS for 10 min and subsequently incubated in blocking buffer (150 mM NaCl, 15 mM Hepes/KOH, 2 mM MgCl<sub>2</sub>, 0.1 mM EGTA, 0.2% Triton X-100, 0.5% fish skin gelatin, 2% BSA) for 1.5–2 h. Antibodies were diluted in blocking buffer and incubated for 1–1.5 h (primary) or 45–60 min (secondary) followed by intensive washing with blocking buffer. Cells were postfixed in 4% paraformaldehyde/PBS for 5 min, washed in PBS/Tween and counterstained in 2 µg/ml DAPI (4',6-diamidino-2-phenylindole) for 10 min, washed in PBS. Cells were mounted in antifade mounting medium (Vectashield (Vector Laboratories)) and the cover slips sealed with nail varnish onto a conventional microscopic slide. For the specification of antibodies see Supplementary Table 2.

**Replication pulse labeling (RL) by replication scratch labeling<sup>34</sup>.** Cells cultivated on high precision coverslips (thickness 0.170 mm) grown to 50–80% confluency were transferred into a dry empty tissue dish after draining off excess medium. Thirty microliters of a prewarmed labeling solution containing 20 µM Cy3-dUTP (homemade) or Alexa 594-5-dUTP (Life technologies) was evenly distributed over the coverslip. With the tip of a hypodermic needle parallel scratches at distances of ~100 µm were quickly applied to the cell layer. Cells were

incubated for 1 min in the incubator, then a few ml of pre-warmed medium was added to the dish. After 30 min medium was exchanged to remove non-incorporated nucleotides. This procedure preserves the RAD21-mClover fluorescence after labeling.

### RL by incorporation of 5-Ethynyl-dU (EdU) and detection via click chemistry.

This approach was used for RL in MLN after 30 h auxin treatment (compare Fig. 6e) since these cells are prone to detachment upon scratching. EdU was added at a final concentration of 10  $\mu$ M to the medium for 15 min. Incorporated EdU was detected according to manufacturer's instructions (baseclick) by a Cu(I) catalyzed cycloaddition reaction that covalently attaches a fluorescent dye containing a reactive azide group to the ethynyl-group of the nucleotide<sup>68</sup>. For visualization of RDs, the dye 6-FAM-Azide (baseclick) at a final concentration of 20  $\mu$ M was used.

After either labeling approach cells were washed in 1 $\times$ PBS, fixed with 4% formaldehyde/PBS for 10 min and permeabilized with 0.5% Triton X-100/PBS/Tween 0.02% for 10 min. Cells were counterstained in 1  $\mu$ g/ml DAPI and mounted in antifade mounting medium (Vectashield (Vector Laboratories)); for details, see ref. 67).

**Hi-C in situ analysis of untreated and auxin-treated cells.** HCT-116-RAD21-mAC cells were plated in 6-well plates with either complete media, or complete media with 500  $\mu$ M auxin (IAA) for 6 h (as in ref. 15) or 28 h (to enrich for post-mitotic cells with MLN). Cells were crosslinked with 1% formaldehyde directly on the plate for 10 min and then quenched with glycine. The crosslinked cells were then scraped off and in situ Hi-C was performed. In brief, cells were permeabilized with nuclei intact, the DNA was digested overnight with MboI, the 5'-overhangs were filled in while incorporating bio-dUTP, and the resulting blunt end fragments were ligated together. Crosslinks were then reversed overnight, the DNA was sheared to 300–500 bp for Illumina sequencing, biotinylated ligation junctions were captured using streptavidin beads and then prepped for Illumina sequencing. We prepared three libraries (two biological replicates) each for each time point (untreated 6 h, treated 6 h, untreated 28 h, treated 28 h). All Hi-C data were processed using Juicer<sup>69,70</sup>. The data were aligned against the hg19 reference genome. All contact matrices used for further analysis were KR-normalized with Juicer. Comparison of compartment strengthening to histone modification clusters was done as in ref. 15. Histone modification data for 9 marks (H3K36me3, H3K27Ac, H3K4me1, H4K16Ac, H3K79me2, H2AZ, H4K20me3, H3K27me3, and H3K9me3) generated from untreated and 6-hour treated cells in<sup>15</sup> was grouped into six clusters using k-means clustering. For the k-means clustering, the histone modification data were first converted into a z-score value for each mark in order to account for differences in the dynamic range between marks.

**Repli-Seq of untreated or auxin-treated cells.** HCT116-RAD21-mAC cells were synchronized in G1 with lovastatin following a protocol of ref. 71. Cells were incubated with 20  $\mu$ M Lovastatin (Mevinolin) (LKT Laboratories M1687) for 24 h to synchronize in G1. Five-hundred micromolar auxin or DMSO was added 6 h before release from lovastatin block. To release from G1 block, lovastatin was washed away with three washes of PBS and warm media plus 2 mM Mevalonic acid (Sigma-Aldrich M4667) and 500  $\mu$ M auxin or DMSO. Cells were released for 10, 14, 18, and 22 h. Two hours before the time point 100  $\mu$ M BrdU was added to label nascent replication. After fixation, equal numbers of cells from each release time point were pooled together for early/late repli-seq processing<sup>36</sup>. Repli-Seq data were processed as described in ref. 36. In brief, data were aligned to the hg19 reference genome using bowtie2, deduplicated with samtools, and the log<sub>2</sub> ratio between early and late timepoints was calculated.

**3D DNA-FISH.** Labeled chromosome painting probes delineating human chromosomes 4-(BIO), 12-(DIG) and 19-Cy3 were used. Following the protocol described in ref. 20, 30 ng of each labeled probe and a 20-fold excess of COT-1 DNA was dissolved per 1  $\mu$ l hybridization mix (50% formamide/2 $\times$  SSC/10% dextran sulfate). Cells were fixed with 4% formaldehyde/PBS for 10 min. After a stepwise exchange with 0.5% Triton X-100/PBS, cells were permeabilized with 0.5% Triton X-100/PBS for 10 min. Further pretreatment steps included incubation in 20% glycerol (1 h), several freezing/thawing steps in liquid N<sub>2</sub>, incubation in 0.1 N HCl (5 min) and subsequent storage in 50% formamide/2 $\times$  SSC overnight. After simultaneous denaturation of probe and cells (2 min at 76 °C), hybridization was performed at 37 °C for 48 h. After stringent washing in 0.1 $\times$ SSC at 60 °C, biotin was detected by streptavidin-Alexa 488 and DIG by a mouse-anti-DIG antibody conjugated to Cy5. Cells were counterstained in 1  $\mu$ g/ml DAPI, and mounted in antifade mounting medium Vectashield (Vector Laboratories).

**DNA halo preparation.** Cells were incubated for 6 h in 500  $\mu$ M auxin for cohesin depletion. DNA halo preparation was largely performed according to ref. 72. After washing the cells in 1 $\times$ PBS they were incubated for 10 min in a buffer at 4 °C containing 10 mM Tris pH 8, 3 mM MgCl<sub>2</sub>, 0.1 M NaCl, 0.3 M sucrose, protease inhibitors (freshly added to the buffer prior to use) 1  $\mu$ M pepstatin A, 10  $\mu$ M E64, 1 mM AEBSF and 0.5% Nonidet P40. All the following procedures were performed at room temperature. Subsequently, DNA was stained for 4 min with 2  $\mu$ g/ml DAPI. After 1 min in a second extraction buffer (25 mM Tris pH 8, 0.5 M NaCl,

0.2 mM MgCl<sub>2</sub>; protease inhibitors as in nuclei buffer and 1 mM PMSF were added fresh prior to use), cells were incubated 4 min in halo buffer (10 mM Tris pH 8, 2 M NaCl, 10 mM EDTA; protease inhibitors as in nuclei buffer and 1 mM DTT were added fresh prior to use). Finally, cells were washed 1 min each in two washing buffers (25 mM Tris pH 8, 0.2 mM MgCl<sub>2</sub>; the first buffer with and the second without 0.2 M NaCl). After 10 min fixation in 4% formaldehyde/PBS, cells were washed twice in 1 $\times$ PBS and mounted on slides with Vectashield. Nuclear scaffolds and the faded DNA halos were imaged at a widefield microscope (Zeiss Axioplan 2, 100 $\times$ /1.30 NA Plan-Neofluar Oil Ph3 objective; Axiovision software (version 4.8.2.0 SP3); AxioCam mRM camera). Both the total area (At) and the scaffold area (As) of each cell were manually segmented using the software Fiji and the DNA halo area (Ah) calculated as a subtraction of the two (Ah = At - As). The DNA halo radius was subsequently derived with the formula  $R = \sqrt{(Ah/\pi)}$ . Four biological replicates were prepared and measured. For generation of plots and statistical analysis (Wilcoxon test) the software RStudio (version 1.0.143) was used.

**Confocal fluorescence microscopy.** Confocal images were collected using a Leica SP8 confocal microscope equipped with a 405 nm excitation laser and a white light laser in combination with an acousto-optical beam splitter (AOBS). The used confocal system has three different detectors, one photomultiplier tube (PMT) and two hybrid photodetectors (HyD). The microscope was controlled by software from Leica (Leica Application Suite X, ver. 3.5.2.18963). For excitation of DAPI, the 405 nm laser was used, for excitation of Alexa488, Cy3, STAR635P, and Cy5, the white light laser was set to 499, 554, 633, and 649 nm, respectively. The emission signal of DAPI was collected by the PMT (412–512 nm), the emission signals of Alexa488 (506–558 nm), Cy3 (561–661 nm), STAR635P (640–750 nm), and Cy5 (656–780 nm) were collected by the two HyD detectors. Images were acquired with 42 nm pixel steps, 102  $\mu$ s pixel dwell time and twofold line accumulation using a Leica HC PL APO 63 $\times$ /1.30 NA Glycerol immersion objective. The frame size was 37 $\times$ 37  $\mu$ m and the scan speed was 700 Hz. The size of the confocal pinhole was 1 A.U. Confocal image z-stacks were acquired with a step size of 330 nm.

**Live-cell microscopy for long-term observations.** For live-cell imaging, cells were plated on poly-L-Lysine-coated glass-bottom 2-well imaging slides (ibidi), allowing to image control and auxin-treated conditions in parallel. For DNA staining cells were incubated in media containing 500 nM SiR-DNA (Spirochrome) for 1 h before imaging. Timelapse acquisitions were carried out on a Nikon TiE microscope equipped with a Yokogawa CSU-W1 spinning disk confocal unit (50  $\mu$ m pinhole size), an Andor Borealis illumination unit, Andor ALC600 laser beam combiner (405 nm/488 nm/561 nm/640 nm), and Andor IXON 888 Ultra EMCCD camera. The microscope was controlled by software from Nikon (NIS Elements, ver. 5.02.00). Cells were imaged in an environmental chamber maintained at 37 °C with 5% CO<sub>2</sub> (Oko Labs), using a Nikon PlanApo 60 $\times$ /1.49 NA oil immersion objective and a Perfect Focus System (Nikon). Images were recorded every 15 min for 21 h as z-stacks with two planes and a step size of 6  $\mu$ m, unbinned and with a pixel size of 217 nm. For excitation of mClover and SiR-DNA, the 488 and 640 nm laser lines were used, respectively. Fiji software (ImageJ 1.51j)<sup>73</sup> was used to analyze images.

**Quantitation of auxin-induced RAD21-mAID-mClover degradation on single cells after fixation.** HCT-116-RAD21-mAC and HCT-116 wild-type cells were treated with 500  $\mu$ M auxin for 6 h, fixed in 3.7% formaldehyde, permeabilized with 0.7% Triton X-100 for 15 min, counterstained with 1  $\mu$ g/ml DAPI for 10 min and mounted in Vectashield mounting medium (Vector Laboratories). High-throughput imaging of single cells was performed at the wide-field microscope Operetta (40 $\times$ /0.95 NA air objective; Harmony software (version 3.5.1); Jenoptik firecamj203 camera, Perkin Elmer). The high-content images were analyzed on batch through a pipeline created with the Harmony software and nuclei identified based on DAPI signal. The nuclei found on the border of each field were removed and the remaining nuclei were selected based on morphology parameters, such as size and roundness. mClover intensities were then measured within the nuclear mask of the selected nuclei. The fluorescence intensities data were exported into tables and processed in RStudio (version 1.0.143) to produce plots and statistical analysis. For each treatment, the measurements were combined from three biological experiments, each made of two technical replicates. mClover intensities measured from HCT-116 wild-type cells were used as an estimate for the background level. A median of 10 A. U. (arbitrary units) was calculated for the nuclear mClover intensity in wild-type cells (10.23 and 10.56 A. U. in the untreated and in the auxin-treated wild-type cells, respectively). This background value was subtracted from all values measured for the untreated and auxin-treated HCT-116-RAD21-mAC cells.

**Quantitation of auxin-induced RAD21-mAID-mClover degradation on single cells in time-lapse acquisitions.** Nikon spinning disk confocal live-cell time lapses were acquired as described above. For the analysis the lower of the two planes showing interphase cells was used. The detailed description of segmentation and analysis scripts can be found as comments in the scripts which are deposited on GitHub ([https://github.com/CALM-LMU/Cohesin\\_project.git](https://github.com/CALM-LMU/Cohesin_project.git)). In brief, segmentation maps for nuclei in the SiR-DNA channel in confocal time lapses were

obtained by a machine learning-based pixel classification using Ilastik (version 1.3.3) (standard settings). Segmentation maps were manually curated in order to analyze only individual nuclei. Nuclei were traced starting at time frame 1 until the cell entered mitosis and disappeared from the lower imaging plane. The generated segmentation maps were used to select single nuclei in the mClover channel. After background subtraction (modal gray value) the median intensity was measured for each labeled cell over time using Fiji (version 1.51j). Only cells with a mClover intensity above 50 counts were included in the analysis. All data shown are normalized to their starting values. Cells surpassing a fluctuation above the 90% quantile relative to their own rolling mean of 5 timepoints were filtered out. Plots were generated using Python (version 3.7.1).

**DNA content assessment in individual nuclei by integrated DAPI intensity measurement.** DAPI-stained nuclei were acquired using the Nikon spinning disk system described above. Fixed samples of untreated control cells and cells treated with auxin for 30 h were acquired as confocal image z-stacks in 35 planes with a step size of 300 nm using a Nikon PlanApo 100x/1.45 NA oil immersion objective. DAPI was excited with the 405 nm laser line. Segmentation and analysis scripts are described in detail in the scripts which are uploaded on GitHub ([https://github.com/CALM-LMU/Cohesin\\_project.git](https://github.com/CALM-LMU/Cohesin_project.git)). In brief, spinning disk confocal stacks of DAPI-stained nuclei were used for a machine learning-based pixel classification to obtain 3D segmentation maps of nuclei using Ilastik (version 1.3.3) (standard settings). Segmentation maps were manually curated in order to analyze only individual non touching nuclei. After background subtraction (modal gray value) the integrated intensity was measured for each segmented DAPI-stained nucleus by using Fiji (version 1.51j). Plots were generated using R Studio (version 1.0.143).

**Semi-automatic quantification of MLN and mitoses.** Image acquisitions were carried out on the Nikon spinning disk system described above. Using a Nikon PlanApo 100x/1.45 NA oil immersion objective tiled images (3 × 3 with 5% overlap and 131 nm pixel size) were acquired for each condition to increase the number of cells per field of view. Confocal image z-stacks were acquired in two planes with a step size of 6 μm in order to encompass cells, in particular mitotic cells, in different plane levels. DAPI and mClover were excited with 405 or 488 nm laser lines, respectively. All nuclei from each image (average 280 nuclei per image frame) were classified visually into morphologically normal nuclei, mitoses, and MLN. In auxin-treated cells nuclei with persistent RAD21-mClover fluorescence (~2%) were excluded.

**Structured illumination microscopy (SIM).** Super-resolution structured illumination imaging was performed on a DeltaVision OMX V3 system (Applied Precision Imaging/GE Healthcare) equipped with a 100x/1.4 NA UPlan S Apo oil immersion objective (Olympus), Cascade II:512 EMCCD cameras (Photometrics) and 405, 488, and 593 nm lasers (for detailed description, see ref. 74). For sample acquisition oil with a refractive index of RI = 1.512 was used. 3D image stacks were acquired with 15 raw images per plane (five phases, three angles) and an axial distance of 125 nm using DeltaVisionOMX (version 2.25, Applied Precision Imaging/GE Healthcare) and then computationally reconstructed (Wiener filter setting of 0.002, channel-specific optical transfer functions (OTFs)) and color shift corrected using the SoftWoRx software (version 5.1.0, Applied Precision Imaging/GE Healthcare). After establishing 32-bit composite tiff stacks with a custom-made macro in Fiji/ImageJ (<http://rsb.info.nih.gov/ij/>), the data were subsequently aligned again to get a higher alignment precision. These images were then used for measurements in the Volocity software (version 6.1.2., Perkin Elmer).

**Nuclear volume measurements.** Volume measurements were done with the Volocity software (Version 6.1.2.). RGB image stacks were separated in their respective channels and then nuclei structures were obtained and segmented for volume measurements by using the following commands: (1) “Find Objects” (Threshold using: Automatic, Minimum object size: 200 μm<sup>3</sup>), (2) “Dilate” (number of iterations: 15), (3) “Fill Holes in Objects” and (4) “Erode” (number of iterations: 15). In ≈5% of cases these settings had to be adjusted for the challenging task of nuclei segmentation. To confirm statistical significance of volume differences the Mann-Whitney test was applied.

**Segmentation and quantification of RD signals.** Aligned 3D SIM image stacks were used as RGB for object counting and volume measurements in the Volocity software (Version 6.1.2.). For each series between  $n = 7$  and  $n = 11$  nuclei were measured resulting in 31,000–55,000 single values for each series. Image stacks were separated into their respective channels. The segmentation of RD structures was performed with the following software commands: (1) “Find Objects” (Threshold using: Intensity, Lower: 32, Upper: 255), (2) “Separate Touching Objects” (Object size guide of 0.002 μm<sup>3</sup>) and (3) “Exclude Objects by Size”, excluding structures <0.005 μm<sup>3</sup>. This cut-off level largely corresponds to the resolution limit of 3D-SIM (~120 nm lateral/300 nm axial). Exclusion of signals outside a selected nucleus was achieved by the commands “Intersect” and “Compartmentalize”. Segmentation of nuclei was realized by the following commands: (1) “Find Objects” (Threshold using: Intensity), (2) “Dilate”, (3)

“Fill Holes in Objects” and (4) “Erode”. Measured values of individual object counts and segmented RD volumes were displayed as boxplots indicating the median with 25–75% quartiles. Plots were generated using R Studio (version 1.0.143).

**3D assessment of DAPI intensity classes as proxy for chromatin compaction classification.** Nuclei voxels were identified automatically from the DAPI channel intensities using Gaussian filtering and automatic threshold determination. For chromatin quantification a 3D mask was generated in ImageJ to define the nuclear space considered for the segmentation of DAPI signals into seven classes with equal intensity variance by a previously described in house algorithm<sup>27</sup>, available on request. In brief, a hidden Markov random field model classification was used, combining a finite Gaussian mixture model with a spatial model (Potts model), implemented in the statistics software R<sup>75</sup>. This approach allows threshold-independent signal intensity classification at the voxel level, based on the intensity of an individual voxel. Color or gray value heat maps of the seven intensity classes in individual nuclei were performed in ImageJ.

**Quantitative allocation of defined nuclear targets on 3D chromatin compaction classes.** Individual voxels of fluorescent signals of the respective marker channels were segmented by a semi-automatic thresholding algorithm (accessible in VJ Schmid (2020). nucim: Nucleome Imaging Toolbox. R package version 1.0.9. <https://bioimaginggroup.github.io/nucim/>). XYZ-coordinates of segmented voxels were mapped to the seven DNA intensity classes. The relative frequency of intensity weighted signals mapped on each DAPI intensity class was used to calculate the relative distribution of signals over chromatin classes. For each studied nucleus the total number of voxels counted for each intensity class and the total number of voxels identified for the respective fluorescent signals for SC35, RNA Pol II, H3K27me3 was set to 1. As an estimate of over/under representations (relative depletion/enrichment) of marker signals in the respective intensity classes, we calculated the difference between the percentage points obtained for the fraction of voxels for a given DAPI intensity class and the corresponding fraction of voxels calculated for the respective signals. Calculations were performed on single-cell level and average values over all nuclei were used for evaluation and plotting. For a detailed description, see ref. 27.

**Statistics and reproducibility.** Microscopic observations were verified from at least two independent series. Images shown in the figures are representative images from respective experiments. For highly elaborate quantitative 3D analyses of super-resolved image stacks we selected between 7 and 39 nuclei for a given experiment with the precondition of a high staining and structure-preserving quality. No statistical method was used to predetermine sample size. Investigators were not blinded during the experiments and when assessing the outcome. Significance levels were tested by a non-parametric two-sided Wilcoxon test and a Bonferroni-Holm correction was used to avoid errors through multiple testing when applicable (see Source D). Data shown in column graphs represent mean ± standard error of the mean (SEM), as indicated in the figure legends. The variance was similar between the groups that were statistically compared.

**Reporting summary.** Further information on research design is available in the Nature Research Reporting Summary linked to this article.

## Data availability

Raw and processed Hi-C and Repli-Seq data generated as part of this study can be publicly accessed with NCBI GEO accession [GSE145099](https://www.ncbi.nlm.nih.gov/geo/accession/GSE145099). Publicly available ChIP-Seq data used in this study are available at GEO accession [GSE104888](https://www.ncbi.nlm.nih.gov/geo/accession/GSE104888). Raw microscopy data used for Figs. 1–4, 6, 8, Supplementary Figs. 1–8, additional “biological replicates” and complementary experiments can be accessed under <https://doi.org/10.5061/dryad.vt4b8gtqb>, Cohesin depleted cells rebuild functional nuclear compartments after endomitosis, Dryad, Dataset. All other relevant data supporting the key findings of this study are available within the article and its Supplementary Information files or from the corresponding authors upon reasonable request. Source data are provided with this paper.

## Code availability

Code used in this study for 3D assessment of DAPI intensity classes (Fig. 3) and quantitative allocation of defined nuclear targets on 3D chromatin compaction classes (Fig. 4 and Supplementary Fig. 7) is available under <https://bioimaginggroup.github.io/nucim/> and was published in ref. 27. The website provides a detailed installation guide. Custom Python (version 3.7.1) and R (version 1.0.143) scripts for quantification of RAD21 decay and DNA content analysis (Supplementary Figs. 2 and 5) are available under [https://github.com/CALM-LMU/Cohesin\\_project.git](https://github.com/CALM-LMU/Cohesin_project.git) and current versions are provided as Supplementary Software. All Hi-C data were processed using the software package Juicer version 1.5.7, which can be found at <https://github.com/aidenlab/juicer>. Previously published ChIP-Seq data from ref. 15 were clustered using the `scipy.cluster.vq.kmeans` function. Repli-Seq data were processed and analyzed exactly following the code published in ref. 36.

Received: 12 December 2019; Accepted: 28 October 2020;  
Published online: 01 December 2020

## References

- Davidson, I. F. et al. DNA loop extrusion by human cohesin. *Science* **366**, 1338–1345 (2019).
- Fudenberg, G. et al. Formation of chromosomal domains by loop extrusion. *Cell Rep.* **15**, 2038–2049 (2016).
- Parelho, V. et al. Cohesins functionally associate with CTCF on mammalian chromosome arms. *Cell* **132**, 422–433 (2008).
- Rao, S. S. et al. A 3D map of the human genome at kilobase resolution reveals principles of chromatin looping. *Cell* **159**, 1665–1680 (2014).
- Sanborn, A. L. et al. Chromatin extrusion explains key features of loop and domain formation in wild-type and engineered genomes. *Proc. Natl Acad. Sci. USA* **112**, E6456–E6465 (2015).
- Zuin, J. et al. Cohesin and CTCF differentially affect chromatin architecture and gene expression in human cells. *Proc. Natl Acad. Sci. USA* **111**, 996–1001 (2014).
- Jeppsson, K., Kanno, T., Shirahige, K. & Sjogren, C. The maintenance of chromosome structure: positioning and functioning of SMC complexes. *Nat. Rev. Mol. Cell Biol.* **15**, 601–614 (2014).
- Mehta, G. D., Kumar, R., Srivastava, S. & Ghosh, S. K. Cohesin: functions beyond sister chromatid cohesion. *FEBS Lett.* **587**, 2299–2312 (2013).
- Nishiyama, T. Cohesion and cohesin-dependent chromatin organization. *Curr. Opin. Cell Biol.* **58**, 8–14 (2019).
- Peters, J. M., Tedeschi, A. & Schmitz, J. The cohesin complex and its roles in chromosome biology. *Genes Dev.* **22**, 3089–3114 (2008).
- van Ruiten, M. S. & Rowland, B. D. SMC complexes: universal DNA looping machines with distinct regulators. *Trends Genet.* **34**, 477–487 (2018).
- Litwin, I., Pilarczyk, E. & Wysocki, R. The emerging role of cohesin in the dna damage response. *Genes* <https://doi.org/10.3390/genes9120581> (2018).
- Merkenschlager, M. & Nora, E. P. CTCF and cohesin in genome folding and transcriptional gene regulation. *Annu. Rev. Genomics Hum. Genet.* **17**, 17–43 (2016).
- Natsume, T., Kiyomitsu, T., Saga, Y. & Kanemaki, M. T. Rapid protein depletion in human cells by auxin-inducible degron tagging with short homology donors. *Cell Rep.* **15**, 210–218 (2016).
- Rao, S. S. P. et al. Cohesin loss eliminates all loop domains. *Cell* **171**, 305–320 (2017).
- Haarhuis, J. H. & Rowland, B. D. Cohesin: building loops, but not compartments. *EMBO J.* **36**, 3549–3551 (2017).
- Cremer, T. et al. The interchromatin compartment participates in the structural and functional organization of the cell nucleus. *Bioessays* **42**, e1900132 (2020).
- Cremer, T. et al. The 4D nucleome: evidence for a dynamic nuclear landscape based on co-aligned active and inactive nuclear compartments. *FEBS Lett.* **589**, 2931–2943 (2015).
- Kim, Y., Shi, Z., Zhang, H., Finkelstein, I. J. & Yu, H. Human cohesin compacts DNA by loop extrusion. *Science* **366**, 1345–1349 (2019).
- Cremer, M. et al. Multicolor 3D fluorescence in situ hybridization for imaging interphase chromosomes. *Methods Mol. Biol.* **463**, 205–239 (2008).
- Jevtic, P., Edens, L. J., Vukovic, L. D. & Levy, D. L. Sizing and shaping the nucleus: mechanisms and significance. *Curr. Opin. Cell Biol.* **28**, 16–27 (2014).
- Shu, Z., Row, S. & Deng, W. M. Endoreplication: the good, the bad, and the ugly. *Trends Cell Biol.* **28**, 465–474 (2018).
- Langer, S., Geigl, J. B., Ehnle, S., Gangnus, R. & Speicher, M. R. Live cell catapulting and recultivation does not change the karyotype of HCT116 tumor cells. *Cancer Genet. Cytogenet.* **161**, 174–177 (2005).
- Lin, S., Coutinho-Mansfield, G., Wang, D., Pandit, S. & Fu, X. D. The splicing factor SC35 has an active role in transcriptional elongation. *Nat. Struct. Mol. Biol.* **15**, 819–826 (2008).
- Egloff, S. & Murphy, S. Cracking the RNA polymerase II CTD code. *Trends Genet.* **24**, 280–288 (2008).
- Zhou, V. W., Goren, A. & Bernstein, B. E. Charting histone modifications and the functional organization of mammalian genomes. *Nat. Rev. Genet.* **12**, 7–18 (2011).
- Schmid, V. J., Cremer, M. & Cremer, T. Quantitative analyses of the 3D nuclear landscape recorded with super-resolved fluorescence microscopy. *Methods* **123**, 33–46 (2017).
- Miron, E. et al. Chromatin arranges in chains of mesoscale domains with nanoscale functional topography independent of cohesin. *Sci. Adv.* **6**, eaba8811 (2020).
- Schermelleh, L. et al. Subdiffraction multicolor imaging of the nuclear periphery with 3D structured illumination microscopy. *Science* **320**, 1332–1336 (2008).
- Smeets, D. et al. Three-dimensional super-resolution microscopy of the inactive X chromosome territory reveals a collapse of its active nuclear compartment harboring distinct Xist RNA foci. *Epigenetics Chromatin* **7**, 8 (2014).
- Maeshima, K. et al. The physical size of transcription factors is key to transcriptional regulation in chromatin domains. *J. Phys. Condens Matter* **27**, 064116 (2015).
- Dimitrova, D. S. & Berezney, R. The spatio-temporal organization of DNA replication sites is identical in primary, immortalized and transformed mammalian cells. *J. Cell Sci.* **115**, 4037–4051 (2002).
- Jackson, D. A. & Pombo, A. Replicon clusters are stable units of chromosome structure: evidence that nuclear organization contributes to the efficient activation and propagation of S phase in human cells. *J. Cell Biol.* **140**, 1285–1295 (1998).
- Schermelleh, L., Solovei, I., Zink, D. & Cremer, T. Two-color fluorescence labeling of early and mid-to-late replicating chromatin in living cells. *Chromosome Res.* **9**, 77–80 (2001).
- Xiang, W. et al. Correlative live and super-resolution imaging reveals the dynamic structure of replication domains. *J. Cell Biol.* **217**, 1973–1984 (2018).
- Marchal, C. et al. Genome-wide analysis of replication timing by next-generation sequencing with E/L Repli-seq. *Nat. Protoc.* **13**, 819–839 (2018).
- Marchal, C., Sima, J. & Gilbert, D. M. Control of DNA replication timing in the 3D genome. *Nat. Rev. Mol. Cell Biol.* <https://doi.org/10.1038/s41580-019-0162-y> (2019).
- Oldach, P. & Nieduszynski, C. A. Cohesin-mediated genome architecture does not define DNA replication timing domains. *Genes* <https://doi.org/10.3390/genes10030196> (2019).
- Heng, H. H. et al. Chromatin loops are selectively anchored using scaffold/matrix-attachment regions. *J. Cell Sci.* **117**, 999–1008 (2004).
- Diaz-Martinez, L. A. et al. Cohesin is needed for bipolar mitosis in human cells. *Cell Cycle* **9**, 1764–1773 (2010).
- Abramo, K. et al. A chromosome folding intermediate at the condensin-to-cohesin transition during telophase. *Nat. Cell Biol.* <https://doi.org/10.1038/s41556-019-0406-2> (2020).
- Ovrebo, J. I. & Edgar, B. A. Polyploidy in tissue homeostasis and regeneration. *Development* <https://doi.org/10.1242/dev.156034> (2018).
- Mazzi, S., Lordier, L., Debili, N., Raslova, H. & Vainchenker, W. Megakaryocyte and polyploidization. *Exp. Hematol.* **57**, 1–13 (2018).
- Chen, J. et al. Polyploid giant cancer cells (PGCCs): the evil roots of cancer. *Curr. Cancer Drug Targets* **19**, 360–367 (2019).
- Joos, S. et al. Hodgkin's lymphoma cell lines are characterized by frequent aberrations on chromosomes 2p and 9p including REL and JAK2. *Int. J. Cancer* **103**, 489–495 (2003).
- Rouquette, J., Cremer, C., Cremer, T. & Fakan, S. Functional nuclear architecture studied by microscopy: present and future. *Int Rev. Cell Mol. Biol.* **282**, 1–90 (2010).
- Cremer, T., Cremer, M. & Cremer, C. The 4D nucleome: genome compartmentalization in an evolutionary context. *Biochemistry* **83**, 313–325 (2018).
- Rowley, M. J. & Corces, V. G. Organizational principles of 3D genome architecture. *Nat. Rev. Genet.* **19**, 789–800 (2018).
- Zhao, P. A., Rivera-Mulia, J. C. & Gilbert, D. M. Replication domains: genome compartmentalization into functional replication units. *Adv. Exp. Med. Biol.* **1042**, 229–257 (2017).
- Pope, B. D. et al. Topologically associating domains are stable units of replication-timing regulation. *Nature* **515**, 402–405 (2014).
- Moindrot, B. et al. 3D chromatin conformation correlates with replication timing and is conserved in resting cells. *Nucleic Acids Res.* **40**, 9470–9481 (2012).
- Lieberman-Aiden, E. et al. Comprehensive mapping of long-range interactions reveals folding principles of the human genome. *Science* **326**, 289–293 (2009).
- Dixon, J. R. et al. Topological domains in mammalian genomes identified by analysis of chromatin interactions. *Nature* **485**, 376–380 (2012).
- Dixon, J. R., Gorkin, D. U. & Ren, B. Chromatin domains: the unit of chromosome organization. *Mol. Cell* **62**, 668–680 (2016).
- Ibrahim, D. M. & Mundlos, S. The role of 3D chromatin domains in gene regulation: a multi-faceted view on genome organization. *Curr. Opin. Genet. Dev.* **61**, 1–8 (2020).
- Boettiger, A. & Murphy, S. Advances in chromatin imaging at kilobase-scale resolution. *Trends Genet.* **36**, 273–287 (2020).
- Bintu, B. et al. Super-resolution chromatin tracing reveals domains and cooperative interactions in single cells. *Science* <https://doi.org/10.1126/science.aau1783> (2018).
- Ma, H. et al. Spatial and temporal dynamics of DNA replication sites in mammalian cells. *J. Cell Biol.* **143**, 1415–1425 (1998).
- Nakamura, H., Morita, T. & Sato, C. Structural organizations of replicon domains during DNA synthetic phase in the mammalian nucleus. *Exp. Cell Res.* **165**, 291–297 (1986).

60. Baddeley, D. et al. Measurement of replication structures at the nanometer scale using super-resolution light microscopy. *Nucleic Acids Res.* **38**, e8 (2010).
61. Schermelleh, L., Heintzmann, R. & Leonhardt, H. A guide to super-resolution fluorescence microscopy. *J. Cell Biol.* **190**, 165–175 (2010).
62. Cremer, C. & Masters, B. R. Resolution enhancement techniques in microscopy. *Eur. Phys. J. H.* **38**, 281–344 (2013).
63. Trzaskoma, P. et al. Ultrastructural visualization of 3D chromatin folding using volume electron microscopy and DNA in situ hybridization. *Nat. Commun.* **11**, 2120 (2020).
64. Gibcus, J. H. et al. A pathway for mitotic chromosome formation. *Science* <https://doi.org/10.1126/science.aa06135> (2018).
65. Otterstrom, J. et al. Super-resolution microscopy reveals how histone tail acetylation affects DNA compaction within nucleosomes in vivo. *Nucleic Acids Res.* <https://doi.org/10.1093/nar/gkz593> (2019).
66. Ricci, M. A., Manzo, C., Garcia-Parajo, M. F., Lakadamyali, M. & Cosma, M. P. Chromatin fibers are formed by heterogeneous groups of nucleosomes in vivo. *Cell* **160**, 1145–1158 (2015).
67. Markaki, Y., Smeets, D., Cremer, M. & Schermelleh, L. Fluorescence in situ hybridization applications for super-resolution 3D structured illumination microscopy. *Methods Mol. Biol.* **950**, 43–64 (2013).
68. Salic, A. & Mitchison, T. J. A chemical method for fast and sensitive detection of DNA synthesis in vivo. *Proc. Natl Acad. Sci. USA* **105**, 2415–2420 (2008).
69. Durand, N. C. et al. Juicebox provides a visualization system for Hi-C contact maps with unlimited zoom. *Cell Syst.* **3**, 99–101 (2016).
70. Durand, N. C. et al. Juicer provides a one-click system for analyzing loop-resolution Hi-C experiments. *Cell Syst.* **3**, 95–98 (2016).
71. Javanmoghdam-Kamrani, S. & Keyomarsi, K. Synchronization of the cell cycle using lovastatin. *Cell Cycle* **7**, 2434–2440 (2008).
72. Guillou, E. et al. Cohesin organizes chromatin loops at DNA replication factories. *Genes Dev.* **24**, 2812–2822 (2010).
73. Schindelin, J. et al. Fiji: an open-source platform for biological-image analysis. *Nat. Methods* **9**, 676–682 (2012).
74. Dobbie, I. M. et al. OMX: a new platform for multimodal, multichannel wide-field imaging. *Cold Spring Harb. Protoc.* **2011**, 899–909 (2011).
75. Pau, G., Fuchs, F., Sklyar, O., Boutros, M. & Huber, W. EBImage—an R package for image processing with applications to cellular phenotypes. *Bioinformatics* **26**, 979–981 (2010).

## Acknowledgements

We thank Stefan Müller, University of Munich (LMU), for kindly providing chromosome painting probes for 3D-FISH experiments and Irina Solovei, University of Munich (LMU), for generously providing antibodies, lab space and facilities to M.C., and Karsten Rippe (German Cancer Research Center Heidelberg) for discussion. We are most grateful to Toyoaki Natsume from the lab of Masato Kanemaki (Center of Frontier Research, National Institute of Genetics, Mishima, Shizuoka Japan) for providing HCT116-RAD21-mAC cells. K.B. was supported by the International Max Planck Research School for Molecular Life Sciences (IMPRS-LS). Microscopic images were acquired at microscopes of the Center for Advanced Light Microscopy (CALM) at the LMU Munich. This work was supported by grants of the Deutsche Forschungsgemeinschaft (GRK1657/TP1C and CA198/9-2) to M.C.C. and by the DFG Priority Program SPP 2202 to H.H. and H.L. K.B. was supported by a grant from the National Human Genome Research Institute (RM1-HG007743-02CEGS - Center for Photogenomics) given to H.L. and H.H. E.L.A. was supported by an NSF Physics Frontiers Center Award (PHY1427654), the Welch Foundation (Q-1866), a USDA Agriculture and Food Research Initiative Grant

(2017-05741), an NIH 4D Nucleome Grant (U01HL130010), and an NIH Encyclopedia of DNA Elements Mapping Center Award (UM1HG009375).

## Author contributions

T.C. and E.L.A. initiated the study; M.C. and T.C. conceived the microscopic experiments together with H.H., K.B., and A.M. K.B., M.C., A.M., and M.G.O. performed experiments shown in Figs. 1–4, 6, 8, and Supplementary Figs. 1a, 2–7. A.M. and K.B. performed live cell and super-resolution/confocal microscopy; H.H. provided input on quantitative image analysis, including statistical analysis; A.M. performed segmentation analyses and V.J.S. 3D image analyses for chromatin density mapping data; M.G.O. performed 3D rendering of nuclei. SM performed RAD21-mClover intensities by high-throughput imaging and DNA Halo experiments with support of M.C.C. shown in Supplementary Figs. 1b and 8. Hi-C data were generated by S.S.P.R. and E.L.A. with experimental support of N.M. (Fig. 5). Repli-Seq data (Fig. 7) were provided by D.M.G. and K.N.K. H.L. provided input for the 3D imaging part and M.C.C. for the replication part. M.C. and T.C. wrote the manuscript with support from all authors, in particular from E.L.A.

## Funding

Open Access funding enabled and organized by Projekt DEAL.

## Competing interests

The authors declare no competing interests.

## Additional information

Supplementary information is available for this paper at <https://doi.org/10.1038/s41467-020-19876-6>.

Correspondence and requests for materials should be addressed to M.C., H.H. or T.C.

Peer review information *Nature Communications* thanks Kumiko Samejima and the other, anonymous, reviewer(s) for their contribution to the peer review of this work. Peer reviewer reports are available.

Reprints and permission information is available at <http://www.nature.com/reprints>

Publisher's note Springer Nature remains neutral with regard to jurisdictional claims in published maps and institutional affiliations.



**Open Access** This article is licensed under a Creative Commons Attribution 4.0 International License, which permits use, sharing, adaptation, distribution and reproduction in any medium or format, as long as you give appropriate credit to the original author(s) and the source, provide a link to the Creative Commons license, and indicate if changes were made. The images or other third party material in this article are included in the article's Creative Commons license, unless indicated otherwise in a credit line to the material. If material is not included in the article's Creative Commons license and your intended use is not permitted by statutory regulation or exceeds the permitted use, you will need to obtain permission directly from the copyright holder. To view a copy of this license, visit <http://creativecommons.org/licenses/by/4.0/>.

© The Author(s) 2020

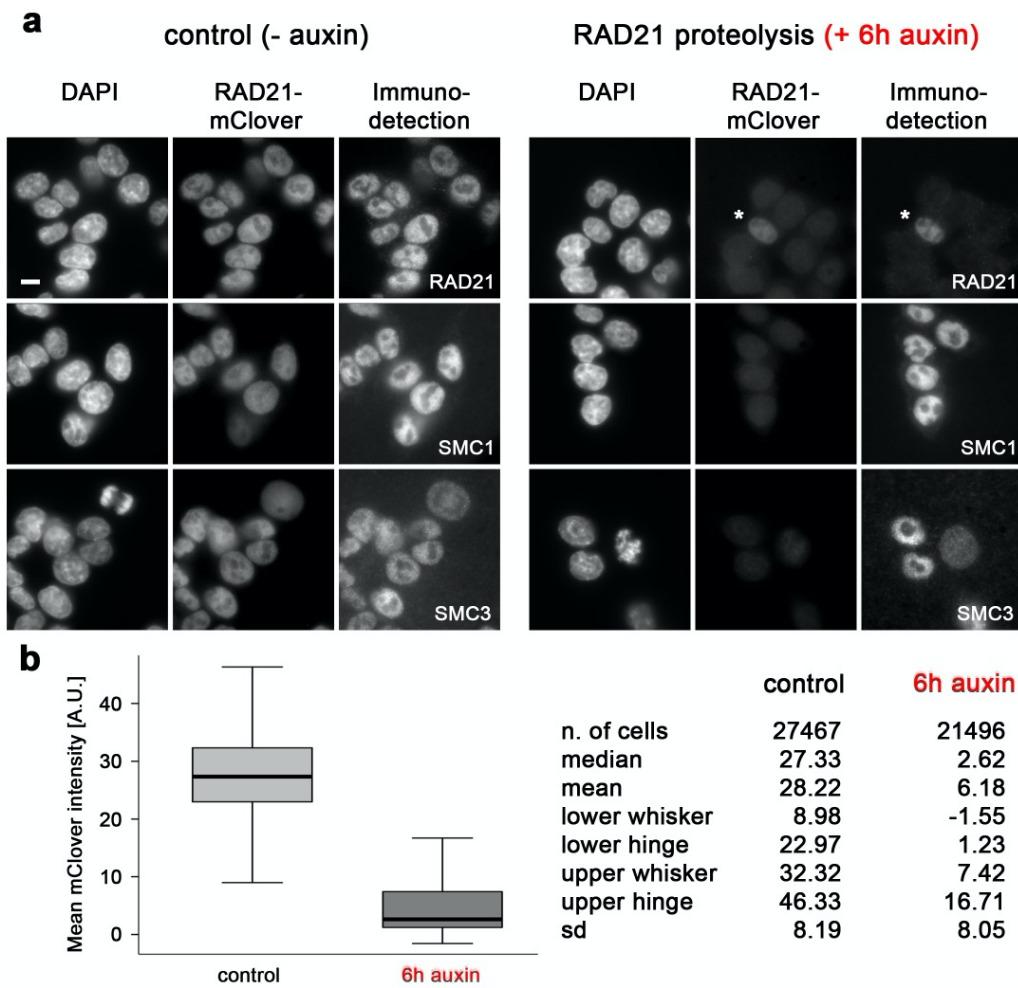
**Supplementary information**

**Cohesin depleted cells rebuild functional nuclear compartments  
after endomitosis**

**Cremer et al.**

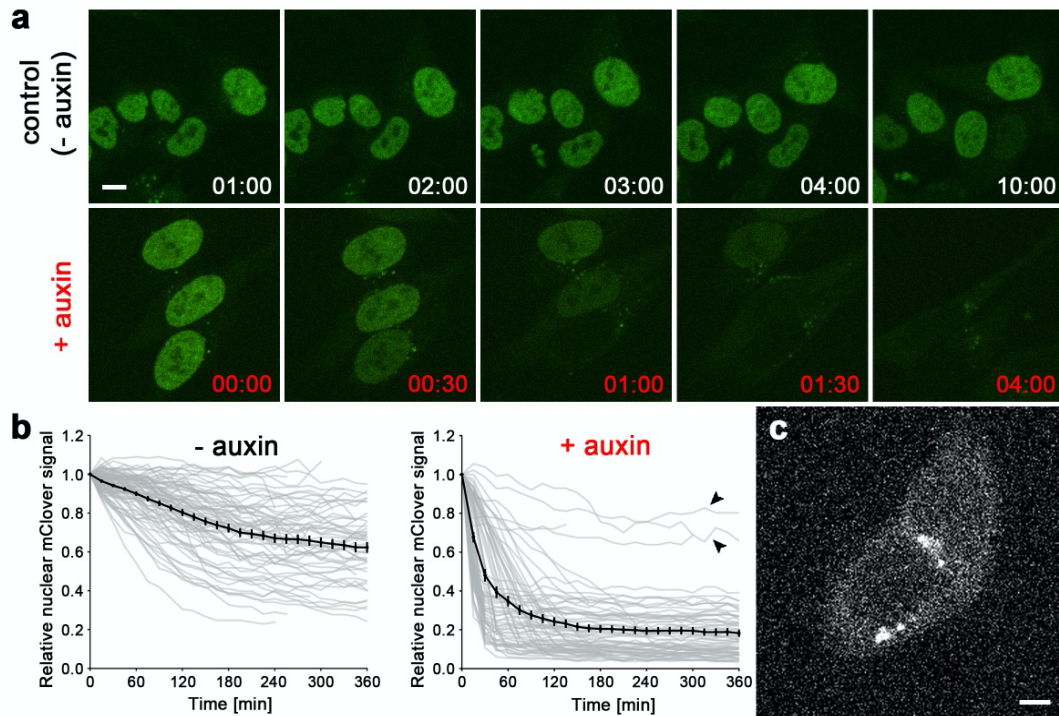
**Supplementary Figures1-8  
Supplementary Notes 1-5  
Supplementary Tables1-2  
Supplementary References**

## Supplementary figures with explanations



**Supplementary Fig. 1: RAD21-mClover proteolysis under auxin treatment**

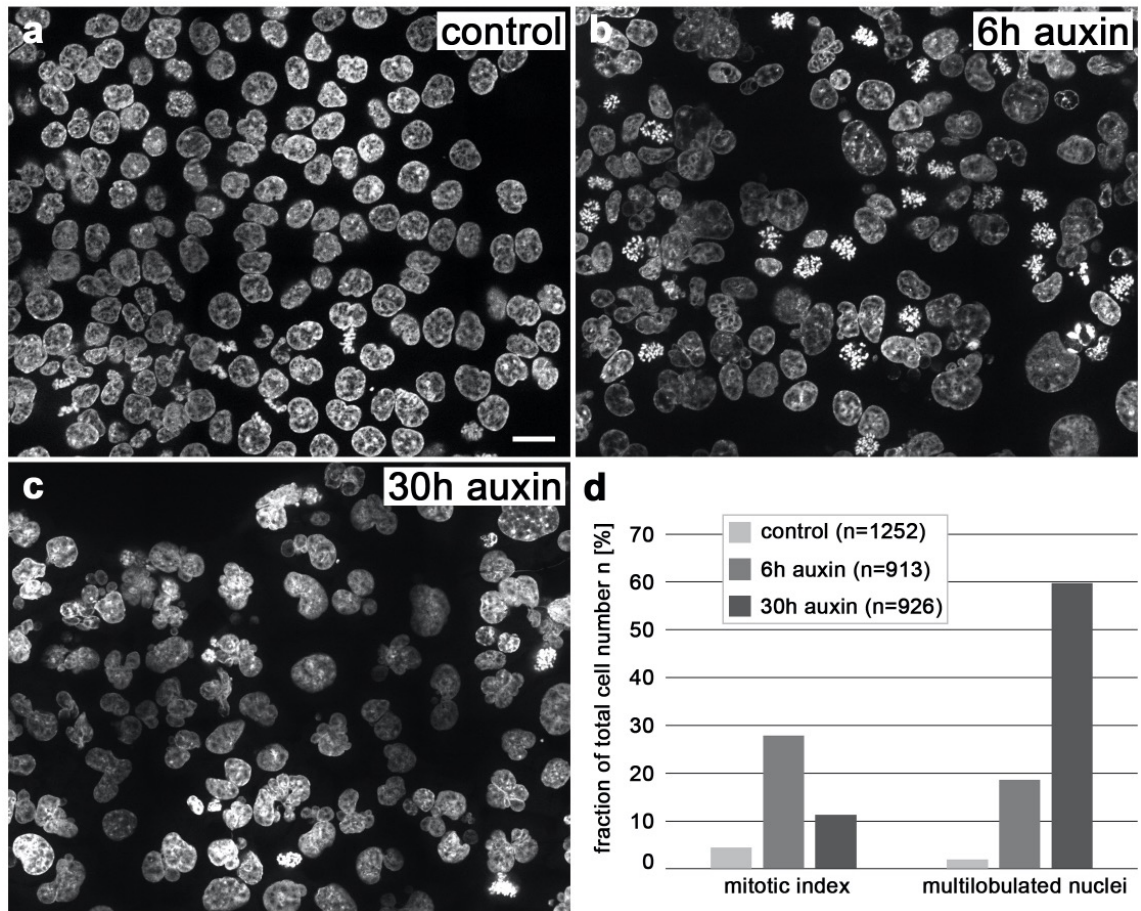
**(a)** Immunodetection of the three major cohesin subunits RAD21, SMC1 and SMC3. Cells treated 6h with auxin (right panel) confirm the loss of RAD21 immunostaining in accordance with loss of RAD21-mClover fluorescence. Asterisk indicates a cell escaping RAD21 proteolysis. SMC1 and SMC3 immunostaining is maintained. Images are representative for two independent experiments. Scale bar: 5  $\mu$ m. **(b)** Averaged RAD21-mClover intensities recorded by high-throughput imaging from single cells of untreated controls (median = 27.33 A.U., n=27467 cells) and auxin treated cells fixed after 6h in 500  $\mu$ M auxin (median = 2.62 A.U., n=21496 cells). Significance was tested by a two-sided Wilcoxon test ( $p < 0.0001$ ) without correction for multiple testing. For details, see Methods. The small overlap between cohorts is likely due to the small fraction of cells escaping AID induced RAD21 proteolysis in the auxin cohort and to cells that lack RAD21-mClover expression in control cells (compare Supplementary Fig. 2). Data in b are represented as boxplot where the middle line indicates the median, the lower and upper hinges correspond to the 25% and 75% quartiles, the upper whisker extends to the largest value no further than 1.5 x IQR (inter-quartile range) from the hinge and the lower whisker extends to the smallest value from the hinge at most 1.5 x IQR. Source data are provided as a Source Data file



**Supplementary Fig. 2: Time course and quantitative measurement of auxin induced RAD21-mClover degradation based on single cell analyses from live cell observations**

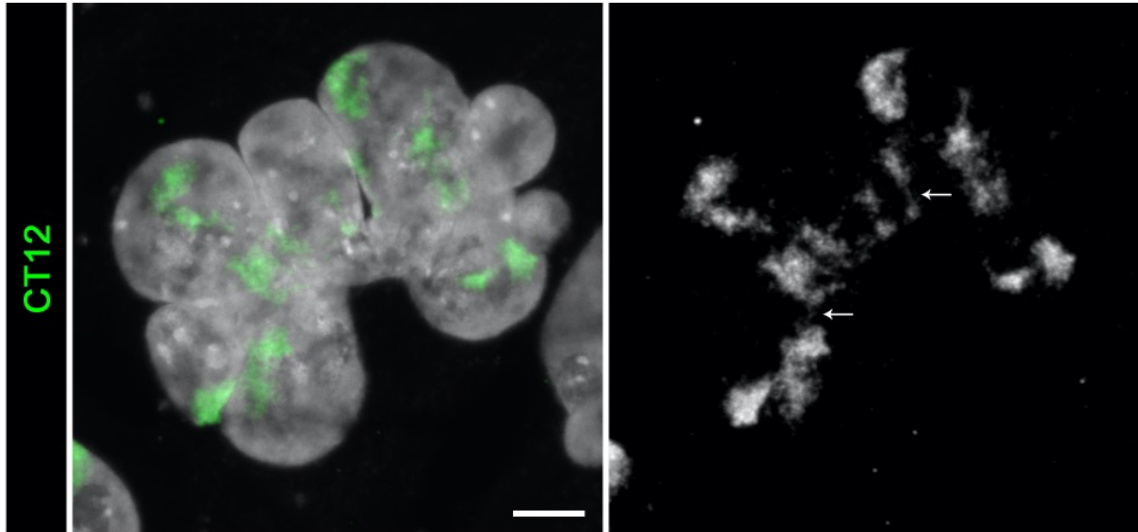
(a) Upper row: selected time points of time lapse imaging ( $\Delta t=15\text{min}$ ) in control cells (- auxin) show largely persistence of RAD21-mClover fluorescence over 10 h. Lower row: gradual decrease of RAD21-mClover fluorescence shown for selected time points in auxin treated cells recorded under same imaging conditions. RAD21-mClover fluorescence appears accomplished between time point 01:30-04:00 after addition of  $500\ \mu\text{M}$  auxin. Scale bar:  $5\ \mu\text{m}$ . (b) Quantitative analysis of single cell nuclear RAD21-mClover fluorescence recorded over 6h from live cell experiment shown in (a). Time course of nuclear fluorescence was analyzed by use of automated image data analysis and segmentation tools (see materials and methods). In control cells nuclear fluorescence decreases to a mean value of  $\sim 60\%$  of the starting value due to imaging related bleaching. Auxin treatment reduces RAD21-mClover fluorescence to an average of  $\sim 20\%$  of the starting value, this value settles after  $\sim 3\text{h}$ . Arrows indicate cells that apparently escaped auxin degradation in this experiment. Control cells:  $n=82$ ; auxin-treated cells:  $n=69$ . Data are represented as mean  $\pm$  SEM. (c) Fluorescent degradation products of RAD21-mClover around the nucleus (cf. bright speckles) and in the cytoplasm, that can affect the results of the automated analysis. Data in a-c show representative cells from one of the three independent experiments. Scale bars:  $5\ \mu\text{m}$ . Source data are provided as a Source Data file.

**Supplementary Note 1:** AID triggers proteasomal degradation of a tagged protein by ubiquitination, while its expression continues. It can be assumed that the remaining fluorescence in auxin treated cells mostly originates from RAD21-mClover in proteasomes associated with the cytoskeleton, centrosomes and the outer surface of the endoplasmic reticulum<sup>1</sup>, while the fraction of RAD21 within an intact cohesin ring is neglectable. Note also the observation of a residual fluorescence of  $\sim 10\%$  of mClover signals was described in the original publication by<sup>2</sup> after addition of  $500\ \mu\text{M}$  auxin.



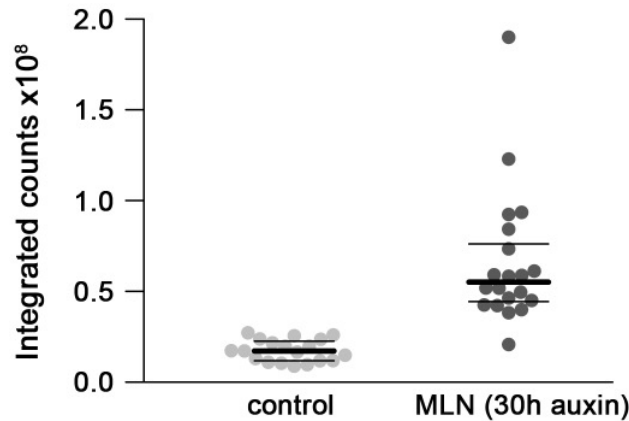
**Supplementary Fig. 3: Transient increase of mitotic index and fraction of MLN after cohesin depletion**

(a-c) Representative images (z-projections from two optical sections with  $\Delta z = 6 \mu\text{m}$ ) of (a) DAPI stained control nuclei; (b) nuclei fixed 6h after auxin treatment showing the accumulation of mitoses; (c) nuclei fixed 30h after auxin treatment with highly enriched MLN. Scale bar: 20  $\mu\text{m}$ . Images are representative images from two independent experiments. (d) Quantification of mitotic index and fraction of MLN in control and cohesin depleted nuclei (control: light gray, n=1252, 6h auxin: gray, n=913, 30h auxin: dark gray, n=913 cells). Data are represented as mean. Apoptotic and morphologically inconspicuous nuclei with distinct micronuclei were excluded from the MLN fraction. Source data are provided as a Source Data file.



**Supplementary Fig. 4: Selective presentation of chromosome territory (CT) 12 reveals a tearing apart of painted regions**

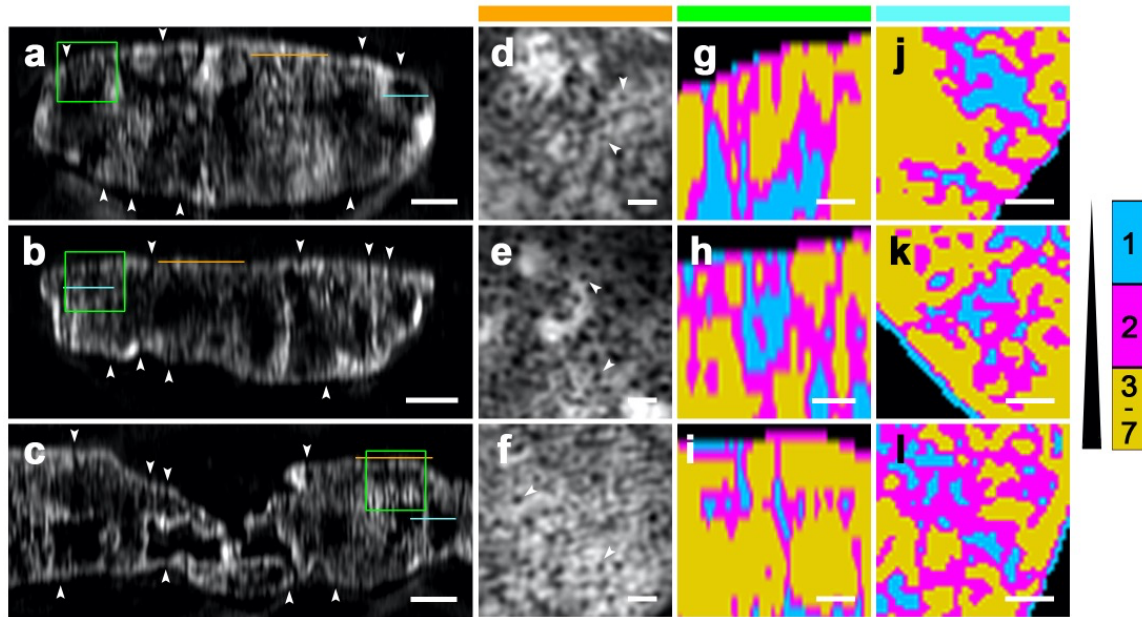
(Left) Exemplary cohesin depleted postmitotic MLN (DAPI: gray, shown also in Fig. 2d) with apparently >4 variably sized painted regions for CT 12 in different lobuli (green). (Right) Selective presentation of painted regions (gray) reveal thin chromatin bridges between them (arrows). Scale bar: 5  $\mu$ m



**Supplementary Fig. 5: DNA content measurements in controls and cohesin depleted postmitotic multilobulated nuclei (MLN)**

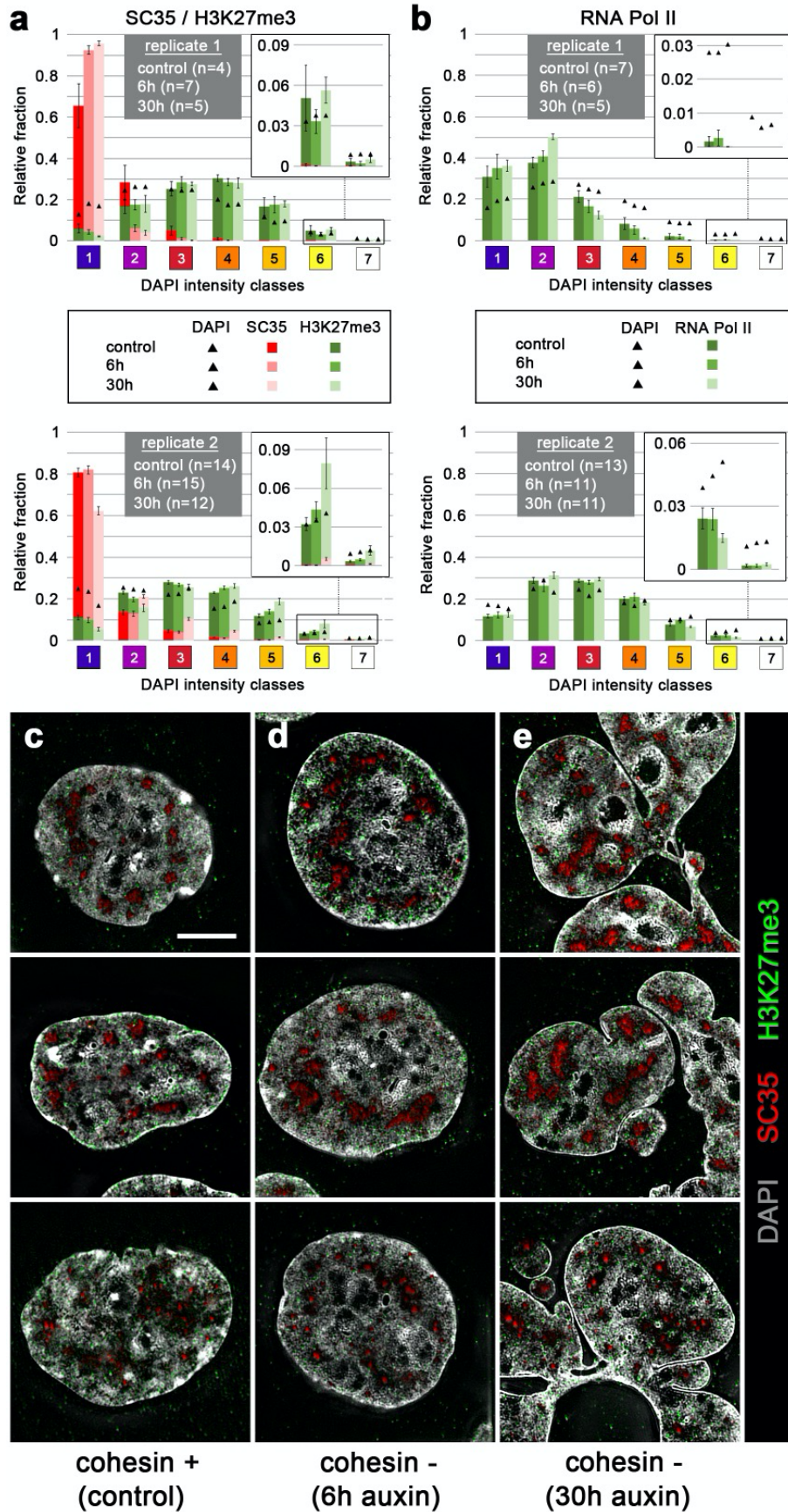
DNA content of single interphase nuclei based on integrated DAPI intensities of confocal sections in control cells (n=19, light gray) and postmitotic cohesin depleted MLN after 30h auxin treatment (n=20, dark gray). Control cells show a narrow distribution reflecting the DNA content in G1, S, G2 phase (1n – 2n). MLN show an overall increased DNA content with a wide range. Note that these cells arise from an endomitosis with a 2n DNA content. MLN can pass through another full round of replication (compare Fig. 6E in the main text) increasing their DNA content up to 4n. Data are represented as single data points with the median as thick line and the first and third quartiles as thin lines. Source data are provided as a Source Data file.

**Supplementary Note 2:** DAPI based single cell DNA content measurements may not reflect the absolute DNA content and a quantitative comparison of cells with highly different morphologies should be interpreted with caution<sup>4</sup>. However, the increased DNA content of cohesin depleted MLN is robust.



**Supplementary Fig. 6: Maintenance of a 3D network of the interchromatin compartment (IC) channel system after cohesin depletion and its reconstitution in MLN after mitosis**

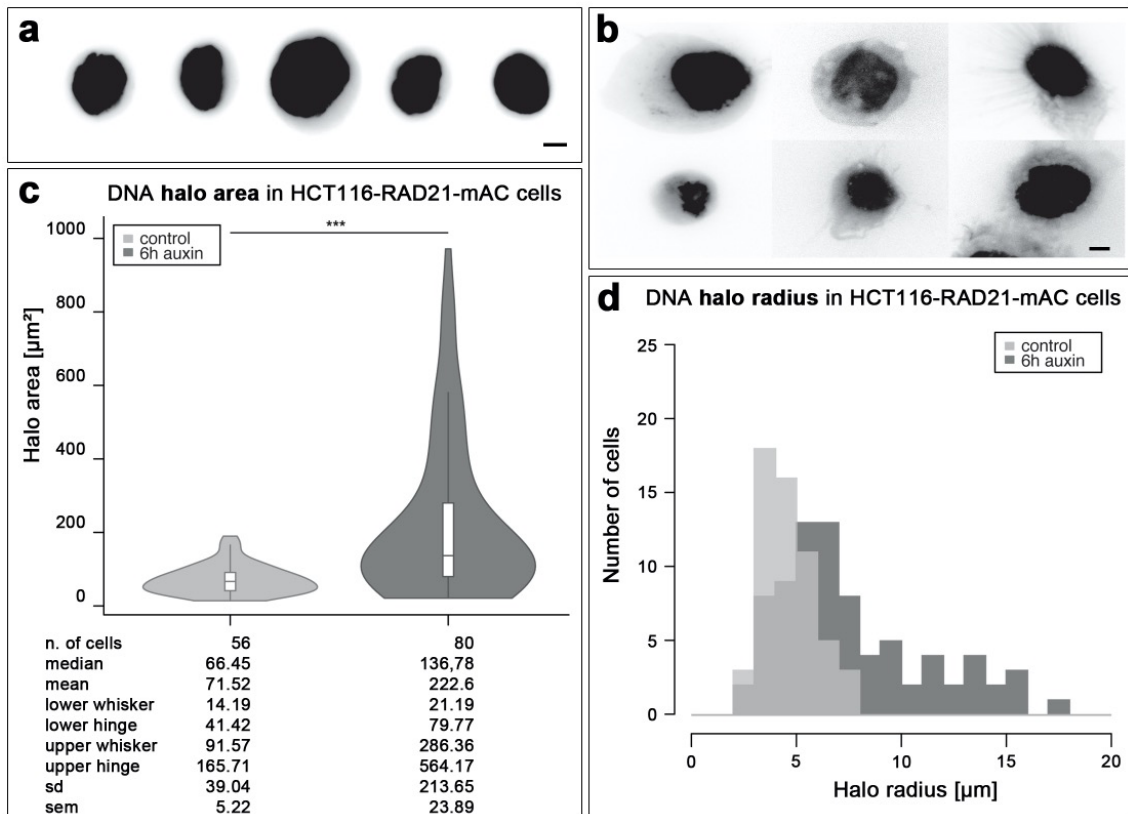
(a-c) Z-sections from DAPI stained nuclei shown in Fig. 3a-c demonstrate IC-channels (arrowheads) extending between nuclear envelope associated chromatin domains into the nuclear interior, where they form wide IC-lacunae. Scale bars: 2  $\mu\text{m}$ . (d-f) Apical XY-sections from respective nuclei (indicated as orange lines in a-c) delineating the passage of IC channels through peripheral heterochromatin at the nuclear lamina (not shown) where IC-channels are noted as black holes. Scale bars: 0.5  $\mu\text{m}$ . (g-i) Inset magnifications from z-sections of nuclei shown in a-c (indicated as green frames) presented with three color coded DAPI intensity classes 1 (blue), 2 (purple), 3-7 (merged in beige; for description see Fig 3) further illustrate the extension of IC-channels from the nuclear periphery into the interior and the expansion of the IC into extended IC-lacunae (class 1) both within the control nucleus (g), and cohesin depleted pre- and postmitotic nuclei (h,i). The apparent predominance of a vertical channel alignment in z-sections is a consequence of the lower resolution in z (axial,  $\sim 250$  nm) compared to xy (perpendicular to the optical axis,  $\sim 125$  nm)<sup>5</sup>. (i-l) XY-sections from respective nuclei (indicated as blue lines in a-c) demonstrate the occurrence of transversal channels from the lateral periphery towards the nuclear interior in line with a three-dimensional network. Scale bars: 0.5  $\mu\text{m}$ .



Supplementary Fig. 7: Interexperimental variability of quantitative mapping of SC35, H3K27me3, RNA Pol II on chromatin compaction maps (legend continued on next page)

This figure provides an extension of data shown in Fig. 4 to exemplify interexperimental variability. **(a,b)** Separate presentation of replicates 1 and 2 which were performed about one year apart from each other with relative enrichments and depletions of **(a)** SC35 (red) and H3K4me3 (green) (rep1: n=4, rep2: n=14; 6h: rep1: n=7, rep2: n=15; 30h: rep1: n=5, rep2: n=12 cells) and **(b)** RNA Pol II (green) (control: rep1: n=7, rep2: n=13; 6h: rep1: n=6, rep2: n=11; 30h: rep1: n=5, rep2: n=11 cells) in the 7 DAPI intensity classes marked as black triangles (for explanation of details see the main text). Data in (a) and (b) are represented as mean  $\pm$  SEM. Source data are provided as a Source Data file. **(c-e)** Mid-SIM sections from **(c)** control nuclei, **(d)** cohesin depleted nuclei fixed after 6 h auxin treatment, **(e)** partial sections of post-endomitotic MLN fixed 30 h after auxin treatment are shown with DAPI stained DNA (gray), immunostained SC35 (red) and H3K27me3 (green). SC35 marked speckles in IC lacunas demonstrate compaction differences between speckles in both control and cohesin depleted nuclei.

**Supplementary Note 3:** Technical parameters for image recording and quantitative image analysis were kept constant in both experiments. Therefore, they are an unlikely source to explain interexperimental differences. Instead, unperceived biological differences between the cultures studied in the two experiments may explain why RNA Pol II was particularly enriched in classes 1 and 2 (IC and lining chromatin) in one experiment, and in classes 2 and 3 in another experiment. Although culture conditions appeared to be the same, parameters, which may affect the dynamics of higher order chromatin arrangements in cycling cells have remained elusive. The cultures were not synchronized and the two time points chosen for fixation of auxin treated cells (6h and 30h) have to be considered as snap-shots. Different conformations of SC35 (shown in A-C) constituting a component in nuclear speckles composed of several protein complexes in a multilayered organization, was described <sup>3</sup>, but underlying causes have remained elusive.



### Supplementary Fig. 8: Enlargement of DNA Halos after cohesin depletion

**(a-b)** Representative images of DNA halos stained with DAPI recorded from four independent experiments. The faded DNA halo surrounding a brighter insoluble nuclear scaffold corresponds to the DNA loops, whose extent reflects the degree of structural organization of chromatin. **(a)** Typical nuclei from control cells with small, rather uniform, and well delimited halos. **(b)** Halos of cohesin depleted cells show variable shapes and size, often ending up in extruded bundles of DNA fibers. Scale bar: 5  $\mu\text{m}$ . **(c)** Violin plot showing the differences in area of the DNA halo between control (light gray) and cohesin depleted cells (6h of auxin treatment, gray), determined as described in Methods. Cohesin depleted cells show up to five times larger halos.  $p$ -value  $< 0.0001$  (\*\*\*) using a two-sided Wilcoxon test without correction for multiple testing. Data in c are represented as violin plot where the middle line indicates the median, the lower and upper hinges correspond to the 25% and 75% quartiles, the upper whisker extends to the largest value no further than  $1.5 \times \text{IQR}$  (inter-quartile range) from the hinge and the lower whisker extends to the smallest value from the hinge at most  $1.5 \times \text{IQR}$ . The violin represents the data distribution. **(d)** Distribution of radial values of DNA halos for the two populations shown in (c). Source data are provided as a Source Data file.

**Supplementary Table 1: Glossary with explanatory notes of current terminologies for higher order chromatin structures and nuclear compartmentalization**

**Supplementary Note 4:** Microscopic and Hi-C studies have been used to explore nuclear landscapes in many species and cell types. These studies have yielded different terminologies, whose relationships are by no means obvious. This table serves as a glossary of terms currently used in (a) microscopic studies and (b) in Hi-C and related studies. The lack of a common terminology in 4D nucleome research, except for a general consent on chromosome territories (CTs), reflects unsolved gaps and inconsistencies regarding the 3D and 4D (space-time) organization of structural entities and their suspected functional roles.

**(a) Terminology based on microscopic studies**

<p><b>nucleosome clutches (NCs) nanodomains (NDs)</b> <small>6,7</small></p>	<p>NCs/NDs with sizes of a few kb may represent the smallest structural entities of chromatin organization above the level of individual nucleosomes. Nucleosomes in NCs/NDs may be so densely packed that macromolecular aggregates can exert their functions only at the surface of NCs/NDs. 4D organization of NCs/NDs has remained elusive.</p>
<p><b>chromatin loops</b> <small>8</small></p>	<p>The 3D and 4D structure of chromatin loops is currently studied with super-resolved fluorescence microscopy and electron microscopy. The actual compaction of DNA/chromatin within loops is not known.</p>
<p><b>~1 Mb chromatin domains (CDs)</b> <small>9-13</small></p>	<p>The microscopic definition of ~1Mb chromatin domains (CDs) in early microscopic studies was based on replication domains (RDs) (see below). CDs with less compact chromatin are enriched with epigenetic marks of transcriptionally competent chromatin, whereas CDs with chromatin of higher compaction are enriched with marks for repressed chromatin. In a most recent study, Miron et al. described CDs as ~200-300 nm-wide mesoscale domains, composed of aggregated nucleosomes with nanoscale functional topography independent of cohesin.</p>
<p><b>TAD-like domains</b> <small>14,15</small></p>	<p>TAD-like domains were demonstrated at the single cell level by optical reconstruction of chromatin architecture (ORCA). This approach combines oligopaint-FISH with super-resolution fluorescence microscopy. In cohesin depleted cells, a more stochastic placement of borders between TAD-like domains was detected.</p>
<p><b>replication foci, replication domains (RDs)</b> <small>12,16-18</small></p>	<p>RDs with an estimated DNA content of ~1Mb were first detected in mammalian cells by pulse-labelling of replicating DNA during S-phase with halogenated nucleotides. At high resolution, RDs represent assemblies of several replicons with ~100–200 kb. RDs are stably maintained over subsequent cell cycles independent of their association with the transcription machinery. Chromatin assembled in early replicating RDs is enriched with active genes, whereas mid- and late-replicating RDs comprise mostly repressed chromatin.</p>
<p><b>chromatin domain clusters (CDCs) and CD chains</b> <small>9,13,19</small></p>	<p>CDCs comprise a peripheral layer of low compacted, transcriptionally competent CDs and an internal core of more compact, transcriptionally repressed CDs. CDs form interlinked chains surrounded by an RNA-populated interchromatin compartment (see below).</p>
<p><b>chromosome territory (CT)</b> <small>20</small></p>	<p>Evidence for a territorial arrangement of chromosomes (CTs) in cell nuclei was obtained in a wide range of animal and plant species by microscopic studies.</p>
<p><b>interchromatin compartment (IC)</b> <small>9,21</small></p>	<p>The IC refers to a contiguous 3D channel network, connected to nuclear pore complexes and expanding throughout the nucleus between CDs and CDCs. The finest ramifications of the IC have not yet been defined, but may extend between neighboring nucleosome clutches (NCs) or nanodomains (NDs). Wider IC-lacunae harbor large macromolecular complexes, e.g. splicing speckles. The IC may serve as a 'road' system for import of macromolecules, distribution to macromolecular complexes to sites of need, and mRNA export.</p>

<p><b>perichromatin region (PR)</b> 9,10</p>	<p>The PR comprises low compacted, transcriptionally competent chromatin and lines the borders of IC channels and lacunas. It is easily accessible for factors and factor complexes pervading the IC or released from nuclear bodies and splicing speckles. The PR is enriched in regulatory and coding sequences of active genes and represents the nuclear subcompartment, where most of the transcription, splicing of primary transcripts, as well as transcription of regulatory RNAs takes place.</p>
<p><b>active nuclear compartment (ANC)</b> 9,21</p>	<p>The ANC is formed by the IC together with the PR.</p>
<p><b>inactive nuclear compartment (INC)</b> 9,21</p>	<p>The INC comprises both CDs with repressed genes located in the interior of CDCs ('facultative' heterochromatin) and clusters of 'constitutive' heterochromatin. Like the ANC, the INC is pervaded by IC-channels.</p>

**(b) Terminology based on Hi-C and biochemical evidence**

<p><b>contact domains and boundaries</b> 22-24</p>	<p>Contact domains refer to an interval exhibiting increased contact frequency between loci inside this interval versus outside, i.e an on-diagonal square in a Hi-C map. Contact domains detected in population Hi-C studies do not represent an individual chromatin structure, but rather a statistical feature of a cell population. Contact domains can form as a result of loop extrusion<sup>22,24</sup> or compartmentalization<sup>23</sup>. Boundaries detected in Hi-C experiments represent transition points between contact domains.</p>
<p><b>loop domains</b> 22,24-26</p>	<p>Loop domains refer to a subset of contact domains that exhibit additional increased frequency between the ends of the interval, i.e. peaks in the corner. They are frequently, but not exclusively anchored by a cohesin ring at a pair of convergent CTCF binding sites, and they are thought to form as a result of loop extrusion.</p>
<p><b>compartment domains</b> 27</p>	<p>Compartment domains are a subset of contact domains which, in addition to exhibiting increased contact frequency inside the domain interval versus outside, also exhibit an elevated contact frequency with other compartment domains of the same "type" as compared with other compartment domains of a different "type". This manifests as plaid/checkerboard patterns in a Hi-C map. Compartment domains can vary drastically in size, and compartment domains as small as with a DNA content of only ~10-15 kb have been detected in Drosophila with high-resolution Hi-C. Compartment domains form independently of cohesin-dependent loop extrusion, thus compartment domains are neither mutually exclusive nor hierarchical to loop domains, compartment domains can span multiple loop domains, multiple compartment domains of different types (for instance, active and repressed) can be spanned by a single loop domain, or a compartment domain and loop domain can be coincident.</p>
<p><b>topologically associating domains (TADs)</b> 23,28-31</p>	<p>TADs generally refer to intervals exhibiting increased contact frequency between loci inside the interval versus outside along with additional constraints that have varied depending on the study (for instance: some have indicated a general size range of few hundred kb to 1Mb; some have imposed the requirement that TADs be contained within a contiguous compartment interval of the same type; some have defined TADs as only those intervals that demonstrate increased within-interval contact frequency as a result of loop extrusion).</p>

<p><b>replication domains (RD)</b> <small>32-38</small></p>	<p>400-800kb sized RDs were first noted in repli-seq experiments as developmental switches - that is the unit of DNA that changes replication timing coordinately. The regulatory mechanism(s) that specify the replication timing of RDs in a timely manner despite stochastic origin firing are currently not known.</p>
<p><b>compartment A compartment B</b> <small>23,25,27,29,39,40</small></p>	<p>Compartment A is globally defined by all compartment domains of subtype A, generally corresponding active chromatin, and compartment B by all compartment domains of subtype B, generally corresponding to repressed chromatin. Compartment A and B correspond to the two main pattern types observed in the plaid/checkerboard patterns in Hi-C maps. It has also been demonstrated that these two main compartment types can be further subdivided into subcompartments that correlate with distinct patterns of chromatin modifications on the basis of variations in contact patterns.</p>
<p><b>chromosome territories (CTs)</b> <small>23</small></p>	<p>CTs were demonstrated by enhanced contact frequency between all pairs of loci within a single chromosome in comparison with neighboring chromosomes.</p>

**Supplementary Note 5:** A comparison of the terminologies described above demonstrates the strength and weaknesses of microscopic and Hi-C strategies. Whereas ensemble Hi-C has the tremendous advantage of revealing 3D DNA-DNA contact frequencies in a genome wide manner, advanced microscopy has started to pave the way to high-resolution studies of chromatin dynamics at the single cell level<sup>13,41</sup> and has become the method of choice to identify the 3D network of channels that connect higher order chromatin structures in the nuclear interior with the nuclear pores<sup>21</sup>.

A common terminology should be based on clearly defined experimental approaches. For instance, a contact domain as defined in the glossary, does not depend on size scale, so no false sense of the size of the feature is implied that may be due just to the limitations of the resolution of the Hi-C map. In this sense, all loop domains, TADs and compartment domains can be subsumed under the heading of contact domains, notwithstanding major differences in their size ranges. Furthermore, the definition of a loop domain as a special sort of contact domain is independent of the question, whether a given loop is formed by CTCF/cohesin or other mechanisms. The 4D organization of such loops in living cells has remained elusive. Current perspectives range from an open architecture, where DNA targets in the loop interior are easily accessible for macromolecular complexes to highly compact structures, which constrains the accessibility of individual macromolecules and excludes larger macromolecular complexes. The history of the term chromosome can serve as a case in point for the importance to avoid an overloading of terms with unproven functional speculations. When Wilhelm Waldeyer (1836-1921) introduced this term in 1888<sup>42</sup> he was aware of August Weismann's (1834-1914) ingenious, but highly speculative theory of heredity (reviewed in<sup>43</sup>). He even referred to Johann Friedrich Miescher's (1844-1895) discovery of "nuclein" and to Albrecht Kossel's (1853-1927) early publications on "histon" and "adenin" (reviewed in<sup>44</sup>). Waldeyer, however, preferred to propose the name chromosomes to emphasize the possibility of coloring the worm-like entities, seen during mitosis, by certain stains. This term has remained open for all conceptual changes, which happened thereafter with regard to the structure and function of chromosomes to the present day.

(c) Our preliminary attempt to integrate the different perspectives of microscopy and Hi-C and tentatively suggest the following hypotheses:

- Active and repressed CDs are located within the ANC and INC, respectively. We equate the ANC with compartment A and the INC with compartment B defined by Hi-C experiments.
- CDs within the ANC may be equated with compartment domains A, CDs located in the INC with compartment domains B.
- Based on evidence that RDs, CDs and compartment domains, but not TADs, were detected in cohesin depleted cells, we suggest to equate RDs with CDs and compartment domains rather than with TADs. This view is, however, challenged by the observation of TAD-like domains in experiments that combined oligo-paint FISH of sequence-defined TADs with super-resolved fluorescence microscopy. These experiments may indicate that the failure to detect TADs in cohesin-depleted cells in ensemble Hi-C experiments is not due to a real loss of structural entities, but to apparently random cell-to-cell shifts of boundaries, demarcating neighboring TADs.

- Chromatin domain clusters (CDCs) carry more compact and mostly repressed CDs in their interior, and less compact, transcriptionally competent CDs at their periphery. The latter are closely associated with IC-channels and wider lacunas, carrying splicing speckles and other nuclear bodies. This reasoning is consistent with a nanoscale zonation of euchromatic and heterochromatic regions in CDCs.
- CDs, which mostly contain transcriptionally competent or active chromatin, may include short segments with repressive epigenetic signatures, whereas a CD comprising mostly repressed chromatin, may carry short segments with epigenetic marks signifying their transcriptional competence. These segments (named compartmental domains<sup>27</sup>) may comprise only a few kb, even only a single transcription unit. An active gene, located within a repressed CD, provides an anomaly like a grain of sugar in a pepper box. Vice versa, a repressed gene, located within a mostly active CD, reminds of a grain of pepper in a sugar box. Such examples do not invalidate the current concept of a hierarchically defined structural and functional higher order chromatin organization but necessitate a reconsideration of this concept. More detailed comparisons between the nuclear landscapes present in different cell types and species are required to solve this problem.
- A role of IC-channels as structural and functional boundaries between CDs and CDCs located on both sides has been considered but neither experimentally proven nor falsified.

Manipulations of defined target DNA sequences and proteins, respectively, will help to test our present and other hypotheses as rigorously as possible, and to explore the molecular mechanisms involved in the impact of the formation, preservation and changes of structural entities on nuclear functions.

**Supplementary Table 2: list of used antibodies**

<b><i>Antibodies</i></b>	<b><i>Dilution</i></b>	<b><i>Supplier</i></b>	<b><i>Catalog number</i></b>
RAD21	1:200	Abcam	ab154769
SMC1	1:200	Bethyl laboratories	A300-055A
SMC3	1:200	Bethyl laboratories	A300-060A
Goat anti rabbit Cy3	1:200	Dianova	111-165-045
Mouse anti SC35	1:1000	Sigma	S4045
Mouse anti RNA Pol II Ser5P	1:500	Abcam	ab5408
Rabbit anti H3K27me3	1:500	Active Motif	39155
Donkey anti mouse Alexa 488	1:400	Life technologies	A21202
Donkey anti rabbit Alexa 594	1:400	Life technologies	A21207
Mouse anti digoxigenin Cy5	1:100	Sigma	D8156
Streptavidin Alexa 488	1:200	Invitrogen	S-11223

## Supplementary References

- 1 Wojcik, C. & DeMartino, G. N. Intracellular localization of proteasomes. *Int J Biochem Cell Biol* **35**, 579-589, doi:10.1016/s1357-2725(02)00380-1 (2003).
- 2 Natsume, T., Kiyomitsu, T., Saga, Y. & Kanemaki, M. T. Rapid Protein Depletion in Human Cells by Auxin-Inducible Degron Tagging with Short Homology Donors. *Cell Rep* **15**, 210-218, doi:10.1016/j.celrep.2016.03.001 (2016).
- 3 Fei, J. *et al.* Quantitative analysis of multilayer organization of proteins and RNA in nuclear speckles at super resolution. *J Cell Sci* **130**, 4180-4192, doi:10.1242/jcs.206854 (2017).
- 4 Roukos, V., Pegoraro, G., Voss, T. C. & Misteli, T. Cell cycle staging of individual cells by fluorescence microscopy. *Nat Protoc* **10**, 334-348, doi:10.1038/nprot.2015.016 (2015).
- 5 Schermelleh, L., Heintzmann, R. & Leonhardt, H. A guide to super-resolution fluorescence microscopy. *J Cell Biol* **190**, 165-175, doi:jcb.201002018 [pii]10.1083/jcb.201002018 (2010).
- 6 Otterstrom, J. *et al.* Super-resolution microscopy reveals how histone tail acetylation affects DNA compaction within nucleosomes in vivo. *Nucleic Acids Res*, doi:10.1093/nar/gkz593 (2019).
- 7 Ricci, M. A., Manzo, C., Garcia-Parajo, M. F., Lakadamyali, M. & Cosma, M. P. Chromatin fibers are formed by heterogeneous groups of nucleosomes in vivo. *Cell* **160**, 1145-1158, doi:10.1016/j.cell.2015.01.054 (2015).
- 8 Boettiger, A. & Murphy, S. Advances in Chromatin Imaging at Kilobase-Scale Resolution. *Trends Genet* **36**, 273-287, doi:10.1016/j.tig.2019.12.010 (2020).
- 9 Cremer, T. *et al.* The 4D nucleome: Evidence for a dynamic nuclear landscape based on co-aligned active and inactive nuclear compartments. *FEBS Lett* **589**, 2931-2943, doi:10.1016/j.febslet.2015.05.037 (2015).
- 10 Cremer, T. *et al.* Chromosome territories, interchromatin domain compartment, and nuclear matrix: an integrated view of the functional nuclear architecture. *Crit Rev Eukaryot Gene Expr* **10**, 179-212 (2000).
- 11 Jackson, D. A. & Pombo, A. Replicon clusters are stable units of chromosome structure: evidence that nuclear organization contributes to the efficient activation and propagation of S phase in human cells. *J Cell Biol* **140**, 1285-1295, doi:10.1083/jcb.140.6.1285 (1998).
- 12 Ma, H. *et al.* Spatial and temporal dynamics of DNA replication sites in mammalian cells. *J Cell Biol* **143**, 1415-1425 (1998).
- 13 Miron, E. *et al.* Chromatin arranges in chains of mesoscale domains with nanoscale functional topography independent of cohesin. *Science Advances* **6**, eaba8811, doi:DOI: 10.1126/sciadv.aba8811 (2020).
- 14 Bintu, B. *et al.* Super-resolution chromatin tracing reveals domains and cooperative interactions in single cells. *Science* **362**, doi:10.1126/science.aau1783 (2018).
- 15 Mateo, L. J. *et al.* Visualizing DNA folding and RNA in embryos at single-cell resolution. *Nature* **568**, 49-54, doi:10.1038/s41586-019-1035-4 (2019).
- 16 Baddeley, D. *et al.* Measurement of replication structures at the nanometer scale using super-resolution light microscopy. *Nucleic Acids Res* **38**, e8, doi:10.1093/nar/gkp901 (2010).
- 17 Nakamura, H., Morita, T. & Sato, C. Structural organizations of replicon domains during DNA synthetic phase in the mammalian nucleus. *Exp Cell Res* **165**, 291-297, doi:10.1016/0014-4827(86)90583-5 (1986).
- 18 Xiang, W. *et al.* Correlative live and super-resolution imaging reveals the dynamic structure of replication domains. *J Cell Biol* **217**, 1973-1984, doi:10.1083/jcb.201709074 (2018).
- 19 Schmid, V. J., Cremer, M. & Cremer, T. Quantitative analyses of the 3D nuclear landscape recorded with super-resolved fluorescence microscopy. *Methods* **123**, 33-46, doi:10.1016/j.ymeth.2017.03.013 (2017).
- 20 Cremer, T. & Cremer, M. Chromosome territories. *Cold Spring Harb Perspect Biol* **2**, a003889, doi:10.1101/cshperspect.a003889 (2010).
- 21 Cremer, T. *et al.* The Interchromatin Compartment Participates in the Structural and Functional Organization of the Cell Nucleus. *Bioessays* **42**, e1900132, doi:10.1002/bies.201900132 (2020).
- 22 Fudenberg, G. *et al.* Formation of Chromosomal Domains by Loop Extrusion. *Cell Rep* **15**, 2038-2049, doi:10.1016/j.celrep.2016.04.085 (2016).
- 23 Lieberman-Aiden, E. *et al.* Comprehensive mapping of long-range interactions reveals folding principles of the human genome. *Science* **326**, 289-293, doi:10.1126/science.1181369 (2009).
- 24 Sanborn, A. L. *et al.* Chromatin extrusion explains key features of loop and domain formation in wild-type and engineered genomes. *Proc Natl Acad Sci U S A* **112**, E6456-6465, doi:10.1073/pnas.1518552112 (2015).
- 25 Rao, S. S. *et al.* A 3D map of the human genome at kilobase resolution reveals principles of chromatin looping. *Cell* **159**, 1665-1680, doi:10.1016/j.cell.2014.11.021 (2014).
- 26 Rao, S. S. P. *et al.* Cohesin Loss Eliminates All Loop Domains. *Cell* **171**, 305-320 e324, doi:10.1016/j.cell.2017.09.026 (2017).
- 27 Rowley, M. J. & Corces, V. G. Organizational principles of 3D genome architecture. *Nat Rev Genet* **19**, 789-800, doi:10.1038/s41576-018-0060-8 (2018).
- 28 Dixon, J. R., Gorkin, D. U. & Ren, B. Chromatin Domains: The Unit of Chromosome Organization. *Mol Cell* **62**, 668-680, doi:10.1016/j.molcel.2016.05.018 (2016).
- 29 Dixon, J. R. *et al.* Topological domains in mammalian genomes identified by analysis of chromatin interactions. *Nature* **485**, 376-380, doi:10.1038/nature11082 (2012).
- 30 Sexton, T. *et al.* Three-dimensional folding and functional organization principles of the Drosophila genome. *Cell* **148**, 458-472, doi:10.1016/j.cell.2012.01.010 (2012).
- 31 Szabo, Q. *et al.* TADs are 3D structural units of higher-order chromosome organization in Drosophila. *Sci Adv* **4**, eaar8082, doi:10.1126/sciadv.aar8082 (2018).

- 32 Marchal, C., Sima, J. & Gilbert, D. M. Control of DNA replication timing in the 3D genome. *Nat Rev Mol Cell Biol*, doi:10.1038/s41580-019-0162-y (2019).
- 33 Miura, H. *et al.* Single-cell DNA replication profiling identifies spatiotemporal developmental dynamics of chromosome organization. *Nature Genetics* **51**, 1356–1368 (2019).
- 34 Moindrot, B. *et al.* 3D chromatin conformation correlates with replication timing and is conserved in resting cells. *Nucleic Acids Res* **40**, 9470-9481, doi:10.1093/nar/gks736 (2012).
- 35 Pope, B. D. *et al.* Topologically associating domains are stable units of replication-timing regulation. *Nature* **515**, 402-405, doi:10.1038/nature13986 (2014).
- 36 Sima, J. *et al.* Identifying cis Elements for Spatiotemporal Control of Mammalian DNA Replication. *Cell* **176**, 816-830 e818, doi:10.1016/j.cell.2018.11.036 (2019).
- 37 Takahashi, S. *et al.* Genome-wide stability of the DNA replication program in single mammalian cells. *Nature Genetics* **51**, 529-540 (2019).
- 38 Zhao, P. A., Rivera-Mulia, J. C. & Gilbert, D. M. Replication Domains: Genome Compartmentalization into Functional Replication Units. *Adv Exp Med Biol* **1042**, 229-257, doi:10.1007/978-981-10-6955-0\_11 (2017).
- 39 Beagrie, R. A. *et al.* Complex multi-enhancer contacts captured by genome architecture mapping. *Nature* **543**, 519-524, doi:10.1038/nature21411 (2017).
- 40 Cardozo Gizzi, A. M., Cattoni, D. I. & Nollmann, M. TADs or no TADs: Lessons From Single-cell Imaging of Chromosome Architecture. *J Mol Biol* **432**, 682-693, doi:10.1016/j.jmb.2019.12.034 (2020).
- 41 Shaban, H. A., Barth, R., Recoules, L. & Bystricky, K. Hi-D: Nanoscale mapping of nuclear dynamics in single living cells. *bioRxiv566638*, doi:doi: <https://doi.org/10.1101/405969> (2020).
- 42 Waldeyer, W. Karyokinesis and its relation to the process of fertilization. *QJ microsc Sci* **30**, 159-281 (1888).
- 43 Cremer, T. & Cremer, C. Rise, fall and resurrection of chromosome territories: a historical perspective. Part I. The rise of chromosome territories. *Eur J Histochem* **50**, 161-176 (2006).
- 44 Cremer, T. & Cremer, C. Centennial of Wilhelm Waldeyer's introduction of the term "chromosome" in 1888. *Cytogenet. Cell Genet.* **48**, 65-67 (1988).

## **4.2 Site-specific antibody fragment conjugates for reversible staining in fluorescence microscopy**



## Accepted Article

**Title:** Site-Specific Antibody Fragment Conjugates for Reversible Staining in Fluorescence Microscopy

**Authors:** Jonathan Schwach, Ksenia Kolobynina, Katharina Brandstetter, Marcus Gerlach, Philipp Ochtrop, Jonas Helma, Christian P. R. Hackenberger, Hartmann Harz, M. Cristina Cardoso, Heinrich Leonhardt, and Andreas Stengl

This manuscript has been accepted after peer review and appears as an Accepted Article online prior to editing, proofing, and formal publication of the final Version of Record (VoR). This work is currently citable by using the Digital Object Identifier (DOI) given below. The VoR will be published online in Early View as soon as possible and may be different to this Accepted Article as a result of editing. Readers should obtain the VoR from the journal website shown below when it is published to ensure accuracy of information. The authors are responsible for the content of this Accepted Article.

**To be cited as:** *ChemBioChem* 10.1002/cbic.202000727

**Link to VoR:** <https://doi.org/10.1002/cbic.202000727>

## Site-Specific Antibody Fragment Conjugates for Reversible Staining in Fluorescence Microscopy

Jonathan Schwach<sup>[a]</sup>, Ksenia Kolobynina<sup>[b]</sup>, Katharina Brandstetter<sup>[a]</sup>, Marcus Gerlach<sup>[c]</sup>, Philipp Ochtrop<sup>[d]</sup>, Jonas Helma<sup>[c]</sup>, Christian P. R. Hackenberger<sup>[d,e]</sup>, Hartmann Harz<sup>[a]</sup>, M. Cristina Cardoso<sup>[b]</sup>, Heinrich Leonhardt<sup>[a]</sup>, Andreas Stengl<sup>\*,[a]</sup>

<sup>[a]</sup> J. Schwach, K. Brandstetter, Dr. H. Harz, Prof. Dr. H. Leonhardt, Dr. A. Stengl  
Ludwig-Maximilians-Universität München, Department of Biology II, Human Biology and  
BioImaging, 82152 Planegg-Martinsried, Germany

<sup>[b]</sup> K. Kolobynina, Prof. Dr. M. C. Cardoso  
Technical University of Darmstadt, Department of Biology, Cell Biology and Epigenetics,  
Schnittspahnstr. 10, 64287 Darmstadt, Germany

<sup>[c]</sup> Dr. M. Gerlach, Dr. J. Helma  
Tubulis GmbH,  
BioSysM, Butenandtstrasse 1, 81377, Munich, Germany

<sup>[d]</sup> Prof. Dr. C. P. R. Hackenberger, Philipp Ochtrop  
Leibniz-Forschungsinstitut für Molekulare Pharmakologie (FMP), Department Chemical Biology,  
Robert-Rössle-Strasse 10, 13125 Berlin, Germany

<sup>[e]</sup> Prof. Dr. C. P. R. Hackenberger  
Humboldt Universität zu Berlin, Department of Chemistry,  
Brook-Taylor-Strasse 2, 12489 Berlin, Germany

### Keywords

Site-specific antibody conjugates, Tub-tag labelling, peptide nucleic acids, nanobody, super resolution microscopy, immunofluorescence staining

## Abstract

Antibody conjugates have taken a great leap forward as tools in basic and applied molecular life sciences, which was enabled by the development of chemoselective reactions for the site-specific modification of proteins. Antibody-oligonucleotide conjugates combine the antibody's target specificity with the reversible, sequence-encoded binding properties of oligonucleotides like DNAs or PNAs, allowing sequential imaging of large numbers of targets in a single specimen. In this report, we use the Tub-tag<sup>®</sup> technology in combination with Cu-catalyzed azide-alkyne-cycloaddition for the site-specific conjugation of single DNA and PNA strands to an eGFP-binding nanobody. We show binding of the conjugate to recombinant eGFP and subsequent sequence-specific annealing of fluorescently labelled imager strands. Furthermore, we reversibly stain eGFP-tagged proteins in human cells, thus demonstrating the suitability of our conjugation strategy to generate antibody-oligonucleotides for reversible immunofluorescence imaging.

## Introduction

Proteins, especially antibodies, have been widely used as important tools in basic research and more recently as diagnostic and therapeutic agents.<sup>[1-2]</sup> Site- or residue-specific modification of antibodies with additional moieties ranging from small chemical compounds to large polypeptides has further expanded their field of use. This advancement was enabled by the development of chemoselective or bioorthogonal reactions and incorporation of unnatural amino acids into antibodies.<sup>[3]</sup> Antibody-oligonucleotide conjugates represent particularly interesting modalities, since they combine two key advantages of their building blocks in a single entity: specific antigen binding of antibodies with sequence-dependent hybridization of oligonucleotides to complementary strands. The former allows specific binding of target proteins in complex contexts such as cells, while the latter can be used for tunable, thus, reversible attachment of additional functionalities such as fluorophores. Unsurprisingly, protein-oligonucleotide conjugates have seen great use in a variety of applications ranging from protein immobilization,<sup>[4]</sup> bioanalytics<sup>[5-7]</sup> to material science.<sup>[8-10]</sup> Moreover, antibody-oligonucleotide conjugates have been employed in fluorescence and super resolution microscopy<sup>[11-12]</sup> since they resolve limitations that come with standard fluorophore-conjugated antibodies.

Although fluorophore-conjugated antibodies are one of the most common staining reagents due to their broad spectrum of targets, the virtually irreversible binding of antibodies and the spectral overlap between fluorophores heavily limit the number of individual targets that can be investigated at the same time. To overcome this problem, efforts have been devoted to develop protocols to either elute the antibodies<sup>[13-14]</sup> or chemically inactivate the fluorophores in between successive imaging rounds. However, these techniques involve harsh washing steps and thereby potentially alter epitope accessibility for the following imaging probes. Thus, elution of the previous probe should ideally be rapid and buffer conditions mild to preserve sample integrity. An elegant way to achieve this goal was developed for super-resolution microscopy called DNA-Point Accumulation for Imaging in Nanoscale Topography (DNA-PAINT).<sup>[15]</sup> DNA-PAINT exploits the transient binding of fluorophore-coupled oligonucleotides (imager strands) to their complementary sequence (docking strands) for reversible immobilization. The tunability of the binding strength between oligonucleotides allows for rapid exchange of fluorophores under mild washing conditions.<sup>[16-17]</sup>

Techniques to generate oligonucleotide-conjugated antibodies have subsequently received increasing interest. Common protocols involve bifunctional linkers that target exposed residues of amino acids on the protein surface.<sup>[18-20]</sup> However, conjugation stoichiometry is challenging to control depending on the abundance of the reactive surface residue. Other approaches that allow site-specific conjugation rely on guiding the reaction via a complementary template,<sup>[21]</sup> the incorporation of unnatural amino acids,<sup>[22-23]</sup> targeting unique or rare amino acids on native proteins<sup>[24]</sup> or the use of tag-enzyme pairs.<sup>[25-28]</sup> We previously established the Tub-tag<sup>□</sup> conjugation technology for bioorthogonal, chemo-enzymatic labelling of proteins<sup>[29-30]</sup> The Tub-tag<sup>□</sup> technology makes use of the enzyme tubulin tyrosine ligase (TTL) as a highly flexible tool for protein modification, that accepts a broad range of tyrosine derivatives as substrates enabling various bioorthogonal chemistries. We demonstrated its suitability for functionalization with small molecules<sup>[31]</sup> as well as protein-protein ligation.<sup>[32]</sup> In this work, we present the Tub-tag<sup>□</sup> mediated, efficient and site-specific generation of nanobody-DNA and -PNA conjugates in a 1:1 stoichiometry that can readily be used for reversible stainings in confocal fluorescence microscopy.

## Results and Discussion

Our approach combines enzyme-catalyzed ligation of a reactive chemical handle to an eGFP-binding nanobody (GBP) with Cu[I] catalyzed alkyne-azide cycloaddition (CuAAC) to conjugate the oligonucleotide (Fig. 1A). As proof-of-principle, we employ these conjugates for reversible staining of eGFP-fusion protein expressing cells in confocal fluorescence microscopy (Fig. 1B). In a first step, TTL recognizes the C-terminal Tub-tag<sup>□</sup> on the protein and site-specifically ligates O-propargyl-L-tyrosine to the C-terminus of the antibody. This introduces an alkyne group to the protein that can be used as a chemical handle for following reactions. Second, we utilize CuAAC for conjugation of an azide containing deoxyribonucleic acid (DNA) or peptide nucleic acid (PNA) to form a stable bond between antibody and oligonucleotide at a 1:1 stoichiometry. We envisioned that the unique characteristics of PNAs such as higher melting temperature and non-charged backbone would additionally broaden the general applicability of this strategy alternative to DNA-conjugation.

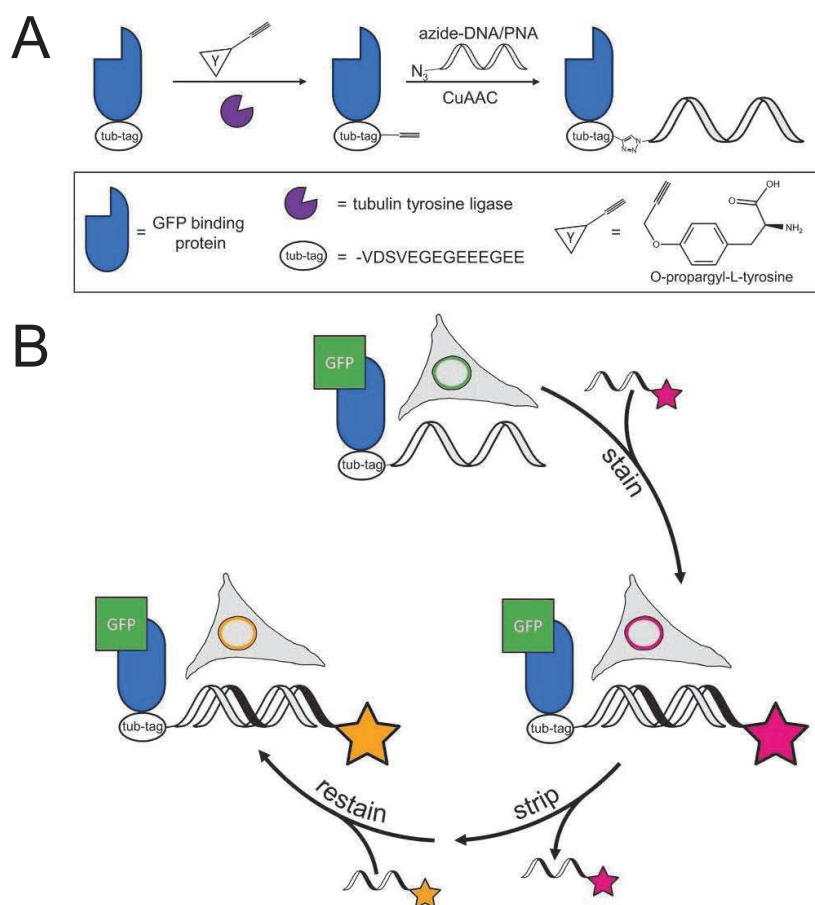


**Figure 1. Functionalization strategy for generation of nanobody-oligonucleotide conjugates and usage for reversible stainings in fluorescence microscopy.** (A) Schematic representation of the site-specific ligation of single-stranded oligonucleotides to the C-terminus of Tub-tagged nanobodies in a two-step process. First, an alkyne handle is introduced by the tubulin-tyrosine ligase (TTL) catalyzed ligation of O-propargyl-L-tyrosine to the Tub-tag. Second, azide-DNA or azide-PNA is conjugated to the alkyne handle by Copper catalyzed azide-alkyne cycloaddition (CuAAC). (B) Reversible immunofluorescence staining by hybridization of a fluorescent imager strand with the nanobody-oligonucleotide conjugate. Stripping of the imager strand allows for restaining of the sample.

We first set out to generate antibody-DNA/PNA conjugates via Tub-tag<sup>□</sup> technology and CuAAC based on previously published optimizations<sup>[32]</sup> and used eGFP-binding protein as a model antibody fragment. SDS-polyacrylamide gel electrophoresis and Coomassie staining confirmed efficient conjugation of both azide-DNA (yield: 55.9%) and azide-PNA (yield: 66.1%) to alkyne-modified GBP at 4x molar excess of azide-oligo over nanobody (Fig. 2A).

We hypothesized that especially the DNA oligonucleotide will strongly influence the total charge of the conjugated molecule so that unfunctionalized alkynyl GBP can be separated from the conjugate. Therefore, we performed mass spectrometry (Fig. S1) and anion exchange

chromatography (AEX) to further validate our observation from the gel electrophoresis. Notably, we observed a strong shift towards higher ionic strength for GBP-DNA conjugate compared to unfunctionalized alkynyl GBP indicating stronger interaction with the stationary phase (Fig. 2B). In addition, the GBP-DNA conjugate and free azide-DNA were not separable to baseline, suggesting that binding to the stationary phase is mediated by the DNA oligonucleotide to a major degree. Nevertheless, AEX allows for removal of non-conjugated alkynyl antibody as demonstrated by SDS-PAGE (Fig. 2A) and partial depletion of free DNA in the final product. In contrast, the antibody-PNA conjugates shifted towards lower ionic strengths. In accordance with this observation, free azide-PNA molecules eluted during the column wash since PNA does not carry strong negative charge (Fig. 2B).

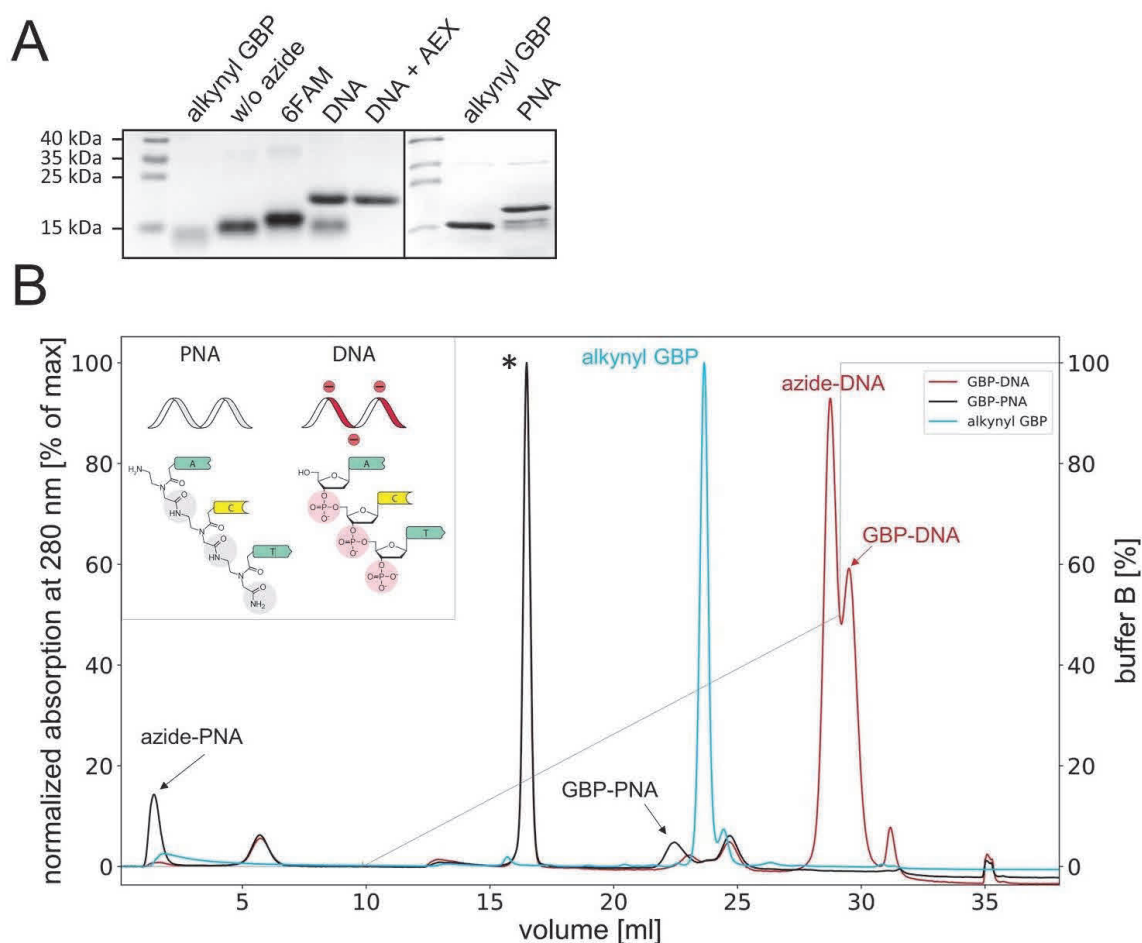


**Figure 2. TTL catalyzed enzymatic incorporation of O-propargyl-L-tyrosine and subsequent conjugation of azide modified 15 bp DNA and PNA strands by CuAAC . A)** Coomassie staining of SDS gels of functionalized alkynyl GBP (cropped sections, contrast adjusted, full images can be found in Fig. S2). Alkynyl GBP was generated by TTL catalyzed ligation of O-propargyl-L-tyrosine (298  $\mu$ M GBP-TT, 29.8  $\mu$ M TTL and 10 mM O-propargyl-L-tyrosine for 3 h at 30  $^{\circ}$ C). Conjugation with azide-DNA was performed using 40  $\mu$ M alkynyl GBP and 160  $\mu$ M azide-DNA; conjugation with azide-PNA was performed

using 60  $\mu\text{M}$  alkynyl GBP and 120  $\mu\text{M}$  azide-PNA (0.25 mM  $\text{CuSO}_4$ , 1.25 mM THPTA, 5 mM aminoguanidine and 5 mM sodium ascorbate). **B)** Analytical anion exchange chromatography of the raw conjugation products of A). Absorption (280nm) is normalized to the strongest signal. The peak marked with (\*) represents EDTA (see supplementary Fig. S3).

Taken together, these findings not only confirm that our chemo-enzymatic functionalization approach is capable of generating protein-oligonucleotide conjugates with high efficiency, but also that unfunctionalized alkynyl protein is separable from the conjugate product by AEX and free azide-oligonucleotides can be at least partially depleted.

To determine whether the antibody-oligonucleotide can bind both target and the complementary imager strand, we performed an *in vitro* binding assay on immobilized purified protein using either eGFP (target) or BSA (negative control). We detected strong signals for both DNA- and PNA-conjugate when the sample was hybridized with the complementary imager DNA-strand. Using either BSA as target protein or a non-complementary imager strand lead only to a minor increase of fluorescence (Fig. 3 top). This result confirmed that the functionality of both the antibody and the DNA docking strand was preserved by our conjugation strategy, since our conjugate was able to bind both eGFP and the complementary imager strand. Based on these findings, we were prompted to test our conjugate on fixed cells which provide a much more complex environment that could potentially lead to a higher degree of unspecific staining. Therefore, we used transiently transfected HEK293F cells expressing eGFP-actin fusion protein and repeated the staining similar to the previous experiment (Fig. 3 bottom). We observed the strongest signal in eGFP-actin transfected cells when staining with the complementary imager strand. Untransfected cells that do not express eGFP did not show elevated levels of fluorescence in the imager strand channel. Staining with non-complementary imager strand resulted in a minor increase of background fluorescence in both transfected and untransfected cells, suggesting that this effect is inherent to unspecific binding of the DNA or fluorophore itself to cellular components but not due to interaction with the docking strand. Antibody-PNA conjugate yielded higher fluorescence intensity, potentially indicating stronger binding of the DNA imager strand to PNA than to DNA as reported previously.<sup>[33]</sup>

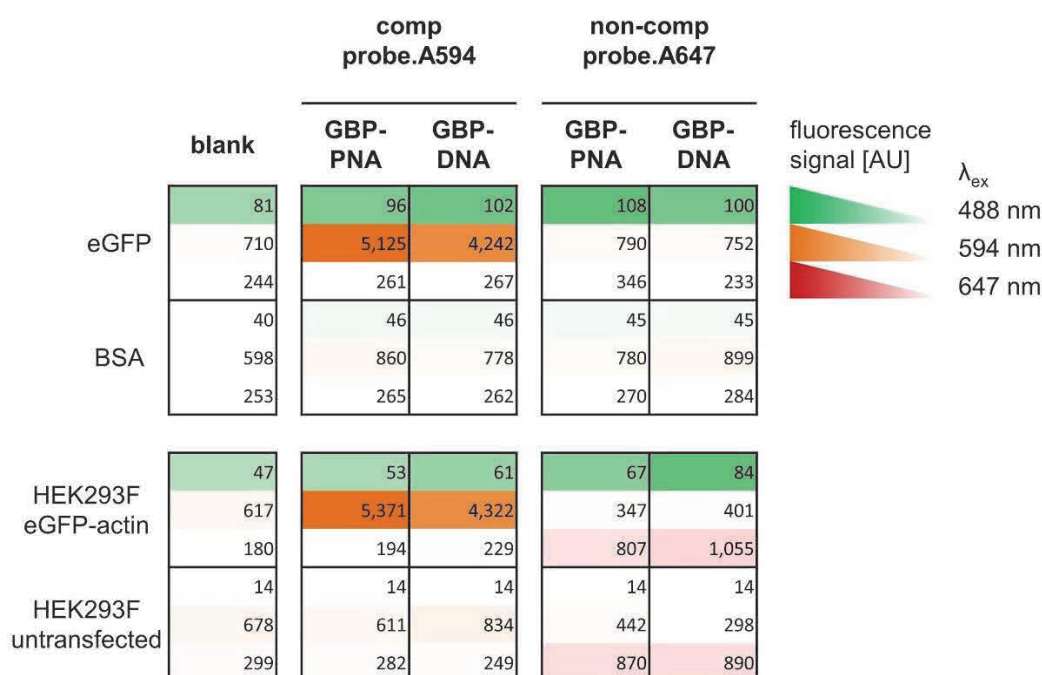


**Figure 3. Nanobody-oligonucleotide conjugates exhibit binding to their target protein and allow sequence-specific annealing of fluorescently labelled imager strands.** Top: Binding of nanobody-oligonucleotide conjugates to purified eGFP and annealing of a either complementary fluorescent imager strand (comp probe.A594) or non-complementary fluorescent imager strand (non-comp probe.A647). Bottom: Binding of nanobody-oligonucleotide conjugates to eGFP-actin expressing cells. Imager strands were used as in the top panels. Fluorescence signal intensity per well is represented by the respective color coding.

These promising results encouraged us to test whether the conjugate can be used for reversible immunostainings in confocal fluorescence microscopy. To this end, we stained fixed HEK293F and HeLa cells expressing either eGFP-LaminB1 or eGFP-PCNA fusion proteins, respectively, with DNA-conjugated nanobody. To verify that the imager strand can be detached from the docking strand, we stripped the samples with formamide containing buffer and performed restaining using an imager strand with the same sequence but different fluorophore as visualized in Fig. 1B. For both target proteins, we observed distinct nuclear staining with strong colocalization of imager strand and eGFP-LaminB1 or eGFP-PCNA, respectively (Fig. 4). After stripping off the first imager strand, we detected practically no remaining fluorescence although we used a highly sensitive detector, suggesting that the imager strand was efficiently detached from the DNA-docking strand. Restaining with a second imager strand led again to colocalization of eGFP and imager strand fluorescence (Fig. 4). Thus, this result demonstrates that the nanobody-DNA conjugate remains intact during the washing and that the staining is reversible. In contrast, nanobody-PNA conjugates showed residual fluorescence after washing in cell stainings (Fig. S4) as well as *in vitro* binding assays (Fig. S5). This observation is potentially due to stronger hybridization of PNA/DNA duplexes and might be resolved by optimization of washing conditions

or altering the sequence to lower hybridization temperatures. For nanobody-DNA and -PNA conjugates we observed minor background staining of the nucleus in all cells even without expression of eGFP (Fig. S6) which supports the assumption that the background is likely caused by nonspecific interaction of the DNA-imager strand with genomic DNA.

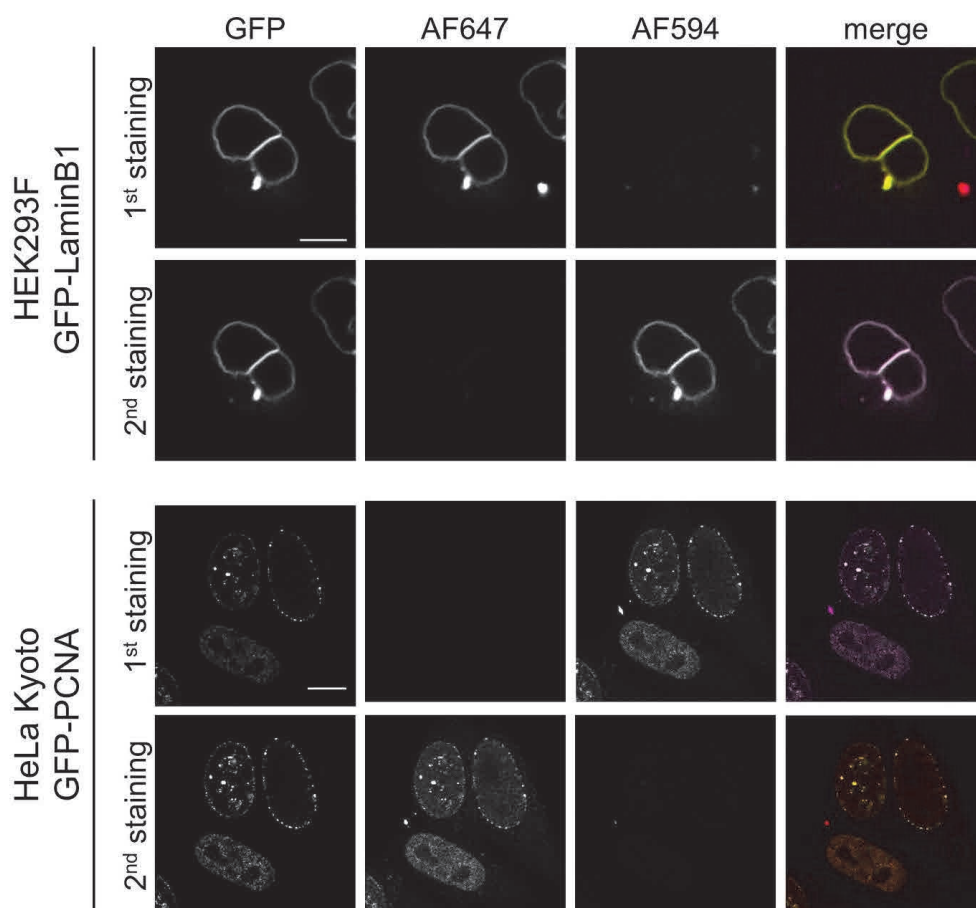


**Figure 4. Nanobody-oligonucleotide conjugates are suitable for reversible staining of cells in fluorescence microscopy.** Top: Staining of HEK293F cells expressing eGFP-LaminB1. eGFP-LaminB1 is stained by binding of the nanobody-DNA conjugate and subsequent annealing of a complementary imager strand leading to colocalized signal of imager strand and eGFP. Disruption of the interaction of imager and docking strand leads to almost complete removal of fluorescence, allowing for restaining with a complementary imager strand in a different channel. Bottom: Staining of HeLa Kyoto cells expressing eGFP-PCNA. Staining was performed identically to the top panel. Scale bars represent 10  $\mu\text{m}$ .

In summary, we show herein a novel conjugation technique for generation of nanobody-DNA and -PNA conjugates. Our approach allows the site-specific conjugation in 1:1 stoichiometry with high efficiency as shown by SDS-PAGE and anion exchange chromatography. In addition, binding assays on immobilized protein show a strong and specific staining towards the epitope of the antibody. Moreover, we demonstrate quick and efficient reversibility of the staining by using

confocal fluorescence microscopy, which is a key requirement for multiplexing via fluorophore exchange. Thus, our technology provides a new tool for chemo-enzymatic generation of protein-oligonucleotide conjugates. The defined 1:1 stoichiometry of our conjugation strategy provides a valuable advantage over currently state-of-the-art functionalization of surface exposed amino acids, where neither the stoichiometry nor the functionalization site is defined.

## Acknowledgments

We thank Hans C. Mescheder for countless scientific conversations and critical suggestions contributing to the advancement of this project. Furthermore, we thank Dominik Schumacher for scientific input regarding the Tub-tag<sup>□</sup> technology.

## Funding

This work was supported by grants from the Deutsche Forschungsgemeinschaft (DFG, German Research Foundation) within the SPP1623 to C.P.R.H. (HA 4468/9-1, 9-2 and 10-2), H.L. (LE 721/13-1, 13-2) and M.C.C. (CA 198/8-1, 8-2), GRK1657/TP1B to M.C.C., GRK1721 to H.L. and the Leibniz Association with the Leibniz Wettbewerb (T18/2017) to C.P.R.H and H.L..

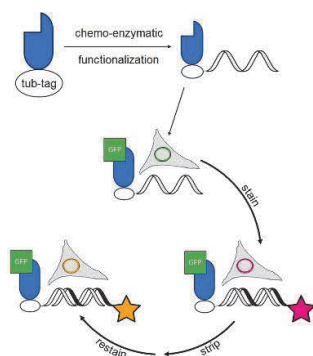
## Conflicts of interest

The Tub-tag<sup>□</sup> technology is part of a patent application filed by C.P.R.H, H.L. and J.H.. M.G. and J.H. are employees of Tubulis GmbH.

## References

- [1] D. Schumacher, C. P. Hackenberger, *Curr Opin Chem Biol* **2014**, *22*, 62-69.
- [2] J. Helma, M. C. Cardoso, S. Muyldermans, H. Leonhardt, *J Cell Biol* **2015**, *209*, 633-644.
- [3] K. Lang, J. W. Chin, *ACS Chemical Biology* **2014**, *9*, 16-20.
- [4] Z. Zhao, J. Fu, S. Dhakal, A. Johnson-Buck, M. Liu, T. Zhang, N. W. Woodbury, Y. Liu, N. G. Walter, H. Yan, *Nature Communications* **2016**, *7*, 10619.
- [5] Y. Xiang, Y. Lu, *Nature Chemistry* **2011**, *3*, 697-703.
- [6] J. A. G. L. van Buggenum, J. P. Gerlach, S. Eising, L. Schoonen, R. A. P. M. van Eijl, S. E. J. Tanis, M. Hogeweg, N. C. Hubner, J. C. van Hest, K. M. Bongers, K. W. Mulder, *Scientific Reports* **2016**, *6*, 22675.
- [7] J. Wiener, D. Kokotek, S. Rosowski, H. Lickert, M. Meier, *Scientific reports* **2020**, *10*, 1457-1457.
- [8] C. Hou, S. Guan, R. Wang, W. Zhang, F. Meng, L. Zhao, J. Xu, J. Liu, *The Journal of Physical Chemistry Letters* **2017**, *8*, 3970-3979.
- [9] J. R. McMillan, C. A. Mirkin, *J Am Chem Soc* **2018**, *140*, 6776-6779.
- [10] L. Gogolin, H. Schroeder, A. Itzen, R. S. Goody, C. M. Niemeyer, C. F. W. Becker, *ChemBioChem* **2013**, *14*, 92-99.
- [11] S. S. Agasti, Y. Wang, F. Schueder, A. Sukumar, R. Jungmann, P. Yin, *Chemical Science* **2017**, *8*, 3080-3091.
- [12] F. Schueder, M. T. Strauss, D. Hoerl, J. Schnitzbauer, T. Schlichthaerle, S. Strauss, P. Yin, H. Harz, H. Leonhardt, R. Jungmann, *Angew Chem Int Ed Engl* **2017**, *56*, 4052-4055.
- [13] C. Wählby, F. Erlandsson, E. Bengtsson, A. Zetterberg, *Cytometry* **2002**, *47*, 32-41.
- [14] K. D. Micheva, S. J. Smith, *Neuron* **2007**, *55*, 25-36.

- [15] R. Jungmann, C. Steinhauer, M. Scheible, A. Kuzyk, P. Tinnefeld, F. C. Simmel, *Nano Letters* **2010**, *10*, 4756-4761.
- [16] R. Jungmann, M. S. Avendaño, J. B. Woehrstein, M. Dai, W. M. Shih, P. Yin, *Nature Methods* **2014**, *11*, 313.
- [17] Y. Wang, J. B. Woehrstein, N. Donoghue, M. Dai, M. S. Avendaño, R. C. J. Schackmann, J. J. Zoeller, S. S. H. Wang, P. W. Tillberg, D. Park, S. W. Lapan, E. S. Boyden, J. S. Brugge, P. S. Kaeser, G. M. Church, S. S. Agasti, R. Jungmann, P. Yin, *Nano Lett* **2017**, *17*, 6131-6139.
- [18] C. M. Niemeyer, T. Sano, C. L. Smith, C. R. Cantor, *Nucleic Acids Res* **1994**, *22*, 5530-5539.
- [19] H. Gong, I. Holcomb, A. Ooi, X. Wang, D. Majonis, M. A. Unger, R. Ramakrishnan, *Bioconjugate Chemistry* **2016**, *27*, 217-225.
- [20] A. V. Maerle, M. A. Simonova, V. D. Pivovarov, D. V. Voronina, P. E. Drobyazina, D. Y. Trofimov, L. P. Alekseev, S. K. Zavriev, D. Y. Ryazantsev, *PloS one* **2019**, *14*, e0209860-e0209860.
- [21] C. B. Rosen, A. L. B. Kodal, J. S. Nielsen, D. H. Schaffert, C. Scavenius, A. H. Okholm, N. V. Voigt, J. J. Enghild, J. Kjems, T. Tørring, K. V. Gothelf, *Nature Chemistry* **2014**, *6*, 804-809.
- [22] K. Lang, J. W. Chin, *Chemical Reviews* **2014**, *114*, 4764-4806.
- [23] D. Katrekar, A. M. Moreno, G. Chen, A. Worlikar, P. Mali, *Scientific Reports* **2018**, *8*, 3589.
- [24] M.-A. Kasper, M. Glanz, A. Stengl, M. Penkert, S. Klenk, T. Sauer, D. Schumacher, J. Helma, E. Krause, M. C. Cardoso, H. Leonhardt, C. Hackenberger, *Angewandte Chemie* **2019**, *0*.
- [25] M. W.-L. Popp, J. M. Antos, H. L. Ploegh, *Current Protocols in Protein Science* **2009**, *56*, 15.13.11-15.13.19.
- [26] D. Rabuka, J. S. Rush, G. W. deHart, P. Wu, C. R. Bertozzi, *Nat Protoc* **2012**, *7*, 1052-1067.
- [27] V. Siegmund, S. Schmelz, S. Dickgiesser, J. Beck, A. Ebenig, H. Fittler, H. Frauendorf, B. Piater, U. A. K. Betz, O. Avrutina, A. Scrima, H.-L. Fuchsbaauer, H. Kolmar, *Angewandte Chemie International Edition* **2015**, *54*, 13420-13424.
- [28] M. Rashidian, J. K. Dozier, M. D. Distefano, *Bioconjugate Chemistry* **2013**, *24*, 1277-1294.
- [29] D. Schumacher, J. Helma, F. A. Mann, G. Pichler, F. Natale, E. Krause, M. C. Cardoso, C. P. Hackenberger, H. Leonhardt, *Angewandte Chemie International Edition* **2015**, *54*, 13787-13791.
- [30] D. Schumacher, O. Lemke, J. Helma, L. Gerszonowicz, V. Waller, T. Stoschek, P. M. Durkin, N. Budisa, H. Leonhardt, B. G. Keller, C. P. R. Hackenberger, *Chemical Science* **2017**, *8*, 3471-3478.
- [31] M. Effenberger, A. Stengl, K. Schober, M. Gerget, M. Kampick, T. R. Müller, D. Schumacher, J. Helma, H. Leonhardt, D. H. Busch, *The Journal of Immunology* **2019**, *ji1801435*.
- [32] A. Stengl, M. Gerlach, M.-A. Kasper, C. P. R. Hackenberger, H. Leonhardt, D. Schumacher, J. Helma, *Organic & Biomolecular Chemistry* **2019**, *17*, 4964-4969.
- [33] M. C. Chakrabarti, F. P. Schwarz, *Nucleic Acids Res* **1999**, *27*, 4801-4806.



**Protein oligonucleotide conjugates.** We present a novel strategy for efficient and site-specific generation of nanobody-oligonucleotide conjugates in a 1:1 stoichiometry by Tub-tag mediated conjugation. We show proof-of-concept that these conjugates can readily be used for reversible stainings in confocal fluorescence microscopy.

## **Supplementary Information**

## Experimental Procedures

### Oligonucleotide sequences

name	sequence 5' -> 3' / N -> C	functionalization
DNA docking strand	TAACTGGACTTCATC	5' azide
PNA docking strand	TAACTGGACTTCATC	N-term N3-acetic acid
DNA probe.A594	GATGAAGTCCAGTTA	3' AF594
DNA probe A647	GATGAAGTCCAGTTA	3' AF647
DNA non-complementary	GTTTCATGTGCTGATT	3' AF647

5' azide-DNA docking strand was purchased from metabion. N terminally modified N3-acetic acid PNA docking strand was purchased from Eurogentech. Fluorophore conjugated DNA imager strands were purchased from Eurofins.

### TTL expression and purification

Tubulin tyrosine ligase (TTL) was expressed and purified as previously published. <sup>[1]</sup>

In short, TTL was expressed as a N-terminally His-tagged SUMO-TTL fusion protein in pET28 backbone in *E. coli* BL21(DE3) cells. Expression was induced with 0.5 mM IPTG for 18 h at 18 °C. Cells were lysed for 2 h at 4 °C in TTL binding buffer (20 mM Tris, 250 mM NaCl, 20 mM Imidazole, 3 mM  $\beta$ -mercaptoethanol, pH 8.2) in the presence of 100  $\mu$ g/ml lysozyme and 25  $\mu$ g/ml DNase followed by sonification (7x8 s, 40 % amplitude, Branson Sonifier) and centrifugation at 20.000 g for 30 min, 4 °C for debris removal. Purification was done on an Äkta pure system (GE Healthcare Life Sciences) using a 5 ml HisTrap HP column (GE Healthcare Life Sciences) according to the manufacturer's instructions. Peak fractions were pooled, desalted on a PD10 column (GE Healthcare Life Sciences) and the buffer exchanged to TTL storage buffer (20 mM MES, 100 mM KCl, 10 mM MgCl<sub>2</sub>, 50 mM L-glutamate, 50 mM L-arginine, 3 mM  $\beta$ -mercaptoethanol, pH 7.0).

### Expression of N-terminally His-tagged GBP-TT and eGFP

Green fluorescent protein binding nanobody (GBP) was expressed and purified as previously published. <sup>1</sup>

In short, nanobody was expressed with N-terminal His-tag and C-terminal tub-tag in *E. coli* JM109 cells. Expression was induced with 1 mM IPTG and bacteria incubated at 18 °C, 180 rpm over night. Cells were lysed for 2 h in NiNTA binding buffer (20 mM Tris-HCl, 250 mM NaCl, 20 mM imidazole, pH 8.2) in the presence of 100  $\mu$ g/ml lysozyme and 25  $\mu$ g/ml DNase

followed by sonification (7x8 s, 40 % amplitude, Branson Sonifier) and centrifugation at 20.000 g for 30 min, 4 °C for debris removal. Purification was done on an Äkta pure system (GE Healthcare Life Sciences) using a 5 ml HisTrap HP column (GE Healthcare Life Sciences) according to the manufacturer's instructions. Peak fractions were pooled, concentrated in Amicon Ultra Centrifugal Filters (4 ml, 3 NMWL, Merck Millipore) and buffer exchanged to 1x PBS using Zeba Spin desalting columns (7 MWCO). The eluate was injected onto a Superdex 200 Increase 300/10 column (GE Healthcare Life Sciences) at a flow rate of 1 ml/min in PBS. Peak fractions were pooled and concentrated in Amicon Ultra Centrifugal Filters (4 ml, 3 NMWL, Merck Millipore).

His-tagged eGFP was thankfully provided by H. Flaswinkel (LMU Munich, Germany) and expressed and purified in the same manner as described above for GBP-TT.

### **GBP DNA/PNA conjugation**

Conjugation of nanobodies via CuAAC was adapted from a previous publication. <sup>[2]</sup>

The ligation of O-propargyl-L-tyrosine to GBP-TT was catalyzed by the TTL enzyme in TTL reaction buffer (20 mM MOPS, 100 mM KCl, 10 mM MgCl<sub>2</sub>, 2.5 mM ATP and 5 mM reduced glutathione, pH 7.0) using 298 µM GBP-TT, 29.8 µM TTL and 10 mM O-propargyl-L-tyrosine in minimal volume. The reaction was incubated for 3 h at 30 °C and desalted via Zeba Spin desalting columns (7 MWCO, Thermo Fisher Scientific) for removal of excess O-propargyl-L-tyrosine.

For conjugation of O-propargyl-L-tyrosine-GBP with 3-azido-DNA binding strands (metabion), CuAAC reactions were performed in volumes of up to 115 µl with either 40 µM alkynyl-GBP and 4x excess of azide-DNA for SDS-PAGE and analytical AEX or 70 µM concentration of propargyl-GBP and 2x excess of azide-DNA for preparative AEX in CuAAC reaction buffer (final concentrations in the reaction: 0.25 mM CuSO<sub>4</sub>, 1.25 mM THPTA, 5 mM aminoguanidine, 5 mM sodium ascorbate, 20 mM MOPS, pH 7.0) for 1 h at 25 °C. The reaction was immediately quenched by the addition of 50 mM EDTA and samples were desalted via Zeba Spin desalting columns (7 MWCO) to 1x PBS. Conjugation with N-terminally modified azido-PNA (Eurogentech) was performed as described above using 60 µM propargyl-GBP with 2x excess of azido-PNA. For control reactions, 10 mM 6-Fluorescein azide (baseclick) were used. Reaction products were analyzed by Coomassie staining and anion exchange chromatography. Reaction efficiency was calculated by densitometric analysis using GelAnalyzer (GelAnalyzer 19.1, [www.gelanalyzer.com](http://www.gelanalyzer.com), by Istvan Lazar Jr., PhD and Istvan Lazar Sr., PhD, CSc)

### **Purification of nanobody conjugates by anion exchange chromatography**

Preparative anion exchange chromatography was performed on an Äkta pure system (GE Healthcare Life Sciences) using a ResourceQ column (Amersham Pharmacia Biotech) equilibrated in buffer A (20 mM MOPS, pH 7.0). Separation was performed by linear increase to 50% buffer B (20 mM MOPS, 1 M NaCl, pH 7.0) over 20 CV followed by 100% buffer B for 5 CV

and protein absorption measured at 280 nm. Peak fractions were collected, concentrated using Amicon Ultra Centrifugal Filters (0.5 ml, 3 NMWL, Merck Millipore) and buffer exchanged to 1x PBS using Zeba Spin desalting columns (7 MWCO).

### **Quadrupol time-of-flight mass spectrometry of intact proteins**

Intact proteins were analyzed using a Waters H-class instrument equipped with a quaternary solvent manager, a Waters sample manager-FTN, a Waters PDA detector and a Waters column manager with an Acquity UPLC protein BEH C4 column (300 Å, 1.7 µm, 2.1 mm x 50 mm). 3 µl of buffered Protein solution were injected and eluted with a flow rate of 0.3 ml/min. The following gradient was used: A: 0.01% FA in H<sub>2</sub>O; B: 0.01% FA in MeCN. 5-95% B 0-6 min. Mass analysis was conducted with a Waters XEVO G2-XS QToF analyzer. Proteins were ionized in positive ion mode applying a cone voltage of 40 kV. Raw data was analyzed with MaxEnt 1 and the recorded ion series was deconvoluted for a mass range from 3000 to 25000 Da.

### **Antigen binding and imager strand annealing/dissociation assay**

Purified eGFP (the antigen) was immobilized on 96-well µClear plates multiwell plates (Greiner) at a concentration of 5 µM for 1 h at room temperature. Antigen coated wells and uncoated control wells were blocked with 1% BSA solution for 1 h at room temperature followed by two washing steps with PBST (PBS/0.05 % Tween20). 7.5 µM GBP-PNA and GBP-DNA conjugate were added to for 1 h at room temperature followed by three PBST wash steps. Fluorophore labelled DNA strands (imager strands) with DNA sequences complementary or non-complementary to the GBP-conjugated oligonucleotide were added at 10 µM for 30 min and washed three times with PBST. Fluorescence signal was recorded on a Tecan Infinite 1000 multiwell plate reader system with excitation wavelengths set to 488 nm (eGFP), 603 nm (Atto594) and 646 nm (Atto647) and emission wavelength to 509 nm, 626 nm and 664 nm, respectively. Mean fluorescence intensity of duplicate wells was calculated and depicted as colour intensities.

For *in vitro* cell binding assays, eGFP-actin transfected or untransfected control cells were seeded on 96-well µClear plates multiwell plates (Greiner), fixed and permeabilized as described in the imaging section below. Wells were blocked with 1% BSA solution for 1 h at room temperature followed by two washing steps with PBST (PBS/0.05 % Tween20). 7.5 µM GBP-PNA conjugate were added to for 1 h at room temperature followed by three PBST wash steps. Fluorophore labelled DNA strands (imager strands) with DNA sequences complementary or non-complementary to the GBP-conjugated oligonucleotide were added at 10 µM for 30 min and washed three times with PBST. The annealed imager strand was dissociated by a 2 h wash in PBS/50% formamide, followed by three PBST wash steps. Imager strand was re-annealed for 1 h at room temperature followed by three PBST wash steps. Fluorescence signal was recorded on a Tecan Infinite 1000 multiwell plate reader system with excitation wavelengths set to 603 nm (Atto594) and emission wavelength to 626 nm. Mean fluorescence intensity of duplicate wells was calculated and depicted as colour intensities.

## Cell lines generation and cell culture

HEK293Freestyle (Thermo Fisher Scientific) cells were seeded on poly-L-lysine coated  $\mu$ -Slide 8 Well ibiTreat (cat.no 80826, ibidi) containing DMEM/F12 medium (Thermo Fisher Scientific) supplemented with 10% FBS at 40.000 cells per well and incubated at 37 °C in a humidified atmosphere of 5% CO<sub>2</sub> to allow attachment. Cells were transiently transfected with plasmid bearing eGFP gene and laminB1 gene (Daigle *et al.*, 2001) at DNA concentration of 2.5  $\mu$ g/ml using MAXreagent (Thermo Fisher Scientific).

The human cervical carcinoma HeLa Kyoto cells (ATCC No. CCL-2), HeLa Kyoto eGFP-PCNA cells, HeLa Kyoto mCherry-PCNA cells, and HeLa Kyoto eGFP-laminB1 cells were grown in DMEM medium supplemented with 10% FCS, L-glutamine and antibiotics at 37 °C in a humidified atmosphere of 5% CO<sub>2</sub>. HeLa Kyoto cell lines expressing fluorescent PCNA variants were generated in (Chagin *et al.*, 2016) using the Flp-In recombinant system. HeLa Kyoto eGFP-laminB1 cells were obtained by transfection with the plasmid bearing eGFP gene and laminB1 gene (Daigle *et al.*, 2001). Positively transfected cells were selected visually. Cells were seeded on the  $\mu$ -Slide 8 Well ibiTreat (cat.no 80826, ibidi) at a concentration 20.000 cells per well. Cells were incubated for 24 h in a humidified atmosphere as described above.

## Cell staining with conjugates, imaging and microscopy

eGFP-laminB1 transfected HEK cells were fixed in PBS/4% PFA solution for 10 min at room temperature, washed twice in PBS/0.05% Tween20 (Carl Roth) and permeabilized with PBS/0,25% TritonX-100 (Sigma Aldrich) for 10 min at room temperature. Cells were washed in PBS, blocked in PBS/5% BSA for 1 h at room temperature and incubated overnight at 4 °C with anion exchange purified DNA/PNA conjugated nanobody (16,6  $\mu$ M in PBS/5% BSA). Samples were washed twice in PBS and stained with 10 nM imager strand for 5 min at room temperature in imaging buffer (500 mM NaCl in PBS, pH 8.0) followed by two washes with imaging buffer prior to imaging. After imaging, samples were washed twice in 0.01x PBS followed by two washes in stripping buffer (PBS/30% formamide for DNA-GBP and PBS/50% formamide for PNA-GBP samples) with 3 min incubation times at room temperature. Samples were washed twice in PBS prior to restaining. For HeLa Kyoto and HeLa Kyoto with fluorescent variants of PCNA and laminB1 the staining procedure was identical as for HEK cells.

For HEK293F cells, spinning disk confocal imaging was carried out on a Nikon TiE microscope equipped with a Yokogawa CSU-W1 spinning disk confocal unit (50  $\mu$ m pinhole size), an Andor Borealis illumination unit, Andor ALC600 laser beam combiner (405 nm / 488 nm / 561 nm / 640 nm), and Andor IXON 888 Ultra EMCCD camera. The microscope was controlled by software from Nikon (NIS Elements, ver. 5.02.00). Images were acquired with a pixel size of 217 nm using a Nikon CFI Apochromat TIRF 60x NA 1.49 oil immersion objective (Nikon). eGFP, Alexa594 and Alexa647 were excited for 500 ms using the 488, 561 and 640 nm laser lines, respectively. The emission of eGFP, Alexa594 and Alexa647 was captured by using a 525/50 nm, a 600/50 nm and a 700/75 nm filter, respectively. In addition, differential interference contrast (DIC) images were acquired. Confocal microscopy images of HeLa Kyoto cells were acquired using a Leica TCS

SP5II confocal laser scanning microscope (Leica Microsystems, Wetzlar, Germany) equipped with an oil immersion Plan-Apochromat x100/1.44 NA objective lens (pixel size in XY set to 100 nm, Z-step=290 nm) and laser lines at 488, 561 and 633 nm. For the second round of imaging cells were recorded as z-stacks with a z-spacing of 290 nm to find the exact plane corresponding to the first round of imaging.

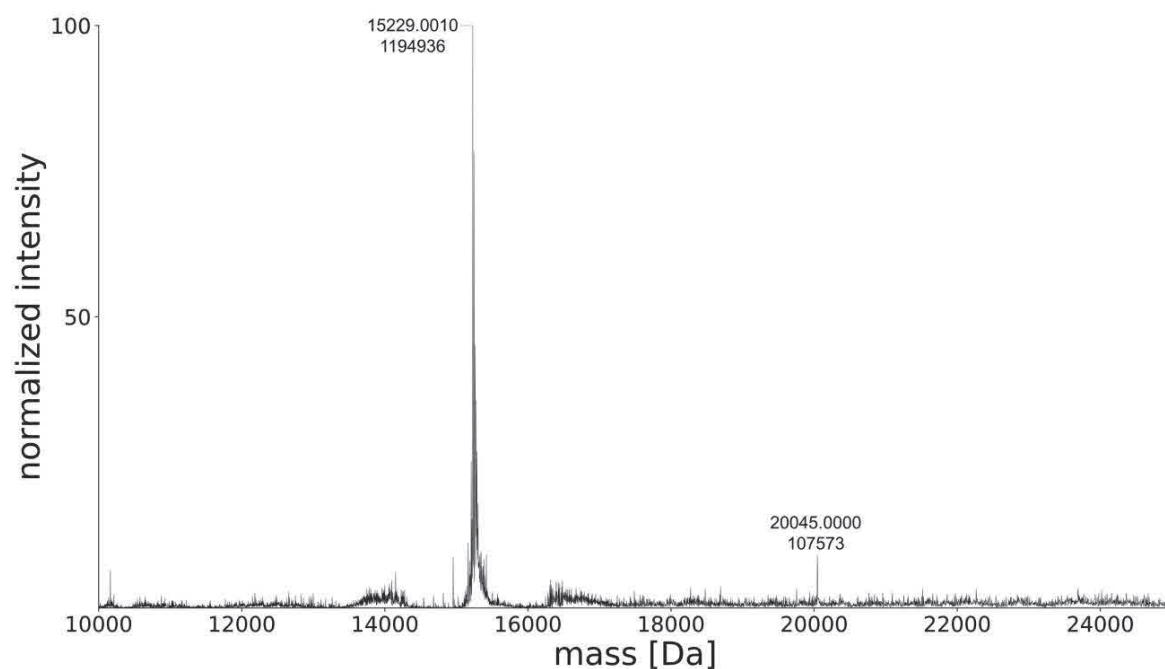


**Figure S1: Quadrupol time-of-flight mass spectrometry of alkynyl GBP functionalized with azide-DNA.** Calculated mass of alkynyl-GBP: 15229 Da. Calculated mass of GBP-DNA conjugate: 20045 Da (15229 Da alkynyl GBP + 4816 Da of azide-DNA).

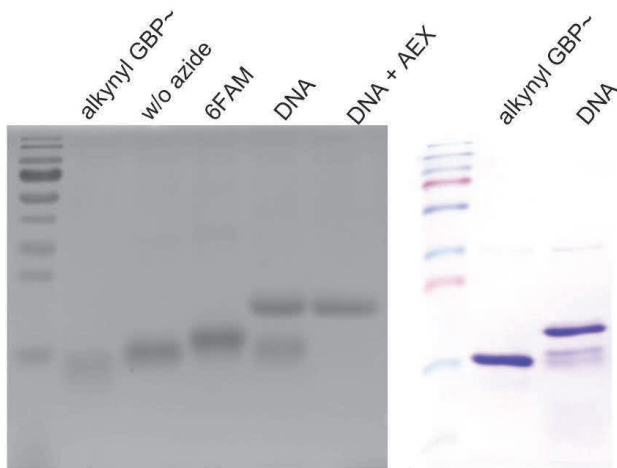


**Figure S2: Uncropped and unadjusted images of coomassie stained SDS gels.** Left image was recorded in grayscale right image in color mode. SDS-PAGE analysis of functionalized alkynyl GBP as shown in Figure 2A. Alkynyl GBP was generated by TTL catalyzed ligation of O-propargyl-L-tyrosine (298  $\mu\text{M}$  GBP-TT, 29.8  $\mu\text{M}$  TTL and 10 mM O-propargyl-L-tyrosine for 3 h at 30  $^{\circ}\text{C}$ ). Conjugation with azide-DNA was performed using 40  $\mu\text{M}$  alkynyl GBP and 160  $\mu\text{M}$  azide-DNA; conjugation with azide-PNA was performed using 60  $\mu\text{M}$  alkynyl GBP and 120  $\mu\text{M}$  azide-PNA (0.25 mM  $\text{CuSO}_4$ , 1.25 mM THPTA, 5 mM aminoguanidine and 5 mM sodium ascorbate).

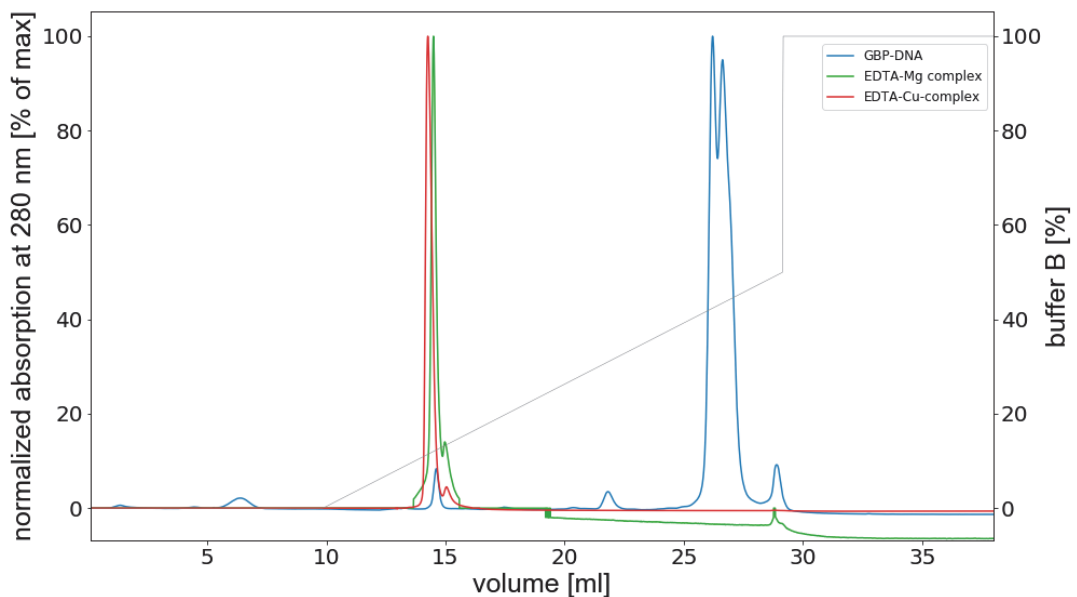


**Figure S3: Anion exchange chromatography of EDTA in complex with Cu or Mg ions.** Overlay of EDTA chromatograms with GBP-DNA conjugate chromatogram shows elution of residual EDTA that was added for competitive complexation of Cu ions in the buffer exchanged conjugation product

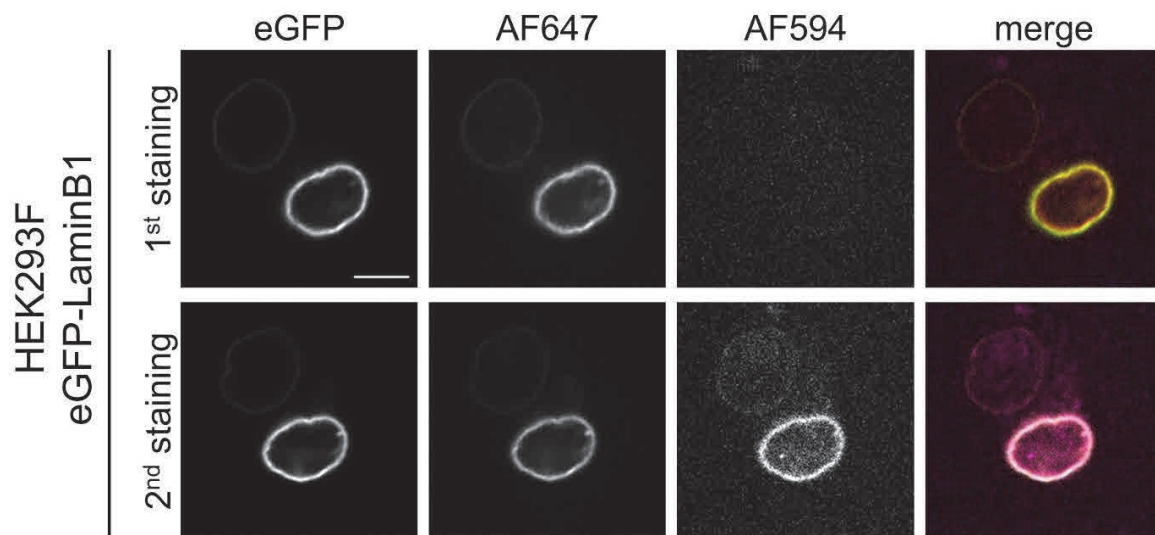


**Figure S4. Staining of HEK293F cells expressing eGFP-Lamin.** eGFP-LaminB1 is stained by binding of the nanobody-PNA conjugate and subsequent annealing of a complementary imager strand leading to colocalized signals of imager strand and eGFP. Attempted disruption under the same conditions as for nanobody-DNA conjugate does not lead to a major decrease in fluorescence. However, annealing of a second imager strand leads to additional signal in the respective channel. Scale bar represents 10  $\mu\text{m}$ .

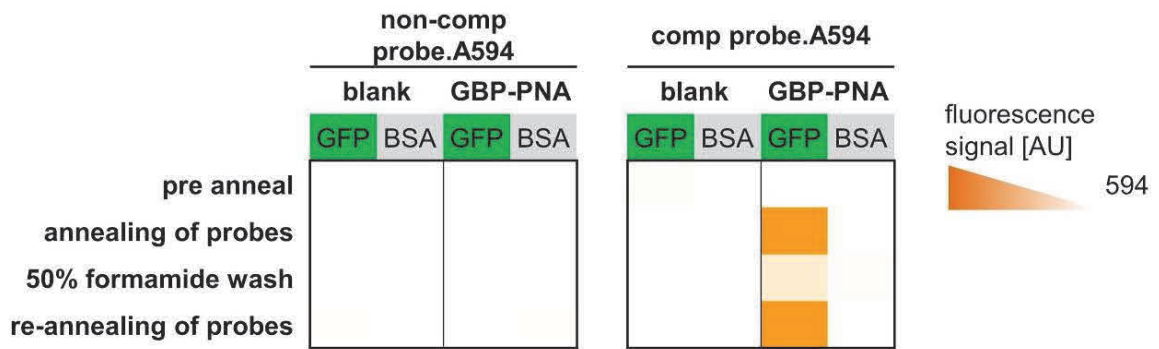


**Figure S5. *In vitro* binding assay of GBP-PNA conjugates.** Sequence-specific binding of imager strands to GBP-PNA conjugates bound to immobilized eGFP and reversible annealing of fluorescent imager strands. Disruption with formamide leads to an incomplete decrease in fluorescence. Fluorescence signal intensity per well is represented by the respective colour coding.

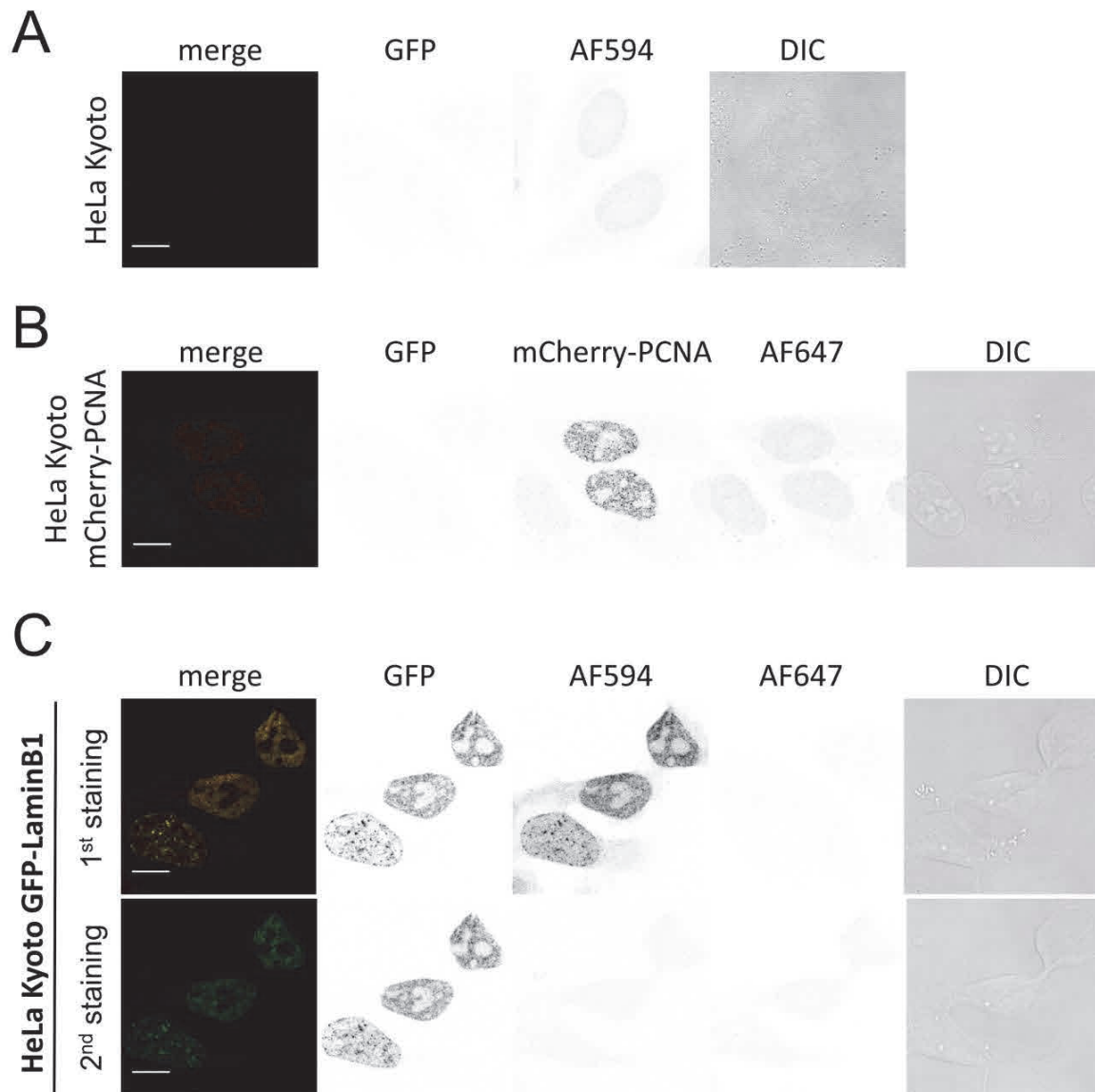


**Figure S6. HeLa Kyoto cell lines expressing (A) no fluorescent protein, treated with GBP-DNA conjugate followed by addition of complementary imager strand (AF594), (B) mCherry-PCNA fusion protein, treated with GBP-DNA conjugate followed by addition of complementary imager strand (AF647) or (C) GFP-LaminB1, treated with GBP-DNA conjugate followed by addition of complementary (AF594) and non-complementary (AF647) imager strand (1<sup>st</sup> and 2<sup>nd</sup> staining, respectively).** Staining with nanobody-DNA conjugate and subsequent annealing of imager strand leads to a minor, non-specific background signal especially within the nucleus. Expression of mCherry-PCNA does not lead to colocalization of mCherry and imager strand. Expression of GFP and binding of GBP-DNA conjugate enables specific binding of complementary imager strand, but not a non-complementary sequence. Scale bars represent 10  $\mu\text{m}$ .

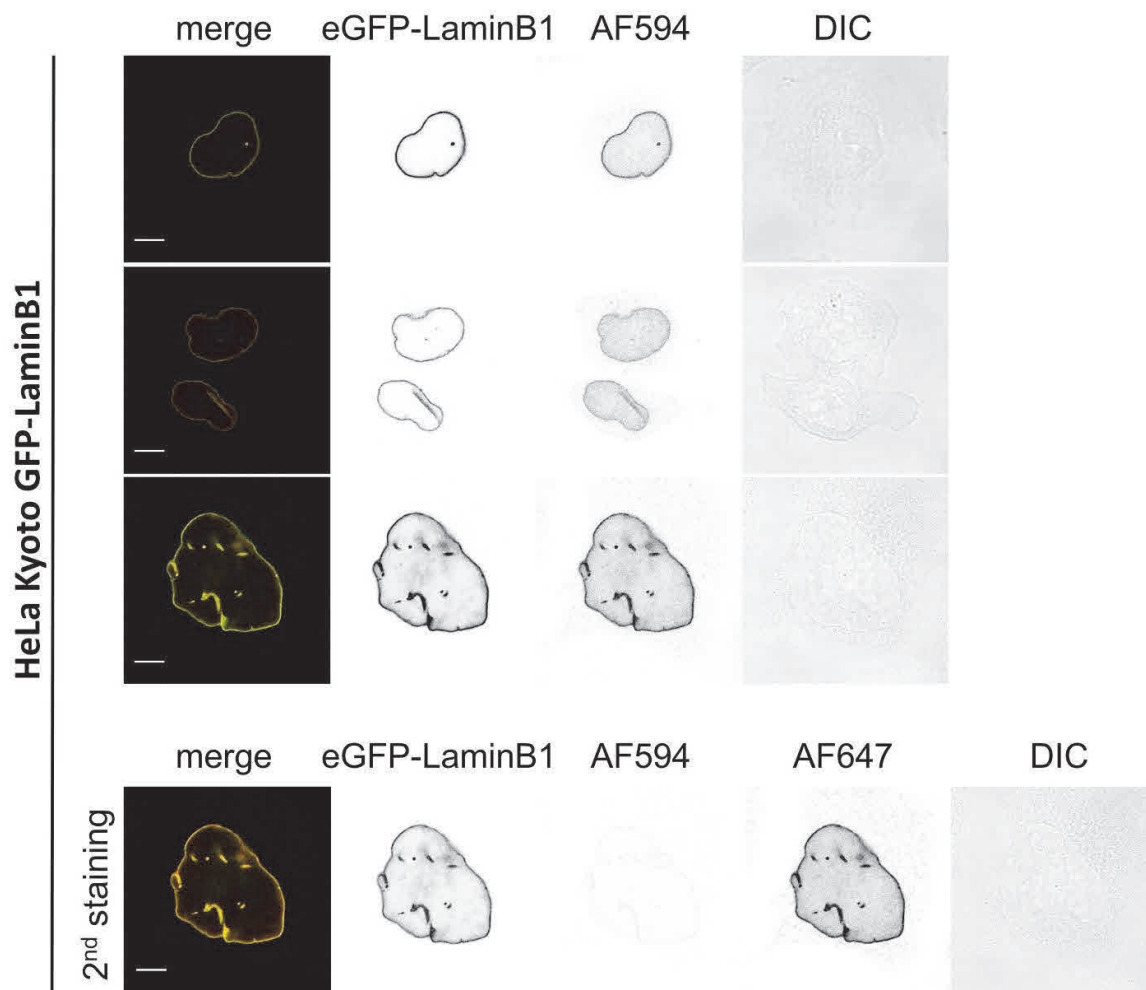


**Figure S7. Staining of HeLa Kyoto cells expressing eGFP-LaminB1.** eGFP-LaminB1 was stained by binding of the nanobody-DNA conjugate and subsequent annealing of a complementary imager strand leading to colocalized signals of imager strand and eGFP. Disruption of the interaction of imager and docking strand leads to almost complete loss of fluorescence, allowing for restaining with a complementary imager strand detectable in a different channel (bottom panels). Scale bars represent 10  $\mu$ m.

## References

- [1] D. Schumacher, J. Helma, F. A. Mann, G. Pichler, F. Natale, E. Krause, M. C. Cardoso, C. P. Hackenberger, H. Leonhardt, *Angewandte Chemie International Edition* **2015**, *54*, 13787-13791.
- [2] A. Stengl, M. Gerlach, M.-A. Kasper, C. P. R. Hackenberger, H. Leonhardt, D. Schumacher, J. Helma, *Organic & Biomolecular Chemistry* **2019**, *17*, 4964-4969.

### **4.3 Comparison of DNase I hypersensitive and insensitive chromatin in human cells by super-resolution microscopy and computer simulations**

Manuscript in preparation

## **Comparison of DNase I hypersensitive and insensitive chromatin in human cells by super-resolution microscopy and computer simulation**

Katharina Brandstetter<sup>1#</sup>, Tilo Zülske<sup>2#</sup>, Tobias Ragoczy<sup>3</sup>, David Hörl<sup>1</sup>, John Stamatoyannopoulos<sup>3,4</sup>, Heinrich Leonhardt<sup>1</sup>, Gero Wedemann<sup>2\*</sup>, Hartmann Harz<sup>1\*</sup>

<sup>1</sup> Human Biology & BioImaging, Faculty of Biology, Ludwig-Maximilians Universität München, Germany

<sup>2</sup> Institute for Applied Computer Science, Hochschule Stralsund, Germany

<sup>3</sup> Altius Institute for Biomedical Research, Seattle, WA, 98121, USA

<sup>4</sup> Departments of Genome Sciences and Medicine, University of Washington, Seattle, WA

# equal contribution

\* corresponding authors

### **Abstract**

Methodological advances in conformation capture techniques have fundamentally changed our understanding of chromatin architecture. However, the fine structure of chromatin and its cell-to-cell variance are less studied. By using a combination of high throughput super resolution microscopy and coarse-grained modelling we investigated properties of active and inactive chromatin in interphase nuclei. Using DNase I hypersensitivity as a criterion, we have selected prototypic active and inactive regions from ENCODE data that are representative for K562 and more than 150 other cell types. By using oligoFISH and automated STED microscopy we systematically measured physical distances of 5kb DNA stretches in both regions. These measurements result in highly resolved distance distributions which are skewed and range from very compact to almost elongated configurations of more than 200 nm length for both the active and inactive region. Coarse-grained modelling of the respective DNA stretches suggests that in regions with high DNase I hypersensitivity cell-to-cell differences in nucleosome density determine the histogram shape. Simulations of the inactive region cannot sufficiently describe the compaction measured by microscopy, although internucleosomal interactions were elevated and when the linker histone H1 was included in the model. At the same time the skewness of the microscopy-based distance distribution indicates high cell-to-cell differences also in inactive chromatin regions. Our data suggest that direct enhancer-promoter contacts, which most models of enhancer action assume, happen for proximal regulatory elements in a probabilistic manner due to chromatin flexibility.

### **Keywords**

Chromatin structure, fluorescence in situ hybridization, STED microscopy, coarse-grained modeling, nucleosome occupancy, DNase I hypersensitivity

### **Background**

For almost one hundred years it has been known that interphase chromatin can be distinguished by means of light microscopy into less dense euchromatin and denser packed heterochromatin (Heitz, 1928b; Trojer and Reinberg, 2007). Later it became clear that nucleosomes are the basic building blocks organizing DNA packaging and are therefore central to the organization of chromatin density (Kornberg, 1974). Groundbreaking electron microscopic studies showed the tight interaction between nucleosomes and DNA forming an 11 nm thick fiber (Luger et al., 1997; Olins and Olins, 1974). Recent work reveals a more random, heterogeneous structure of chromatin (Maeshima et al., 2019; Mirny, 2011). This view is supported by electron microscopic studies and super resolution fluorescence microscopy that show interphase chromatin to be organized in a flexible and disordered structure where regions with higher nucleosome density are interspersed with nucleosome depleted regions (Fussner et al., 2012; Konig et al., 2007; Ou et al., 2017; Ricci et al., 2015).

The landscape of chromatin states is much more diverse than the originally described eu- and heterochromatin suggest. By analyzing genome-wide distribution patterns of chromatin associated proteins, posttranslational histone modifications and DNase I hypersensitivity with algorithms like ChromHMM and Segway, up to 51 chromatin classes were proposed (Consortium, 2012; Ernst and Kellis, 2010; Ernst et al., 2011; Fillion et al., 2010; Hoffman et al., 2012; Hoffman et al., 2013; Ram et al., 2011). DNase I hypersensitivity (DHS) is a criterion that can also be used alone to subdivide chromatin in regulatory or active DNA with high DHS as opposed to inactive regions with low DHS.

Posttranslational histone modifications of the active chromatin classes, like acetylation, usually reduce nucleosome interaction and thus produce an open, less densely packed chromatin (Görisch et al., 2005; Moller et al., 2019; Nozaki et al., 2017; Zhang et al., 2017). Inactive classes are often characterized by methylation marks on histone 3 (H3K9me2/3), which can be bound by the heterochromatic protein 1 (HP1), thereby compacting chromatin (Allshire and Madhani, 2018). However, large parts of inactive and more densely packed chromatin do not carry significant amounts of posttranslational histone modifications (Ernst and Kellis, 2010). Other mechanism must therefore be responsible for compaction.

A remarkable feature of chromatin is its dynamic and fluid nature which has been observed in several fluorescence imaging studies (Chen et al., 2013; Germier et al., 2017; Gu et al., 2018; Hajjoul et al., 2013; Heun et al., 2001; Levi et al., 2005; Lucas et al., 2014; Ma et al., 2019; Marshall et al., 1997; Shaban et al., 2018; Zidovska et al., 2013) and is the reason for the large cell-to-cell variability in the structure of chromatin domains (Bintu et al., 2018). Changes in nucleosome occupancy are actively regulated and can drastically affect the 3D genome architecture as it has been shown e.g. by the effects of tumor necrosis factor alpha on human endothelial cells (Diermeier et al., 2014). Even at the level of single nucleosomes a significant and dynamic cell-to-cell variability can be found (Lai et al., 2018). The recently developed Fiber-seq method reveals that regulatory elements are actuated in an all-or-none fashion, thereby replacing a canonical nucleosome (Stergachis et al., 2020). In addition to pioneer transcription factors some chromatin remodelers are known to exhibit nucleosome eviction activity (Becker and Workman, 2013; Dultz et al., 2018; Hargreaves and Crabtree, 2011). Together these examples show that, depending on the regulatory context, the number and exact position of nucleosomes in active chromatin of eukaryotes can dynamically change.

Computational studies show a close link between nucleosome positions and the spatial structure of chromatin (Parmar and Padinhateeri, 2020) which was explored by applying coarse-grained computer simulations by many groups (e.g. Clauvelin et al., 2015; Collepardo-Guevara and Schlick, 2014; Nordenskiöld et al., 2017). These studies demonstrate, for example, that different repeat lengths are responsible for more open or closed chromatin configurations (Kepper et al., 2008). Moving even only a single nucleosome can strongly influence the spatial structure (Muller et al.,

## RESULTS

---

2014). Thus, including the real length of the linker DNA into coarse-grained models is required to obtain realistic results (Muller et al., 2014).

In our research, we investigated structural differences between FISH-labeled active and inactive 5 kb chromatin stretches of prototypical chromatin regions, selected on the basis of the presence or absence of DNase I hypersensitivity. By measuring the distance between labeled endpoints with systematic 3D STED microscopy and comparing this data with coarse-grained Monte Carlo simulations (Muller et al., 2014; Stehr et al., 2008b) we aimed to find underlying organizational principles. In active chromatin simulated data match the microscopic data well, assuming cell-to-cell variability in nucleosomal density. For inactive chromatin, the fit between model and microscopic measurements was generally lower, indicating additional compaction mechanisms that act in parallel to increased internucleosomal energy and the presence of the linker histone H1. Regardless of whether chromatin is active or inactive, our results reveal two striking features for 5 kb segments: (i) all distance distributions are skewed indicating an underlying cell-to-cell variance in chromatin organization, (ii) distributions cover a wide range of distances from less than 50 nm to more than 200 nm.

### Results

Chromatin organization of active and inactive chromatin was analyzed in K-562 cells using systematic super-resolution microscopy of DNA sequences labeled with directly labeled oligoFISH probes and comparison with simulated 3D chromatin configurations generated by a coarse-grained model. The K-562 cell line is well suited for computer simulations as a wealth of information like genome-wide ChIP-seq data, comprehensive maps of posttranslational nucleosome modifications and nucleosome positioning generated by the ENCODE project are available (Consortium, 2012; Davis et al., 2018).

#### STED microscopy is useful to research prototypic chromatin regions in the kb range

By using data from the ENCODE project we selected a 20 kb region on chromosome 11 (hg19, chr11: 118955404 - 118977871) which exhibits very high hypersensitivity to DNase I in not only K-562, but also more than 150 other cell types. Moreover, this region is flanked up- and downstream by highly active chromatin (Fig. 1 a). For inactive chromatin the selection criteria were analogous: missing DNase I hypersensitivity over 30 kb in 651 investigated cell types with over 2 Mb without DHS in K-562 cells (Fig. 1 b). The selected 20 kb inactive region is also located on chromosome 11 (hg19, chr11: 55580425 - 55603312). For each of these 20 kb regions 5 oligoFISH probe sets (A, B, C, D, E; Fig. 1 a,b) were designed, dividing the 20 kb into four approximately 5 kb long stretches from midpoint to midpoint of the respective probe set (probe set combinations: AB, BC, CD, DE). Each oligoFISH probe set consisted of 30 oligonucleotides (directly fluorescently labeled 40mers) covering a region of about 1.5 - 2 kb (Fig. 1 a, b, Supplementary Table 1). These small genomic distances are expected to result in spatial distances falling below the resolution limit of light microscopy (Mateo et al.,

2019) which is about 250 nm in the x- and y- dimensions and more than 500 nm in z (Sahl et al., 2017). Two color super resolution 2D and 3D STED microscopy was employed to overcome this limitation. STED microscopy is not prone to any chromatic shift if (present case) the different fluorophores are depleted by the same doughnut (Göttfert et al., 2013). The two-color approach also allows the use of subpixel localization techniques to measure distances below the resolution limit of the STED microscope.

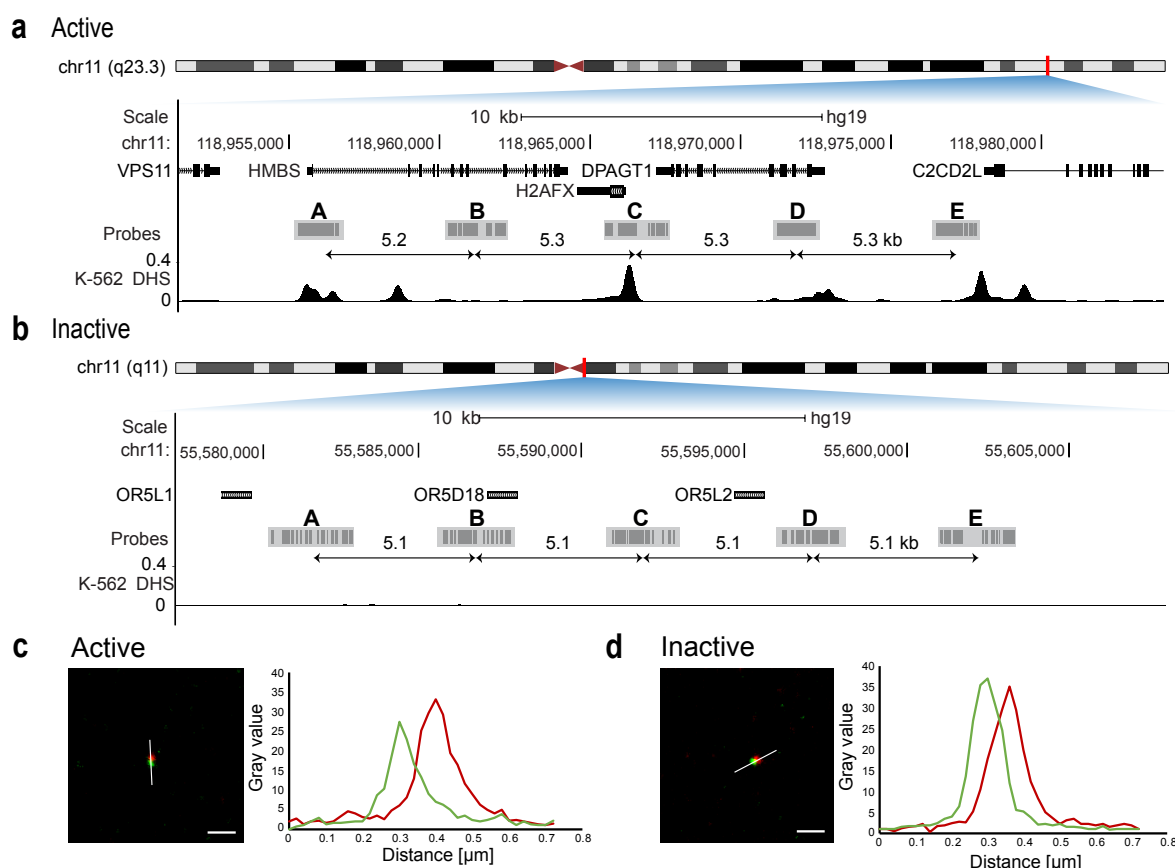


**Fig. 1: Properties of active and inactive region and FISH probe design.** Both regions are located on chromosome 11. (a) The active region contains genes HMBS, H2AFX and DPAGT1. The probe sets are almost equally spaced (5.2, 5.3, 5.3, 5.3 kb midpoint to midpoint) and mostly cover DNase I hypersensitive sites. (b) The inactive region contains genes for olfactory receptors. The region shows no DNase I hypersensitivity and the probe sets are equally spaced (5.1 kb midpoint to midpoint). (c, d) Example images show STED detail images of FISH spots in two colors for active (c) and inactive (d). Measured distance of these shown spot pairs represents the mean of the population. Plots depict intensity values for both colors along lines of interest (white lines). Scale bar = 500 nm

### Inactive regions are more compact than active regions

Recent studies reveal a high cell-to-cell variance of the spatial genome organization (Ashwin et al., 2020; Finn et al., 2019; Funke et al., 2016). To study the chosen regions, we applied high throughput 2D STED microscopy to generate data with high statistical power characterizing the folding of 5 kb stretches of active and inactive chromatin. For each of the 8 investigated 5 kb stretches between 484 and 1621 single cell measurements were analyzed. The median projected distance between two FISH spots flanking a typical 5 kb interval of active chromatin is 82 nm (Fig. 2 a), and 55 nm in

## RESULTS

inactive chromatin (Fig. 2 b). Shorter double spot distances indicate a higher degree of chromatin compaction whereas larger distances suggest less compaction. Thus, data of the current measurement are in line with published data showing active chromatin to be less compacted compared to inactive chromatin (Boettiger et al., 2016). As expected, the distributions of the FISH spot distances of active and inactive chromatin differ significantly as shown in a cumulative distribution plot (Fig. 2 c,  $p < 2 \times 10^{-16}$ ).

The four measured intervals in the active chromatin region differ from one another. We found some significant deviations with the maximum difference in the median projected distance of 16 nm ( $p < 0.0001$ , CD versus DE) (Fig. 2a, Supplementary Table). In active chromatin, folding variability is expected since each 5 kb segment is composed of different proportions of exons, introns, enhancers and other regulatory sequences. Surprisingly, we also found highly significant differences between the investigated intervals in inactive chromatin. We expected much less difference in compaction because inactive chromatin is expected to be more uniform as it does not harbor active regulatory elements and nucleosome occupancy is not modified by transcriptional activity (Fig. 2b, Supplementary Fig. 1). The maximum difference in the median projected distance was 12 nm within the inactive chromatin group ( $p < 0.0001$ , AB versus DE, Supplementary Table).

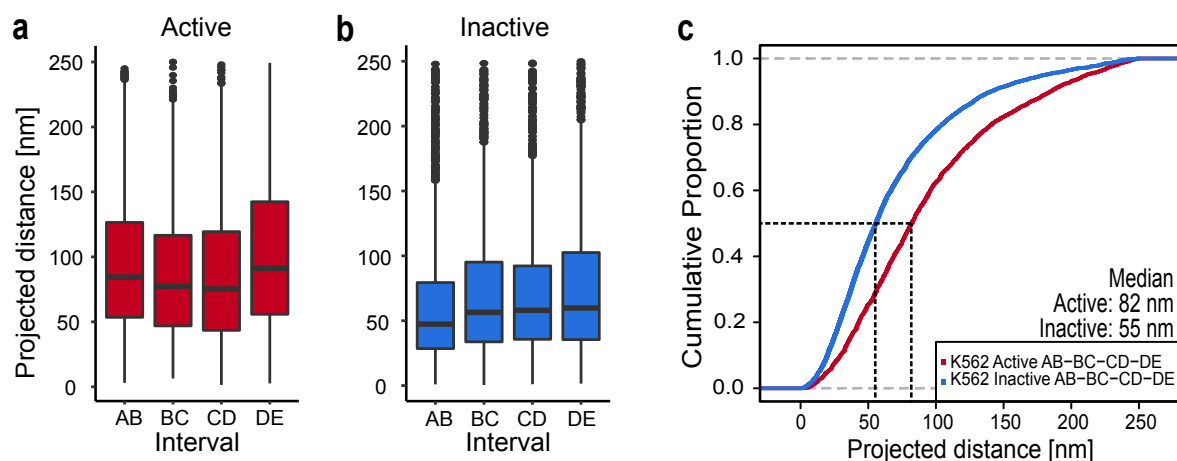


**Fig. 2: 2D STED distance measurements showed that the inactive region is more compact than the active region (a) Boxplot for the active region for all four measured intervals (AB:  $n=672$ , BC:  $n=540$ , CD:  $n=484$ , DE:  $n=566$ ,  $n$ =single-cell measurements from three independent replicates). (b) Boxplot for the inactive region for all four measured intervals (AB:  $n=1585$ , BC:  $n=1621$ , CD:  $n=1200$ , DE:  $n=1395$ ,  $n$ =single-cell measurements from three independent replicates). (c) Cumulative distribution of measured distances showed differences in distributions between active (red) and inactive (blue) region. The curves showed measured projected distances for all four intervals for active and inactive. The median is the value at the 50 % proportion (black dashed line). For the active region the median is 82 nm, for the inactive region it is 55 nm.**

For a more in-depth analysis we selected two regions each of the active and inactive sets which are representative of the respective group in 2D STED measurements. We chose interval AB for the active region and CD for the inactive region (Fig. 2 a, b).

### Assigning the input parameter for coarse-grained modeling

The exact position of nucleosomes is an important input parameter for coarse-grained models and strongly affects simulated structures (Muller et al., 2014). Nucleosomal positioning can be determined by micrococcal nuclease digestion followed by deep sequencing (MNase-seq) (Cui and Zhao, 2012). Here we used ENCODE MNase-seq tracks of K-562 cells which are derived from cell populations and therefore often show a seemingly overlapping nucleosome pattern (UCSC Accession: wgEncodeEH000921, GEO Accession: GSM920557). These data are unsuitable for our coarse-grained model, as it requires non-overlapping unique nucleosome positions as input. Therefore, we computed the most probable non-overlapping nucleosome populations by applying the NucPosSimulator (Schopflin et al., 2013). Experimentally derived nucleosome occupancy and computed most probable nucleosome positions of active region AB and inactive region CD are shown in Fig. 3 a and b. Nucleosome positions of the respective flanking regions can be found in Supplementary Fig. 2. For the nucleosomal repeat length (NRL) of chromosome 11 we calculated a mean value of 183.4 +/- 66.3 bp applying NucPosSimulator (Fig. 3 c). The mean NRL of the in detail studied active (AB) and inactive (CD) region is 179,6 bp and 179,1 bp, respectively (Fig. 3 d). Both values are in the range of the NRL of chromosome 11.

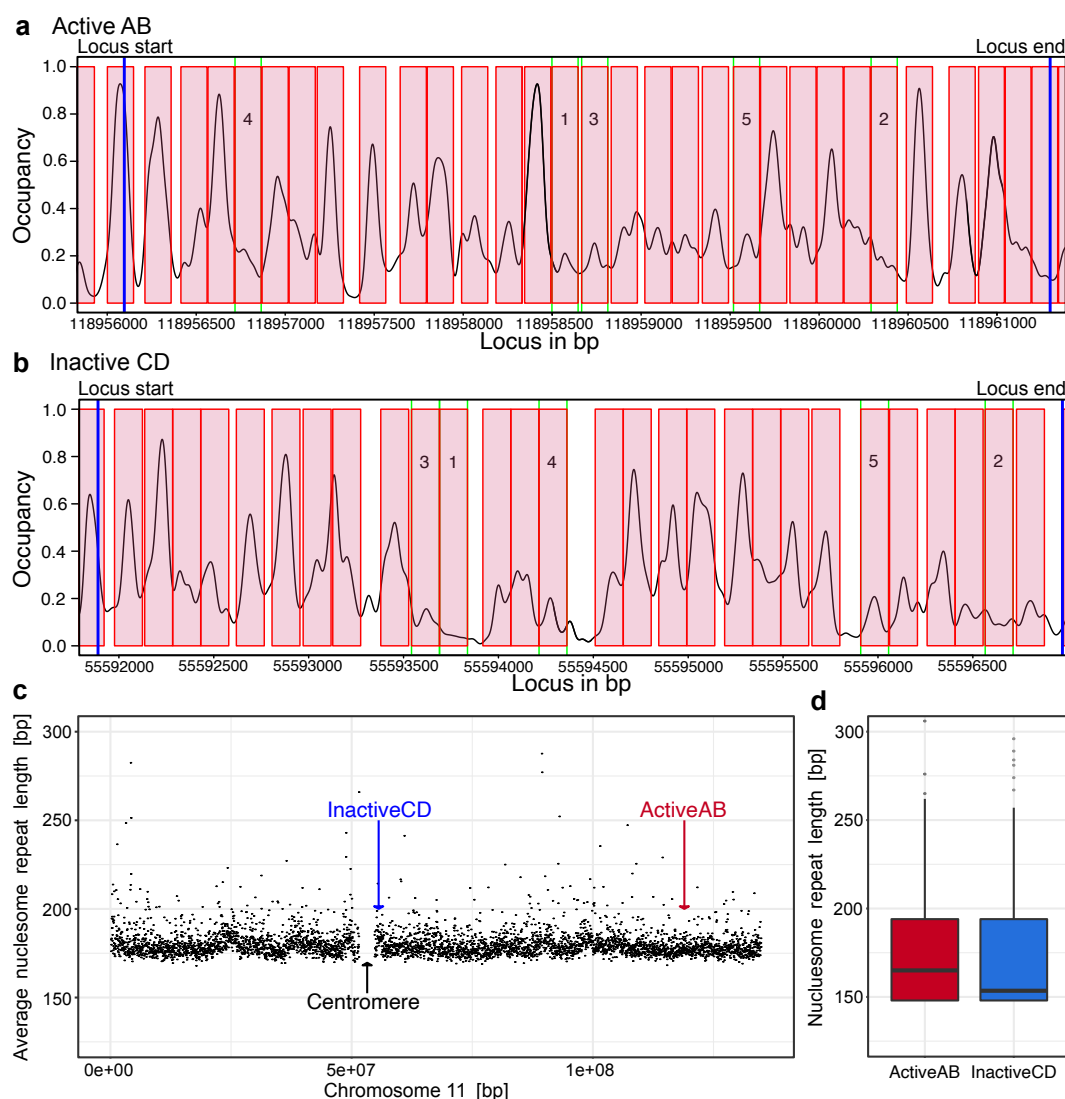


**Fig. 3: Nucleosome positions and nucleosome repeat length were calculated using the NucPosSimulator.** Nucleosome positions (red boxes) for Active AB (a) and Inactive CD (b) based on MNase-seq occupancy tracks (black line). Blue lines indicate start and end of the investigated loci. (c) Mean values of the NRL of a sliding window of the size 30000 bp. Values larger than 500 and windows with fewer than 3 nucleosomes were omitted. The mean NRL for chromosome 11 was 183,4 +/- 66.3 bp. (d) Investigated active and inactive regions as marked in the plot (arrows in c) are 179,6 bp and 179,1 bp, respectively.

The internucleosomal energy is another important parameter in all coarse-grained models and depends on the solvent (Mangenot et al., 2002) and histone modification (Funke et al., 2016). Literature values for this energy range from 3 to 10 kT (Funke et al., 2016; Kepper et al., 2011; Norouzi and Zhurkin, 2018). Nucleosomes containing unmodified histones have a higher interaction energy, whereas modifications like acetylation weaken internucleosomal interactions (Funke et al., 2016). Since the inactive chromatin examined here does not exhibit significant histone modifications, we have used a value from the upper range of the literature values (8 kT) to simulate this chromatin type. Conversely, the active region features many posttranslational histone modifications (Supplementary Fig. 1 b), and we thus used half the energy (4 kT) to compute the respective structures.

#### **The nucleosome density varies from cell to cell in active chromatin**

Microscopic data shown so far are 2D data which underestimate the real 3D distances between the FISH spots since the cells are rotated randomly relative to the optical axis of the microscope. Only 3D single-cell microscopy allows the study of real distances between two spots on a single-cell level and to compare data between microscopy and simulation. Therefore, we performed 3D STED measurements which require careful correction for refractive index mismatch between immersion fluid of the objective lens and the embedding medium (see Materials and Methods). The 3D microscopy data of all segments are shown in Supplementary Fig. 3.

The 3D STED measurements for the 5 kb AB interval in the active chromatin region revealed distances ranging from < 50 nm to 250 nm with a mean distance of 115 nm (n= 762, Fig. 4 a). Remarkably, in active chromatin elongated configurations can be found which results in a skewed distribution of the microscopic distance measurements. To understand this phenomenon better we performed coarse-grained computer modelling of the nucleosome chain. The most probable nucleosome position calculated by the NucPosSimulator from MNase-seq data was used by our coarse-grained model that included elastic, electrostatic properties and excluded volume effects to compute a statistically relevant ensemble of 172 statistically independent 3D conformations of the nucleosome chain in the active region. In order to compare the simulated data with the microscopic data, the distances between the simulated sequence segments which correspond to those of the microscopic measurements were determined. In this way, a distance histogram was generated from the simulated data, which can be directly compared to the microscopic data (Fig. 4 b-g). The computed distributions were narrower, and the mean distance was about a standard deviation shorter than the microscopically measured distribution (Fig. 4 b).

We hypothesized that in the microscopy experiment we do not have chromatin with all nucleosomes bound, but a mixture of configurations with numbers of nucleosomes that differ from cell-to-cell. This hypothesis was tested by computer simulations, where the least probable nucleosomes were removed. To find the weakest bound nucleosomes, we analyzed the mean value from the occupancy data calculated by NucPosSimulator (cf. Supplementary for details). Next, we computed statistically relevant ensembles of 3D structures by replacing the weakest nucleosome by naked DNA (-1, Fig. 4 c). The same was done by replacing two (Fig. 4 d), three (Fig. 4 e), four (Fig. 4 f) and five (Fig. 4 g) nucleosomes according to their rank order of binding strength. Indeed, a reduction of the total nucleosome number resulted in increasingly larger mean distances, but none of the individual distributions were comparable with the microscopically measured distribution. By applying a least square fit (see Materials and Methods), the different distance distributions were combined and resulted in a mixed distance histogram that mimics the histogram based on microscopic data (Fig. 4 h). Example images show that both fibers with all nucleosomes and with a reduced nucleosome number (-5) can have short and long end-to-end distances (Fig. 4 i, j).

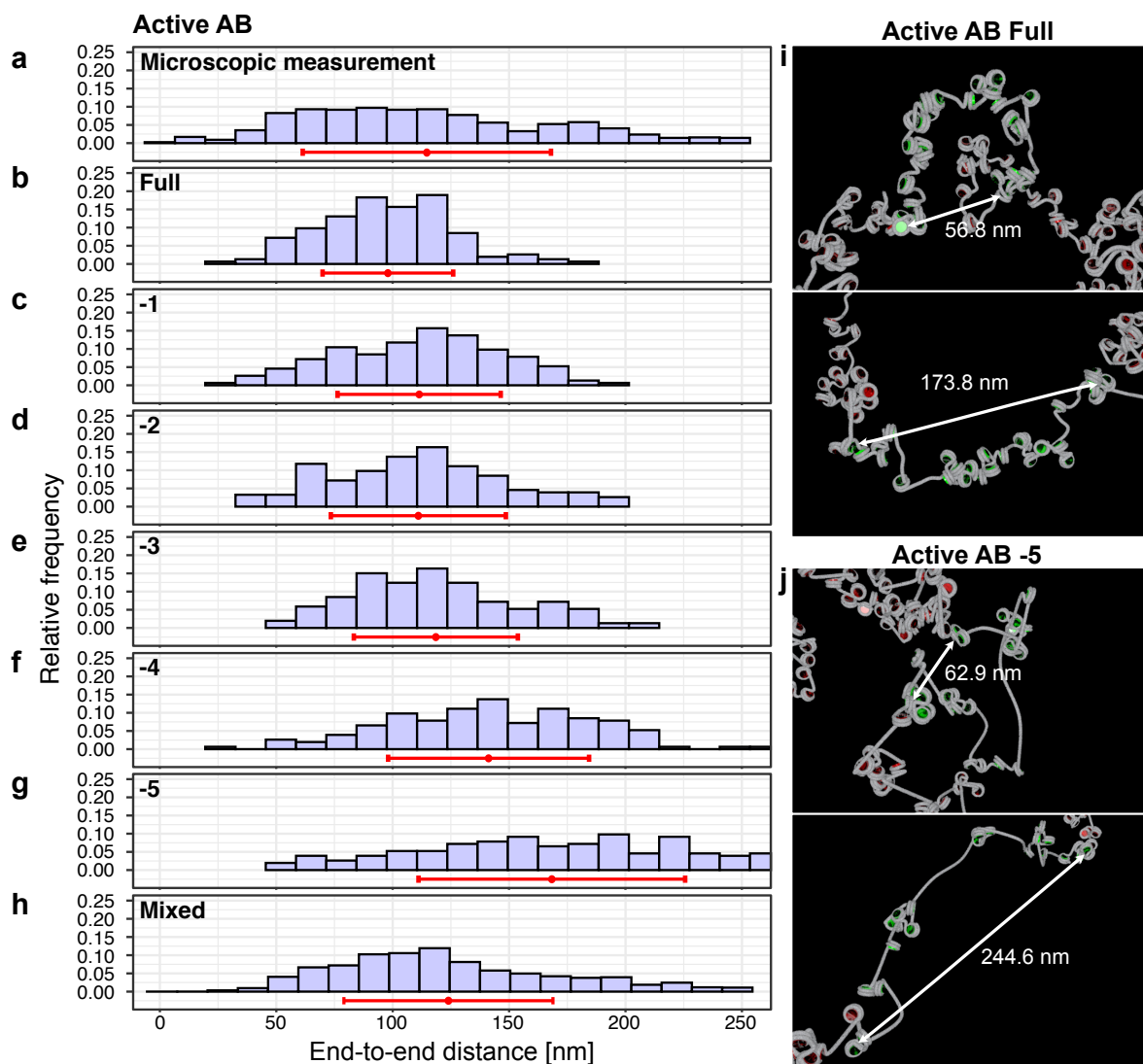


**Fig. 4: Distance distributions from microscopic experiments and from computer simulations of the active region.** (a) 3D STED measurements of active AB result in a distance distribution ranging from < 50 nm to 250 nm with a mean of 115 nm  $\pm$  53 nm (n= 762 single-cell measurements from three independent replicates). (b-h) For computer simulations results are shown for the region active AB with all nucleosomes (Full) (b), with 1 to 5 nucleosomes replaced by naked DNA (c-g) and a combined plot (h). Mean value (red dot) and standard deviation (red line) are shown for each distribution. In the combined plot (h) the distributions have the weight 0.38, 0.00, 0.14, 0.00, 0.13, 0.24 (from all nucleosomes to -5 nucleosomes). (i-j) Example images of simulated chromatin fibers for active region AB (green nucleosomes) with all nucleosomes (i) and with 5 nucleosomes less (j) and the adjacent areas (red nucleosomes). The upper image in (i) and (j) shows a configuration resulting in a short end-to-end distance indicated by a white arrow, the lower image depicts a large end-to-end distance. Simulated chromatin structures show local accumulations of a few nucleosomes connected by stretches with low nucleosome occupancy. These structures are remarkably similar to recently published light and electron microscopic data of interphase chromatin (Ou et al., 2017; Ricci et al., 2015).

### An inactive region is compacted by different mechanisms

3D-STED distance histograms of the inactive region CD were compared with simulated data by the same strategy as above. The comparison showed that the computed mean distance was ~40 nm larger than the microscopically measured one when an attractive internucleosomal energy of 4 kT was used for the (Fig. 5). As argued earlier, an increase of the interaction energy to 8 kT seems to be more realistic for simulating inactive chromatin. However, this approach delivered structures with the mean value of the simulated distance distribution that are only a few nm shorter (Fig. 5). Obviously, additional mechanisms compact the inactive chromatin of the investigated region.

ENCODE data show no pronounced histone modifications or repetitive DNA sequences in the inactive region CD, which makes chromatin compaction by binding of Polycomb group proteins or heterochromatinization unlikely. Therefore, other mechanisms must be considered, such as the binding of linker histone 1 (H1), which has long been known to have a chromatin-compacting effect (Van Holde, 1989). H1 is included in the computer model by different angles of the attached linker DNA at the nucleosomes (Kepper et al., 2008). These angles were derived by a systematic analysis of data from reconstituted fibers (Stehr et al., 2010). It can be expected that details of the angles vary since the chicken linker histone H5, for example, causes different angles than H1 (Stehr et al., 2010). However, all variants of H1 lead to higher chromatin compaction.

In fact, simulations with a H1 to nucleosome ratio of 1:1 led to more compact structures. This effect is especially pronounced at 4 kT and weaker in simulations using a maximal internucleosomal attraction energy of 8 kT (Fig. 5 d,e). To explore the effects of different stoichiometry of H1 we performed computer simulations of a random 50% nucleosome binding. The width of the length distribution is widened only by a small amount (Fig. 5f).

In summary, the efforts to shift the distance distribution to short values were partially successful. Larger distances as found in microscopic measurements might be caused by evicted nucleosomes as in active regions.

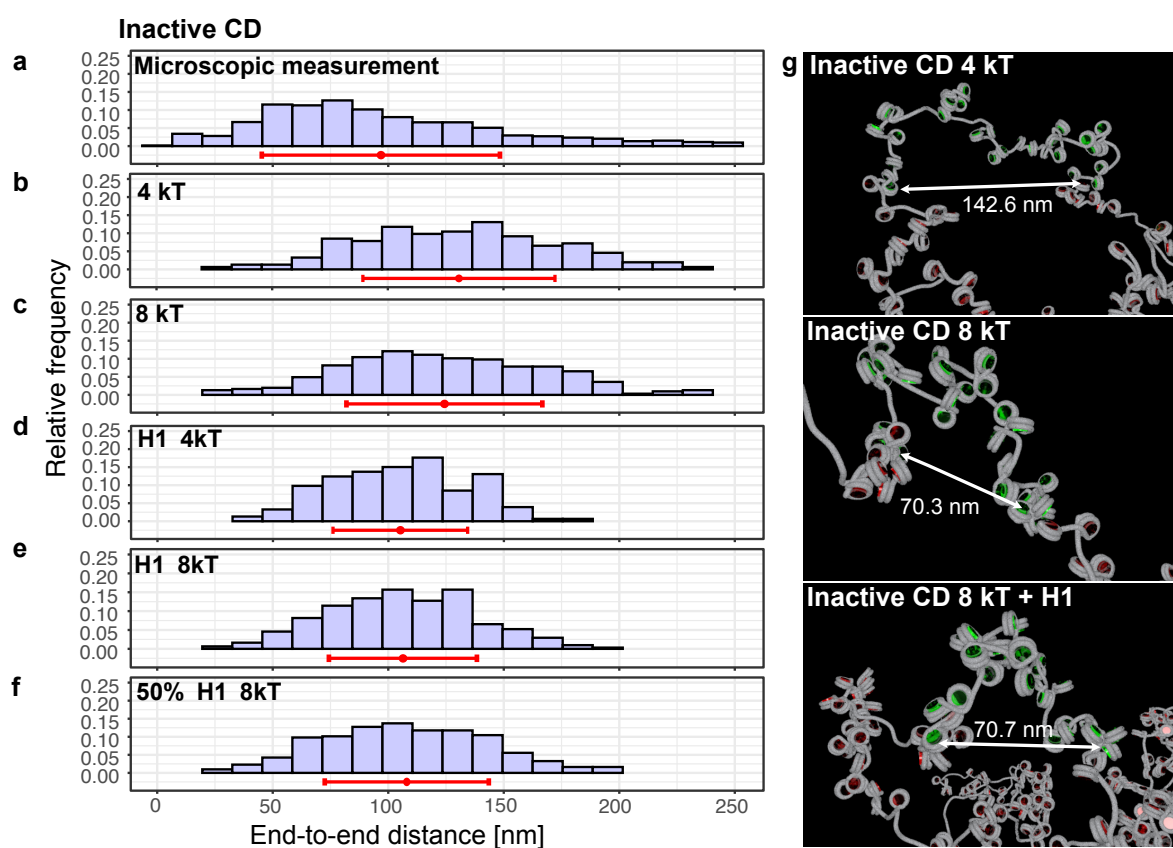


**Fig. 5: Distance distributions from microscopic experiments and from computer simulations of the inactive region.** (a) 3D STED measurement of inactive CD results in a skewed distance distribution with the mass of the distribution towards shorter distances and a mean of  $97 \text{ nm} \pm 52 \text{ nm}$  ( $n=1320$  single-cell measurements from three independent replicates). (b-f) Computed distance distributions with different maximal internucleosomal interactions (4 kT (b, d) and 8 kT (c, e, f)), with (d, e) or without (b, c) linker histone H1 and a random distribution of binding of 50% H1 (f). Mean value (red dot) and standard deviation (red line) are shown for each distribution.

## Discussion

By using high-throughput super-resolution microscopy, we studied the conformation of 5 kb chromatin stretches which are located in active and inactive chromatin. The selected areas are prototypic for the respective chromatin class because patterns of prominent or absent DHS spreads over hundreds of kb around the selected region and can be found in more than 150 cell types. Considering the great similarity within the four active and four inactive intervals studied here, it can be assumed that the structural principles described apply to significant parts of the genome.

In both active and inactive chromatin, 3D spatial distances between the endpoints of the 5 kb segments differ from cell to cell resulting in a broad right-skewed distance distribution with the mass of the distribution shifted more to shorter values in inactive chromatin. In contrast, simulations with different nucleosome occupancies, changed internucleosomal energies or deviations from stoichiometric H1 binding led to far narrower distance distributions. Therefore,

the large width of the distance distribution seems to be a feature that is caused by the summation of cell-to-cell differences in the resulting histogram.

Unexpectedly, we found in both active and inactive chromatin very elongated chromatin configurations with 5 kb exhibiting lengths of over 200 nm. For comparison, a stretched beads-on-a-string chromatin fiber of 5 kb has a length of 243 nm (Carlson and Olins, 1976). In simulations with our coarse-grained model elongated chromatin configurations are more probable if a number of nucleosomes is replaced by naked DNA. Therefore, it is important to investigate which nucleosomes have the weakest occupancy in our model. Indeed, 8 of the 10 most weakly bound nucleosomes in the active region are localized within DHSs (Supplementary Fig. 2 a), a result that is consistent with genome-wide measurements (Stergachis et al., 2020).

The perspective of cell-to-cell differences in nucleosome density in active DNA is supported by different lines of evidence: (i) while at certain positions nucleosomes seem to be positioned with high precision (Baldi et al., 2020), generally nucleosome positions can vary substantially from cell to cell (Schopflin et al., 2013), (ii) transcription factors compete cooperatively with nucleosomes for access to DNA (Mirny, 2010; Svaren et al., 1994), (iii) pioneer transcription factors and chromatin remodeling complexes can change nucleosome occupancy (Zaret, 2020), (iv) DNase I footprinting shows that a regulatory site is about 200 bp in length with typically 5-6 directly bound transcription factors which fits well to DNA length occupied by a single nucleosome (Vierstra et al., 2020), (v) regulatory elements are actuated in an all-or-none fashion and replace thereby a canonical nucleosome (Stergachis et al., 2020), (vi) upregulation of genes is known to reduce the number of bound nucleosomes (Diermeier et al., 2014).

In our simulation DNA stretches without nucleosomes are handled as linker DNA with the respective elastic and electrostatic properties. However, in a physiological context evicted nucleosomes could be replaced by transcription factors as outlined above. Crystal structures show that many TFs do not bend DNA, which also applies to members of the large family of TFs with a C<sub>2</sub>H<sub>2</sub> zinc finger motive (Panne et al., 2007; Kim and Berg, 1996; Pavletich and Pabo, 1991). This supports the conclusion that the replacement of nucleosomes by transcription factors may lead to an elongation of the DNA structure.

As described earlier, the microscopic measurements of inactive chromatin reveal a compaction that can be partially explained by an increase in the strength of internucleosomal interactions or by the additional introduction of the linker histone H1. Given the vast number of variables and mechanisms affecting chromatin structure it is difficult to confidently identify further mechanisms of compaction. We speculate that the density of the surrounding chromatin that has not been taken into account in this study and by others may play a role. Microscopic measurements show that the inactive region investigated here is expected to be embedded in a more compact chromatin environment (Supplementary Fig. 4). Indeed, preliminary modeling approaches reveal that the environment has a large influence on chromatin packing density. This mechanism might be particularly important for the inactive chromatin under investigation here,

which lacks significant amounts of posttranslational histone modifications and therefore the measured compaction cannot be explained by heterochromatinization by HP1 or Polycomb protein repression.

Microscopic data of the inactive region also exhibits elongated chromatin configurations (>200 nm) which can be best explained in our model by a reduced nucleosome density varying from cell to cell. In fact, the data shown in Fig. 3 b support this hypothesis as weakly bound nucleosomes also exist in inactive chromatin and could therefore explain not only the elongated configurations but also the wide distance distribution. Nucleosome eviction is only well studied in active chromatin regions, but the results shown here suggest that the phenomenon could also occur in inactive chromatin. The underlying mechanisms are certainly quite different from those in active chromatin. However, our interpretation of the data is that even inactive chromatin is subject to continuous reorganization.

An extensive body of literature (for review, see Schoenfelder and Fraser (2019)) on chromatin architecture focuses on the formation of chromatin loops bringing regulatory elements into close contact and thus regulating gene expression. Distances below which an enhancer is thought to activate a promoter range from less than 150 nm (Mateo et al., 2019) to 300 nm (Chen et al., 2018b). Here we show by high-throughput microscopy of human chromatin that on average more than 52.5 % of the 5 kb endpoints will approach to less than 100 nm (value derived from data of Fig. 4 a (Active: 45%) and Fig. 5 a (Inactive: 60%)). Interestingly, also inactive chromatin that does not have any active binding sites for regulatory factors shows significant incidents of end-to-end contacts. Apparently, thermodynamically driven spontaneous movements can bring regulatory elements into close contact with their promoters that are only a few kb distant from one another. Considering that 142,000 proximal enhancer-like elements can be found in the human genome at a distance of less than 2 kb (Moore et al., 2020), these spontaneous movements of chromatin could significantly influence gene regulation.

## Material & Methods

**Cell culture of K-562 cells.** Human erythroleukemia K-562 cells were grown in RPMI-1640 medium (Sigma) supplemented with 10% FBS (Sigma) and 1% v/v penicillin/streptomycin (Sigma) in cell culture flasks. Cells were cultured at 37°C in 5% CO<sub>2</sub> and regularly tested for mycoplasma contamination.

**oligoFISH probes.** Details of oligo probe design and sample preparation are part of a pending publication of the Altius Institute, Seattle, USA.

**Selection criteria for regions used in this study.** The regions that were used to study chromatin states were chosen upon different criteria. The inactive and active region were characterized in an unbiased way depending on their DNase I hypersensitivity and not depending on the genes within the regions. Therefore, regions that show DNase I hypersensitivity signals that are typical for a lot of different cell types were chosen. The regions were universally active (over 150 cell types) or universally inactive (651 cell types without DHS in over 30 kb, K-562 cells without DHS in hundreds of kb) in different cell types. Both the region itself and the flanking regions showed a similar

## RESULTS

---

strength of DNase I hypersensitivity signal. In addition, the probe sets were spaced approximately 5 kb (midpoint to midpoint) from each other and, for the active region, were mostly placed on DHS peaks.

**Sample preparation for FISH and SiR-DNA staining.** Samples were prepared the same way as for two color FISH. In this case only one probe pool (B for active and inactive region) with an Atto-594 dye label was used for hybridization. Instead of DAPI counterstaining, the samples were stained in 2.5  $\mu\text{M}$  SiR-DNA in 2x SSC for 1 h in a humid chamber. Subsequently, slides were washed two times with 2x SSC for 5 minutes. Coverslips were mounted on microscopic slides with MOWIOL (2.5 % DABCO, pH 7.0), dried for 30 min and sealed with nail polish.

**STED microscopy for FISH two color imaging.** Image acquisitions were carried out on a 3D STED microscope system from Abberior Instruments equipped with two pulsed excitation lasers (594, 0.3 mW and 640 nm, 1.2 mW), one pulsed depletion laser (775 nm, 1.2 W) and Avalanche photodiodes for detection. A 100x UPlanSApo 1.4 NA oil immersion objective (Olympus) was used for all acquisitions.

The STED hardware was controlled with Python scripts by using the specpy interface to the microscope control software Inspector (versions 0.13 and 14.0, Abberior Instruments). To find oligoFISH spot pairs confocal dual color 50  $\mu\text{m}$  x 50  $\mu\text{m}$  x 5  $\mu\text{m}$  (for 2D and 3D acquisitions) volumes were acquired using 100  $\mu\text{m}$  pinhole, 150 nm pixel size, 250 nm z-steps, 10  $\mu\text{s}$  pixel dwell time, no line accumulation and excitation laser powers of 18.8% for 594 nm and 19.3 % for 640 nm. Confocal scans were investigated, points were detected with a Laplacian-of-Gaussian blob detector in both channels and nuclear regions exhibiting signals in both color channels no more than 5 pixels apart from one another were determined. At these points of interest, STED detail stacks (3  $\mu\text{m}$  x 3  $\mu\text{m}$  x 1.4  $\mu\text{m}$ ) were acquired. For 2D STED acquisitions, the spatial light modulator (SLM) was used to generate a 2D STED depletion pattern and stacks were acquired with 200 nm z steps, 7 planes, 20 nm pixel size, 10  $\mu\text{s}$  pixel dwell time, 5x line accumulation, 100  $\mu\text{m}$  pinhole, excitation laser power 53.5% for 594 nm, 53.5% for 640 nm and 29.6% for 775 nm depletion laser power. For 3D STED acquisitions, careful correction for refractive index mismatch between immersion fluid of the microscope objective and the cell is crucial. Therefore, immersion oil with a refractive index of 1.522 was used for 3D acquisitions. The SLM modulator was set to generate a 3D STED depletion pattern and stacks (3  $\mu\text{m}$  x 3  $\mu\text{m}$  x 1.5  $\mu\text{m}$ ) were imaged with 60 nm z steps, 25 planes, 45 nm pixel size, 10  $\mu\text{s}$  pixel dwell time, 5x line accumulation, 45  $\mu\text{m}$  pinhole, excitation laser power 53.5% for 594 nm, 53.5 % for 640 nm and 29.6% for 775 nm depletion laser power. The process was repeated for the next overview scan. The focus position was updated to the plane of maximum intensity in the previous overview image to allow for overnight imaging without focus loss. By moving the stage in x and y in a spiral pattern, overview scans followed by STED detail scans were acquired until a pre-set amount of time had passed.

**STED microscopy for FISH and SiR-DNA co-imaging.** Image acquisitions were carried out on a 3D STED microscope system from Abberior Instruments described above using a 100x UPlanSApo 1.4 NA oil immersion objective (Olympus). The STED hardware was controlled with Python scripts as described above. To find oligoFISH spots in 594 nm confocal dual color 50  $\mu\text{m}$  x 50  $\mu\text{m}$  x 7  $\mu\text{m}$  volumes were acquired using 100  $\mu\text{m}$  pinhole, 150 nm pixel size, 10  $\mu\text{s}$  pixel dwell time, no line accumulation and excitation laser powers of 18.8 % for 594 nm and 19.3 % for 640 nm. Confocal scans were investigated, points were detected with a Laplacian-of-Gaussian blob detector in the 594 nm channel. At these points of interest, STED detail stacks (3  $\mu\text{m}$  x 3  $\mu\text{m}$  x 7  $\mu\text{m}$ , 20 nm pixel size) were acquired using the 594 nm laser for excitation. To get the surrounding SiR-DNA signal a 15 x 15  $\mu\text{m}$  (30 nm pixel size, 1 plane) field of view was acquired around the same points of interest using the 640 nm laser. By moving the stage in x and y in a spiral pattern,

overview scans followed by STED detail scans were acquired until a pre-set amount of time had passed.

**STED microscopy image analysis for FISH spot distances.** Though the automated data acquisition process produced large numbers of images, some of these were of insufficient quality for further analysis due to poor signal to noise ratio or spot detection only in one channel caused by premature bleaching or sample drift. Therefore, supervised machine learning was used as a quality control step to automatically classify STED stacks into ‘good’ or ‘bad’. An experienced scientist classified about more than two thousand sum projections of oligoFISH STED stacks as “analyzable data” or “not analyzable data”. Features extracted from the sum projections of his ground truth dataset were used to train a Random Forest classifier that could be used to automatically classify further acquisitions. All machine learning was done in Python using scikit-learn.

Detailed spot analysis was performed on the analyzable data to determine the coordinates of both FISH spots in their respective STED channels. The algorithm searched for the spot pair with the brightest signal and saved their subpixel coordinates for further statistical analysis. After a rough spot detection with a Laplacian-of-Gaussian blob detector, subpixel localization was performed by fitting a multidimensional Gaussian using the Levenberg-Marquardt algorithm. 3D coordinates were transformed into projected 2D coordinates by omitting the z coordinate.

**Chromatin environment of single FISH spots.** To determine the relative chromatin compaction at the FISH spot, a maximum z-projection of the FISH stack was overlaid onto the single SiR-DNA plane (scaled with bilinear interpolation to match pixel sizes). In the resulting images, the spot position and nuclear outlines were annotated by hand. To reduce out-of-focus signal, a rolling-ball (radius=50px) background subtraction was performed on the SiR channel. For each image, the quantile of the SiR intensity at the FISH spot location with respect to all pixels in the nuclear annotation (smoothed with a Gaussian blur with sigma=1px) was determined. The results were visualized as boxplots and statistical significance of differences between inactive and active loci was assessed via a two-sided Mann-Whitney U test.

**Properties and resolution of STED microscopy.** For Fig. 2 z-stacks with a spacing between planes of 200 nm were acquired using 2D STED. When using 2D STED only the x-, y- resolution is higher than the diffraction limit, in our case about 50 nm, but the z-resolution is identical to the resolution of a confocal microscope which is around 500 nm (Sahl et al., 2017). FISH spots were localized in these image stacks by fitting a 3D gaussian to the data. Under this condition the x-, y- localization is much more precise than the z- localization. Therefore, only the 2D information was used for data shown in Fig. 2. The measured projected distance is in most cases shorter than the true distance, since the projection equals only to the real distance if the spot pair is parallel to the projection plane.

When using 3D STED, the resolution increases in x, y and z is higher than the diffraction limit. Due to the distribution of depletion light in all three dimensions the resolution improvement in x and y is less compared to 2D STED and leads to a resolution of ~80 nm in x, y and z.

### 3D-Model

Since atomistic modelling of chains with many nucleosomes is not possible, coarse-grained models are widely used. We applied the simulation procedure as described in Müller et al. and we follow the description given there (Müller et al., 2014) and we follow the description given there (Müller et al., 2014). Chromatin is modeled as a chain of segments, in which spherocylindrical units describing the nucleosomes are connected by cylindrical segments describing the linker DNA. Each segment  $i$  possesses a position and a local coordinate system consisting of three

perpendicular unit vectors ( $\widehat{u}_i, \widehat{v}_i, \widehat{f}_i$ ) that describe its torsional orientation (Supplementary Figure 5). Vector  $\widehat{u}_i$  is parallel to the direction of the segment i.e., the vector  $\vec{s}_i$  from its position to the position of the next segment. The position of the center of the nucleosome and its orientation is computed from the center of the nucleosome segment by the length  $d$  and 6 angles describing the relative orientation (Supplementary Figure 6). Systems without linker histone and with linker histone differ by the set of angles (Stehr et al., 2010).

Derived from the positions of nucleosomes on the genome the linker DNA has different length. Therefore, the segments modelling the linker DNA needs to have different lengths. The number of base pairs of a linker length is converted to nanometers by multiplied by 0.34 nm/bp. Each linker DNA is modelled by at least 2 segments. If the linker length is larger than 20 nm the number of segments is calculated by (*rounding linker length/10nm*) up.

### Simulation protocol

A Monte Carlo (MC) algorithm was utilized to create a statistical relevant set of configurations satisfying the Boltzmann distribution (Metropolis et al., 1953). In order to overcome local energy minima (Stehr et al., 2008b) we applied a replica exchange procedure introduced by Swendsen and Wang (Swendsen and Wang, 1986). Here,  $M$  replicas of the system were simulated with Metropolis Monte Carlo simultaneously, each at a different temperature  $T_i$ . After a fixed number of MC simulation steps replicas with adjacent temperatures ( $T_i, T_{i+1}$ ) the temperature is swapped with the probability:

$$\min[1, \exp(-(\beta_i - \beta_{i+1})(E_{i+1} - E_i))], \quad (1)$$

with  $\beta_i = 1/(k_B T_i)$ ,  $k_B$  being the Boltzmann constant and  $E_i$  the energy of the system  $i$ . Before the simulations the set of temperatures was determined utilizing a feedback-optimized approach (Katzgraber et al., 2006). This algorithm optimizes the distribution of temperatures iteratively, such that the diffusion of replicas from the highest to the lowest temperature and vice versa is improved in each iteration. The procedure is more efficient by starting with system, that was pre-relaxed utilizing a simulated annealing approach (Stehr et al., 2008b).

### Elastic energies

Elastic interactions are modelled by harmonic potentials. The strength constants of the interactions are named  $a_{(Y)}^{(X)}$  where  $X$  denotes the type of interaction ( $s$ =stretching,  $b$ =bending,  $t$ =torsion) and  $Y$  the interaction partners (DNA or nucleosome). The energy for stretching is calculated by:

$$E_{stretch} = \frac{a_Y^{(s)}}{b_i^0} (b_i - b_i^0)^2, \quad (2)$$

where  $b_i$  is the current length and  $b_i^0$  is the equilibrium length of the segment. The bending energy is given by:

$$E_{bending} = \frac{a_Y^{(b)}}{b_i^0} \theta_i^2, \quad (3)$$

Where  $\theta_i$  is calculated from  $\cos(\theta_i) = \widehat{B}_i \widehat{u}_{i+1}$  with  $\widehat{B}_i$  being the equilibrium direction of the next segment and  $\widehat{u}_{i+1}$  its actual direction. The torsional energy is computed as:

$$E_{torsion} = \frac{a_i \gamma_i^{(t)}}{b_i} (\alpha_i + \gamma_i - \tau_i)^2, \quad (4)$$

Where angles  $\alpha_i$ , and  $\gamma_i$  are from Euler-transformation ( $\alpha_i, \beta_i, \gamma_i$ ) from the local coordinate system from segment  $i$  to segment  $i+1$ . The angle  $\tau_i$  is the intrinsic twist (Klenin et al., 1998).

### Internucleosomal interaction

The internucleosomal interaction is described by a shifted 12-6 Lennard-Jones potential

$$E_{internuc} = 4\varepsilon(\hat{\delta}_1, \hat{\delta}_2, \hat{r}) \left[ \left( \frac{\sigma_0}{|\hat{r}| - \sigma(\hat{\delta}_1, \hat{\delta}_2, \hat{r}) + \sigma_0} \right)^{12} - \left( \frac{\sigma_0}{|\hat{r}| - \sigma(\hat{\delta}_1, \hat{\delta}_2, \hat{r}) + \sigma_0} \right)^6 \right], \quad (5)$$

where  $\hat{\delta}_1$  and  $\hat{\delta}_2$  denote the orientation of the nucleosome and  $\hat{r}$  the distance between the centers of the nucleosomes. The shape of the nucleosome and the spatial dependency of the internucleosomal interaction strength is modelled by  $\varepsilon$  and  $\sigma$  depending of  $\hat{\delta}_1, \hat{\delta}_2$  and  $\hat{r}$ . This is implemented by a series expansion in S-functions (Zewdie, 1998):

$$\sigma(\hat{\delta}_1, \hat{\delta}_2, \hat{r}) = \sigma_0[\sigma_{000}S_{000} + \sigma_{cc2}(S_{202} + S_{022}) + \sigma_{220}S_{220} + \sigma_{222}S_{222} + \sigma_{224}S_{224}], \quad (6)$$

And

$$\varepsilon(\hat{\delta}_1, \hat{\delta}_2, \hat{r}) = \varepsilon[\varepsilon_{000}S_{000} + \varepsilon_{cc2}(S_{202} + S_{022}) + \varepsilon_{220}S_{220} + \varepsilon_{222}S_{222} + \varepsilon_{224}S_{224}], \quad (7)$$

The expansion coefficients were chosen to the dimensions a nucleosome and to achieve a ratio of interaction energies of 1/12 between side-by-side and top-on-top oriented nucleosomes. Further details on the energy terms are given in (Stehr et al., 2008b) and in the supplemental material of (Stehr et al., 2010). The influence of the nucleosome tails is included in the choice of the strength of  $\varepsilon$  (Stehr et al., 2008b).

### DNA-Nucleosome excluded volume

The volume of DNA segments is approximated by spheres. The minimal distance  $d$  between the center of DNA sphere and a spherocylinder describing the nucleosomes is computed. The excluded volume energies  $E_{DNA-Nuc}$  is described as the sum of the individual excluded volume energies  $E'_{DNA-Nuc}$  computed for DNA sphere and the volume of the nucleosome:

$$E'_{DNA-Nuc} = \begin{cases} 0 & \text{if } d \geq r_n + r_d \\ k(d - r_n - r_d)^{12} & \text{else} \end{cases}, \quad (8)$$

with  $r_n = (5.5/2)$  nm and  $r_d = 1.2$  nm.

### Electrostatic energy of linker DNA

A DNA segment is modelled by a chain of charged spheres. The GROMACS unit system was used which is based on nm, ps, K, electron charge (e) and atomic mass unit (u) (Hess et al., 2008).

The electrostatic energy of two spheres with charge  $q_1$  and  $q_2$  and radius  $a$  separated by a center-to-center distance  $r$  can be approximated by the electrostatic part of the Derjaguin-Landau-Verwey-Overbeek theory (Levin, 2002; Walker et al., 2011) as

$$E_{el}(r) = \frac{1}{4\pi\epsilon\epsilon_0} q_1 q_2 \left( \frac{e^{\kappa a}}{1 + \kappa a} \right)^2 \frac{e^{-\kappa r}}{r}, \quad (9)$$

## RESULTS

---

With  $\kappa$  being the inverse Debye length calculated by:

$$\kappa^2 = \frac{2e_c^2 \rho N_A}{\epsilon \epsilon_0 k_B T}, \quad (\text{I0})$$

For the values listed in Table S1  $\kappa$  yields  $\kappa = 1.0387 \text{ nm}^{-1}$  which corresponds to a Debye length of  $\lambda_D = \kappa^{-1} = 0.96 \text{ nm}$ .

The charge of a DNA segment is given by  $q = \nu d$ , with  $\nu$  being the nominal line charge density ( $-2/0.34 e_c \text{ nm}^{-1}$ ) and  $d$  the length of the DNA represented by the sphere. The line charge density  $\nu$  of the DNA must be adapted to the effective charge density  $\nu^*$

$$\nu^* = \nu \chi_{CR} \chi_{PBS}, \quad (\text{II})$$

Where  $\chi_{CR}$  is the charge adaptation factor and  $\chi_{PBS}$  accounts for the geometry of subsequent overlapping beads and for deviations due to using an approximation instead of the exact Poisson-Boltzmann (PB) equation (Maffeo et al., 2010). Here, we use for  $\chi_{CR}$  a value of 0.42 as derived in (Maffeo et al., 2010). The adaptation factor  $\chi_{PBS}$  was determined by relating this potential to previous description as cylindrical segments (Maffeo et al., 2010).

### Preparation and Simulation

For the preparation of the simulation data, we first selected an appropriate human genome dataset (MNase-seq of K-562 cells from the ENCODE project ENCSR000CXQ (Consortium, 2012; Davis et al., 2018)) in BigWig format (ENCF000VNN). Next, we converted this file into the WIG-Format applying the BigWig2Wig-tool and finally in a BED format by a simple awk-script. Reads from chromosome II were extracted applying another simple UNIX-awk-script. In order to avoid false positive nucleosome positions blacklisted regions were filtered out (<https://www.encodeproject.org/files/ENCF000TDO/>). Best nucleosome positions were determined with NucPosSimulator (Schopflin et al., 2013) generating a BED file containing the nucleosome positions and the occupancy i.e., the number of read centers counted per base pair, smoothed with a Gaussian kernel and normalized. For identifying the least probable nucleosome the mean occupancy values of the 147 bp regions classified as nucleosomes by NucPosSimulator were determined and sorted. After removing the chosen number of nucleosomes with the smallest values, we generated a nucleosome chain with like lengths as in the region and performed computer simulations (Mörl et al., 2019). In order to incorporate effects of surrounding chromatin nucleosomes 20 kb were included at both sites of both investigated regions. The simulations were carried out on the linux cluster in Stralsund and the North German Supercomputing Alliance (HLRN) in Berlin.

### Calculation of Nucleosome Repeat Length

The nucleosome repeat length (NRL) of whole chromosome II was determined analyzing the chrII BED-file as described in the previous section. In a preparatory step nucleosome positions for the whole chromosome II were determined applying NucPosSimulator. From resulting sorted paired end nucleosome reads the repeat length between adjacent nucleosomes was calculated by subtracting the last base pair to the first base pair of the following nucleosome read. The average NRL a sliding window was calculated for a window size of 30000 bp. From this dataset windows with less than 3 nucleosomes e.g. in the centromere were removed applying filter-function from R package "dplyr" (filter(dataset(`#Nucs` != 0))). The developed script (plotNRL.R) is published in a codeocean.com capsule (link).

### Simulation Software

The software was developed in the Wedemann group in the last decades and used in many studies. It is written in C++ and was adapted for the use of shared-memory parallel architectures according to the OpenMP standard. The replica exchange algorithm was implemented for distributed memory architectures using Message Passing Interface (MPI). The simulation software was verified with an extensive set of unit tests and tests using simplified chain models which reproduced the expected analytical values. In addition, for visualization of chromatin structures, a modular software was developed visualization of trajectories simulated by Monte Carlo procedures. The software cannot be made public at the moment, since it contains code under copyright by other parties.

### Statistics and reproducibility

No statistical method was used to predetermine sample size. Investigators were not blinded during the experiments and when assessing the outcome. For each experiment data were collected from at least three biological replicates.

2D and 3D distance data were cut off at the maximum length of a theoretical beads-on-a-string fiber, since it is very unlikely that genomic regions are present in the nucleus more stretched than a fully stretched beads-on-a-string fiber in the nucleus. To calculate the length of a beads-on-a-string fiber the following formula was used: genomic length [bp] \* 0.34 nm (size of one base) / 7 (Carlson and Olins, 1976). For 5 kb genomic distances the cut-off for measured distances was at 250 nm. 15 kb genomic distances were cut off at 730 nm.

Plots in Fig. 2-5 were generated using ggplot in R Studio. Significance levels were always tested by a non-parametric two-sided Wilcoxon test and a Bonferroni-Holm correction was used to avoid errors through multiple testing when applicable. Data in Fig. 2 and 3 are represented as boxplots where the middle line indicates the median, the lower and upper hinges correspond to the 25% and 75% quartiles, the upper whisker extends to the largest value no further than 1.5 x IQR (interquartile range) from the hinge and the lower whisker extends to the smallest value from the hinge at most 1.5 x IQR. The data acquisition, image processing and analysis was done in an unbiased way by automation.

## RESULTS

---

### References

Allshire, R.C., and Madhani, H.D. (2018). Ten principles of heterochromatin formation and function. *Nature Reviews Molecular Cell Biology* 19, 229.

Ashwin, S.S., Maeshima, K., and Sasai, M. (2020). Heterogeneous fluid-like movements of chromatin and their implications to transcription. *Biophys Rev* 12, 461-468.

Baldi, S., Korber, P., and Becker, P.B. (2020). Beads on a string—nucleosome array arrangements and folding of the chromatin fiber. *Nature structural & molecular biology* 27, 109-118.

Becker, P.B., and Workman, J.L. (2013). Nucleosome remodeling and epigenetics. *Cold Spring Harbor Perspectives in Biology* 5, a017905.

Bintu, B., Mateo, L.J., Su, J.-H., Sinnott-Armstrong, N.A., Parker, M., Kinrot, S., Yamaya, K., Boettiger, A.N., and Zhuang, X. (2018). Super-resolution chromatin tracing reveals domains and cooperative interactions in single cells. *Science* 362, eaau1783.

Boettiger, A.N., Bintu, B., Moffitt, J.R., Wang, S., Beliveau, B.J., Fudenberg, G., Imakaev, M., Mirny, L.A., Wu, C.T., and Zhuang, X. (2016). Super-resolution imaging reveals distinct chromatin folding for different epigenetic states. *Nature* 529, 418-422.

Branco, M.R., and Pombo, A. (2006). Intermingling of chromosome territories in interphase suggests role in translocations and transcription-dependent associations. *PLoS Biol* 4, e138.

Carlson, R.D., and Olins, D.E. (1976). Chromatin model calculations: Arrays of spherical v bodies. *Nucleic Acids Research* 3, 89-100.

Chen, B., Gilbert, L.A., Cimini, B.A., Schnitzbauer, J., Zhang, W., Li, G.-W., Park, J., Blackburn, E.H., Weissman, J.S., and Qi, L.S. (2013). Dynamic imaging of genomic loci in living human cells by an optimized CRISPR/Cas system. *Cell* 155, 1479-1491.

Chen, H., Levo, M., Barinov, L., Fujioka, M., Jaynes, J.B., and Gregor, T. (2018). Dynamic interplay between enhancer–promoter topology and gene activity. *Nature genetics* 50, 1296-1303.

Clauvelin, N., Lo, P., Kulaeva, O., Nizovtseva, E., Diaz-Montes, J., Zola, J., Parashar, M., Studitsky, V., and Olson, W. (2015). Nucleosome positioning and composition modulate in silico chromatin flexibility. *Journal of Physics: Condensed Matter* 27, 064112.

Collepardo-Guevara, R., and Schlick, T. (2014). Chromatin fiber polymorphism triggered by variations of DNA linker lengths. *Proceedings of the National Academy of Sciences* 111, 8061-8066.

Consortium, E.P. (2012). An integrated encyclopedia of DNA elements in the human genome. *Nature* 489, 57-74.

Cui, K., and Zhao, K. (2012). Genome-wide approaches to determining nucleosome occupancy in metazoans using MNase-Seq. *Methods Mol Biol* 833, 413-419.

Davis, C.A., Hitz, B.C., Sloan, C.A., Chan, E.T., Davidson, J.M., Gabdank, I., Hilton, J.A., Jain, K., Baymuradov, U.K., Narayanan, A.K., *et al.* (2018). The Encyclopedia of DNA elements (ENCODE): data portal update. *Nucleic Acids Res* 46, D794-d801.

Diermeier, S., Kolovos, P., Heizinger, L., Schwartz, U., Georgomanolis, T., Zirkel, A., Wedemann, G., Grosveld, F., Knoch, T.A., and Merkl, R. (2014). TNF $\alpha$  signalling primes chromatin for NF- $\kappa$ B binding and induces rapid and widespread nucleosome repositioning. *Genome biology* 15, 536.

Dultz, E., Mancini, R., Polles, G., Vallotton, P., Alber, F., and Weis, K. (2018). Quantitative imaging of chromatin decompaction in living cells. *Mol Biol Cell*, mbcE17110648.

Ernst, J., and Kellis, M. (2010). Discovery and characterization of chromatin states for systematic annotation of the human genome. *Nature biotechnology* 28, 817-825.

Ernst, J., Kheradpour, P., Mikkelsen, T.S., Shores, N., Ward, L.D., Epstein, C.B., Zhang, X., Wang, L., Issner, R., and Coyne, M. (2011). Mapping and analysis of chromatin state dynamics in nine human cell types. *Nature* 473, 43-49.

Filion, G.J., van Bommel, J.G., Braunschweig, U., Talhout, W., Kind, J., Ward, L.D., Brugman, W., de Castro, I.J., Kerkhoven, R.M., Bussemaker, H.J., *et al.* (2010). Systematic protein location mapping reveals five principal chromatin types in *Drosophila* cells. *Cell* 143, 212-224.

Finn, E.H., Pegoraro, G., Brandao, H.B., Valton, A.L., Oomen, M.E., Dekker, J., Mirny, L., and Misteli, T. (2019). Extensive Heterogeneity and Intrinsic Variation in Spatial Genome Organization. *Cell* 176, 1502-1515 e1510.

Funke, J.J., Ketterer, P., Lieleg, C., Schunter, S., Korber, P., and Dietz, H. (2016). Uncovering the forces between nucleosomes using DNA origami. *Science advances* 2, e1600974.

Fussner, E., Strauss, M., Djuric, U., Li, R., Ahmed, K., Hart, M., Ellis, J., and Bazett-Jones, D.P. (2012). Open and closed domains in the mouse genome are configured as 10-nm chromatin fibres. *EMBO Rep* 13, 992-996.

Germier, T., Kocanova, S., Walther, N., Bancaud, A., Shaban, H.A., Sellou, H., Politi, A.Z., Ellenberg, J., Gallardo, F., and Bystricky, K. (2017). Real-time imaging of a single gene reveals transcription-initiated local confinement. *Biophysical journal* 113, 1383-1394.

Görisch, S.M., Wachsmuth, M., Tóth, K.F., Lichter, P., and Rippe, K. (2005). Histone acetylation increases chromatin accessibility. *Journal of cell science* 118, 5825-5834.

Göttfert, F., Wurm, C.A., Mueller, V., Berning, S., Cordes, V.C., Honigmann, A., and Hell, S.W. (2013). Coaligned dual-channel STED nanoscopy and molecular diffusion analysis at 20 nm resolution. *Biophysical journal* 105, L01-L03.

Gu, B., Swigut, T., Spencley, A., Bauer, M.R., Chung, M., Meyer, T., and Wysocka, J. (2018). Transcription-coupled changes in nuclear mobility of mammalian cis-regulatory elements. *Science*.

Hajjoul, H., Mathon, J., Ranchon, H., Goiffon, I., Mozziconacci, J., Albert, B., Carrivain, P., Victor, J.-M., Gadal, O., and Bystricky, K. (2013). High-throughput chromatin motion tracking in living yeast reveals the flexibility of the fiber throughout the genome. *Genome research* 23, 1829-1838.

Hargreaves, D.C., and Crabtree, G.R. (2011). ATP-dependent chromatin remodeling: genetics, genomics and mechanisms. *Cell research* 21, 396-420.

## RESULTS

---

Heitz, E. (1928). Das Heterochromatin der Moose. *Jahrb Wiss Bot* 69, 762-818.

Hess, B., Kutzner, C., van der Spoel, D., and Lindahl, E. (2008). GROMACS 4: Algorithms for Highly Efficient, Load-Balanced, and Scalable Molecular Simulation. *J Chem Theory Comput* 4, 435-447.

Heun, P., Laroche, T., Shimada, K., Furrer, P., and Gasser, S.M. (2001). Chromosome dynamics in the yeast interphase nucleus. *Science* 294, 2181-2186.

Hoffman, M.M., Buske, O.J., Wang, J., Weng, Z., Bilmes, J.A., and Noble, W.S. (2012). Unsupervised pattern discovery in human chromatin structure through genomic segmentation. *Nature Methods* 9, 473-476.

Hoffman, M.M., Ernst, J., Wilder, S.P., Kundaje, A., Harris, R.S., Libbrecht, M., Giardine, B., Ellenbogen, P.M., Bilmes, J.A., Birney, E., *et al.* (2013). Integrative annotation of chromatin elements from ENCODE data. *Nucleic acids research* 41, 827-841.

Katzgraber, H.G., Trebst, S., Huse, D.A., and Troyer, M. (2006). Feedback-optimized parallel tempering Monte Carlo. *Journal of Statistical Mechanics: Theory and Experiment* 2006, P03018.

Kepper, N., Ettig, R., Stehr, R., Marnach, S., Wedemann, G., and Rippe, K. (2011). Force spectroscopy of chromatin fibers: extracting energetics and structural information from Monte Carlo simulations. *Biopolymers* 95, 435-447.

Kepper, N., Foethke, D., Stehr, R., Wedemann, G., and Rippe, K. (2008). Nucleosome geometry and internucleosomal interactions control the chromatin fiber conformation. *Biophys J* 95, 3692-3705.

Klenin, K., Merlitz, H., and Langowski, J. (1998). A Brownian dynamics program for the simulation of linear and circular DNA and other wormlike chain polyelectrolytes. *Biophys J* 74, 780-788.

Konig, P., Braunfeld, M.B., Sedat, J.W., and Agard, D.A. (2007). The three-dimensional structure of in vitro reconstituted *Xenopus laevis* chromosomes by EM tomography. *Chromosoma* 116, 349-372.

Kornberg, R.D. (1974). Chromatin structure: a repeating unit of histones and DNA. *Science* 184, 868-871.

Lai, B., Gao, W., Cui, K., Xie, W., Tang, Q., Jin, W., Hu, G., Ni, B., and Zhao, K. (2018). Principles of nucleosome organization revealed by single-cell micrococcal nuclease sequencing. *Nature* 562, 281-285.

Levi, V., Ruan, Q., Plutz, M., Belmont, A.S., and Gratton, E. (2005). Chromatin dynamics in interphase cells revealed by tracking in a two-photon excitation microscope. *Biophysical journal* 89, 4275-4285.

Levin, Y. (2002). Electrostatic correlations: from plasma to biology. *Reports on progress in physics* 65, 1577.

Lucas, J.S., Zhang, Y., Dudko, O.K., and Murre, C. (2014). 3D trajectories adopted by coding and regulatory DNA elements: first-passage times for genomic interactions. *Cell* 158, 339-352.

- Luger, K., Mader, A.W., Richmond, R.K., Sargent, D.F., and Richmond, T.J. (1997). Crystal structure of the nucleosome core particle at 2.8 Å resolution. *Nature* 389, 251-260.
- Ma, H., Tu, L.C., Chung, Y.C., Naseri, A., Grunwald, D., Zhang, S., and Pederson, T. (2019). Cell cycle- and genomic distance-dependent dynamics of a discrete chromosomal region. *J Cell Biol.*
- Maeshima, K., Ide, S., and Babokhov, M. (2019). Dynamic chromatin organization without the 30-nm fiber. *Curr Opin Cell Biol* 58, 95-104.
- Maffeo, C., Schopflin, R., Brutzer, H., Stehr, R., Aksimentiev, A., Wedemann, G., and Seidel, R. (2010). DNA-DNA interactions in tight supercoils are described by a small effective charge density. *Phys Rev Lett* 105, 158101.
- Mangenot, S., Leforestier, A., Vachette, P., Durand, D., and Livolant, F. (2002). Salt-induced conformation and interaction changes of nucleosome core particles. *Biophysical journal* 82, 345-356.
- Markaki, Y., Smeets, D., Fiedler, S., Schmid, V.J., Schermelleh, L., Cremer, T., and Cremer, M. (2012). The potential of 3D-FISH and super-resolution structured illumination microscopy for studies of 3D nuclear architecture: 3D structured illumination microscopy of defined chromosomal structures visualized by 3D (immuno)-FISH opens new perspectives for studies of nuclear architecture. *Bioessays* 34, 412-426.
- Marshall, W., Straight, A., Marko, J., Swedlow, J., Dernburg, A., Belmont, A., Murray, A., Agard, D., and Sedat, J. (1997). Interphase chromosomes undergo constrained diffusional motion in living cells. *Current Biology* 7, 930-939.
- Mateo, L.J., Murphy, S.E., Hafner, A., Cinquini, I.S., Walker, C.A., and Boettiger, A.N. (2019). Visualizing DNA folding and RNA in embryos at single-cell resolution. *Nature* 568, 49-54.
- Metropolis, N., Rosenbluth, A.W., Rosenbluth, M.N., Teller, A.H., and Teller, E. (1953). Equation of state calculations by fast computing machines. *The journal of chemical physics* 21, 1087-1092.
- Mirny, L.A. (2010). Nucleosome-mediated cooperativity between transcription factors. *Proceedings of the National Academy of Sciences* 107, 22534-22539.
- Mirny, L.A. (2011). The fractal globule as a model of chromatin architecture in the cell. *Chromosome Res* 19, 37-51.
- Moller, J., Lequieu, J., and de Pablo, J.J. (2019). The free energy landscape of internucleosome interactions and its relation to chromatin fiber structure. *ACS central science* 5, 341-348.
- Moore, J.E., Purcaro, M.J., Pratt, H.E., Epstein, C.B., Shores, N., Adrian, J., Kawli, T., Davis, C.A., Dobin, A., and Kaul, R. (2020). Expanded encyclopaedias of DNA elements in the human and mouse genomes. *Nature* 583, 699-710.
- Mörl, M.-C., Zülske, T., Schöpflin, R., and Wedemann, G. (2019). Data formats for modelling the spatial structure of chromatin based on experimental positions of nucleosomes. *AIMS Biophysics* 6, 83.

## RESULTS

---

Muller, O., Kepper, N., Schopflin, R., Ettig, R., Rippe, K., and Wedemann, G. (2014). Changing chromatin fiber conformation by nucleosome repositioning. *Biophys J* 107, 2141-2150.

Nordenskiöld, L., Lyubartsev, A.P., and Korolev, N. (2017). *Coarse-grained modeling of nucleosomes and chromatin* (CRC Press).

Norouzi, D., and Zhurkin, V.B. (2018). Dynamics of chromatin fibers: comparison of monte carlo simulations with force spectroscopy. *Biophysical journal* 115, 1644-1655.

Nozaki, T., Imai, R., Tanbo, M., Nagashima, R., Tamura, S., Tani, T., Joti, Y., Tomita, M., Hibino, K., Kanemaki, M.T., *et al.* (2017). Dynamic Organization of Chromatin Domains Revealed by Super-Resolution Live-Cell Imaging. *Mol Cell* 67, 282-293 e287.

Olins, A.L., and Olins, D.E. (1974). Spheroid chromatin units (v bodies). *Science* 183, 330-332.

Ou, H.D., Phan, S., Deerinck, T.J., Thor, A., Ellisman, M.H., and O'Shea, C.C. (2017). ChromEMT: Visualizing 3D chromatin structure and compaction in interphase and mitotic cells. *Science* 357.

Parmar, J.J., and Padinhateeri, R. (2020). Nucleosome positioning and chromatin organization. *Current Opinion in Structural Biology* 64, 111-118.

Ram, O., Goren, A., Amit, I., Shores, N., Yosef, N., Ernst, J., Kellis, M., Gymrek, M., Issner, R., and Coyne, M. (2011). Combinatorial patterning of chromatin regulators uncovered by genome-wide location analysis in human cells. *Cell* 147, 1628-1639.

Ricci, M.A., Manzo, C., Garcia-Parajo, M.F., Lakadamyali, M., and Cosma, M.P. (2015). Chromatin fibers are formed by heterogeneous groups of nucleosomes in vivo. *Cell* 160, 1145-1158.

Sahl, S.J., Hell, S.W., and Jakobs, S. (2017). Fluorescence nanoscopy in cell biology. *Nature reviews Molecular cell biology* 18, 685.

Schoenfelder, S., and Fraser, P. (2019). Long-range enhancer-promoter contacts in gene expression control. *Nat Rev Genet* 20, 437-455.

Schopflin, R., Teif, V.B., Muller, O., Weinberg, C., Rippe, K., and Wedemann, G. (2013). Modeling nucleosome position distributions from experimental nucleosome positioning maps. *Bioinformatics* 29, 2380-2386.

Shaban, H.A., Barth, R., and Bystricky, K. (2018). Formation of correlated chromatin domains at nanoscale dynamic resolution during transcription. *Nucleic acids research* 46, e77-e77.

Solovei, I., Cavallo, A., Schermelleh, L., Jaunin, F., Scasselati, C., Cmarko, D., Cremer, C., Fakan, S., and Cremer, T. (2002). Spatial preservation of nuclear chromatin architecture during three-dimensional fluorescence in situ hybridization (3D-FISH). *Exp Cell Res* 276, 10-23.

Stehr, R., Kepper, N., Rippe, K., and Wedemann, G. (2008). The effect of internucleosomal interaction on folding of the chromatin fiber. *Biophys J* 95, 3677-3691.

---

Stehr, R., Schopflin, R., Ettig, R., Kepper, N., Rippe, K., and Wedemann, G. (2010). Exploring the conformational space of chromatin fibers and their stability by numerical dynamic phase diagrams. *Biophys J* 98, 1028-1037.

Stergachis, A.B., Debo, B.M., Haugen, E., Churchman, L.S., and Stamatoyannopoulos, J.A. (2020). Single-molecule regulatory architectures captured by chromatin fiber sequencing. *Science* 368, 1449-1454.

Svaren, J., Klebanow, E., Sealy, L., and Chalkley, R. (1994). Analysis of the competition between nucleosome formation and transcription factor binding. *Journal of Biological Chemistry* 269, 9335-9344.

Swendsen, R.H., and Wang, J.S. (1986). Replica Monte Carlo simulation of spin glasses. *Phys Rev Lett* 57, 2607-2609.

Trojer, P., and Reinberg, D. (2007). Facultative heterochromatin: is there a distinctive molecular signature? *Molecular cell* 28, 1-13.

Van Holde, K.E. (1989). *Chromatin* (Heidelberg: Springer Science & Business Media).

Vierstra, J., Lazar, J., Sandstrom, R., Halow, J., Lee, K., Bates, D., Diegel, M., Dunn, D., Neri, F., and Haugen, E. (2020). Global reference mapping of human transcription factor footprints. *Nature* 583, 729-736.

Walker, D.A., Kowalczyk, B., de la Cruz, M.O., and Grzybowski, B.A. (2011). Electrostatics at the nanoscale. *Nanoscale* 3, 1316-1344.

Wurm, C.A., Neumann, D., Schmidt, R., Egner, A., and Jakobs, S. (2010). Sample preparation for STED microscopy. In *Live cell imaging* (Springer), pp. 185-199.

Zaret, K.S. (2020). Pioneer Transcription Factors Initiating Gene Network Changes. *Annual Review of Genetics* 54.

Zewdie, H. (1998). Computer simulation studies of liquid crystals: A new Corner potential for cylindrically symmetric particles. *The Journal of chemical physics* 108, 2117-2133.

Zhang, R., Erler, J., and Langowski, J. (2017). Histone acetylation regulates chromatin accessibility: role of H4KI6 in inter-nucleosome interaction. *Biophysical journal* 112, 450-459.

Zidovska, A., Weitz, D.A., and Mitchison, T.J. (2013). Micron-scale coherence in interphase chromatin dynamics. *Proceedings of the National Academy of Sciences* 110, 15555-15560.

**Supplementary information**

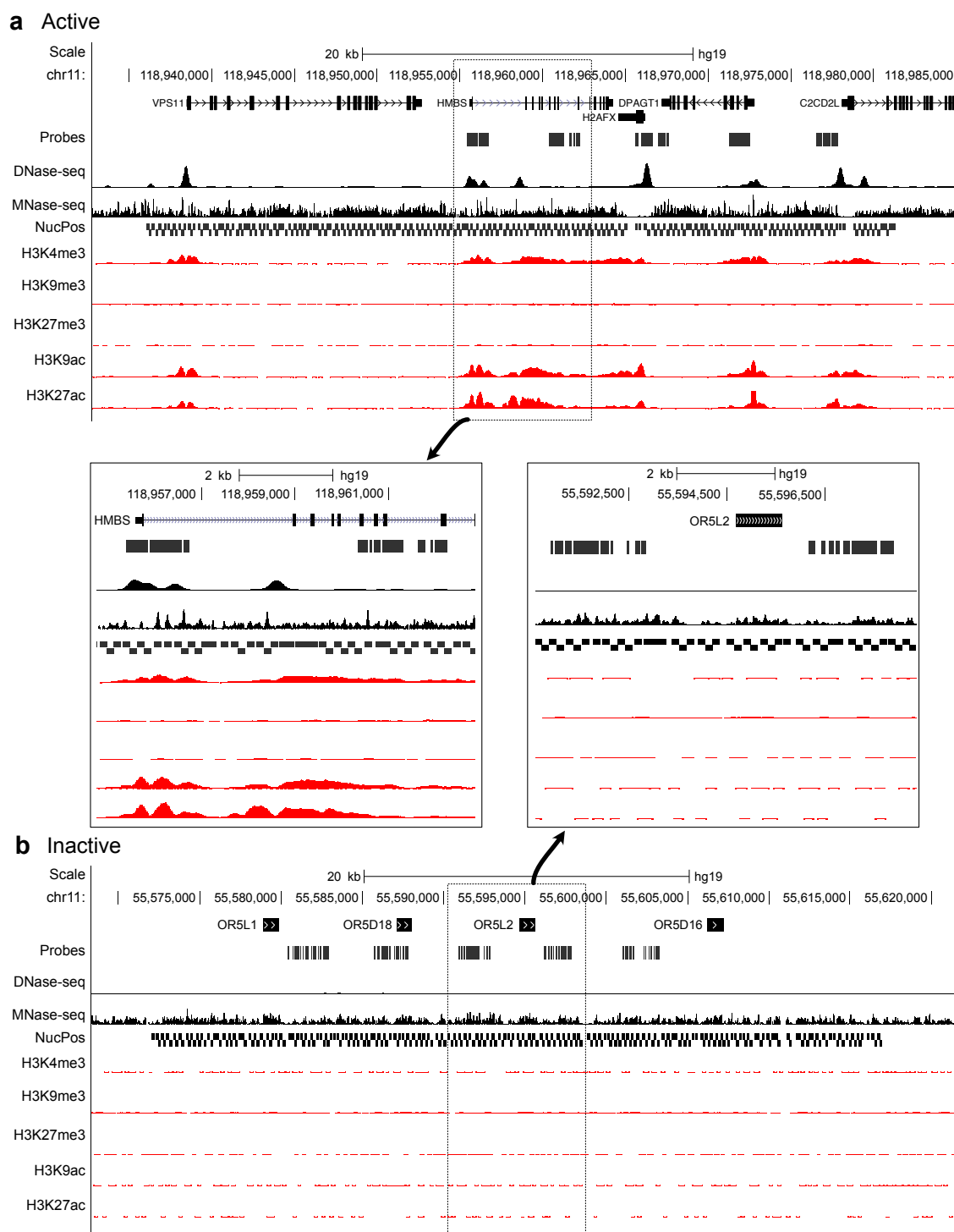
**Comparison of DNase I hypersensitive and insensitive chromatin in human cells by super-resolution microscopy and computer simulation**

**Brandstetter et al.**

**Supplementary figures 1 – 6**

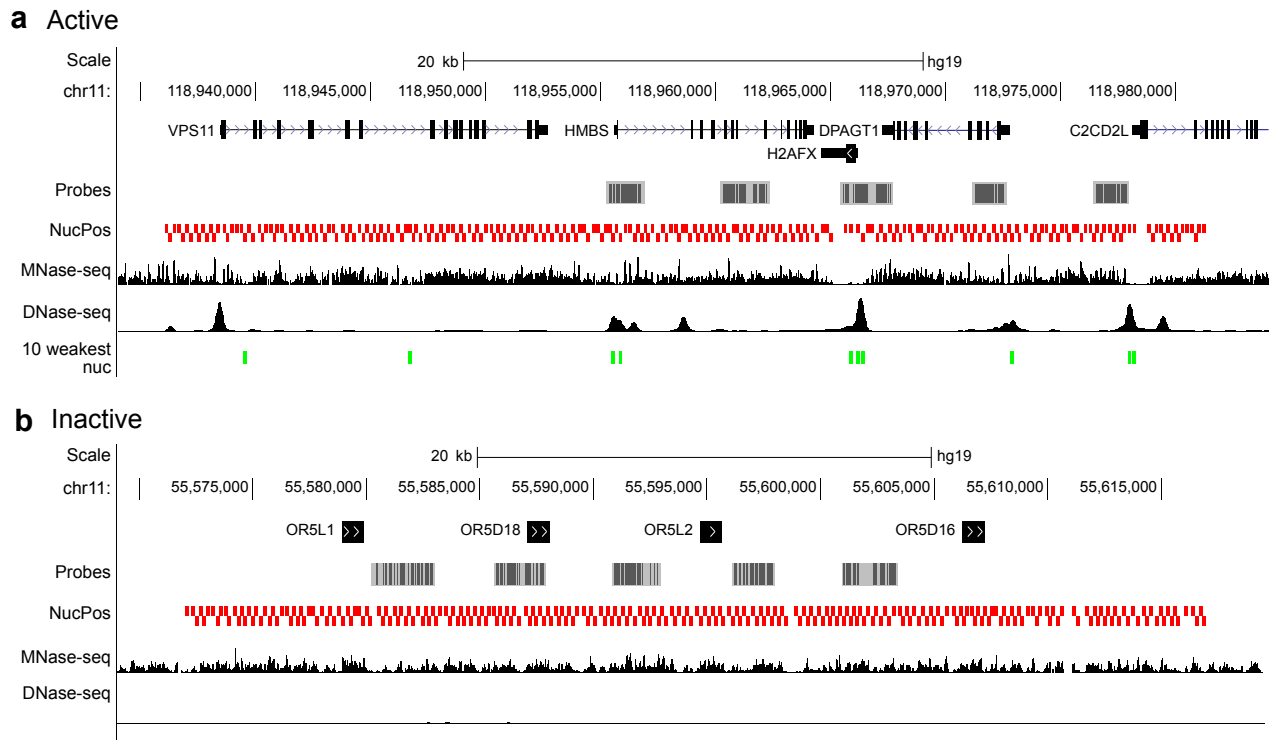
**Supplementary table 1**

## Supplementary figures with explanation

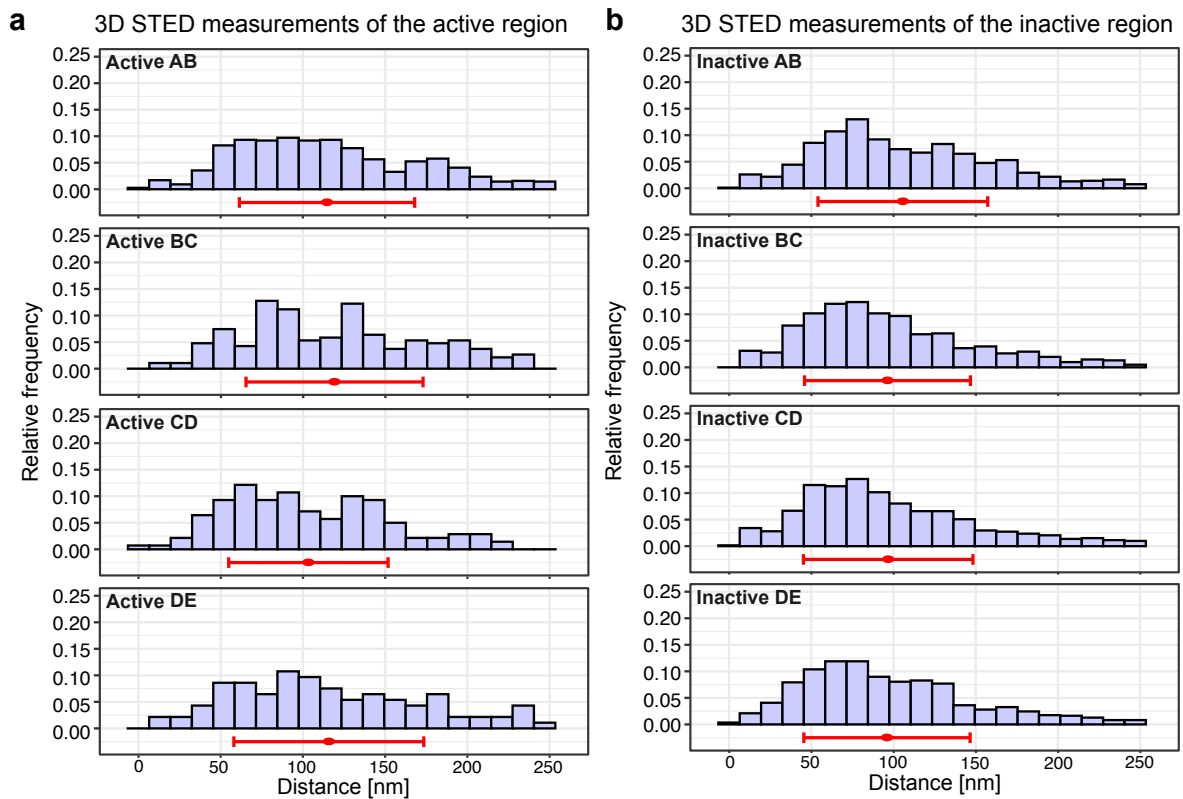


**Supplementary figure 1:** Active (a) and inactive (b) genomic regions with genes, probe sets, DNase-seq, MNase-seq, nucleosome positions from NucPosSimulator, H<sub>3</sub>K<sub>4</sub>me<sub>3</sub>, H<sub>3</sub>K<sub>9</sub>me<sub>3</sub>, H<sub>3</sub>K<sub>27</sub>me<sub>3</sub>, H<sub>3</sub>K<sub>9</sub>ac, H<sub>3</sub>K<sub>27</sub>ac. Boxes and insets mark the investigated regions Active AB and Inactive CD with the same tracks. Tracks show that inactive region has almost no histone modifications while the active region contains active marks like H<sub>3</sub>K<sub>4</sub>me<sub>3</sub>, H<sub>3</sub>K<sub>9</sub>ac and H<sub>3</sub>K<sub>27</sub>ac.

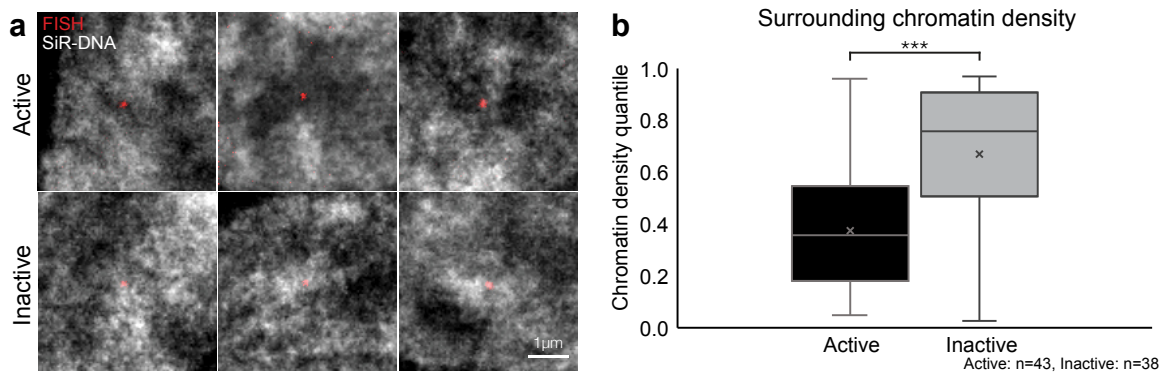
## RESULTS



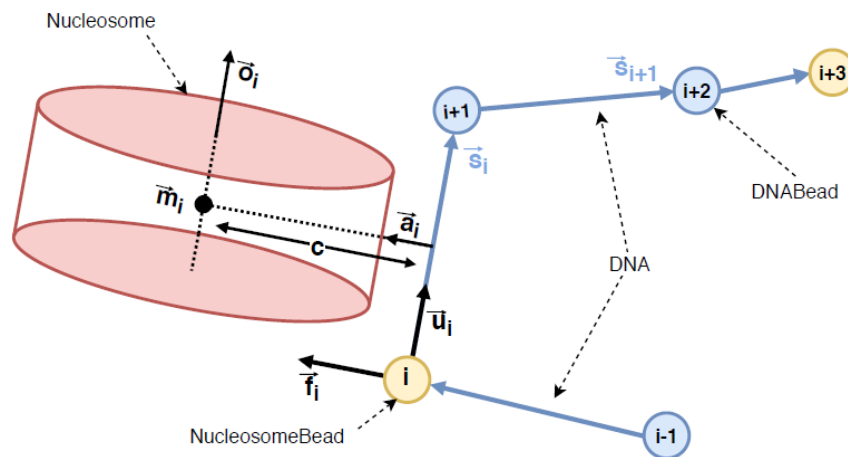
**Supplementary figure 2:** Active (a) and inactive (b) genomic regions on chromosome II with genes, probe sets, nucleosome positions from NucPosSimulator (red), MNase-seq and DNase-seq tracks and the 10 weakest nucleosomes for the active region (green) (a).



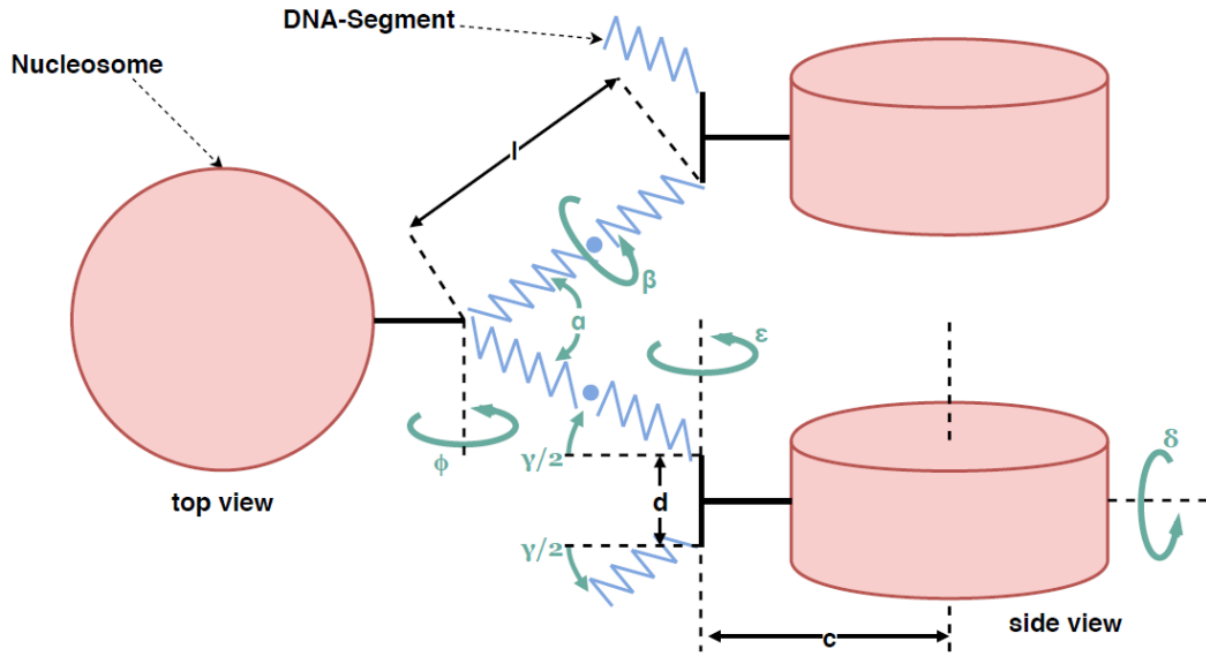
**Supplementary figure 3:** Distance histograms from 3D STED measurements for all four intervals (AB, BC, CD, DE) in active (a) and inactive (b). The mean for each histogram is indicated by the red dot and the standard deviation by the red line.



**Supplementary figure 4:** Chromatin environment of the active and inactive region. (a) Representative images for the active (upper row) and inactive (lower row) region labeled with one FISH probe set (red) and chromatin labeled with SiR-DNA (gray). Scale bar = 1  $\mu\text{m}$ . (b) Chromatin density quantile for active (black) and inactive (gray) differ significantly. Inactive region is embedded in higher density chromatin, while active chromatin is surrounded by lower density chromatin.



**Supplementary figure 5:** Model of a nucleosome chain.  $i$  represents the position of the bead in the chain, yellow circles indicate nucleosome bead positions, and blue circles indicate DNA bead positions. The nucleosome is represented by a red cylinder. The segment vector  $\vec{s}_i$  points from one bead to the next bead. A local coordination system  $(\hat{u}_i, \hat{v}_i, \hat{f}_i)$  (not shown) describes the orientation of a bead. Vector  $\vec{m}_i$  describes the direction from the center of the segment to the nucleosome center, and  $c$  is its length, and vector  $\vec{o}_i$  describes the orientation of the nucleosome.



**Supplementary figure 6:** The relative orientation of the nucleosome is described by the angles  $\alpha$ ,  $\delta$ ,  $\epsilon$ ,  $\gamma$ ,  $\phi$  (modified from Rippe et al. (2012)).  $\beta$  is the torsional orientation of subsequent nucleosomes.  $l$  is the length of the DNA modeling the linker DNA,  $d$  the distance between the entry and the exit point of the linker DNA at the nucleosome,  $c$  the distance between the center of the nucleosome segment and the center of the oblate sphero-cylinder modeling of the nucleosome.

**Supplementary table 1: Simulation Parameters and Constants**

$e_c$	$1.602 * 10^{-19} C$	Electric charge unit
$v$	$-2/0.34 e_c nm^{-1}$	Line charge density of DNA
$\rho$	$0.1 * 10^{24} mol nm^{-3}$	Molarity of the monovalent solution
$N_A$	$6.022 * 10^{23} mol^{-1}$	Avogadro constant
$\epsilon$	80	Value for the dielectric value in the solution
$\epsilon_0$	$(4\pi f)^{-1}$	Dielectric constant
$f$	$138.935 kJ nm mol^{-1} e_c^{-2}$	Electric conversion factor
$k_B$	$8.314513 * 10^{-3} kJ mol^{-1} K^{-1}$	Boltzmann constant
$a$	1.2 nm	Radius of the DNA model sphere
$T$	293 K	Temperature of the solution
	$4 * 10^7$	simulation steps for internucleosomal interaction strength 4 kT
	$8 * 10^7$	simulation steps for internucleosomal interaction strength 8 kT
	10 nm	maximum DNA segment length
	5.5 nm	nucleosome height
	11 nm	nucleosome diameter
	293 K	minimum temperature used for replica exchange procedure
	700 K	maximum temperature used for replica exchange procedure

	16	number of temperatures used for replica exchange procedure for internucleosomal interaction strength 4 kT
	32	number of temperatures used for replica exchange procedure for internucleosomal interaction strength 8 kT
	<i>4 kT and 8 kT (Inactive)</i>	$\varepsilon$ for $E_{internuc}$
	5.5 nm	$\sigma$ for $E_{internuc}$
	665	$a_{DNA}^{(s)}$
	665	$a_{NUC}^{(s)}$
	120.44	$a_{DNA}^{(b)}$
	120.44	$a_{NUC}^{(b)}$
	219.25	$a_{DNA}^{(t)}$
	782.85	$a_{NUC}^{(t)}$
	1.2 kJ * mol <sup>-1</sup>	Lennard jones $\varepsilon$ for DNA
	2.0 kJ * mol <sup>-1</sup>	Lennard jones $\sigma$ for DNA
	$S000 = 1.6957$	interaction potential nucleosome s-functions
	$Scc2 = -0.7641$	
	$S220 = -0.1480$	
	$S222 = -0.2582$	
	$S224 = 0.5112$	
	$E000 = 2.7206$	
	$Ecc2 = 6.0995$	
	$E220 = 3.3826$	
	$E222 = 7.1036$	
	$E224 = 3.2870$	



## 5 DISCUSSION

In the field of chromatin architecture, some discrepancies remain which arise because results and conclusions are based on different approaches. Due to cell-to-cell variability, the findings from single-cell measurements and population-based techniques can be very different. Microscopic approaches often have a different view on nuclear structures than biochemical ones, which leads to apparent contradictions. In general, the use of different methods has enabled many advances in the field of nuclear organization, but multi-method studies must also aim to combine the results to understand the structures described more holistically. This will be attempted in the presented work, even if this goal can certainly only be achieved to some extent.

Three articles from different areas of research on nuclear architecture are the basis of this thesis: (i) a multi-method study on the influence of cohesin on the nuclear architecture, (ii) a novel fluorescence labeling technique and (iii) the attempt to understand the chromatin conformation on a scale of 5 kb using a combination of microscopic measurements and computer simulations.

### 5.1 Effects of cohesin loss on the functional chromatin landscape

Cohesin is a multi-subunit protein complex which consists of SMC1, SMC3, RAD21, SAI and SA2 in human cells. With its ring-like structure cohesin functions in sister chromatid cohesion for correct chromosome segregation, in repair of double-strand breaks and moreover in chromatin loop formation on a sub-Mb level by extrusion of DNA between convergent CTCF binding sites (Davidson et al., 2019; Fudenberg et al., 2016; Parelho et al., 2008; Rao et al., 2014; Sanborn et al., 2015; Zuin et al., 2014) (for review, see Jeppsson et al. (2014); Litwin et al. (2018); Mehta et al. (2013); Merkschlager and Nora (2016); Nishiyama (2019); Peters et al. (2008); van Ruiten and Rowland (2018)). The cohesin complex is fundamentally important for a functional nuclear organization. Since cohesin is involved in many fundamental processes, homozygous knockouts of proteins of the cohesin complex in mice lead to early embryonic lethality (Singh and Gerton, 2015). Inducible depletion of essential proteins makes it possible to study the effects of their loss. The auxin-inducible degron (mAID) is a small tag that can be fused to proteins and allows inducible depletion (Natsume et al., 2016). Upon addition of auxin, the endogenously expressed ubiquitin ligase OsTIR1 ubiquitinylates the mAID tag which leads to proteasomal degradation of the tagged protein. By using this mAID system for RAD21 in human cells (HCT116-RAD21-mAID) a Hi-C study found that after 6 h of cohesin depletion TADs were completely lost (Rao et al., 2017). The Hi-C map still displayed the typical diagonal but the triangles representing TADs were missing. The checker-board pattern of the Hi-C map was enhanced in cohesin depleted cells indicating a stronger compartmentalization in A- and B-compartment. In contrast, an imaging-based study using the same cells showed that even without cohesin chromatin is structured in TAD-like domains and the more random positioning of boundaries between these TAD-like domains in single cells leads to a loss of TADs on a population level (Bintu et al., 2018). In our paper “Cohesin

depleted cells rebuild functional nuclear compartments after endomitosis” we aimed to study the functional implications of a loss of cohesin on global nuclear architecture with a multi-methodical approach (Cremer et al., 2020a). We used live-cell time lapse imaging, super-resolution microscopy, Hi-C and Repli-seq on HCT116-RAD21-mAID cells. My contribution to this work was designing imaging experiments and performing (i) live-cell imaging to track cell cycle progression, in particular mitotic progression, of cohesin depleted cells in comparison to control cells, (ii) confocal microscopy of stained chromosome territories in pre- and postmitotic cohesin depleted cells as well as control cells, (iii) quantitative analyses including statistics on different acquired image data sets.

By long-term live-cell imaging, we found that cell cycle progression in cohesin depleted cells was unsuspecting until they entered mitosis. The cells formed condensed chromosomes and proceeded into metaphase where the progression in mitosis seemed to be stalled. After an elongated metaphase, cohesin depleted cells attempted to properly divide their chromosomes but they could not complete karyo- and cytokinesis and each cell formed one cell with a multilobulated nucleus (MLN). By chromosome painting we found that cells with MLN had four chromosome territories for the painted chromosomes which is a double chromosome set. We also found that cohesin depleted mitotic cells often showed misalignment of chromosomes during chromatid segregation. Cohesin is known to mediate proper spindle-pole formation and attachment of microtubules to kinetochores (Jeppsson et al., 2014; Mehta et al., 2013) which might be the reason for the disturbed karyokinesis in cohesin depleted cells. Most of bound cohesin is lost from chromosome arms during mitosis and the condensin complex is responsible for loop formation in mitotic chromosomes (Abramo et al., 2019). During telophase loading of cohesin onto DNA starts which might lead to problems with completion of mitosis and cytokinesis when cohesin is depleted.

By processing super-resolution images of chromatin, we could use the ANC (active nuclear compartment)/ INC (inactive nuclear compartment) model to describe nuclear organization by segmenting the chromatin in 7 density classes, from chromatin-depleted interchromatin channels to very dense heterochromatin areas in the nucleus (Cremer et al., 2020b; Cremer et al., 2015). This model can also be used to quantify the distribution of nuclear markers like RNA Pol II, SC35 and H3K27me3. We found that pre-mitotic cohesin depleted cells had a normal organization of chromatin and nuclear markers according to an undisturbed ANC/INC model. Post-endomitotic MLN rebuild a typical nuclear organization with an interchromatin channel network and normal ANC and INC domains besides their morphological abnormality. The distribution of the functional marker RNA Pol II, SC35 and H3K27me3 was also retained in MLN.

The Hi-C maps of post-endomitotic MLN did not show the typical triangles but a stronger checkerboard pattern similar to pre-mitotic cohesin depleted cells which was shown earlier (Rao et al., 2017). Thus, MLN lost their TADs on a population level. Positioning of TAD boundaries is in many cases mediated through loop extrusion by cohesin (Kim et al., 2019) and the loss of cohesin for 6 h

leads to a more random positioning of TAD boundaries in single cells and seemingly lost TADs in cell populations (Bintu et al., 2018). The checker-board pattern on the Hi-C maps of MLN were enhanced indicating a cohesin-independent increased compartmentalization in A- and B-compartments.

By labeling of newly replicated DNA, we found that pre-mitotic cohesin depleted nuclei and post-endomitotic cohesin depleted MLN were able to pass through S-phase with typical replication patterns. Moreover, cohesin depleted cells both before and after mitosis preserved the ratio of early to late replicating DNA indicating a correct replication timing as shown by Repli-seq. These findings indicate that important functions of chromatin were retained after cohesin depletion. However, we found hints that cohesin is indispensable for correct formation of replication domains as seen by increased number, volume and heterogeneity of replication domains in cohesin depleted cells.

During our multi-methodical study, we found that terms and definitions for chromatin and chromatin domains were developed by the use of the different approaches and the relationship between terminologies is not obvious, which leads to an increasing tension between the experts in the different fields. In our study, we gave a definition of terminology based on microscopy and on Hi-C/biochemical studies and we aimed to explain links between some of the described terms (see Supplementary Information, section 4.1).

The apparent contradiction between Hi-C (complete loss of TAD structure upon cohesin loss) and fluorescence microscopy (intact nuclear architecture upon cohesin loss) might be dissolved by mechanisms that can form local domains without cohesin and thus without loop extrusion. Such a mechanism is also suggested by data from Bintu et al., who used super-resolution microscopy on cohesin depleted cells and detected TAD-like domains with varying domain boundaries in single cells (Bintu et al., 2018). These domains could take over some of the functions of TADs based on loop extrusion, as the effects of cohesin loss on transcription were shown to be modest (Rao et al., 2017). TADs that are visible in Hi-C maps are typically present in a fraction of cells (<50%) (Finn et al., 2019), but as we have shown TADs do not determine chromatin structure and patterns as detectably by fluorescence microscopy. These data suggest, that more or less dense chromatin regions are depicted as checker-board pattern in Hi-C maps.

Overall, our study showed that cohesin is very important for a proper organization of different chromatin domains but, if cohesin is depleted, many organizational principles are still intact. Furthermore, this study is one example where some of the different research strategies in chromatin architecture were combined in order to detect and better understand changes of nuclear morphology and spatial organization including chromatin domains, interchromatin channels and contact frequencies.

## 5.2 Fluorescence in situ hybridization labeling strategies

Fluorescence in situ hybridization is a powerful tool to sequence-specifically visualize DNA in the nucleus (Rudkin and Stollar, 1977). Labeling with FISH has been optimized further since its development (Gall and Pardue, 1969). Especially the use of oligo-based probes has made FISH a very versatile technique because it enabled to decrease the size of the labeled DNA sequence in comparison to BAC probes and probe generation became more straight-forward (Boettiger and Murphy, 2020). When using oligo-based FISH many protocols involve a second hybridization step where the fluorescently labeled readout probe is hybridized to the readout overhang on the oligos bound to the target. On the one hand, this approach has several advantages like (i) fluorophores can easily be exchanged and therefore the same probe set can be used in different colors, (ii) readout probes can be removed and washed off again without another heat involving step which allows sequential imaging of different probe sets in the same sample and (iii) only the readout oligo has to be modified by an expensive fluorescent label which is more cost-effective than labeling every oligo from the probe sets. On the other hand, there are also disadvantages, e.g. (i) the second hybridization step reduces penetrance, especially when very small regions are marked with few oligo probes because the signal can fall below the detection limit, (ii) due to the lower penetrance, larger target regions must be selected to allow more oligos to bind which can lead to reduced spatial resolution and (iii) a quantification of bound oligos is not possible when a second hybridization step is needed. These disadvantages show the benefit of directly labeled oligoprobe sets, which allow targets of only 1.5 - 2 kb to be labeled and detected with superresolution microscopy. Therefore, we used this precise oligoFISH method to measure short genomic distances in the manuscript “Comparison of DNase I hypersensitive and insensitive chromatin in human cells by super-resolution microscopy and computer simulation” (Brandstetter et al., in preparation).

Other FISH methods use amplification of the signal to improve signal intensity when labeling small targets, like SABER-FISH (Kishi et al., 2019) or ClampFISH (Rouhanifard et al., 2019). Especially in the case of RNA-FISH signal amplification can improve labeling since individual RNA molecules often need to be made visible. However, the signal is not only amplified for the actual target but also for unspecifically bound oligos resulting in an increased background signal. Therefore, signal amplification is useful for microscope set-ups with insensitive detectors and it does not have an advantage when using set-ups with single-molecule sensitivity.

FISH protocols usually include harsh treatments like heat and chemicals to denature the DNA and make it accessible for the FISH probe. These harsh conditions can lead to artefacts influencing the nanostructure of DNA. Since nowadays FISH is often combined with super-resolution microscopy, even the smallest disturbance of the structure could lead to artefacts and misinterpretations. An early study by Solovei et al. in 2002 raised concerns on imaging the ultrastructure of 3D-FISH labeled nuclear targets with confocal microscopy (Solovei et al., 2002). They concluded that the structure of chromatin domains down to a size of ~1 Mb could be

preserved. When 3D-SIM became an applicable super-resolution technique, Markaki et al. found that adapted FISH protocols can be used for super-resolution microscopy of chromatin ultrastructure (Markaki et al., 2012). In the recent years, FISH – especially oligo-based FISH – has been used for extensive studies of different aspects of chromatin organization, e.g. (i) volume measurements of domains with different epigenetic states (Boettiger et al., 2016), (ii) microscopic retracing of TAD structure and understanding of contact frequency (Bintu et al., 2018; Finn et al., 2019), (iii) the influence of enhancer-promoter interactions on gene expression investigated by RNA-FISH (Benabdallah et al., 2019; Mateo et al., 2019; Williamson et al., 2016). Compared to the older studies mentioned above, which investigated the effects of FISH treatment on chromatin ultrastructure, the reaction conditions of more recent publications are rather harsh (Table 1). These harsh conditions improve the penetrance of probe sets which ultimately leads to better resolution due to e.g., labeling of a smaller structure, better signal-to-noise ratio for subpixel localization and gapless labeling for walking along chromosomes. These studies have provided valuable insights into structural details of chromatin and there is no evidence that the reaction conditions cause artefacts, although many of these studies use super-resolution microscopy. Thus, it can be assumed that the FISH protocol used in our study yields reliable results in combination with STED super-resolution microscopy (Brandstetter et al., in preparation).

Table 1: FISH reaction conditions of Solovei et al., 2002 and Markaki et al., 2012 which studied artefacts in chromatin ultrastructure after FISH and more recent example publications for comparison.

Publication	Denaturation step	Hybridization step	Sample type
Solovei et al., 2002	75 °C, 2 min	37 °C, 2 d	Human cells
Branco and Pombo, 2006	80 °C, 8 min	37 °C, > 40 h	Cryosections
Markaki et al., 2012	76 °C, 2 min	37 °C, 2 – 3 d	Mouse cells
Beliveau et al., 2015	92 °C, 2.5 min	42 °C, over night	Drosophila and human cells
Boettiger et al., 2016	78 °C, 2.5 min	47 °C, 16 – 20 h	Drosophila cells
Bintu et al., 2018	86 °C, 3 min	47 °C, 16 – 18 h	Human cells
Mateo et al., 2019	90 °C, 10 min	42 °C, over night	Drosophila embryos
Benabdallah et al., 2019	75 °C, 15 min, and 80 °C, 20 min	37 °C, over night	Mouse cells
Finn et al., 2019	85 °C, 7.5 min	37 °C, 72 h	Human cells
Brandstetter et al., in preparation	81 °C, 3 min	37 °C, 16 – 20 h	Human cells

However, completely different strategies have been published that avoid heat as the most likely source of artefacts in the preparation of the FISH sample. One such method is RASER-FISH (resolution after single-strand exonuclease resection-FISH) where one strand of the DNA double-strand is digested by an exonuclease allowing to freely access the other strand with FISH probes

for hybridization (Brown et al., 2018). However, the digestion of one DNA strand might also lead to a disruption of chromatin's fine structure. An alternative way to improve hybridization conditions could be the use of PNAs in DNA-FISH. PNAs have the ability to invade the DNA double-strand without denaturation (Saarbach et al., 2019). If this property could reliably be used, heat-free PNA hybridization could enable even more detailed analyses of nanostructures in the nucleus. PNAs have another advantage: PNA-DNA double strands are more stable than a DNA-DNA double-strand (Pellestor and Paulasova, 2004). If PNAs are used as a readout probe, this advantage could be beneficial for labeling efficiency on the one hand, on the other hand the more stable binding also leads to difficulties when the readout probe should be washed out for multiple rounds of labeling. In our study "Site-specific antibody fragment conjugates for reversible staining in fluorescence microscopy" we showed that PNA and DNA can be site-specifically coupled to antibody fragments via the Tub-tag and can be visualized for fluorescence microscopy by complementary fluorescently labeled oligonucleotides (Schwach et al., 2020). I contributed to this study by performing spinning disk microscopy of cells labeled with the newly developed antibody fragments and analyzing the corresponding images. The presented technology enables to combine the target protein specificity of antibodies and the sequence-specific binding properties of oligonucleotides for reversible sequential multicolor labeling. By using an eGFP-binding nanobody site specifically coupled with single-stranded DNA or PNA oligonucleotides we label eGFP-LaminB1 or eGFP-PCNA in fixed cells. We observed that both nanobody-DNA and nanobody-PNA conjugates labeled with a DNA imager strand properly stain the respective target. The imager strand could be efficiently detached from the DNA docking strand with formamide buffer and a second round of labeling yielded again a proper staining. However, the DNA imager strand could not be efficiently removed from the nanobody-PNA conjugates leading to a residual signal after washing. This observation hints at the stronger interaction between PNA and DNA and could potentially be optimized by altering washing conditions.

We showed that PNAs can be coupled to antibody fragments and used for imaging purposes, however, the advantages of PNAs can be fully exploited when they are used as readout probes for FISH. The following properties make fluorescently labeled PNAs ideal readout probes for FISH methods based on oligos with overhangs: (i) due to their low charge PNAs have a low tendency to bind unspecifically to DNA and therefore reduce fluorescent background, (ii) they form very stable DNA-PNA double strands resulting in a higher labeling density. Hence, the use of PNA readout probes in fluorescence microscopy has advantages such as more precise localization of labeled spots and higher penetrance.

### 5.3 Characterization of active and inactive interphase chromatin

oligoFISH with directly labeled oligo probes is suitable for high-precision centroid distance measurements with superresolution microscopy like STED, since the marked region can be very small (1.5-2 kb) on the one hand and on the other hand also provides bright signals due to the high label density. Furthermore, hybridization conditions were optimized for low hybridization temperatures and short hybridization times to minimize disruption of chromatin fine structure. In our manuscript “Comparison of DNase I hypersensitive and insensitive chromatin in human cells by super-resolution microscopy and in-silico simulations” we study the fine structure of chromatin and characterize structural differences of active and inactive interphase chromatin (Brandstetter et al., in preparation). We designed five oligoFISH probes sets for both chromatin classes and the interval between the midpoints of neighboring probe sets was approximately 5 kb. In combination with STED microscopy, we systematically measured distances between dual-color FISH labeled double spots. We used the K-562 cell line for our study since a variety of data, e.g., ChIP-seq for histone modifications, MNase-seq and DNase-seq, is available through the ENCODE project. DNase I hypersensitivity is a widely accepted marker for active regulatory chromatin. Therefore, the regions investigated in our study were chosen based on their DNase I hypersensitivity. The active region has high DNase I hypersensitive sites (DHSs) in K-562 cells and in over 150 other cell types. Missing DHS in K-562 and 651 other cell types characterizes the inactive region. Both regions show the same high/low DHS in the up- and downstream flanking regions. My contribution to this work was (i) designing and performing sample preparation and super-resolution STED imaging, (ii) analysis and interpretation of microscopically acquired data sets, (iii) analysis and interpretation of published ENCODE data using the UCSC genome browser, (iv) writing of the manuscript.

Our 2D STED measurements resulted in data sets with a high statistical power due to the large sample size but only the projected distances can be measured. The distances differ significantly between the active and inactive region as expected. Inactive chromatin is thought to be more compact than active chromatin which resulted in more short distances for the inactive region in our measurements.

With 3D STED exact single-cell 3D distances were determined resulting in a distance distribution histogram of the cell population. The distributions are broad with a tendency to shorter distances which is more pronounced in the inactive region. This broad distribution indicates a large cell-to-cell variability. For both active and inactive, distances of under 50 nm to over 200 nm were observed. Interestingly, such elongated configurations are also possible in the inactive region. For comparison, 5 kb of a stretched beads-on-a-string fiber have a length of 243 nm (Carlson and Olins, 1976). These findings indicate that both active and inactive chromatin are flexible and have the ability to form both compact and elongated configurations.

In order to interpret microscopic data and to find potential underlying mechanisms we applied coarse-grained modeling of the respective chromatin regions (Muller et al., 2014; Stehr et al.,

2008a). With ENCODE MNase-seq tracks of K-562 cells and the software NucPosSimulator we calculated the most probable nucleosome positions which were used within the coarse-grained model to simulate chromatin fibers (Muller et al., 2014; Schopflin et al., 2013). An important input parameter that influences the simulated chromatin fibers is the maximum energy between nucleosomes. The interaction strength is dependent on the solvent (Mangenot et al., 2002) and on histone modifications (Funke et al., 2016). A maximum interaction energy has been observed for unmodified nucleosomes, while acetylation of histones leads to a reduced interaction energy (Funke et al., 2016). Since the active region harbors acetylated histones and other modifications, we used an interaction energy of 4 kT. The inactive region contains mostly unmodified histones and therefore we doubled the energy (8 kT). Both energy values are in the range of published data (Funke et al., 2016; Kepper et al., 2011; Norouzi and Zhurkin, 2018). The result of the simulation is many different chromatin structures which are all thermodynamically possible and could therefore also occur in nature. In the simulated configurations the same distances were measured that were examined microscopically. The distance histograms from simulated fibers can therefore be directly compared to microscopically measured data.

For the active region fully occupied with nucleosomes simulated distances were shorter on average than data from the microscopic measurements. When the number of nucleosomes was reduced sequentially by removing the five most weakly bound nucleosomes from the investigated 5 kb the distance distributions shifted more to longer distances. A mixture of the different distributions matched the microscopic data. Therefore, the broad distribution of distances indicates a great variability of nucleosome density from cell to cell. Genome-wide measurements have shown that especially at DHSs nucleosomes are weakly bound and can be replaced by transcription factors (Stergachis et al., 2020). Moreover, differences in nucleosome occupancy can be assumed because of other known aspects of which some are covered in the following. Nucleosome positioning is in some genomic regions very precise (e.g. around transcription start sites) but mostly varies a lot (Schopflin et al., 2013). Nucleosome remodeling complexes and pioneer transcription factors influence nucleosome occupancy (Zaret, 2020). Transcription factors and nucleosomes compete for DNA access (Mirny, 2010; Svaren et al., 1994). The regulatory site typically occupied by 5-6 transcription factors has a size of about 200 bp which is approximately the length occupied by one nucleosome (Vierstra et al., 2020). Most of the known transcription factors have been shown to not bend DNA when binding which suggests that unbound DNA leads to an elongation of the DNA structure (Kim and Berg, 1996; Panne et al., 2007; Pavletich and Pabo, 1991). Upregulated gene expression leads to a reduction of bound nucleosomes (Diermeier et al., 2014). The active region investigated here has a high level of transcription in K-562 cells almost as high as expression of housekeeping genes like GAPDH, RPL19 and PPIA seen in RNA-seq data from the ENCODE project (Consortium, 2012).

Simulations of inactive chromatin did not lead to very well matching distance distributions. Even with a higher internucleosomal energy the resulting distances were on average longer than in the

microscopic measurements. Also, the introduction of linker histone H1 to the model (Kepper et al., 2008) did not lead to sufficient compaction in the simulation. Heterochromatin formation by HP1 via H3K9me3 (Allshire and Madhani, 2018) or repression by Polycomb via H3K27me3 (van Mierlo et al., 2019) plays most likely no role since histones in the inactive region are mostly unmodified. One aspect which might influence compaction in inactive chromatin is the density of surrounding chromatin. Our microscopic measurements show that the density of chromatin environment is higher for the inactive region, as expected. However, introduction of such environmental effects in chromatin models are computationally very demanding and not yet available for larger-scale simulations. For the simulated configurations, especially the ones with H1, long distances were missing in the histogram. This indicates that, even if the inactive region is more compacted by a stronger internucleosomal interaction and H1, varying nucleosome density could lead to elongated structures.

For both active and inactive chromatin, we did not consider the cell cycle phase in which the studied cells were. Therefore, some of the more elongated configurations in both active and inactive chromatin could be caused by actively ongoing replication in the respective region. However, we would not expect elongation of the structure due to replication since no more than 200 bp were shown to be nucleosome-free behind the replication fork (Ramachandran and Henikoff, 2015).

Overall, we could show that inactive chromatin is more compact than active chromatin in interphase. However, by microscopic measurements we found that 5 kb in both active and inactive chromatin can span over 200 nm indicating elongated configurations. We conclude from our simulations that cell-to-cell variability of nucleosome density can explain the observed elongated configurations in active chromatin, which is in accordance with published data. The presence of elongated configurations in inactive chromatin indicates that nucleosome density also varies in inactive chromatin. The large cell-to-cell variability shown here supports findings from others that chromatin is a highly dynamic structure.

Our study combines the methods FISH, super-resolution microscopy and computational modeling. However, the biological interpretation of microscopic results and understanding of potential underlying mechanisms can be difficult. Therefore, the use of coarse-grained modeling in combination with such super-resolution imaging might support identification and understanding of novel mechanisms and provides additional insights into spatial organization of chromatin.

## 5.4 Conclusion

Francis Crick suggested already in 1978 that possibly not only the sequence information of chromatin but also its 3D structure could be of great importance and might influence gene regulation (Crick, 1978). Indeed, the key role of spatial organization of chromatin in many fundamental cellular processes became more and more clear. The development of many advanced methods allowed to study nuclear architecture and therefore helped to gain insights into organizational patterns of chromatin in interphase and mitosis. In recent years, further advances in live-cell and single-cell techniques were made and it becomes clear that chromatin is not stiff and immobile but rather flexible, dynamic and subject to constant remodeling (Maeshima et al., 2019; Misteli, 2020). The 4D information, meaning not only space but also time, adds another important layer of chromatin organization and leads to a great cell-to-cell heterogeneity. Thus, understanding the complexity of chromatin and the effects of chromatin dynamics in space and time on its function remains challenging.

## 6 REFERENCES

- Abramo, K., Valton, A.L., Venev, S.V., Ozadam, H., Fox, A.N., and Dekker, J. (2019). A chromosome folding intermediate at the condensin-to-cohesin transition during telophase. *Nat Cell Biol* *21*, 1393-1402.
- Ahmed, K., Dehghani, H., Rugg-Gunn, P., Fussner, E., Rossant, J., and Bazett-Jones, D.P. (2010). Global chromatin architecture reflects pluripotency and lineage commitment in the early mouse embryo. *PLoS one* *5*, e10531.
- Albert, I., Mavrich, T.N., Tomsho, L.P., Qi, J., Zanton, S.J., Schuster, S.C., and Pugh, B.F. (2007). Translational and rotational settings of H2A. Z nucleosomes across the *Saccharomyces cerevisiae* genome. *Nature* *446*, 572-576.
- Alexander, J.M., Guan, J., Li, B., Maliskova, L., Song, M., Shen, Y., Huang, B., Lomvardas, S., and Weiner, O.D. (2019). Live-cell imaging reveals enhancer-dependent Sox2 transcription in the absence of enhancer proximity. *Elife* *8*.
- Alipour, E., and Marko, J.F. (2012). Self-organization of domain structures by DNA-loop-extruding enzymes. *Nucleic acids research* *40*, 11202-11212.
- Allfrey, V.G., Faulkner, R., and Mirsky, A. (1964). Acetylation and methylation of histones and their possible role in the regulation of RNA synthesis. *Proceedings of the National Academy of Sciences of the United States of America* *51*, 786.
- Allshire, R.C., and Madhani, H.D. (2018). Ten principles of heterochromatin formation and function. *Nature Reviews Molecular Cell Biology* *19*, 229.
- Altmann, R. (1889). Ueber nucleinsäuren. *Arch f Anatomie u Physiol* *1*, 524-536.
- Anton, T., Bultmann, S., Leonhardt, H., and Markaki, Y. (2014). Visualization of specific DNA sequences in living mouse embryonic stem cells with a programmable fluorescent CRISPR/Cas system. *Nucleus* *5*, 163-172.
- Arya, G., and Schlick, T. (2009). A tale of tails: how histone tails mediate chromatin compaction in different salt and linker histone environments. *The Journal of Physical Chemistry A* *113*, 4045-4059.
- Arya, G., Zhang, Q., and Schlick, T. (2006). Flexible histone tails in a new mesoscopic oligonucleosome model. *Biophysical journal* *91*, 133-150.
- Ashwin, S.S., Maeshima, K., and Sasai, M. (2020). Heterogeneous fluid-like movements of chromatin and their implications to transcription. *Biophys Rev* *12*, 461-468.
- Avery, O.T., MacLeod, C.M., and McCarty, M. (1944). Studies on the chemical nature of the substance inducing transformation of pneumococcal types: induction of transformation by a desoxyribonucleic acid fraction isolated from pneumococcus type III. *The Journal of experimental medicine* *79*, 137-158.
- Baldi, S., Korber, P., and Becker, P.B. (2020). Beads on a string—nucleosome array arrangements and folding of the chromatin fiber. *Nature structural & molecular biology* *27*, 109-118.
- Bannister, A.J., and Kouzarides, T. (2011). Regulation of chromatin by histone modifications. *Cell research* *21*, 381-395.

## REFERENCES

---

- Barbieri, M., Chotalia, M., Fraser, J., Lavitas, L.-M., Dostie, J., Pombo, A., and Nicodemi, M. (2012). Complexity of chromatin folding is captured by the strings and binders switch model. *Proceedings of the National Academy of Sciences* *109*, 16173-16178.
- Becker, P.B., and Hörz, W. (2002). ATP-dependent nucleosome remodeling. *Annual review of biochemistry* *71*, 247-273.
- Becker, P.B., and Workman, J.L. (2013). Nucleosome remodeling and epigenetics. *Cold Spring Harbor Perspectives in Biology* *5*, a017905.
- Beliveau, B.J., Boettiger, A.N., Nir, G., Bintu, B., Yin, P., Zhuang, X., and Wu, C.T. (2017). In Situ Super-Resolution Imaging of Genomic DNA with OligoSTORM and OligoDNA-PAINT. *Methods Mol Biol* *1663*, 231-252.
- Beliveau, B.J., Joyce, E.F., Apostolopoulos, N., Yilmaz, F., Fonseka, C.Y., McCole, R.B., Chang, Y., Li, J.B., Senaratne, T.N., Williams, B.R., *et al.* (2012). Versatile design and synthesis platform for visualizing genomes with Oligopaint FISH probes. *Proc Natl Acad Sci U S A* *109*, 21301-21306.
- Beliveau, B.J., Kishi, J.Y., Nir, G., Sasaki, H.M., Saka, S.K., Nguyen, S.C., Wu, C.T., and Yin, P. (2018). OligoMiner provides a rapid, flexible environment for the design of genome-scale oligonucleotide in situ hybridization probes. *Proc Natl Acad Sci U S A* *115*, E2183-E2192.
- Benabdallah, N.S., Williamson, I., Illingworth, R.S., Kane, L., Boyle, S., Sengupta, D., Grimes, G.R., Therizols, P., and Bickmore, W.A. (2019). Decreased Enhancer-Promoter Proximity Accompanying Enhancer Activation. *Mol Cell* *76*, 473-484 e477.
- Benayoun, B.A., Pollina, E.A., Ucar, D., Mahmoudi, S., Karra, K., Wong, E.D., Devarajan, K., Daugherty, A.C., Kundaje, A.B., and Mancini, E. (2014). H3K4me3 breadth is linked to cell identity and transcriptional consistency. *Cell* *158*, 673-688.
- Berger, F. (2019). Emil Heitz, a true epigenetics pioneer. *Nature Reviews Molecular Cell Biology* *20*, 572-572.
- Betzig, E. (1995). Proposed method for molecular optical imaging. *Optics letters* *20*, 237-239.
- Bickmore, W.A. (2013). The spatial organization of the human genome. *Annu Rev Genomics Hum Genet* *14*, 67-84.
- Bienko, M., Crosetto, N., Teytelman, L., Klemm, S., Itzkovitz, S., and Van Oudenaarden, A. (2013). A versatile genome-scale PCR-based pipeline for high-definition DNA FISH. *nature methods* *10*, 122-124.
- Bintu, B., Mateo, L.J., Su, J.-H., Sinnott-Armstrong, N.A., Parker, M., Kinrot, S., Yamaya, K., Boettiger, A.N., and Zhuang, X. (2018). Super-resolution chromatin tracing reveals domains and cooperative interactions in single cells. *Science* *362*, eaau1783.
- Bishop, T.C. (2005). Molecular dynamics simulations of a nucleosome and free DNA. *Journal of Biomolecular Structure and Dynamics* *22*, 673-685.
- Boettiger, A., and Murphy, S. (2020). Advances in Chromatin Imaging at Kilobase-Scale Resolution. *Trends in Genetics* *36*, 273-287.
- Boettiger, A.N., Bintu, B., Moffitt, J.R., Wang, S., Beliveau, B.J., Fudenberg, G., Imakaev, M., Mirny, L.A., Wu, C.T., and Zhuang, X. (2016). Super-resolution imaging reveals distinct chromatin folding for different epigenetic states. *Nature* *529*, 418-422.

- Bouchet-Marquis, C., Dubochet, J., and Fakan, S. (2006). Cryoelectron microscopy of vitrified sections: a new challenge for the analysis of functional nuclear architecture. *Histochemistry and cell biology* *125*, 43-51.
- Boveri, T. (1888). *Zellen-Studien: Die Befruchtung und Teilung des Eies von Ascaris megalocephala* (G. Fischer).
- Boveri, T. (1909). Die Blastomerenkerne von *Ascaris megalocephala*. *Archiv für Zellforschung* *3*, 181.
- Bowerman, S., and Wereszczynski, J. (2016). Effects of macroH2A and H2A. Z on nucleosome dynamics as elucidated by molecular dynamics simulations. *Biophysical journal* *110*, 327-337.
- Boyle, A.P., Davis, S., Shulha, H.P., Meltzer, P., Margulies, E.H., Weng, Z., Furey, T.S., and Crawford, G.E. (2008). High-resolution mapping and characterization of open chromatin across the genome. *Cell* *132*, 311-322.
- Boyle, S., Gilchrist, S., Bridger, J.M., Mahy, N.L., Ellis, J.A., and Bickmore, W.A. (2001). The spatial organization of human chromosomes within the nuclei of normal and emerin-mutant cells. *Human molecular genetics* *10*, 211-220.
- Boyle, S., Rodesch, M.J., Halvensleben, H.A., Jeddloh, J.A., and Bickmore, W.A. (2011). Fluorescence in situ hybridization with high-complexity repeat-free oligonucleotide probes generated by massively parallel synthesis. *Chromosome Res* *19*, 901-909.
- Bracegirdle, B. (1989). The development of biological preparative techniques for light microscopy, 1839–1989. *Journal of Microscopy* *155*, 307-318.
- Brackey, C.A., Marenduzzo, D., and Gilbert, N. (2020). Mechanistic modeling of chromatin folding to understand function. *Nature Methods* *17*, 767-775.
- Brackley, C.A., Johnson, J., Kelly, S., Cook, P.R., and Marenduzzo, D. (2016). Simulated binding of transcription factors to active and inactive regions folds human chromosomes into loops, rosettes and topological domains. *Nucleic acids research* *44*, 3503-3512.
- Brackley, C.A., Johnson, J., Michieletto, D., Morozov, A.N., Nicodemi, M., Cook, P.R., and Marenduzzo, D. (2017). Nonequilibrium chromosome looping via molecular slip links. *Physical review letters* *119*, 138101.
- Bradbury, S. (1989). Landmarks in biological light microscopy. *Journal of Microscopy* *155*, 281-305.
- Brandstetter, K., Zülske, T., Ragozy, T., Hörl, D., Stamatoyannopoulos, J.A., Leonhardt, H., Wedemann, G., and Harz, H. (in preparation). Comparison of DNase I hypersensitive and insensitive chromatin in human cells by super-resolution microscopy and computer simulations.
- Briand, N., and Collas, P. (2020). Lamina-associated domains: peripheral matters and internal affairs. *Genome biology* *21*, 1-25.
- Brockers, K., and Schneider, R. (2019). Histone H1, the forgotten histone (Future Medicine).
- Brown, J.M., Roberts, N.A., Graham, B., Waithe, D., Lagerholm, C., Telenius, J.M., De Ornellas, S., Oudelaar, A.M., Scott, C., Szczerbal, I., *et al.* (2018). A tissue-specific self-interacting chromatin domain forms independently of enhancer-promoter interactions. *Nature Communications* *9*, 3849.
- Buenrostro, J.D., Giresi, P.G., Zaba, L.C., Chang, H.Y., and Greenleaf, W.J. (2013). Transposition of native chromatin for fast and sensitive epigenomic profiling of open chromatin, DNA-binding proteins and nucleosome position. *Nature methods* *10*, 1213-1218.

## REFERENCES

---

- Cao, K., Lailier, N., Zhang, Y., Kumar, A., Uppal, K., Liu, Z., Lee, E.K., Wu, H., Medrzycki, M., and Pan, C. (2013). High-resolution mapping of h1 linker histone variants in embryonic stem cells. *PLoS Genet* 9, e1003417.
- Cardozo Gizzi, A.M., Cattoni, D.I., Fiche, J.B., Espinola, S.M., Gurgo, J., Messina, O., Houbron, C., Ogiyama, Y., Papadopoulos, G.L., Cavalli, G., *et al.* (2019). Microscopy-Based Chromosome Conformation Capture Enables Simultaneous Visualization of Genome Organization and Transcription in Intact Organisms. *Mol Cell* 74, 212-222 e215.
- Carlson, R.D., and Olins, D.E. (1976). Chromatin model calculations: Arrays of spherical v bodies. *Nucleic Acids Research* 3, 89-100.
- Cattoni, D.I., Gizzi, A.M.C., Georgieva, M., Di Stefano, M., Valeri, A., Chamousset, D., Houbron, C., Déjardin, S., Fiche, J.-B., and González, I. (2017). Single-cell absolute contact probability detection reveals chromosomes are organized by multiple low-frequency yet specific interactions. *Nature communications* 8, 1-10.
- Chargaff, E., Zamenhof, S., and Green, C. (1950). Human Desoxypentose Nucleic Acid: Composition of Human Desoxypentose Nucleic Acid. *Nature* 165, 756-757.
- Chen, B., Gilbert, L.A., Cimini, B.A., Schnitzbauer, J., Zhang, W., Li, G.-W., Park, J., Blackburn, E.H., Weissman, J.S., and Qi, L.S. (2013). Dynamic imaging of genomic loci in living human cells by an optimized CRISPR/Cas system. *Cell* 155, 1479-1491.
- Chen, B., Zou, W., Xu, H., Liang, Y., and Huang, B. (2018a). Efficient labeling and imaging of protein-coding genes in living cells using CRISPR-Tag. *Nature Communications* 9, 5065.
- Chen, C., Lim, H.H., Shi, J., Tamura, S., Maeshima, K., Surana, U., and Gan, L. (2016). Budding yeast chromatin is dispersed in a crowded nucleoplasm in vivo. *Molecular biology of the cell* 27, 3357-3368.
- Chen, H., Levo, M., Barinov, L., Fujioka, M., Jaynes, J.B., and Gregor, T. (2018b). Dynamic interplay between enhancer–promoter topology and gene activity. *Nature genetics* 50, 1296-1303.
- Chen, K.H., Boettiger, A.N., Moffitt, J.R., Wang, S., and Zhuang, X. (2015). RNA imaging. Spatially resolved, highly multiplexed RNA profiling in single cells. *Science* 348, aaa6090.
- Cheung, V., Nowak, N., Jang, W., Kirsch, I., Zhao, S., Chen, X.-N., Furey, T., Kim, U.-J., Kuo, W.-L., and Olivier, M. (2001). Integration of cytogenetic landmarks into the draft sequence of the human genome. *Nature* 409, 953-958.
- Chodavarapu, R.K., Feng, S., Bernatavichute, Y.V., Chen, P.-Y., Stroud, H., Yu, Y., Hetzel, J.A., Kuo, F., Kim, J., and Cokus, S.J. (2010). Relationship between nucleosome positioning and DNA methylation. *Nature* 466, 388-392.
- Chubb, J.R., Boyle, S., Perry, P., and Bickmore, W.A. (2002). Chromatin motion is constrained by association with nuclear compartments in human cells. *Curr Biol* 12, 439-445.
- Chung, J.H., Whiteley, M., and Felsenfeld, G. (1993). A 5' element of the chicken  $\beta$ -globin domain serves as an insulator in human erythroid cells and protects against position effect in *Drosophila*. *Cell* 74, 505-514.
- Clauvelin, N., Lo, P., Kulaeva, O., Nizovtseva, E., Diaz-Montes, J., Zola, J., Parashar, M., Studitsky, V., and Olson, W. (2015). Nucleosome positioning and composition modulate in silico chromatin flexibility. *Journal of Physics: Condensed Matter* 27, 064112.

- Collepardo-Guevara, R., and Schlick, T. (2014). Chromatin fiber polymorphism triggered by variations of DNA linker lengths. *Proceedings of the National Academy of Sciences* *111*, 8061-8066.
- Compton, J.L., Bellard, M., and Chambon, P. (1976). Biochemical evidence of variability in the DNA repeat length in the chromatin of higher eukaryotes. *Proceedings of the National Academy of Sciences* *73*, 4382-4386.
- Consortium, E.P. (2012). An integrated encyclopedia of DNA elements in the human genome. *Nature* *489*, 57-74.
- Crawford, G.E., Holt, I.E., Mullikin, J.C., Tai, D., Green, E.D., Wolfsberg, T.G., Collins, F.S., and Center, N.I.o.H.I.S. (2004). Identifying gene regulatory elements by genome-wide recovery of DNase hypersensitive sites. *Proceedings of the National Academy of Sciences* *101*, 992-997.
- Cremer, M., Brandstetter, K., Maiser, A., Rao, S.S.P., Schmid, V.J., Guirao-Ortiz, M., Mitra, N., Mamberti, S., Klein, K.N., Gilbert, D.M., *et al.* (2020a). Cohesin depleted cells rebuild functional nuclear compartments after endomitosis. *Nature Communications* *11*, 6146.
- Cremer, M., Küpper, K., Wagler, B., Wizelman, L., Hase, J.v., Weiland, Y., Kreja, L., Diebold, J., Speicher, M.R., and Cremer, T. (2003). Inheritance of gene density-related higher order chromatin arrangements in normal and tumor cell nuclei. *The Journal of cell biology* *162*, 809-820.
- Cremer, M., Von Hase, J., Volm, T., Brero, A., Kreth, G., Walter, J., Fischer, C., Solovei, I., Cremer, C., and Cremer, T. (2001). Non-random radial higher-order chromatin arrangements in nuclei of diploid human cells. *Chromosome research* *9*, 541-567.
- Cremer, T., Cremer, C., Baumann, H., Luedtke, E., Sperling, K., Teuber, V., and Zorn, C. (1982a). Rabl's model of the interphase chromosome arrangement tested in Chinese hamster cells by premature chromosome condensation and laser-UV-microbeam experiments. *Human genetics* *60*, 46-56.
- Cremer, T., Cremer, C., Schneider, T., Baumann, H., Hens, L., and Kirsch-Volders, M. (1982b). Analysis of chromosome positions in the interphase nucleus of Chinese hamster cells by laser-UV-microirradiation experiments. *Human genetics* *62*, 201-209.
- Cremer, T., and Cremer, M. (2010). Chromosome territories. *Cold Spring Harb Perspect Biol* *2*, a003889.
- Cremer, T., Cremer, M., Hübner, B., Silaharoglu, A., Hendzel, M., Lanctôt, C., Strickfaden, H., and Cremer, C. (2020b). The interchromatin compartment participates in the structural and functional organization of the cell nucleus. *Bioessays* *42*, 1900132.
- Cremer, T., Cremer, M., Hubner, B., Strickfaden, H., Smeets, D., Popken, J., Sterr, M., Markaki, Y., Rippe, K., and Cremer, C. (2015). The 4D nucleome: Evidence for a dynamic nuclear landscape based on co-aligned active and inactive nuclear compartments. *FEBS Lett* *589*, 2931-2943.
- Creyghton, M.P., Cheng, A.W., Welstead, G.G., Kooistra, T., Carey, B.W., Steine, E.J., Hanna, J., Lodato, M.A., Frampton, G.M., and Sharp, P.A. (2010). Histone H3K27ac separates active from poised enhancers and predicts developmental state. *Proceedings of the National Academy of Sciences* *107*, 21931-21936.
- Crick, F.H. (1978). Chromosome Structure And Function: Future Prospects. In *Gene Expression* (Elsevier), pp. 293-298.
- Croft, J.A., Bridger, J.M., Boyle, S., Perry, P., Teague, P., and Bickmore, W.A. (1999). Differences in the localization and morphology of chromosomes in the human nucleus. *Journal of Cell Biology* *145*, 1119-1131.

## REFERENCES

---

- Cui, K., and Zhao, K. (2012). Genome-wide approaches to determining nucleosome occupancy in metazoans using MNase-Seq. *Methods Mol Biol* 833, 413-419.
- Davidson, I.F., Bauer, B., Goetz, D., Tang, W., Wutz, G., and Peters, J.-M. (2019). DNA loop extrusion by human cohesin. *Science*, eaaz3418.
- Davis, C.A., Hitz, B.C., Sloan, C.A., Chan, E.T., Davidson, J.M., Gabdank, I., Hilton, J.A., Jain, K., Baymuradov, U.K., Narayanan, A.K., *et al.* (2018). The Encyclopedia of DNA elements (ENCODE): data portal update. *Nucleic Acids Res* 46, D794-d801.
- Deichmann, U. (2015). Chromatin: Its history, current research, and the seminal researchers and their philosophy. *Perspectives in biology and medicine* 58, 143-164.
- Dekker, J., Rippe, K., Dekker, M., and Kleckner, N. (2002). Capturing chromosome conformation. *science* 295, 1306-1311.
- Deng, D., Yan, C., Pan, X., Mahfouz, M., Wang, J., Zhu, J.K., Shi, Y., and Yan, N. (2012). Structural basis for sequence-specific recognition of DNA by TAL effectors. *Science* 335, 720-723.
- Derr, N.D., Goodman, B.S., Jungmann, R., Leschziner, A.E., Shih, W.M., and Reck-Peterson, S.L. (2012). Tug-of-war in motor protein ensembles revealed with a programmable DNA origami scaffold. *Science* 338, 662-665.
- Diermeier, S., Kolovos, P., Heizinger, L., Schwartz, U., Georgomanolis, T., Zirkel, A., Wedemann, G., Grosveld, F., Knoch, T.A., and Merkl, R. (2014). TNF $\alpha$  signalling primes chromatin for NF- $\kappa$ B binding and induces rapid and widespread nucleosome repositioning. *Genome biology* 15, 536.
- Dixon, J.R., Selvaraj, S., Yue, F., Kim, A., Li, Y., Shen, Y., Hu, M., Liu, J.S., and Ren, B. (2012). Topological domains in mammalian genomes identified by analysis of chromatin interactions. *Nature* 485, 376-380.
- Dostie, J., Richmond, T.A., Arnaout, R.A., Selzer, R.R., Lee, W.L., Honan, T.A., Rubio, E.D., Krumm, A., Lamb, J., Nusbaum, C., *et al.* (2006). Chromosome Conformation Capture Carbon Copy (5C): a massively parallel solution for mapping interactions between genomic elements. *Genome Res* 16, 1299-1309.
- Dultz, E., Mancini, R., Polles, G., Vallotton, P., Alber, F., and Weis, K. (2018). Quantitative imaging of chromatin decompaction in living cells. *Mol Biol Cell*, mbcE17110648.
- Eissenberg, J.C., Cartwright, I.L., Thomas, G.H., and Elgin, S.C. (1985). Selected topics in chromatin structure. *Annual review of genetics* 19, 485-536.
- Eltsov, M., MacLellan, K.M., Maeshima, K., Frangakis, A.S., and Dubochet, J. (2008). Analysis of cryo-electron microscopy images does not support the existence of 30-nm chromatin fibers in mitotic chromosomes in situ. *Proceedings of the National Academy of Sciences* 105, 19732-19737.
- Ernst, J., and Kellis, M. (2010). Discovery and characterization of chromatin states for systematic annotation of the human genome. *Nature biotechnology* 28, 817-825.
- Ernst, J., Kheradpour, P., Mikkelsen, T.S., Shores, N., Ward, L.D., Epstein, C.B., Zhang, X., Wang, L., Issner, R., and Coyne, M. (2011). Mapping and analysis of chromatin state dynamics in nine human cell types. *Nature* 473, 43-49.
- Eslami-Mossallam, B., Schiessel, H., and van Noort, J. (2016). Nucleosome dynamics: Sequence matters. *Advances in colloid and interface science* 232, 101-113.

- Falk, M., Feodorova, Y., Naumova, N., Imakaev, M., Lajoie, B.R., Leonhardt, H., Joffe, B., Dekker, J., Fudenberg, G., and Solovei, I. (2019). Heterochromatin drives compartmentalization of inverted and conventional nuclei. *Nature* *570*, 395-399.
- Ferrai, C., de Castro, I.J., Lavitas, L., Chotalia, M., and Pombo, A. (2010). Gene positioning. *Cold Spring Harbor perspectives in biology* *2*, a000588.
- Filion, G.J., van Bemmel, J.G., Braunschweig, U., Talhout, W., Kind, J., Ward, L.D., Brugman, W., de Castro, I.J., Kerkhoven, R.M., Bussemaker, H.J., *et al.* (2010). Systematic protein location mapping reveals five principal chromatin types in *Drosophila* cells. *Cell* *143*, 212-224.
- Finn, E.H., Pegoraro, G., Brandao, H.B., Valton, A.L., Oomen, M.E., Dekker, J., Mirny, L., and Misteli, T. (2019). Extensive Heterogeneity and Intrinsic Variation in Spatial Genome Organization. *Cell* *176*, 1502-1515 e1510.
- Fiorillo, L., Bianco, S., Esposito, A., Conte, M., Sciarretta, R., Musella, F., and Chiariello, A.M. (2019). A modern challenge of polymer physics: Novel ways to study, interpret, and reconstruct chromatin structure. *Wiley Interdisciplinary Reviews: Computational Molecular Science*, e1454.
- Flemming, W. (1882). *Zellsubstanz, kern und zelltheilung* (FCW Vogel).
- Franke, M., Ibrahim, D.M., Andrey, G., Schwarzer, W., Heinrich, V., Schöpflin, R., Kraft, K., Kempfer, R., Jerković, I., and Chan, W.-L. (2016). Formation of new chromatin domains determines pathogenicity of genomic duplications. *Nature* *538*, 265-269.
- Franklin, R.E., and Gosling, R.G. (1953). Molecular configuration in sodium thymonucleate. *Nature* *171*, 740-741.
- Fudenberg, G., Abdennur, N., Imakaev, M., Goloborodko, A., and Mirny, L.A. (2017). Emerging evidence of chromosome folding by loop extrusion. Paper presented at: Cold Spring Harbor symposia on quantitative biology (Cold Spring Harbor Laboratory Press).
- Fudenberg, G., Imakaev, M., Lu, C., Goloborodko, A., Abdennur, N., and Mirny, L.A. (2016). Formation of chromosomal domains by loop extrusion. *Cell reports* *15*, 2038-2049.
- Funke, J.J., Ketterer, P., Lieleg, C., Schunter, S., Korber, P., and Dietz, H. (2016). Uncovering the forces between nucleosomes using DNA origami. *Science advances* *2*, e1600974.
- Fussner, E., Strauss, M., Djuric, U., Li, R., Ahmed, K., Hart, M., Ellis, J., and Bazett-Jones, D.P. (2012). Open and closed domains in the mouse genome are configured as 10-nm chromatin fibres. *EMBO Rep* *13*, 992-996.
- Gall, J.G., and Pardue, M.L. (1969). Formation and detection of RNA-DNA hybrid molecules in cytological preparations. *Proceedings of the National Academy of Sciences* *63*, 378-383.
- Gan, L., Ladinsky, M.S., and Jensen, G.J. (2013). Chromatin in a marine picoeukaryote is a disordered assemblage of nucleosomes. *Chromosoma* *122*, 377-386.
- Garcia-Ramirez, M., Dong, F., and Ausio, J. (1992). Role of the histone "tails" in the folding of oligonucleosomes depleted of histone H1. *Journal of Biological Chemistry* *267*, 19587-19595.
- Gelali, E., Girelli, G., Matsumoto, M., Wernersson, E., Custodio, J., Mota, A., Schweitzer, M., Ferenc, K., Li, X., Mirzazadeh, R., *et al.* (2019). iFISH is a publically available resource enabling versatile DNA FISH to study genome architecture. *Nature Communications* *10*, 1636.

## REFERENCES

---

- Germier, T., Kocanova, S., Walther, N., Bancaud, A., Shaban, H.A., Sellou, H., Politi, A.Z., Ellenberg, J., Gallardo, F., and Bystricky, K. (2017). Real-time imaging of a single gene reveals transcription-initiated local confinement. *Biophysical journal* *113*, 1383-1394.
- Gesson, K., Rescheneder, P., Skoruppa, M.P., von Haeseler, A., Dechat, T., and Foisner, R. (2016). A-type lamins bind both hetero-and euchromatin, the latter being regulated by lamina-associated polypeptide 2 alpha. *Genome research* *26*, 462-473.
- Gilmour, D.S., and Lis, J.T. (1984). Detecting protein-DNA interactions in vivo: distribution of RNA polymerase on specific bacterial genes. *Proceedings of the National Academy of Sciences* *81*, 4275-4279.
- Gilmour, D.S., and Lis, J.T. (1985). In vivo interactions of RNA polymerase II with genes of *Drosophila melanogaster*. *Molecular and Cellular Biology* *5*, 2009.
- Giresi, P.G., Kim, J., McDaniell, R.M., Iyer, V.R., and Lieb, J.D. (2007). FAIRE (Formaldehyde-Assisted Isolation of Regulatory Elements) isolates active regulatory elements from human chromatin. *Genome research* *17*, 877-885.
- Godde, J., and Widom, J. (1992). Chromatin structure of *Schizosaccharomyces pombe*: a nucleosome repeat length that is shorter than the chromosomal DNA length. *Journal of molecular biology* *226*, 1009-1025.
- Görisch, S.M., Wachsmuth, M., Tóth, K.F., Lichter, P., and Rippe, K. (2005). Histone acetylation increases chromatin accessibility. *Journal of cell science* *118*, 5825-5834.
- Göttfert, F., Wurm, C.A., Mueller, V., Berning, S., Cordes, V.C., Honigmann, A., and Hell, S.W. (2013). Coaligned dual-channel STED nanoscopy and molecular diffusion analysis at 20 nm resolution. *Biophysical journal* *105*, L01-L03.
- Gross, D.S., and Garrard, W.T. (1988). Nuclease hypersensitive sites in chromatin. *Annual review of biochemistry* *57*, 159-197.
- Gu, B., Comerci, C.J., McCarthy, D.G., Saurabh, S., Moerner, W., and Wysocka, J. (2020). Opposing Effects of Cohesin and Transcription on CTCF Organization Revealed by Super-resolution Imaging. *Molecular Cell*.
- Gu, B., Swigut, T., Spencley, A., Bauer, M.R., Chung, M., Meyer, T., and Wysocka, J. (2018). Transcription-coupled changes in nuclear mobility of mammalian cis-regulatory elements. *Science*.
- Gustafsson, M.G. (2005). Nonlinear structured-illumination microscopy: wide-field fluorescence imaging with theoretically unlimited resolution. *Proceedings of the National Academy of Sciences* *102*, 13081-13086.
- Hajjoul, H., Mathon, J., Ranchon, H., Goiffon, I., Mozziconacci, J., Albert, B., Carrivain, P., Victor, J.-M., Gadal, O., and Bystricky, K. (2013). High-throughput chromatin motion tracking in living yeast reveals the flexibility of the fiber throughout the genome. *Genome research* *23*, 1829-1838.
- Hansen, J.C., Connolly, M., McDonald, C.J., Pan, A., Pryamkova, A., Ray, K., Seidel, E., Tamura, S., Rogge, R., and Maeshima, K. (2018). The 10-nm chromatin fiber and its relationship to interphase chromosome organization. *Biochem Soc Trans* *46*, 67-76.
- Hansen, K.H., Bracken, A.P., Pasini, D., Dietrich, N., Gehani, S.S., Monrad, A., Rappsilber, J., Lerdrup, M., and Helin, K. (2008). A model for transmission of the H3K27me3 epigenetic mark. *Nature cell biology* *10*, 1291-1300.

- Hargreaves, D.C., and Crabtree, G.R. (2011). ATP-dependent chromatin remodeling: genetics, genomics and mechanisms. *Cell research* *21*, 396-420.
- Harp, J.M., Hanson, B.L., Timm, D.E., and Bunick, G.J. (2000). Asymmetries in the nucleosome core particle at 2.5 Å resolution. *Acta Crystallogr D Biol Crystallogr* *56*, 1513-1534.
- Heitz, E. (1928a). Das heterochromatin der moose (Boroträger).
- Heitz, E. (1928b). Das Heterochromatin der Moose. *Jahrb Wiss Bot* *69*, 762-818.
- Hell, S.W., and Wichmann, J. (1994). Breaking the diffraction resolution limit by stimulated emission: stimulated-emission-depletion fluorescence microscopy. *Opt Lett* *19*, 780-782.
- Hershberg, E.A., Close, J.L., Camplisson, C.K., Attar, S., Chern, R., Liu, Y., Akilesh, S., Nicovich, P.R., and Beliveau, B.J. (2020). PaintSHOP enables the interactive design of transcriptome-and genome-scale oligonucleotide FISH experiments. *bioRxiv*.
- Hess, B., Kutzner, C., van der Spoel, D., and Lindahl, E. (2008). GROMACS 4: Algorithms for Highly Efficient, Load-Balanced, and Scalable Molecular Simulation. *J Chem Theory Comput* *4*, 435-447.
- Heun, P., Laroche, T., Shimada, K., Furrer, P., and Gasser, S.M. (2001). Chromosome dynamics in the yeast interphase nucleus. *Science* *294*, 2181-2186.
- Hoffman, M.M., Buske, O.J., Wang, J., Weng, Z., Bilmes, J.A., and Noble, W.S. (2012). Unsupervised pattern discovery in human chromatin structure through genomic segmentation. *Nature Methods* *9*, 473-476.
- Hoffman, M.M., Ernst, J., Wilder, S.P., Kundaje, A., Harris, R.S., Libbrecht, M., Giardine, B., Ellenbogen, P.M., Bilmes, J.A., Birney, E., *et al.* (2013). Integrative annotation of chromatin elements from ENCODE data. *Nucleic acids research* *41*, 827-841.
- Hotchkiss, R.D. (1948). The quantitative separation of purines, pyrimidines, and nucleosides by paper chromatography. *Journal of Biological Chemistry* *175*, 315-332.
- Hsieh, T.-H.S., Weiner, A., Lajoie, B., Dekker, J., Friedman, N., and Rando, O.J. (2015). Mapping nucleosome resolution chromosome folding in yeast by micro-C. *Cell* *162*, 108-119.
- Hu, H., Zhang, H., Wang, S., Ding, M., An, H., Hou, Y., Yang, X., Wei, W., Sun, Y., and Tang, C. (2017). Live visualization of genomic loci with BiFC-TALE. *Sci Rep* *7*, 40192.
- Huang, H., Sabari, B.R., Garcia, B.A., Allis, C.D., and Zhao, Y. (2014). SnapShot: histone modifications. *Cell* *159*, 458-458. e451.
- Huang, K., Li, Y., Shim, A.R., Virk, R.K., Agrawal, V., Eshein, A., Nap, R.J., Almassalha, L.M., Backman, V., and Szleifer, I. (2020). Physical and data structure of 3D genome. *Science advances* *6*, eaay4055.
- Hughes, A. (1959). A history of cytology (Abelard Schuman).
- Jeppsson, K., Kanno, T., Shirahige, K., and Sjögren, C. (2014). The maintenance of chromosome structure: positioning and functioning of SMC complexes. *Nature reviews Molecular cell biology* *15*, 601-614.
- John, S., Sabo, P.J., Thurman, R.E., Sung, M.-H., Biddie, S.C., Johnson, T.A., Hager, G.L., and Stamatoyannopoulos, J.A. (2011). Chromatin accessibility pre-determines glucocorticoid receptor binding patterns. *Nature genetics* *43*, 264-268.

## REFERENCES

---

- Johns, E. (1969). The histones, their interactions with DNA, and some aspects of gene control. Paper presented at: Ciba Foundation Symposium-Homeostatic Regulators (Wiley Online Library).
- Johnson-Buck, A., Nangreave, J., Kim, D.-N., Bathe, M., Yan, H., and Walter, N.G. (2013). Super-resolution fingerprinting detects chemical reactions and idiosyncrasies of single DNA pegboards. *Nano letters* *13*, 728-733.
- Joti, Y., Hikima, T., Nishino, Y., Kamada, F., Hihara, S., Takata, H., Ishikawa, T., and Maeshima, K. (2012). Chromosomes without a 30-nm chromatin fiber. *Nucleus* *3*, 404-410.
- Jungmann, R., Avendaño, M.S., Woehrstein, J.B., Dai, M., Shih, W.M., and Yin, P. (2014). Multiplexed 3D cellular super-resolution imaging with DNA-PAINT and Exchange-PAINT. *Nature Methods* *11*, 313-318.
- Jungmann, R., Scheible, M., and Simmel, F.C. (2012). Nanoscale imaging in DNA nanotechnology. *Wiley Interdisciplinary Reviews: Nanomedicine and Nanobiotechnology* *4*, 66-81.
- Jungmann, R., Steinhauer, C., Scheible, M., Kuzyk, A., Tinnefeld, P., and Simmel, F.C. (2010). Single-molecule kinetics and super-resolution microscopy by fluorescence imaging of transient binding on DNA origami. *Nano letters* *10*, 4756-4761.
- Katzgraber, H.G., Trebst, S., Huse, D.A., and Troyer, M. (2006). Feedback-optimized parallel tempering Monte Carlo. *Journal of Statistical Mechanics: Theory and Experiment* *2006*, P03018.
- Kent, N.A., Adams, S., Moorhouse, A., and Paszkiewicz, K. (2011). Chromatin particle spectrum analysis: a method for comparative chromatin structure analysis using paired-end mode next-generation DNA sequencing. *Nucleic acids research* *39*, e26-e26.
- Kepper, N., Ettig, R., Stehr, R., Marnach, S., Wedemann, G., and Rippe, K. (2011). Force spectroscopy of chromatin fibers: extracting energetics and structural information from Monte Carlo simulations. *Biopolymers* *95*, 435-447.
- Kepper, N., Foethke, D., Stehr, R., Wedemann, G., and Rippe, K. (2008). Nucleosome geometry and internucleosomal interactions control the chromatin fiber conformation. *Biophys J* *95*, 3692-3705.
- Keppler, A., Gendreizig, S., Gronemeyer, T., Pick, H., Vogel, H., and Johnsson, K. (2003). A general method for the covalent labeling of fusion proteins with small molecules in vivo. *Nature biotechnology* *21*, 86-89.
- Kim, C.A., and Berg, J.M. (1996). A 2.2 Å resolution crystal structure of a designed zinc finger protein bound to DNA. *Nature structural biology* *3*, 940-945.
- Kim, Y., Shi, Z., Zhang, H., Finkelstein, I.J., and Yu, H. (2019). Human cohesin compacts DNA by loop extrusion. *Science* *366*, 1345-1349.
- Kishi, J.Y., Lapan, S.W., Beliveau, B.J., West, E.R., Zhu, A., Sasaki, H.M., Saka, S.K., Wang, Y., Cepko, C.L., and Yin, P. (2019). SABER amplifies FISH: enhanced multiplexed imaging of RNA and DNA in cells and tissues. *Nat Methods* *16*, 533-544.
- Klenin, K., Merlitz, H., and Langowski, J. (1998). A Brownian dynamics program for the simulation of linear and circular DNA and other wormlike chain polyelectrolytes. *Biophys J* *74*, 780-788.
- Konig, P., Braunfeld, M.B., Sedat, J.W., and Agard, D.A. (2007). The three-dimensional structure of in vitro reconstituted *Xenopus laevis* chromosomes by EM tomography. *Chromosoma* *116*, 349-372.
- Kornberg, R.D. (1974). Chromatin structure: a repeating unit of histones and DNA. *Science* *184*, 868-871.

- Kornberg, R.D., and Thomas, J.O. (1974). Chromatin structure; oligomers of the histones. *Science* *184*, 865-868.
- Kossel, A. (1911). Ueber die chemische Beschaffenheit des Zellkerns (PA Norstedt).
- Lai, B., Gao, W., Cui, K., Xie, W., Tang, Q., Jin, W., Hu, G., Ni, B., and Zhao, K. (2018). Principles of nucleosome organization revealed by single-cell micrococcal nuclease sequencing. *Nature* *562*, 281-285.
- Lai, W.K., and Pugh, B.F. (2017). Understanding nucleosome dynamics and their links to gene expression and DNA replication. *Nature reviews Molecular cell biology* *18*, 548-562.
- Lakadamyali, M., and Cosma, M.P. (2020). Visualizing the genome in high resolution challenges our textbook understanding. *Nature Methods*.
- Lansdorp, P.M., Verwoerd, N.P., Van De Rijke, F.M., Dragowska, V., Little, M.-T., Dirks, R.W., Raap, A.K., and Tanke, H.J. (1996). Heterogeneity in telomere length of human chromosomes. *Human molecular genetics* *5*, 685-691.
- Levesque, M.J., and Raj, A. (2013). Single-chromosome transcriptional profiling reveals chromosomal gene expression regulation. *Nature methods* *10*, 246-248.
- Levi, V., Ruan, Q., Plutz, M., Belmont, A.S., and Gratton, E. (2005). Chromatin dynamics in interphase cells revealed by tracking in a two-photon excitation microscope. *Biophysical journal* *89*, 4275-4285.
- Levin, Y. (2002). Electrostatic correlations: from plasma to biology. *Reports on progress in physics* *65*, 1577.
- Li, Q., Peterson, K.R., Fang, X., and Stamatoyannopoulos, G. (2002). Locus control regions. *Blood* *100*, 3077-3086.
- Li, Z., and Kono, H. (2016). Distinct roles of histone H3 and H2A tails in nucleosome stability. *Scientific reports* *6*, 31437.
- Lieberman-Aiden, E., van Berkum, N.L., Williams, L., Imakaev, M., Ragoczy, T., Telling, A., Amit, I., Lajoie, B.R., Sabo, P.J., Dorschner, M.O., *et al.* (2009). Comprehensive mapping of long-range interactions reveals folding principles of the human genome. *Science* *326*, 289-293.
- Lin, C., Jungmann, R., Leifer, A.M., Li, C., Levner, D., Church, G.M., Shih, W.M., and Yin, P. (2012). Submicrometre geometrically encoded fluorescent barcodes self-assembled from DNA. *Nature chemistry* *4*, 832-839.
- Litwin, I., Pilarczyk, E., and Wysocki, R. (2018). The emerging role of cohesin in the DNA damage response. *Genes* *9*, 581.
- Los, G.V., Encell, L.P., McDougall, M.G., Hartzell, D.D., Karassina, N., Zimprich, C., Wood, M.G., Learish, R., Ohana, R.F., and Urh, M. (2008). HaloTag: a novel protein labeling technology for cell imaging and protein analysis. *ACS chemical biology* *3*, 373-382.
- Lucas, J.S., Zhang, Y., Dudko, O.K., and Murre, C. (2014). 3D trajectories adopted by coding and regulatory DNA elements: first-passage times for genomic interactions. *Cell* *158*, 339-352.
- Luger, K., Mader, A.W., Richmond, R.K., Sargent, D.F., and Richmond, T.J. (1997). Crystal structure of the nucleosome core particle at 2.8 Å resolution. *Nature* *389*, 251-260.

## REFERENCES

---

- Lukinavičius, G., Blaukopf, C., Pershagen, E., Schena, A., Reymond, L., Derivery, E., Gonzalez-Gaitan, M., D'Este, E., Hell, S.W., and Gerlich, D.W. (2015). SiR–Hoechst is a far-red DNA stain for live-cell nanoscopy. *Nature communications* 6, 1-7.
- Lund, E.G., Duband-Goulet, I., Oldenburg, A., Buendia, B., and Collas, P. (2015). Distinct features of lamin A-interacting chromatin domains mapped by ChIP-sequencing from sonicated or micrococcal nuclease-digested chromatin. *Nucleus* 6, 30-39.
- Luque, A., Collepardo-Guevara, R., Grigoryev, S., and Schlick, T. (2014). Dynamic condensation of linker histone C-terminal domain regulates chromatin structure. *Nucleic acids research* 42, 7553-7560.
- Ma, H., Naseri, A., Reyes-Gutierrez, P., Wolfe, S.A., Zhang, S., and Pederson, T. (2015). Multicolor CRISPR labeling of chromosomal loci in human cells. *Proc Natl Acad Sci U S A* 112, 3002-3007.
- Ma, H., Tu, L.-C., Naseri, A., Chung, Y.-C., Grunwald, D., Zhang, S., and Pederson, T. (2018). CRISPR-Sirius: RNA scaffolds for signal amplification in genome imaging. *Nature Methods* 15, 928-931.
- Ma, H., Tu, L.C., Chung, Y.C., Naseri, A., Grunwald, D., Zhang, S., and Pederson, T. (2019). Cell cycle- and genomic distance-dependent dynamics of a discrete chromosomal region. *J Cell Biol.*
- Ma, Y., Wang, M., Li, W., Zhang, Z., Zhang, X., Tan, T., Zhang, X.-E., and Cui, Z. (2017). Live cell imaging of single genomic loci with quantum dot-labeled TALEs. *Nature Communications* 8, 15318.
- Maeshima, K., Ide, S., and Babokhov, M. (2019). Dynamic chromatin organization without the 30-nm fiber. *Curr Opin Cell Biol* 58, 95-104.
- Maffeo, C., Schopflin, R., Brutzer, H., Stehr, R., Aksimentiev, A., Wedemann, G., and Seidel, R. (2010). DNA-DNA interactions in tight supercoils are described by a small effective charge density. *Phys Rev Lett* 105, 158101.
- Mak, A.N., Bradley, P., Cernadas, R.A., Bogdanove, A.J., and Stoddard, B.L. (2012). The crystal structure of TAL effector PthXo1 bound to its DNA target. *Science* 335, 716-719.
- Mangenot, S., Leforestier, A., Vachette, P., Durand, D., and Livolant, F. (2002). Salt-induced conformation and interaction changes of nucleosome core particles. *Biophysical journal* 82, 345-356.
- Manuelidis, L. (1985). Individual interphase chromosome domains revealed by in situ hybridization. *Human genetics* 71, 288-293.
- Markaki, Y., Smeets, D., Fiedler, S., Schmid, V.J., Schermelleh, L., Cremer, T., and Cremer, M. (2012). The potential of 3D-FISH and super-resolution structured illumination microscopy for studies of 3D nuclear architecture: 3D structured illumination microscopy of defined chromosomal structures visualized by 3D (immuno)-FISH opens new perspectives for studies of nuclear architecture. *Bioessays* 34, 412-426.
- Marshall, W., Straight, A., Marko, J., Swedlow, J., Dernburg, A., Belmont, A., Murray, A., Agard, D., and Sedat, J. (1997). Interphase chromosomes undergo constrained diffusional motion in living cells. *Current Biology* 7, 930-939.
- Mateo, L.J., Murphy, S.E., Hafner, A., Cinquini, I.S., Walker, C.A., and Boettiger, A.N. (2019). Visualizing DNA folding and RNA in embryos at single-cell resolution. *Nature* 568, 49-54.
- Mavrich, T.N., Jiang, C., Ioshikhes, I.P., Li, X., Venters, B.J., Zanton, S.J., Tomsho, L.P., Qi, J., Glaser, R.L., and Schuster, S.C. (2008). Nucleosome organization in the *Drosophila* genome. *Nature* 453, 358-362.

- Mayerova, N., Cipak, L., and Gregan, J. (2020). Cohesin Biology: From Passive Rings to Molecular Motors. *Trends in Genetics*.
- McCord, R.P., Kaplan, N., and Giorgetti, L. (2020). Chromosome conformation capture and beyond: toward an integrative view of chromosome structure and function. *Molecular Cell* *77*, 688-708.
- McDowall, A., Smith, J., and Dubochet, J. (1986). Cryo-electron microscopy of vitrified chromosomes in situ. *The EMBO journal* *5*, 1395-1402.
- McGhee, J.D., Wood, W.I., Dolan, M., Engel, J.D., and Felsenfeld, G. (1981). A 200 base pair region at the 5' end of the chicken adult  $\beta$ -globin gene is accessible to nuclease digestion. *Cell* *27*, 45-55.
- Mehta, G.D., Kumar, R., Srivastava, S., and Ghosh, S.K. (2013). Cohesin: functions beyond sister chromatid cohesion. *FEBS letters* *587*, 2299-2312.
- Melters, D.P., Pitman, M., Rakshit, T., Dimitriadis, E.K., Bui, M., Papoian, G.A., and Dalal, Y. (2019). Intrinsic elasticity of nucleosomes is encoded by histone variants and calibrated by their binding partners. *Proceedings of the National Academy of Sciences* *116*, 24066-24074.
- Merkenschlager, M., and Nora, E.P. (2016). CTCF and cohesin in genome folding and transcriptional gene regulation. *Annual review of genomics and human genetics* *17*, 17-43.
- Metropolis, N., Rosenbluth, A.W., Rosenbluth, M.N., Teller, A.H., and Teller, E. (1953). Equation of state calculations by fast computing machines. *The journal of chemical physics* *21*, 1087-1092.
- Meuleman, W., Muratov, A., Rynes, E., Halow, J., Lee, K., Bates, D., Diegel, M., Dunn, D., Neri, F., and Teodosiadis, A. (2020). Index and biological spectrum of human DNase I hypersensitive sites. *Nature* *584*, 244-251.
- Miescher-Rüsch, F. (1871). Ueber die chemische Zusammensetzung der Eiterzellen.
- Mills, F.C., Fisher, L.M., Kuroda, R., Ford, A.M., and Gould, H.J. (1983). DNase I hypersensitive sites in the chromatin of human  $\mu$  immunoglobulin heavy-chain genes. *Nature* *306*, 809-812.
- Mirny, L.A. (2010). Nucleosome-mediated cooperativity between transcription factors. *Proceedings of the National Academy of Sciences* *107*, 22534-22539.
- Mirny, L.A. (2011). The fractal globule as a model of chromatin architecture in the cell. *Chromosome Res* *19*, 37-51.
- Mirny, L.A., Imakaev, M., and Abdennur, N. (2019). Two major mechanisms of chromosome organization. *Curr Opin Cell Biol* *58*, 142-152.
- Misteli, T. (2020). *The Self-Organizing Genome: Principles of Genome Architecture and Function*. Cell.
- Mitchell-Jordan, S., Chen, H., Franklin, S., Stefani, E., Bentolila, L.A., and Vondriska, T.M. (2012). Features of endogenous cardiomyocyte chromatin revealed by super-resolution STED microscopy. *Journal of molecular and cellular cardiology* *53*, 552-558.
- Miyanari, Y., Ziegler-Birling, C., and Torres-Padilla, M.E. (2013). Live visualization of chromatin dynamics with fluorescent TALEs. *Nat Struct Mol Biol* *20*, 1321-1324.
- Moerner, W.E., and Kador, L. (1989). Optical detection and spectroscopy of single molecules in a solid. *Physical review letters* *62*, 2535.

## REFERENCES

---

- Moller, J., and de Pablo, J.J. (2020). Bottom-Up Meets Top-Down: The Crossroads of Multiscale Chromatin Modeling. *Biophys J* *118*, 2057-2065.
- Moller, J., Lequieu, J., and de Pablo, J.J. (2019). The free energy landscape of internucleosome interactions and its relation to chromatin fiber structure. *ACS central science* *5*, 341-348.
- Moore, J.E., Purcaro, M.J., Pratt, H.E., Epstein, C.B., Shores, N., Adrian, J., Kawli, T., Davis, C.A., Dobin, A., and Kaul, R. (2020). Expanded encyclopaedias of DNA elements in the human and mouse genomes. *Nature* *583*, 699-710.
- Mörl, M.-C., Zülske, T., Schöpflin, R., and Wedemann, G. (2019). Data formats for modelling the spatial structure of chromatin based on experimental positions of nucleosomes. *AIMS Biophysics* *6*, 83.
- Muller, H.J. (1927). Artificial transmutation of the gene. *Science* *66*, 84-87.
- Muller, H.J. (1946). Thomas Hunt Morgan 1866-1945. *Science* *103*, 550-551.
- Muller, O., Kepper, N., Schopflin, R., Ettig, R., Rippe, K., and Wedemann, G. (2014). Changing chromatin fiber conformation by nucleosome repositioning. *Biophys J* *107*, 2141-2150.
- Nasmyth, K., and Haering, C.H. (2009). Cohesin: its roles and mechanisms. *Annual review of genetics* *43*.
- Natale, F., Rapp, A., Yu, W., Maiser, A., Harz, H., Scholl, A., Grulich, S., Anton, T., Hörl, D., Chen, W., *et al.* (2017). Identification of the elementary structural units of the DNA damage response. *Nature Communications* *8*, 15760.
- Natsume, T., Kiyomitsu, T., Saga, Y., and Kanemaki, M.T. (2016). Rapid protein depletion in human cells by auxin-inducible degron tagging with short homology donors. *Cell reports* *15*, 210-218.
- Neguembor, M.V., Sebastian-Perez, R., Aulicino, F., Gomez-Garcia, P.A., Cosma, M.P., and Lakadamyali, M. (2018). (Po) STAC (Po lycistrionic S un TA g modified C RISPR) enables live-cell and fixed-cell super-resolution imaging of multiple genes. *Nucleic acids research* *46*, e30-e30.
- Nielsen, P.E., Egholm, M., Berg, R.H., and Buchardt, O. (1991). Sequence-selective recognition of DNA by strand displacement with a thymine-substituted polyamide. *Science* *254*, 1497-1500.
- Nir, G., Farabella, I., Perez Estrada, C., Ebeling, C.G., Beliveau, B.J., Sasaki, H.M., Lee, S.D., Nguyen, S.C., McCole, R.B., Chatteraj, S., *et al.* (2018). Walking along chromosomes with super-resolution imaging, contact maps, and integrative modeling. *PLoS Genet* *14*, e1007872.
- Nishino, Y., Eltsov, M., Joti, Y., Ito, K., Takata, H., Takahashi, Y., Hihara, S., Frangakis, A.S., Imamoto, N., and Ishikawa, T. (2012). Human mitotic chromosomes consist predominantly of irregularly folded nucleosome fibres without a 30-nm chromatin structure. *The EMBO journal* *31*, 1644-1653.
- Nishiyama, T. (2019). Cohesion and cohesin-dependent chromatin organization. *Current opinion in cell biology* *58*, 8-14.
- NobelPrize.org (2020). Francis Crick – Photo gallery. Nobel Media AB 2020
- Noll, M., and Kornberg, R.D. (1977). Action of micrococcal nuclease on chromatin and the location of histone H1. *Journal of molecular biology* *109*, 393-404.

- Nora, E.P., Goloborodko, A., Valton, A.L., Gibcus, J.H., Uebersohn, A., Abdennur, N., Dekker, J., Mirny, L.A., and Bruneau, B.G. (2017). Targeted Degradation of CTCF Decouples Local Insulation of Chromosome Domains from Genomic Compartmentalization. *Cell* *169*, 930-944 e922.
- Nora, E.P., Lajoie, B.R., Schulz, E.G., Giorgetti, L., Okamoto, I., Servant, N., Piolot, T., van Berkum, N.L., Meisig, J., and Sedat, J. (2012). Spatial partitioning of the regulatory landscape of the X-inactivation centre. *Nature* *485*, 381-385.
- Nordenskiöld, L., Lyubartsev, A.P., and Korolev, N. (2017). Coarse-grained modeling of nucleosomes and chromatin (CRC Press).
- Norouzi, D., and Zhurkin, V.B. (2018). Dynamics of chromatin fibers: comparison of monte carlo simulations with force spectroscopy. *Biophysical journal* *115*, 1644-1655.
- Nozaki, T., Imai, R., Tanbo, M., Nagashima, R., Tamura, S., Tani, T., Joti, Y., Tomita, M., Hibino, K., Kanemaki, M.T., *et al.* (2017). Dynamic Organization of Chromatin Domains Revealed by Super-Resolution Live-Cell Imaging. *Mol Cell* *67*, 282-293 e287.
- Nuebler, J., Fudenberg, G., Imakaev, M., Abdennur, N., and Mirny, L.A. (2018). Chromatin organization by an interplay of loop extrusion and compartmental segregation. *Proceedings of the National Academy of Sciences* *115*, E6697-E6706.
- Ohno, M., Ando, T., Priest, D.G., Kumar, V., Yoshida, Y., and Taniguchi, Y. (2019). Sub-nucleosomal Genome Structure Reveals Distinct Nucleosome Folding Motifs. *Cell* *176*, 520-534 e525.
- Olins, A.L., and Olins, D.E. (1974). Spheroid chromatin units (v bodies). *Science* *183*, 330-332.
- Olins, D.E., and Olins, A.L. (2003). Chromatin history: our view from the bridge. *Nature Reviews Molecular Cell Biology* *4*, 809-814.
- Otterstrom, J., Castells-Garcia, A., Vicario, C., Gomez-Garcia, P.A., Cosma, M.P., and Lakadamyali, M. (2019). Super-resolution microscopy reveals how histone tail acetylation affects DNA compaction within nucleosomes in vivo. *Nucleic acids research* *47*, 8470-8484.
- Ou, H.D., Phan, S., Deerinck, T.J., Thor, A., Ellisman, M.H., and O'Shea, C.C. (2017). ChromEMT: Visualizing 3D chromatin structure and compaction in interphase and mitotic cells. *Science* *357*.
- Oudet, P., Gross-Bellard, M., and Chambon, P. (1975). Electron microscopic and biochemical evidence that chromatin structure is a repeating unit. *Cell* *4*, 281-300.
- Öztürk, M.A., Cojocaru, V., and Wade, R.C. (2018). Dependence of chromatosome structure on linker histone sequence and posttranslational modification. *Biophysical journal* *114*, 2363-2375.
- Panne, D., Maniatis, T., and Harrison, S.C. (2007). An atomic model of the interferon- $\beta$  enhanceosome. *Cell* *129*, 1111-1123.
- Parelho, V., Hadjur, S., Spivakov, M., Leleu, M., Sauer, S., Gregson, H.C., Jarmuz, A., Canzonetta, C., Webster, Z., and Nesterova, T. (2008). Cohesins functionally associate with CTCF on mammalian chromosome arms. *Cell* *132*, 422-433.
- Park, P.J. (2009). ChIP-seq: advantages and challenges of a maturing technology. *Nature Reviews Genetics* *10*, 669-680.
- Parmar, J.J., and Padinhateeri, R. (2020). Nucleosome positioning and chromatin organization. *Current Opinion in Structural Biology* *64*, 111-118.

## REFERENCES

---

- Pavletich, N.P., and Pabo, C.O. (1991). Zinc finger-DNA recognition: crystal structure of a Zif268-DNA complex at 2.1 Å. *Science* *252*, 809-817.
- Pawelcz, N. (2001). Walther Flemming: pioneer of mitosis research. *Nature reviews Molecular cell biology* *2*, 72-75.
- Pellestor, F., Andréo, B., Taneja, K., and Williams, B. (2003). PNA on human sperm: a new approach for in situ aneuploidy estimation. *European journal of human genetics* *11*, 337-341.
- Pellestor, F., and Paulasova, P. (2004). The peptide nucleic acids (PNAs), powerful tools for molecular genetics and cytogenetics. *European journal of human genetics* *12*, 694-700.
- Peric-Hupkes, D., Meuleman, W., Pagie, L., Bruggeman, S.W., Solovei, I., Brugman, W., Gräf, S., Flicek, P., Kerkhoven, R.M., and van Lohuizen, M. (2010). Molecular maps of the reorganization of genome-nuclear lamina interactions during differentiation. *Molecular cell* *38*, 603-613.
- Perišić, O., Portillo-Ledesma, S., and Schlick, T. (2019). Sensitive effect of linker histone binding mode and subtype on chromatin condensation. *Nucleic acids research* *47*, 4948-4957.
- Persson, F., Bingen, P., Staudt, T., Engelhardt, J., Tegenfeldt, J., and Hell, S.W. (2011). Fluorescence nanoscopy of single DNA molecules by using stimulated emission depletion (STED). *Angewandte Chemie International Edition* *50*, 5581-5583.
- Peters, J.-M., Tedeschi, A., and Schmitz, J. (2008). The cohesin complex and its roles in chromosome biology. *Genes & development* *22*, 3089-3114.
- Phillips, J.E., and Corces, V.G. (2009). CTCF: master weaver of the genome. *Cell* *137*, 1194-1211.
- Qin, P., Parlak, M., Kuscu, C., Bandaria, J., Mir, M., Szlachta, K., Singh, R., Darzacq, X., Yildiz, A., and Adli, M. (2017). Live cell imaging of low- and non-repetitive chromosome loci using CRISPR-Cas9. *Nature Communications* *8*, 14725.
- Rabl, C. (1885). Über zelltheilung. *Morphol Jahrb* *10*, 214-330.
- Ram, O., Goren, A., Amit, I., Shores, N., Yosef, N., Ernst, J., Kellis, M., Gymrek, M., Issner, R., and Coyne, M. (2011). Combinatorial patterning of chromatin regulators uncovered by genome-wide location analysis in human cells. *Cell* *147*, 1628-1639.
- Ramachandran, S., and Henikoff, S. (2015). Replicating nucleosomes. *Science Advances* *1*, e1500587.
- Rao, S.S.P., Huang, S.C., Glenn St Hilaire, B., Engreitz, J.M., Perez, E.M., Kieffer-Kwon, K.R., Sanborn, A.L., Johnstone, S.E., Bascom, G.D., Bochkov, I.D., *et al.* (2017). Cohesin Loss Eliminates All Loop Domains. *Cell* *171*, 305-320 e324.
- Rao, Suhas S.P., Huntley, Miriam H., Durand, Neva C., Stamenova, Elena K., Bochkov, Ivan D., Robinson, James T., Sanborn, Adrian L., Machol, I., Omer, Arina D., Lander, Eric S., *et al.* (2014). A 3D Map of the Human Genome at Kilobase Resolution Reveals Principles of Chromatin Looping. *Cell* *159*, 1665-1680.
- Ricci, M.A., Manzo, C., Garcia-Parajo, M.F., Lakadamyali, M., and Cosma, M.P. (2015). Chromatin fibers are formed by heterogeneous groups of nucleosomes in vivo. *Cell* *160*, 1145-1158.
- Richmond, T.J., and Davey, C.A. (2003). The structure of DNA in the nucleosome core. *Nature* *423*, 145-150.

- Richmond, T.J., Finch, J.T., Rushton, B., Rhodes, D., and Klug, A. (1984). Structure of the nucleosome core particle at 7 Å resolution. *Nature* *311*, 532-537.
- Rippe, K., Stehr, R., and Wedemann, G. (2012). Monte Carlo simulations of nucleosome chains to identify factors that control DNA compaction and access. *Innovations in Biomolecular Modeling and Simulations* T Schlick, editor Royal Society of Chemistry, Cambridge, 198-235.
- Rosa, A., and Everaers, R. (2008). Structure and dynamics of interphase chromosomes. *PLoS Comput Biol* *4*, e1000153.
- Rosin, L.F., Nguyen, S.C., and Joyce, E.F. (2018). Condensin II drives large-scale folding and spatial partitioning of interphase chromosomes in *Drosophila* nuclei. *PLoS genetics* *14*, e1007393.
- Rouhanifard, S.H., Mellis, I.A., Dunagin, M., Bayatpour, S., Jiang, C.L., Dardani, I., Symmons, O., Emert, B., Torre, E., Cote, A., *et al.* (2019). ClampFISH detects individual nucleic acid molecules using click chemistry-based amplification. *Nature Biotechnology* *37*, 84-89.
- Routh, A., Sandin, S., and Rhodes, D. (2008). Nucleosome repeat length and linker histone stoichiometry determine chromatin fiber structure. *Proceedings of the National Academy of Sciences* *105*, 8872-8877.
- Rudkin, G.T., and Stollar, B. (1977). High resolution detection of DNA-RNA hybrids in situ by indirect immunofluorescence. *Nature* *265*, 472-473.
- Saarbach, J., Sabale, P.M., and Winssinger, N. (2019). Peptide nucleic acid (PNA) and its applications in chemical biology, diagnostics, and therapeutics. *Current Opinion in Chemical Biology* *52*, 112-124.
- Sabo, P.J., Kuehn, M.S., Thurman, R., Johnson, B.E., Johnson, E.M., Cao, H., Yu, M., Rosenzweig, E., Goldy, J., Haydock, A., *et al.* (2006). Genome-scale mapping of DNase I sensitivity in vivo using tiling DNA microarrays. *Nat Methods* *3*, 511-518.
- Sadaie, M., Salama, R., Carroll, T., Tomimatsu, K., Chandra, T., Young, A.R., Narita, M., Pérez-Mancera, P.A., Bennett, D.C., and Chong, H. (2013). Redistribution of the Lamin B1 genomic binding profile affects rearrangement of heterochromatic domains and SAHF formation during senescence. *Genes & development* *27*, 1800-1808.
- Sahl, S.J., Hell, S.W., and Jakobs, S. (2017). Fluorescence nanoscopy in cell biology. *Nature reviews Molecular cell biology* *18*, 685.
- Sanborn, A.L., Rao, S.S., Huang, S.-C., Durand, N.C., Huntley, M.H., Jewett, A.I., Bochkov, I.D., Chinnappan, D., Cutkosky, A., and Li, J. (2015). Chromatin extrusion explains key features of loop and domain formation in wild-type and engineered genomes. *Proceedings of the National Academy of Sciences* *112*, E6456-E6465.
- Schardin, M., Cremer, T., Hager, H., and Lang, M. (1985). Specific staining of human chromosomes in Chinese hamster x man hybrid cell lines demonstrates interphase chromosome territories. *Human genetics* *71*, 281-287.
- Scheffer, M.P., Eltsov, M., and Frangakis, A.S. (2011). Evidence for short-range helical order in the 30-nm chromatin fibers of erythrocyte nuclei. *Proc Natl Acad Sci U S A* *108*, 16992-16997.
- Schoenfelder, S., and Fraser, P. (2019). Long-range enhancer-promoter contacts in gene expression control. *Nat Rev Genet* *20*, 437-455.

## REFERENCES

---

- Schopflin, R., Teif, V.B., Muller, O., Weinberg, C., Rippe, K., and Wedemann, G. (2013). Modeling nucleosome position distributions from experimental nucleosome positioning maps. *Bioinformatics* 29, 2380-2386.
- Schueder, F., Strauss, M.T., Hoerl, D., Schnitzbauer, J., Schlichthaerle, T., Strauss, S., Yin, P., Harz, H., Leonhardt, H., and Jungmann, R. (2017). Universal Super-Resolution Multiplexing by DNA Exchange. *Angewandte Chemie (International ed in English)* 56, 4052-4055.
- Schwach, J., Kolobynina, K., Brandstetter, K., Gerlach, M., Ochtrop, P., Helma, J., Hackenberger, C.P.R., Harz, H., Cardoso, M.C., Leonhardt, H., *et al.* (2020). Site-Specific Antibody Fragment Conjugates for Reversible Staining in Fluorescence Microscopy. *Chembiochem*.
- Schwarzer, W., Abdennur, N., Goloborodko, A., Pekowska, A., Fudenberg, G., Loe-Mie, Y., Fonseca, N.A., Huber, W., Haering, C.H., and Mirny, L. (2017). Two independent modes of chromatin organization revealed by cohesin removal. *Nature* 551, 51-56.
- Shaban, H.A., Barth, R., and Bystricky, K. (2018). Formation of correlated chromatin domains at nanoscale dynamic resolution during transcription. *Nucleic acids research* 46, e77-e77.
- Shah, P.P., Donahue, G., Otte, G.L., Capell, B.C., Nelson, D.M., Cao, K., Aggarwala, V., Cruickshanks, H.A., Rai, T.S., and McBryan, T. (2013). Lamin B1 depletion in senescent cells triggers large-scale changes in gene expression and the chromatin landscape. *Genes & development* 27, 1787-1799.
- Shah, S., Takei, Y., Zhou, W., Lubeck, E., Yun, J., Eng, C.-H.L., Koulouena, N., Cronin, C., Karp, C., and Liaw, E.J. (2018). Dynamics and spatial genomics of the nascent transcriptome by intron seqFISH. *Cell* 174, 363-376. e316.
- Simonis, M., Klous, P., Splinter, E., Moshkin, Y., Willemsen, R., De Wit, E., Van Steensel, B., and De Laat, W. (2006). Nuclear organization of active and inactive chromatin domains uncovered by chromosome conformation capture–on-chip (4C). *Nature genetics* 38, 1348-1354.
- Singh, V.P., and Gerton, J.L. (2015). Cohesin and human disease: lessons from mouse models. *Current Opinion in Cell Biology* 37, 9-17.
- Solovei, I., Cavallo, A., Schermelleh, L., Jaunin, F., Scasselati, C., Cmarko, D., Cremer, C., Fakan, S., and Cremer, T. (2002). Spatial preservation of nuclear chromatin architecture during three-dimensional fluorescence in situ hybridization (3D-FISH). *Exp Cell Res* 276, 10-23.
- Song, F., Chen, P., Sun, D., Wang, M., Dong, L., Liang, D., Xu, R.-M., Zhu, P., and Li, G. (2014). Cryo-EM study of the chromatin fiber reveals a double helix twisted by tetranucleosomal units. *Science* 344, 376-380.
- Spahn, C., Grimm, J.B., Lavis, L.D., Lampe, M., and Heilemann, M. (2019). Whole-Cell, 3D, and Multicolor STED Imaging with Exchangeable Fluorophores. *Nano Letters* 19, 500-505.
- Spilianakis, C.G., and Flavell, R.A. (2004). Long-range intrachromosomal interactions in the T helper type 2 cytokine locus. *Nature immunology* 5, 1017-1027.
- Stack, S.M., Brown, D.B., and Dewey, W. (1977). Visualization of interphase chromosomes. *Journal of cell science* 26, 281-299.
- Stalder, J., Larsen, A., Engel, J.D., Dolan, M., Groudine, M., and Weintraub, H. (1980). Tissue-specific DNA cleavages in the globin chromatin domain introduced by DNAase I. *Cell* 20, 451-460.
- Stehr, R., Kepper, N., Rippe, K., and Wedemann, G. (2008a). The effect of internucleosomal interaction on folding of the chromatin fiber. *Biophysical journal* 95, 3677-3691.

- Stehr, R., Kepper, N., Rippe, K., and Wedemann, G. (2008b). The effect of internucleosomal interaction on folding of the chromatin fiber. *Biophys J* 95, 3677-3691.
- Stehr, R., Schopflin, R., Ettig, R., Kepper, N., Rippe, K., and Wedemann, G. (2010). Exploring the conformational space of chromatin fibers and their stability by numerical dynamic phase diagrams. *Biophys J* 98, 1028-1037.
- Stergachis, A.B., Debo, B.M., Haugen, E., Churchman, L.S., and Stamatoyannopoulos, J.A. (2020). Single-molecule regulatory architectures captured by chromatin fiber sequencing. *Science* 368, 1449-1454.
- Sturtevant, A.H. (1925). The effects of unequal crossing over at the bar locus in *Drosophila*. *Genetics* 10, 117.
- Svaren, J., Klebanow, E., Sealy, L., and Chalkley, R. (1994). Analysis of the competition between nucleosome formation and transcription factor binding. *Journal of Biological Chemistry* 269, 9335-9344.
- Swendsen, R.H., and Wang, J.S. (1986). Replica Monte Carlo simulation of spin glasses. *Phys Rev Lett* 57, 2607-2609.
- Symmons, O., Pan, L., Remeseiro, S., Aktas, T., Klein, F., Huber, W., and Spitz, F. (2016). The Shh topological domain facilitates the action of remote enhancers by reducing the effects of genomic distances. *Developmental cell* 39, 529-543.
- Szabo, Q., Jost, D., Chang, J.-M., Cattoni, D.I., Papadopoulos, G.L., Bonev, B., Sexton, T., Gurgo, J., Jacquier, C., and Nollmann, M. (2018). TADs are 3D structural units of higher-order chromosome organization in *Drosophila*. *Science advances* 4, eaar8082.
- Teif, V.B., Vainshtein, Y., Caudron-Herger, M., Mallm, J.-P., Marth, C., Höfer, T., and Rippe, K. (2012). Genome-wide nucleosome positioning during embryonic stem cell development. *Nature structural & molecular biology* 19, 1185.
- Thanisch, K., Schneider, K., Morbitzer, R., Solovei, I., Lahaye, T., Bultmann, S., and Leonhardt, H. (2014). Targeting and tracing of specific DNA sequences with dTALEs in living cells. *Nucleic Acids Res* 42, e38.
- Thurman, R.E., Rynes, E., Humbert, R., Vierstra, J., Maurano, M.T., Haugen, E., Sheffield, N.C., Stergachis, A.B., Wang, H., Vernot, B., *et al.* (2012). The accessible chromatin landscape of the human genome. *Nature* 489, 75-82.
- Tolhuis, B., Palstra, R.J., Splinter, E., Grosveld, F., and de Laat, W. (2002). Looping and interaction between hypersensitive sites in the active beta-globin locus. *Mol Cell* 10, 1453-1465.
- Trojer, P., and Reinberg, D. (2007). Facultative heterochromatin: is there a distinctive molecular signature? *Molecular cell* 28, 1-13.
- Uberbacher, E.C., and Bunick, G.J. (1985). X-ray structure of the nucleosome core particle. *J Biomol Struct Dyn* 2, 1033-1055.
- Valouev, A., Johnson, S.M., Boyd, S.D., Smith, C.L., Fire, A.Z., and Sidow, A. (2011). Determinants of nucleosome organization in primary human cells. *Nature* 474, 516-520.
- Van Holde, K.E. (1989). *Chromatin* (Heidelberg: Springer Science & Business Media).
- van Mierlo, G., Veenstra, G.J.C., Vermeulen, M., and Marks, H. (2019). The complexity of PRC2 subcomplexes. *Trends in cell biology* 29, 660-671.

## REFERENCES

---

- van Ruiten, M.S., and Rowland, B.D. (2018). SMC complexes: universal DNA looping machines with distinct regulators. *Trends in Genetics* 34, 477-487.
- Vernimmen, D., Gobbi, M.D., Sloane-Stanley, J.A., Wood, W.G., and Higgs, D.R. (2007). Long-range chromosomal interactions regulate the timing of the transition between poised and active gene expression. *The EMBO journal* 26, 2041-2051.
- Vierstra, J., Lazar, J., Sandstrom, R., Halow, J., Lee, K., Bates, D., Diegel, M., Dunn, D., Neri, F., and Haugen, E. (2020). Global reference mapping of human transcription factor footprints. *Nature* 583, 729-736.
- Waldeyer, W. (1888). Über Karyokinese und ihre Beziehungen zu den Befruchtungsvorgängen. *Archiv für mikroskopische Anatomie* 32, 1.
- Walker, D.A., Kowalczyk, B., de la Cruz, M.O., and Grzybowski, B.A. (2011). Electrostatics at the nanoscale. *Nanoscale* 3, 1316-1344.
- Wang, S., Su, J.H., Beliveau, B.J., Bintu, B., Moffitt, J.R., Wu, C.T., and Zhuang, X. (2016). Spatial organization of chromatin domains and compartments in single chromosomes. *Science* 353, 598-602.
- Watson, J.D., and Crick, F.H. (1953). Molecular structure of nucleic acids: a structure for deoxyribose nucleic acid. *Nature* 171, 737-738.
- Weismann, A. (1883). On heredity. *Essays Upon Heredity and Kindred Problems* 1, 67-106.
- Weismann, A., Poulton, E.B., and Shipley, A.E. (1891). *Essays upon heredity and kindred biological problems*, Vol 1 (Clarendon press).
- Werbin, J.L., Avendaño, M.S., Becker, V., Jungmann, R., Yin, P., Danuser, G., and Sorger, P.K. (2017). Multiplexed Exchange-PAINT imaging reveals ligand-dependent EGFR and Met interactions in the plasma membrane. *Scientific Reports* 7, 12150.
- Wilkins, M.H.F., STOKES, A.R., and Wilson, H.R. (1953). Molecular structure of nucleic acids: molecular structure of deoxyribose nucleic acids. *Nature* 171, 738-740.
- Williamson, I., Lettice, L.A., Hill, R.E., and Bickmore, W.A. (2016). Shh and ZRS enhancer colocalisation is specific to the zone of polarising activity. *Development* 143, 2994-3001.
- Wilson, E.B. (1896). *The cell in development and heredity* (Macmillan).
- Witkin, E.M. (2005). Remembering Rollin Hotchkiss (1911-2004). *Genetics* 170, 1443-1447.
- Woodcock, C. (1973). Ultrastructure of inactive chromatin. Paper presented at: Journal of Cell Biology (ROCKEFELLER UNIV PRESS 1114 FIRST AVE, 4TH FL, NEW YORK, NY 10021).
- Woodcock, C., Safer, J., and Stanchfield, J. (1976). Structural repeating units in chromatin: I. Evidence for their general occurrence. *Experimental cell research* 97, 101-110.
- Woodcock, C.L., Skoultchi, A.I., and Fan, Y. (2006). Role of linker histone in chromatin structure and function: H1 stoichiometry and nucleosome repeat length. *Chromosome Research* 14, 17-25.
- Wu, C. (1980). The 5' ends of *Drosophila* heat shock genes in chromatin are hypersensitive to DNase I. *Nature* 286, 854-860.
- Wutz, G., Várnai, C., Nagasaka, K., Cisneros, D.A., Stocsits, R.R., Tang, W., Schoenfelder, S., Jessberger, G., Muhar, M., and Hossain, M.J. (2017). Topologically associating domains and

chromatin loops depend on cohesin and are regulated by CTCF, WAPL, and PDS5 proteins. *The EMBO journal* *36*, 3573-3599.

Xu, J., Ma, H., Jin, J., Uttam, S., Fu, R., Huang, Y., and Liu, Y. (2018). Super-resolution imaging of higher-order chromatin structures at different epigenomic states in single mammalian cells. *Cell reports* *24*, 873-882.

Yamada, N., Rector, L., Tsang, P., Carr, E., Scheffer, A., Sederberg, M., Aston, M., Ach, R., Tsalenko, A., and Sampas, N. (2011). Visualization of fine-scale genomic structure by oligonucleotide-based high-resolution FISH. *Cytogenetic and genome research* *132*, 248-254.

Yusufzai, T.M., Tagami, H., Nakatani, Y., and Felsenfeld, G. (2004). CTCF tethers an insulator to subnuclear sites, suggesting shared insulator mechanisms across species. *Molecular cell* *13*, 291-298.

Zaret, K.S. (2020). Pioneer Transcription Factors Initiating Gene Network Changes. *Annual Review of Genetics* *54*.

Zewdie, H. (1998). Computer simulation studies of liquid crystals: A new Corner potential for cylindrically symmetric particles. *The Journal of chemical physics* *108*, 2117-2133.

Zhang, D., Huang, P., Sharma, M., Keller, C.A., Giardine, B., Zhang, H., Gilgenast, T.G., Phillips-Cremens, J.E., Hardison, R.C., and Blobel, G.A. (2020). Alteration of genome folding via contact domain boundary insertion. *Nature Genetics* *52*, 1076-1087.

Zhang, H., Emerson, D.J., Gilgenast, T.G., Titus, K.R., Lan, Y., Huang, P., Zhang, D., Wang, H., Keller, C.A., Giardine, B., *et al.* (2019). Chromatin structure dynamics during the mitosis-to-G1 phase transition. *Nature* *576*, 158-162.

Zhang, R., Erler, J., and Langowski, J. (2017). Histone acetylation regulates chromatin accessibility: role of H4K16 in inter-nucleosome interaction. *Biophysical journal* *112*, 450-459.

Zhang, Z., and Pugh, B.F. (2011). High-resolution genome-wide mapping of the primary structure of chromatin. *Cell* *144*, 175-186.

Zhao, Z., Tavoosidana, G., Sjölander, M., Göndör, A., Mariano, P., Wang, S., Kanduri, C., Lezcano, M., Sandhu, K.S., and Singh, U. (2006). Circular chromosome conformation capture (4C) uncovers extensive networks of epigenetically regulated intra-and interchromosomal interactions. *Nature genetics* *38*, 1341-1347.

Zheng, X., Hu, J., Yue, S., Kristiani, L., Kim, M., Sauria, M., Taylor, J., Kim, Y., and Zheng, Y. (2018). Lamins organize the global three-dimensional genome from the nuclear periphery. *Molecular cell* *71*, 802-815. e807.

Zhou, G.-L., Xin, L., Song, W., Di, L.-J., Liu, G., Wu, X.-S., Liu, D.-P., and Liang, C.-C. (2006). Active chromatin hub of the mouse  $\alpha$ -globin locus forms in a transcription factory of clustered housekeeping genes. *Molecular and cellular biology* *26*, 5096-5105.

Zidovska, A., Weitz, D.A., and Mitchison, T.J. (2013). Micron-scale coherence in interphase chromatin dynamics. *Proceedings of the National Academy of Sciences* *110*, 15555-15560.

Zorn, C., Cremer, C., Cremer, T., and Zimmer, J. (1979). Unscheduled DNA synthesis after partial UV irradiation of the cell nucleus: distribution in interphase and metaphase. *Experimental cell research* *124*, 111-119.

Zorn, C., Cremer, T., Cremer, C., and Zimmer, J. (1976). Laser UV microirradiation of interphase nuclei and post-treatment with caffeine. *Human genetics* *35*, 83-89.

## REFERENCES

---

Zuin, J., Dixon, J.R., van der Reijden, M.I., Ye, Z., Kolovos, P., Brouwer, R.W., van de Corput, M.P., van de Werken, H.J., Knoch, T.A., and van IJcken, W.F. (2014). Cohesin and CTCF differentially affect chromatin architecture and gene expression in human cells. *Proceedings of the National Academy of Sciences* *111*, 996-1001.

## 7 APPENDIX

### 7.1 Abbreviations

3C	Chromosome conformation capture
3D	Three-dimensional
4C	Chromosome conformation capture-on-chip/circular chromosome conformation capture
4D	Four-dimensional
5C	chromosome conformation capture carbon copy
ANC	Active nuclear compartment
BAC	Bacterial artificial chromosome
bp	base pair
ChIP-seq	Chromatin immunoprecipitation with high-throughput sequencing
ChromHMM	Multivariate Hidden Markov based model for chromatin
CRISPR	Clustered regularly interspaced short palindromic repeats
DNA	Deoxyribonucleic acid
DNase I	Deoxyribonuclease I
DHS	DNase I hypersensitive site
EM	Electron microscopy
FAIRE-seq	Formaldehyde assisted isolation of regulatory elements
FISH	Fluorescence In Situ Hybridization
H3	Histone 3
H3K4me3	Histone 3 Lysine 4 tri-methylated
H3K9ac	Histone 3 Lysine 9 acetylated
H3K9me3	Histone 3 Lysine 9 tri-methylated
H3K27me3	Histone 3 Lysine 27 tri-methylation
H4K16ac	Histone 4 Lysine 16 acetylated
HDAC	Histone deacetylase
Hi-C	Chromosome conformation capture with high-throughput sequencing
HP1	Heterochromatin protein 1
INC	Inactive nuclear compartment
kb	kilo base
LAD	Lamina associated domain
Mb	mega base
MLN	Multilobulated nucleus/nuclei
MNase	Micrococcal nuclease
NRL	Nucleosome repeat length
ORCA	Optical reconstruction of chromatin architecture

## APPENDIX

---

PAINT	Points accumulation for imaging in nanoscale topography
PALM	Photoactivated localization microscopy
PCR	Polymerase chain reaction
PNA	Peptide nucleic acid
Repli-seq	Replication timing by next-generation sequencing
RNA	Ribonucleic acid
RNA pol II	RNA polymerase II
Seq	Sequencing
SIM	Structured illumination microscopy
SiR-DNA	Silicone rhodamine conjugated to Hoechst 33342
SMLM	Single molecule localization microscopy
STED	Stimulated emission depletion
STORM	Stochastic optical reconstruction microscopy
TAD	Topologically associating domain
TALE	Transcription activator-like effector

## 7.2 Declaration of contribution

### COHESIN DEPLETED CELLS REBUILD FUNCTIONAL NUCLEAR COMPARTMENTS AFTER ENDOMITOSIS

Marion Cremer\*, Katharina Brandstetter\*, Andreas Maiser, Suhas S. P. Rao, Volker J. Schmid, Miguel Guirao-Ortiz, Namita Mitra, Stefania Mamberti, Kyle N. Klein, David M. Gilbert, Heinrich Leonhardt, M. Cristina Cardoso, Erez Lieberman Aiden, Hartmann Harz & Thomas Cremer (\*equal contribution)

The two first authors Marion Cremer and Katharina Brandstetter, as well as the corresponding author Thomas Cremer and supervisor Heinrich Leonhardt, hereby declare their mutual recognition of the shared first authorship of Katharina Brandstetter and Marion Cremer. The equal weighting of the contributions of both authors is justified below:

In the initial phase, Marion Cremer carried out a series of exploratory experiments on the questions of the project, which set the framework for in-depth and further experimental investigations. She has taken over the coordination of the participating working groups from the USA and the writing of the manuscript for the most part.

Katharina Brandstetter further elaborated the initial findings in extensive experiments and carried out additional experiments as well as quantitative evaluations, which contributed significantly to the quality and content of the publication. Her demanding and complex experiments using live-cell microscopy should be mentioned here, with which she was able to gain new and unexpected insights into the mitotic behavior of cells after depletion of cohesin in long-term observations. She was also responsible for the data compilation and was significantly involved in the statistical analysis. In numerous discussions she made important and further contributions to the experimental realization of the project and to the drafting of the manuscript.

---

Marion Cremer

---

Katharina Brandstetter

---

Thomas Cremer

---

Heinrich Leonhardt

The contribution of all authors to this publication can be seen in the section below, as written in the publication:

Thomas Cremer and Erez Lieberman Aiden initiated the study; Marion Cremer and Thomas Cremer conceived microscopic experiments together with Hartmann Harz, **Katharina Brandstetter** and Andreas Maiser. **Katharina Brandstetter**, Marion Cremer and Andreas Maiser performed experiments shown in figures 1-4, 6, 8 and supplementary figures 1a, 2-7. Andreas Maiser and **Katharina Brandstetter** performed live-cell and super-resolution/confocal microscopy; Hartmann Harz provided input on quantitative image analysis, including statistical analysis. Andreas Maiser performed segmentation analysis and Volker J. Schmid image analyses for chromatin density mapping data; Miguel Guirao-Ortiz performed 3D rendering of nuclei. Stefania Mamberti performed RAD21-mClover intensities by high-throughput imaging and DNA Halo experiments with support of M. Cristina Cardoso shown in Supplementary figures 1b and 8. Hi-C data were generated by Suhas S.P. Rao and Erez Lieberman Aiden with experimental support of Namita Mitra (Figure 5). Repli-Seq data (Figure 7) were provided by David M. Gilbert and Kyle N. Klein. Heinrich Leonhardt provided input for the 3D imaging part and M. Cristina Cardoso for the replication part. Marion and Thomas Cremer wrote the manuscript with support from all authors, in particular from Erez Lieberman Aiden.

## SITE-SPECIFIC ANTIBODY FRAGMENT CONJUGATES FOR REVERSIBLE STAINING IN FLUORESCENCE MICROSCOPY

Jonathan Schwach, Ksenia Kolobynina, **Katharina Brandstetter**, Marcus Gerlach, Philipp Ochtrop, Jonas Helma, Christian P.R. Hackenberger, Hartmann Harz, M. Cristina Cardoso, Heinrich Leonhardt, Andreas Stengl

Heinrich Leonhardt and Andreas Stengl conceived the study. Jonathan Schwach and Andreas Stengl performed experiments. **Katharina Brandstetter** performed spinning disk confocal imaging with the help of Hartmann Harz and generated the corresponding panels in figures 4 and S4. Jonathan Schwach wrote the manuscript with help from Andreas Stengl. **Katharina Brandstetter** assisted in manuscript proofreading.

---

Katharina Brandstetter

---

Heinrich Leonhardt

COMPARISON OF DNASE I HYPERSENSITIVE AND INSENSITIVE CHROMATIN IN HUMAN CELLS BY SUPER-RESOLUTION MICROSCOPY AND COMPUTER SIMULATIONS

**Katharina Brandstetter\***, Tilo Zülske\*, Tobias Ragozy, David Hörl, John Stamatoyannopoulos, Heinrich Leonhardt, Gero Wedemann, Hartmann Harz (\*equal contribution)

Manuscript in preparation

This study was conceived and supervised by Hartmann Harz, Gero Wedemann, John Stamatoyannopoulos and Heinrich Leonhardt. **Katharina Brandstetter** designed and performed all microscopic experiments including sample preparation and STED imaging shown in figures 1, 2, 4a, 5a and supplementary figures 3, 4. In addition to the interpretation of the microscopic data, **Katharina Brandstetter** was responsible for the data compilation and project coordination. Tobias Ragozy designed probes and provided input on sample preparation. **Katharina Brandstetter** analyzed and interpreted published ENCODE genome browser data with help from Tobias Ragozy (Supplementary figures 1, 2). David Hörl wrote scripts for microscope automation and image analysis (Supplementary figure 5). Tilo Zülske performed computational modeling with input from Gero Wedemann (Figures 3, 4b-j, 5b-g, Supplementary figures 6, 7). **Katharina Brandstetter** prepared all figures (besides Supplementary figures 6 and 7). The manuscript was written by Hartmann Harz, Gero Wedemann and **Katharina Brandstetter**.

---

Tilo Zülske

---

Katharina Brandstetter

---

Hartmann Harz

---

Heinrich Leonhardt

